UNIVERSITÀ
DEGLI STUDI
DI PADOVA

Sede Amministrativa: Università degli Studi di Padova

Dipartimento di Geoscienze

DOTTORATO DI RICERCA IN SCIENZE DELLA TERRA

CICLO XXVIII

CONTRIBUTION TO THE LATE TRIASSIC GEOCHRONOLOGY BY MAGNETOSTRATIGRAPHIC CORRELATIONS BETWEEN TETHYAN MARINE SECTIONS AND THE NEWARK APTS

(CONTRIBUTO ALLA GEOCRONOLOGIA DEL TRIASSICO SUPERIORE TRAMITE CORRELAZIONI MAGNETOSTRATIGRAFICHE TRA SEZIONI MARINE TETIDEE E IL NEWARK APTS)

Coordinatore : Ch.mo Prof. Fabrizio Nestola

Supervisori : Ch.mo Dott. Manuel Rigo

Ch.mo Prof. Giovanni Muttoni

Dottorando : Matteo Maron

"Die Erde kann zu einer bestimmten Zeit durchaus nur ein Aussehen gehabt haben. Direkte Auskunft hierüber gibt sie nicht. Wir stehen ihr gegenüber wie der Richter gegenüber einem Angeklagten, der jede Auskunft verweigert, und haben die Aufgabe, die Wahrheit auf dem Wege des Indizienbeweises zu ermitteln."

"At a specified time the Earth can have just one configuration. But the Earth supplies no direct information about this. We are like a judge confronted by a defendant who declines to answer, and we must determine the truth from the circumstantial evidence."

(Alfred Wegener, 1920, Die Entstehung der Kontinente und Ozeane/The Origin of Continents and Oceans)

"It strikes me that all our knowledge about the structure of our Earth is very much like what an old hen would know of the hundred-acre field in a corner of which she is scratching."

(Charles Darwin, 1831, Letter to William Darwin Fox)

SUMMARY

ACKNOWLEDGMENTS

I wish to thank my supervisors dr. Manuel Rigo (University of Padova) and prof. Giovanni Muttoni (University of Milano) that gave me the opportunity of this PhD. Thanks for your valuable lessons, for your support and help during those years working together. Thanks to prof. Muttoni that give the opportunity to use the instruments at the Alpine Paleomagnetic Laboratory (ALP) in Peveragno (Cuneo, Italy).

Special thanks to my officemates (and friends) Stefania Sorgato and Mariachiara Zaffani for putting up with me for these years. Thanks for all the great moments together, I am very lucky to have you as friends. I will miss our lunches at the (cheap) Chinese, the Mariachiara's army of handmade Minions above her computer case, the inevitable Stefania's playlist of Michael Bublé songs at Christmas and many other things of our office life.

A special thank to Anna Breda, Nereo Preto, Guido Roghi, Jacopo Dal Corso, Giovanni Gattolin, Angela Bertinelli, Manuela Casacci and Leonardo Solazzi for their helping in the field.

Thanks to those who helped me with the paleomagnetic analyses (and saved me from weeks alone) at the paleomagnetic laboratory in Peveragno (Marta and Leonardo).

Thanks to the people of the paleomagnetic laboratory of "Fort Hoofddijk" (Utrecht, The Netherlands) for the great moments and the free alcohol. A special thanks to Wout Krijgsman, Mark Dekkers, Cor Langereis, Marco Maffione, Maxim Krasnoperov, Annique van der Boon, Nathan Marshall and Christiaan van Baak for their help and support during my period at the "Fort".

Thanks to prof. Wout Krijgsman (Utrecht University) and prof. Valerian Bachtadse (Ludwig-Maximilian University of Munich) that have been so kind to read and evaluate my thesis. I am thankful for your suggestions, and I am glad that you find my thesis interesting.

Thanks to all my friends for all the good times together that made me forget about problems and displeasures.

I am extremely grateful to my parents Antonio and Sandra that always support me in my choices. I am here, presenting my PhD research, thanks to their sacrifices and struggles. Maybe "thank you" sounds reductive, but these two simple words enclose all my gratitude and respect for them.

THESIS OUTLINE

This PhD thesis is subdivided in six chapters.

Chapter I is the state of the art of the Late Triassic chronology. In this part I present the chronostratigraphic organization of the Late Triassic, the history of the Stages (Carnian, Norian and Rhaetian), a detailed explanation of the last options of Late Triassic geochronology, and the aim of my research.

Chapter II represents an introduction to the concepts of paleomagnetism (geomagnetism, magnetic properties of materials, etc.) and to the methods of analysis (instruments, techniques, evaluation of data reliability, etc.).

I present the geological setting of the investigated areas in **Chapter III**, focused mainly on the Late Triassic, and a brief introduction to the stratigraphic sections studied for magnetostratigraphy.

Chapter IV is the discussion of the paleomagnetic data obtained during my PhD. I subdivided the chapter by the considered time intervals: Rhaetian and Carnian Stages. Within these subchapters, I report the results for each Tethyan marine section investigated, with the detailed description of litho- and biostratigraphy, the paleomagnetic data and their interpretation, and the discussion about the magnetostratigraphic correlations here proposed.

In **Chapter V**, I propose an updated Geomagnetic Polarity Time Scale (GPTS) for the Late Triassic, based on literature and on the magnetostratigraphic correlations between Tethyan marine sections and the Newark APTS presented in Chapter IV. In this Chapter, I propose new ages for the Stage boundaries derived from the GPTS.

Chapter VI is the conclusive part of the thesis. It includes a part regarding the magnetostratigraphy of the studied Tethyan marine sections, subdivided as Chapter IV (Rhaetian and Carnian subchapters), and a part about the proposal of GPTS.

ABSTRACT

Chronology of Late Triassic (last Epoch of Triassic Period) is still a debated question. Late Triassic is constrained by two U/Pb ages, one near the Ladinian/Carnian boundary (237.773±0.052 Ma; Alpe di Siusi/Seiser Alm, Italy) and the other at the Rhaetian/Hettangian boundary (201.36±0.17 Ma; Levanto, Peru). Unfortunately, any radiometric age constraints the Stage boundaries of Late Triassic. Many attempts to assign an age to the Stages have been made during the last 20 years, correlating marine sections (usually from Tethys) with the Newark Astrochronological Polarity Time Scale (Newark APTS). The ages obtained was sometimes very different, in particular for the Rhaetian, with a duration that varied from ~2 My to ~9 My depending from the correlation performed with the APTS. The options proposed in the Geological Time Scale 2012 introduced two different ages for both Rhaetian (~205.4 Ma and ~209 Ma) and Norian (~221 Ma and ~228 Ma). The Norian age of ~228 Ma seems coherent with many other correlations between marine sections and the APTS. In an effort to help resolving the issues of the Late Triassic chronology, selected Tethyan marine sections, characterized by a detailed biostratigraphy, have been analyzed for paleomagnetism. The investigation are focused on two main intervals: the Rhaetian and the Carnian. The Rhaetian have been chosen for the reasons explained before (confused chronology), the Carnian because the few magnetostratigraphic data covering this interval, in particular its middle part, must be integrated to obtain a continuous magnetostratigraphy of this Stage. The chosen sections are: Pignola-Abriola, Mount Messapion and the ODP Leg 122-Hole 761C for the Rhaetian; Pignola-2, Dibona, and ODP Leg 122-Holes 759B/760B for the Carnian. The magnetostratigraphy of these sections have been integrated with the data from other Tethyan sections in literature, obtaining a continuous magnetostratigraphy spanning the entire Late Triassic. This composite magnetostratigraphy of Tethyan section has been time-calibrated using the Newark APTS, linked to the composite through the statistical correlations with Pignola-2, Pizzo Mondello, and Pignola-Abriola. The so obtained Geomagnetic Polarity Time Scale (GPTS) has been used to assign an age to the events calibrated to the magnetostratigraphy of the Late Triassic, like the bioevents defining the Stage and substage boundaries, or climatic events as the Carnian Pluvial Event.

RIASSUNTO

La cronologia del Triassico Superiore (l'ultima Epoca del Periodo Triassico) è attualmente materia di dibattito. Il Triassico Superiore e vincolato da due età radiometriche U/Pb, una in prossimità del limite Ladinico/Carnico (237.773±0.052 Ma; Alpe di Siusi/Seiser Alm, Italia) e l'altra al limite Retico/Hettangiano (201.36±0.17 Ma; Levanto, Perù). Purtroppo, nessuna altra età radiometrica vincola direttamente gli altri Piani del Triassico Superiore. Negli ultimi 20 anni sono stati fatti numerosi tentativi di assegnare delle età ai Piani, correlando sezioni marine (solitamente della Tetide) con il Newark Astrochronological Polarity Time Scale (APTS). Le età ottenute sono state talvolta molto diverse, in particolare per il Retico, con una durata variabile da ~2 My a ~9 My a seconda della correlazione con l'APTS. Le opzioni proposte nella Geologic Time Scale 2012 hanno proposto due età diverse sia per il Retico (~204.5 Ma e ~209 Ma) che per il Norico (~221 Ma e ~228 Ma). L'età di ~228 Ma per il Norico sembra coerente con molte altre correlazioni tra sezioni marine e l'APTS. Nel tentativo di contribuire alla risoluzione dei problemi della cronologia del Triassico Superiore, sono state effettuate delle analisi paleomagnetiche su una serie di sezioni marine Tetidee caratterizzate da una biostratigrafia dettagliata. Le indagini sono focalizzate su due principali intervalli di tempo: il Retico e il Carnico. Il Retico è stato scelto per le ragioni spiegate precedentemente (cronologia confusa), il Carnico perché i pochi dati di magnetostratigrafia, in particolare nel Carnico medio, devono essere integrati per ottenere un record completo di questo Piano. Le sezioni scelte per le analisi sono: Pignola-Abriola (Italia), Monte Messapion (Grecia) e Leg 122-Hole 761C dell'ODP (Australia) per il Retico; Pignola-2 (Italia), Dibona (Italia) e Leg 122-Hole 759B/760B dell'ODP (Australia) per il Carnico. I dati di magnetostratigrafia di queste sezioni sono stati integrati con dati da altre sezioni Tetidee in letteratura, ottenendo una magnetostratigrafia continua dell'intero Triassico Superiore. Tale composita è stata calibrata con la Newark APTS, usando come collegamento le correlazioni statistiche tra l'APTS e le sezioni di Pignola-2, Pizzo Mondello e Pignola-Abriola. La Scala-Tempo delle Polarità Geomagnetiche (Geomagnetic Polarity Time Scale – GPTS) così ottenuta è stata usata per assegnare un'età agli eventi calibrati con la magnetostratigrafia del Triassico Superiore, come ad esempio i bioeventi che definiscono i limiti dei Piani e dei sottopiani, oppure gli eventi climatici come il Carnian Pluvial Event.

Chapter I
STATE OF THE ART

1.1 LATE TRIASSIC

Late Triassic is the last Epoch of the Triassic Period. It lasted ~36 My and represents the 70% of the entire Triassic. It is subdivided in three Stages: Carnian, Norian and Rhaetian (as recognized by the Subcommission on Triassic Stratigraphy) (Fig. 1.1). The Carnian has been divided in two substages: Julian and Tuvalian, whereas the Norian has three substages: Lacian, Alaunian and Sevatian (Fig. 1.1).

Carnian, Norian and Rhaetian (and other Triassic Stages) have been originally defined with ammonoid-rich successions of the Northern Calcareous Alps (e.g. Mojsisovics, 1869), in the tentative to unbind the Triassic to the classical definition of von Alberti (1834). The original Triassic was defined on three subsequent continental and shallow-marine German succession: the Buntsandstein, the Muschelkalk and the Keuper. These three formations were diffused in all the southern Germany, but they are difficult to correlate beyond this area. This is why the ammonoid-defined Triassic Stages were preferred to the old definition of the Period.

The base of the of the Carnian Stage (base of the upper Triassic Series) is defined by a GSSP (Global Stratotype Section and Point) located in the Prati di Stuores/ Stuores Wiesen section (Italy, Broglio Loriga et al., 1999; Mietto et al., 2012). The age of the Carnian base is placed at ~237 Ma, confirmed by the U/Pb age obtained from an ash-bed in Seiser Alm/Alpe di Siusi area of 237.773±0.052 Ma (Mietto et al., 2012), biostratigraphically constrained in upper Ladinian (*"Anolcites" neumayiri*/*"Frankites" regoledanus* ammonoid subzones of *Protrachyceras* Zone).

The upper limit of the Late Triassic is defined by the GSSP for the base of the Jurassic System (Hettangian Stage) in the Kuhjoch section (Austria, Hillebrandt et al., 2013). The base of Hettangian is dated at 201.36±0.17 Ma (U/Pb) from ash-beds around the FO of *Psiloceras spelae* in northern Peru (Schoene et al., 2010; Guex et al., 2012; Wotzlaw et al., 2014). The bases of the Norian and the Rhaetian Stages, instead, still not have a ratified GSSP. The candidates of GSSP for the Norian are the Pizzo Mondello (Italy; Muttoni et al., 2004) and the Black Bear Ridge sections (Canada; Orchard et al., 2007), and for the Rhaetian are the Steinbergkogel (Austria; Krystyn et al., 2007a, 2007b) and the Pignola-Abriola sections (Italy; Rigo et al., 2015).

Here follows a detailed description of the Late Triassic Stages and their history.

1.1.1 Carnian

The Carnian was named after the Kärnten (Carinthia) region of Austria, or from the near Carnian Alps, and it was originally associated to the Hallstatt Limestone beds bearing *Trachyceras* and *Tropites* ammonoids (Mojsisovics, 1869). The base of the Carnian was traditionally associated with the FO of ammonoids *Trachyceras* (*T. aon* in Tethys or *T. desatoyense* in North America), although the presence of these ammonoids is asynchronous and not global (e.g. Mietto and Manfrin, 1999). Broglio Loriga et al (1999) proposed the levels recording the FAD of ammonoid *Daxatina canadensis* at the Prati di Stuores/ Stuores Wiesen locality (Dolomites, Italy) as the GSSP of the Carnian, then ratified in 2008 (Mietto et al., 2012). Other markers are the FO of conodont *Paragondolella polygnathiformis* and palynomorphs *Patinasporites densus* and *Vallasporites ignacii*. The Carnian GSSP at Prati di Stuores is just above the base of a normal magnetozone (S2n in Broglio Loriga et al., 1999; Mietto et al., 2012) and a maximum flooding surface within sequence Car1 (*sensu* Gianolla et al., 1998a; named Lad3 in Hardenbol et al., 1998), recognized at least in Tethyan basins (Hardenbol et al., 1998). The Carnian Stage has been subdivided in three substages (Mojsisovics et al., 1895): Cordevolian, Julian and Tuvalian. In recent times, the Cordevolian has been normally included as lower

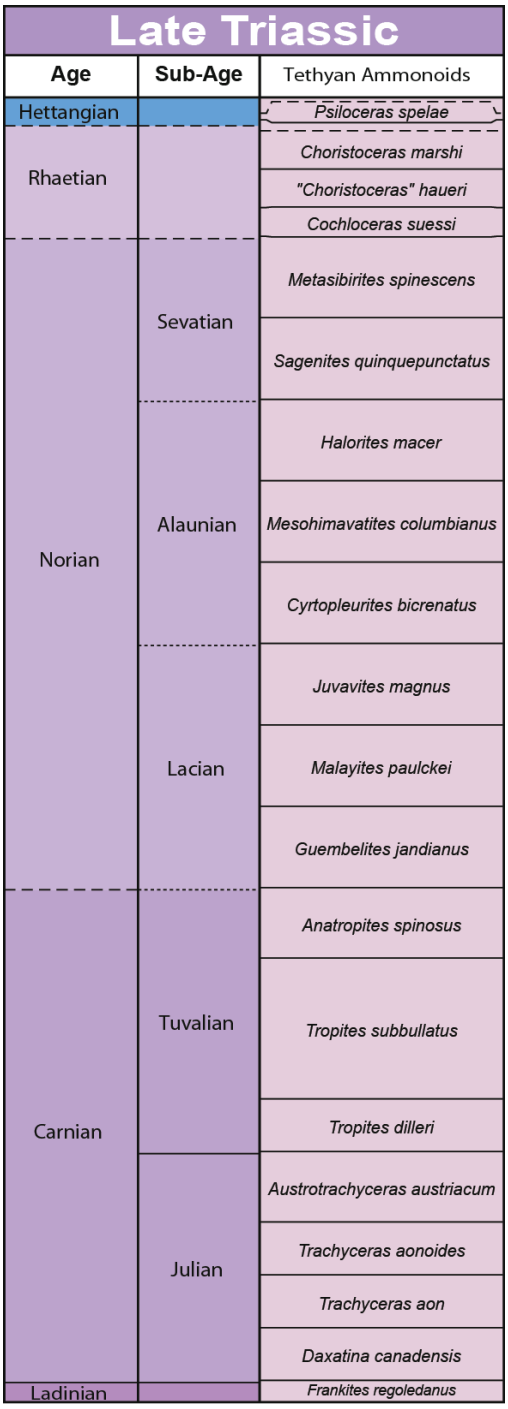

Figure 1.2: Late Triassic geochronology and relative ammonoid biozones. (modified from Gradstein et al., 2012)

Julian. The boundary between Julian and Tuvalian is usually placed with the FO of ammonoids *Tropites* (*T. subullatus* in Tethys, *T. dilleri* in North America) (Fig. 1.1). This boundary is characterized by an important biotic turnover that includes ammonoids, conodonts and radiolarians (Tozer, 1984; Simms and Ruffell, 1989; Kozur and Bachmann, 2010; Mazza et al., 2010). A climate change occurs at the end of the Julian, known as Carnian Pluvial Event (Simms and Ruffel, 1989), Reingraben turnover (Schlager and Schöllnberger, 1974), or Middle Carnian Wet Intermezzo (Kozur and Bachmann, 2010). The decrease in carbonatic fraction in the oceanic basins and the deposition of shales in restricted basins have been interpreted as a rise of the Calcite Compensation Depth (Rigo et al., 2007). The CPE is intended as global, probably triggered by both paleogeographic/oceanographic variations, as well as volcanic events (emplacement of Wrangellia Large Igneous Province; Furin et al., 2006; Dal Corso et al., 2012).

1.1.2 Norian

The name Norian derives from the Roman province of Noria, including the area of Hallstatt (Austria), where Mojsisovics (1869) defined the Stage with strata containing the ammonoid *Pinacoceras metternichi*. Originally, Mojsisovics considered the Norian as older than Carnian, but he recognized the error and change the name of Norian in Juvavian, and calling "Norian" the Hallstatt limestones below the Carnian strata (Mojsisovics, 1892). This created confusion, and Bittner (1892) propose to maintain the orginal name Norian for the strata younger than Carnian and to refer to the older strata as Ladinian.

In North America the beginning of the *Stikinoceras kerri* ammonoid Zone is considered coeval to the base of the Norian (in Tethys is approximated by the *Guembelites jandianus* Zone; Fig. 1.1). The FO of conodont *Metapolygnathus* ex gr. *M. echinatus* approximates the base of the *S. kerri* Zone (Orchard, 2010), and is also approximated with the FO of the bivalves *Halobia austriaca* and *Halobia beyrichi* (McRoberts, 2007). The FO of *M. echinatus* and *H. austriaca* appear associated also in Tethys (e.g. Balini et al., 2010). GSSP candidates for the Norian Stage are Pizzo Mondello in Italy (Muttoni et al., 2001, 2004; Nicora et al., 2007; Balini et al., 2010; Mazza et al., 2012) and Black Bear Ridge in British Columbia (Orchard et al., 2001; Orchard, 2007; McRoberts, 2007). In both the candidate stratigraphic sections, the GSSP corresponds to the level bearing the FAD of conodont *Metapolygnathus echinatus* and is approximated by the FO of bivalve *Halobia austriaca*. In Pizzo Mondello section the Norian base is approximated also by the Last Occurrence

Halobia lenticularis (Balini et al., 2010). Pizzo Mondello section is accompanied by magnetostratigraphy, with the base of the Norian corresponding with the top of a reverse magnetozone (PM4r; Muttoni et al., 2001, 2004) and just above a positive $\delta^{13}C_{carb}$ shift (Nicora et al., 2007; Muttoni et al., 2014). Norian is subdivided in three substages: Lacian, Alaunian and Sevatian. The Lacian/Alaunian boundary is usually defined with the base of the *Cyrtopleurites bicrenatus* ammonoid Zone in Tethys (Fig. 1.1). The Alaunian/Sevatian boundary corresponds to the beginning of the *Gnomohalorites cordilleranus* ammonoid Zone in North America and *Sagenites quinquepunctatus* ammonoid Zone in Tethys (Fig. 1.1). The Sevatian creates problems in defining the base of the Rhaetian. In Tozer (1994) the Rhaetian was not recognized and the Sevatian included the ammonoid Zones traditionally attributed to Rhaetian (*Choristoceras marshi* and *Ch. haueri* Zones). In Krystyn et al. (2007b) the ammonoid Zones *Paracochloceras suessi*/*Sagenites reticulatus*, usually referred to upper Sevatian (uppermost Norian), have been included in the Rhaetian, concurrent with the FO of conodont *Misikella posthernsteini*.

1.1.3 Rhaetian

The Rhaetian Stage has been defined first time by von Gümbel (1859) as "Rhätische Gebilde", with the first occurrence of bivalve *Rhaetavicula contorta* in the Kössen Beds (Austria). The name comes both from the Rhätische Alps and the Roman province of Rhaetium. The Rhaetian was included as the last Stage of the Late Triassic by Mojsisovics et al. (1895), defined as *Avicula contorta* Zone.

Since then, the Rhaetian has been recognized as a Stage (e.g. Pearson, 1970; Ager, 1987), considered a substage of the Norian (e.g. Tozer, 1967; Silberling and Tozer, 1968; Zapfe, 1974; Palmer, 1983) or the first Stage of the Jurassic (with the name of Bavarian; Slavin, 1961, 1963). However, most of the specialists in Triassic stratigraphy (e.g. Kozur and Mock, 1974; Gazdicki et al., 1979; Krystyn 1980, 1990) considered the Rhaetian a Stage of the Late Triassic. In Zapfe (1983) is presented the last report of the International Geoscience Programme (IGCP) 4, in which the Rhaetian is formally included in the Triassic timescale, but only for the Tethyan realm. Only in 1991 the Rhaetian was officially considered a Stage by the Subcommission on Triassic Stratigraphy (STS). Although the Rhaetian is now widely accepted, it lacks of a formal marker defining its base. Kozur (1973) place the base of the Rhaetian with the first appearance (FAD) of the conodont *Misikella posthernsteini*, well distributed in the Tethys but rare in the western margin of Pangea (i.e. North America). The FAD of *M. posthernsteini* is considered almost

coeval with the *Proparvicingula moniliformis* radiolarian Zone (e.g. Kozur, 2003; Giordano et al., 2011; Rigo et al., 2015). Following this last correlation between conodonts and radiolarians, the FAD of *M. posthernsteini* in North America is younger than in Tethys, and the Norian/Rhaetian boundary is approximated by the FAD of the conodont *Epigondolella mosheri* morphotype A (Carter and Orchard, 2007). Recently, the Task Group for Rhaetian Stage placed the base of the Rhaetian with the First Occurrence (FO) of *M. posthersteini* (Krystyn, 2010), also suggesting the following secondary markers:

- the FO of the ammonoid *Paracochloceras suessi* and genus *Cochloceras* (Fig. 1.1)
- the Last Occurrence (LO) of ammonoid genus *Metasibirites* (Fig. 1.1)
- the FO of conodont *E. mosheri* morphotype A
- the FO of the radiolarian *P. moniliformis* and the beginning of the *P. moniliformis* Zone
- the LO of large *Monotis* bivalves, except for the dwarf species (only in Tethys; McRoberts et al., 2008)
- just below a prominent change of magnetic polarity after a long prominent normal magnetozone to a thinner reversal (as seen in many sections of Tethys).

Although ammonoid biostratigraphy is still considered one of the best tool for high-resolution geochronology and correlations in the Triassic (Balini et al., 2010), Norian and Rhaetian ammonoids are documented mostly locally. Conodonts and radiolarians are instead more common and normally used for correlations and geochronological definitions in the Triassic. The use of *Misikella posthernsteini* as a marker of the Norian/Rhaetian boundary (NRB) is widely used, in particular in Tethyan sections. This bioevent has been identified in both the GSSP candidates for the Rhaetian Stage (Steinbergkogel section, Austria; Pignola-Abriola section, Italy).

The Steinbergkogel section (Krystyn et al., 2007a, 2007b) is a pelagic succession of condensed limestone with conodonts, ammonoids and bivalves. The section was named STK-A to differentiate it to the parallel section STK-B+C. In Steinbergkogel three possible markers have been proposed: FO of *Misikella hernsteini* (Krystyn et al., 2007a, 2007b), corresponding to the FO of *Mockina mosheri* morphotype A and close to the FO of ammonoids *Tragorhacorecas* and *Rhaetites*; FAD of *Misikella posthernsteini* (Krystyn et al., 2007a, 2007b), coeval to the base of *Proparvicingula moniliformis* radiolarian Zone and the FO of *Paracochloceras*

suessi; FAD of ammonoid *Vandaites* (Krystyn et al., 2007b), in association with FO of *Cycloceltites* and *Choristoceras* and LO of *Sagenites*, *Dionites* and *Pinacoceras*. The Steinbergkogel section is accompanied by magnetostratigraphy in both STK-A and STK-B+C.

The Pignola-Abriola section (Rigo et al., 2015) is a pelagic succession of cherty limestones with conodonts, radiolarians and bivalves. The section is accompanied by a detailed magnetostratigraphy (presented here in Chapter 4.1.1 and in Maron et al., 2015) and $\delta^{13}C_{org}$ chemostratigraphy (Rigo et al., 2015). The identification of the NRB in Pignola-Abriola section have been proposed with a major negative $\delta^{13}C_{org}$ spike (~-30‰) occurring ~0.5 m below the FAD of *Misikella posthernsteini* and the beginning of *Proparvicingula moniliformis* radiolarian Zone.

1.2 LATE TRIASSIC GEOCHRONOLOGY

The Late Triassic is chronologically constrained at its lower (Ladinian/Carnian) and upper boundary (Rhaetian/Hettangian). In uppermost Ladinian a U/Pb age of 237.773±0.052 Ma (Mietto et al., 2012) was obtained from an ash-bed in Rio Nigra section (Alpe di Siusi/Seiser Alm), biostratigraphically constrained in upper Longobardian (*Protrachyceras* ammonoid Zone, *"Anolcites" neumayri*/*"Frankites" regoledanus* subzones), the last substage of the Ladinian. Using this chronostratigraphic data, Mietto et al. (2012) approximated the age of the Ladinian/Carnian boundary at ~237 Ma. The age assigned to the Rhaetian/Hettangian boundary (201.31±0.18 Ma) was obtained from U/Pb datings (Schoene et al., 2010; Guex et al., 2012) in ash-beds around the FO of ammonoid *Psiloceras spelae* (considered a marker of the Hettangian base; e.g. Guex et al., 2004; Morton and Hesselbo, 2008; Hillebrandt et al., 2013), in a section near Levanto (northern Peru). This age has been recalculated using new tracer calibration by Wotzlaw et al. (2014), obtaining an age for the Rhaetian/Hettangian boundary of 201.36±0.17 Ma. Thus, the base and the top of the Late Triassic are well constrained by radiometric ages, and the correspondent GSSPs, which are the base of the Carnian and base of the Hettangian stages, have been ratified. Instead, the bases of the Norian and the Rhaetian lack of a clear definition. In facts, no radiometric datings (U/Pb, Ar/Ar, etc.) have been provided for those sections characterized by clear biostratigraphic markers of the Stage boundaries, with the only exception of the U/Pb age of 230.91±0.33 Ma, obtained from the Aglianico ash-bed in the Pignola-2 section (Italy, Furin et al., 2006). Hence, there were no possibilities to time calibrate Stages and substages, until in the 1990s the detailed magnetostratigraphic study of the

Newark Basin sedimentary sequence (eastern USA) by Kent et al. (1995) paved the way to a new approach in defining the chronology of the Late Triassic.

1.2.1 The Newark Astrochronological Polarity Time Scale (Newark APTS)

The Newark Supergroup is a continental sedimentary/volcanic sequence deposited during the Late Triassic/earliest Jurassic (Cornet and Olsen, 1985) in a series of rift basins in eastern North America, originated during the initial rift of Pangea. The Newark sedimentary sequence is partially exposed, and most of the sequence comes from a series of cores drilled in different part of the Newark Basin, the most extended rift basin of the Newark Supergroup. The Late Triassic portion is represented by lacustrine/alluvial sediments, organized in three formations: Stockton Fm., Lockatong Fm., and Passaic Fm (Olsen, 1980; Olsen et al., 1996) (Fig. 1.2). The Stockton Fm is dominated by fluvial sequences, with brownish and red conglomerates and arkoses, passing to mudstone in the upper part. The Lockatong Fm is instead typical of lacustrine environment, with prevalent gray mudstone. The Passaic Fm is characterized by red mudstone with sandstone and conglomerate, indicating a filling of the lacustrine basin. Van Houten (1964, 1969, 1980) recognized a hierarchy of lacustrine cycles in the Lockatong Fm, ascribing them to astronomical control of climate. Olsen (1986) recognized these cycles also in the Passaic Fm. Four types of cycles have been identified: Van Houten cycle (~20 kyr; precession cycle), short modulating cycle, McLaughlin cycle (~404 kyr; eccentricity cycle), long modulating cycle. The McLaughlin cycles (McLaughlin, 1933) have the strongest expression in the sedimentary sequence and they have been considered as stratigraphic members (e.g. Kent et al., 1995; Olsen et al., 1996). Later, at the 52 McLaughlin cycles of the Lockatong and Passaic Fms (Olsen et al., 1996), 8 new cycles of the same type have been identified in the upper Stockton Fm (Raven Rock Member) (Kent and Olsen, 1999; Olsen and Kent, 1999) (Fig. 1.2). The Late Triassic sedimentary sequence of the Newark Supergroup is topped by three basalt flows, Hettangian in age (Orange Mt. Basalts, Preakness Basalts, Hook Mt. Basalts) (Fig. 1.2), alternated with two sedimentary formations (Feltville and Towaco Fms), and overlied by the sedimentary Boonton Fm. The basalt flows have been ascribed to the emplacement of the CAMP – Central Atlantic Magmatic Province (Marzoli et al., 1999, 2004).

Kent et al. (1995) performed a detailed magnetostratigraphic investigation on the cores from the Newark Basin stratigraphic sequence, covering more than 5000 m from the Feltville Fm to the base of the Stockton Fm. The final composite of Newark

magnetostratigraphy included 45 magnetozones from E1r to E23n, where E23n have been extended to Boonton Fm following the magnetostratigraphy of the Newark outcrops of Witte et al. (1991). Later, Kent and Olsen (1999) and Olsen and Kent (1999) considered the E23n.2r as a magnetozone, changing its name in E23r. As a consequence, the normal magnetozone above E23r was named E24n (Fig. 1.2). The

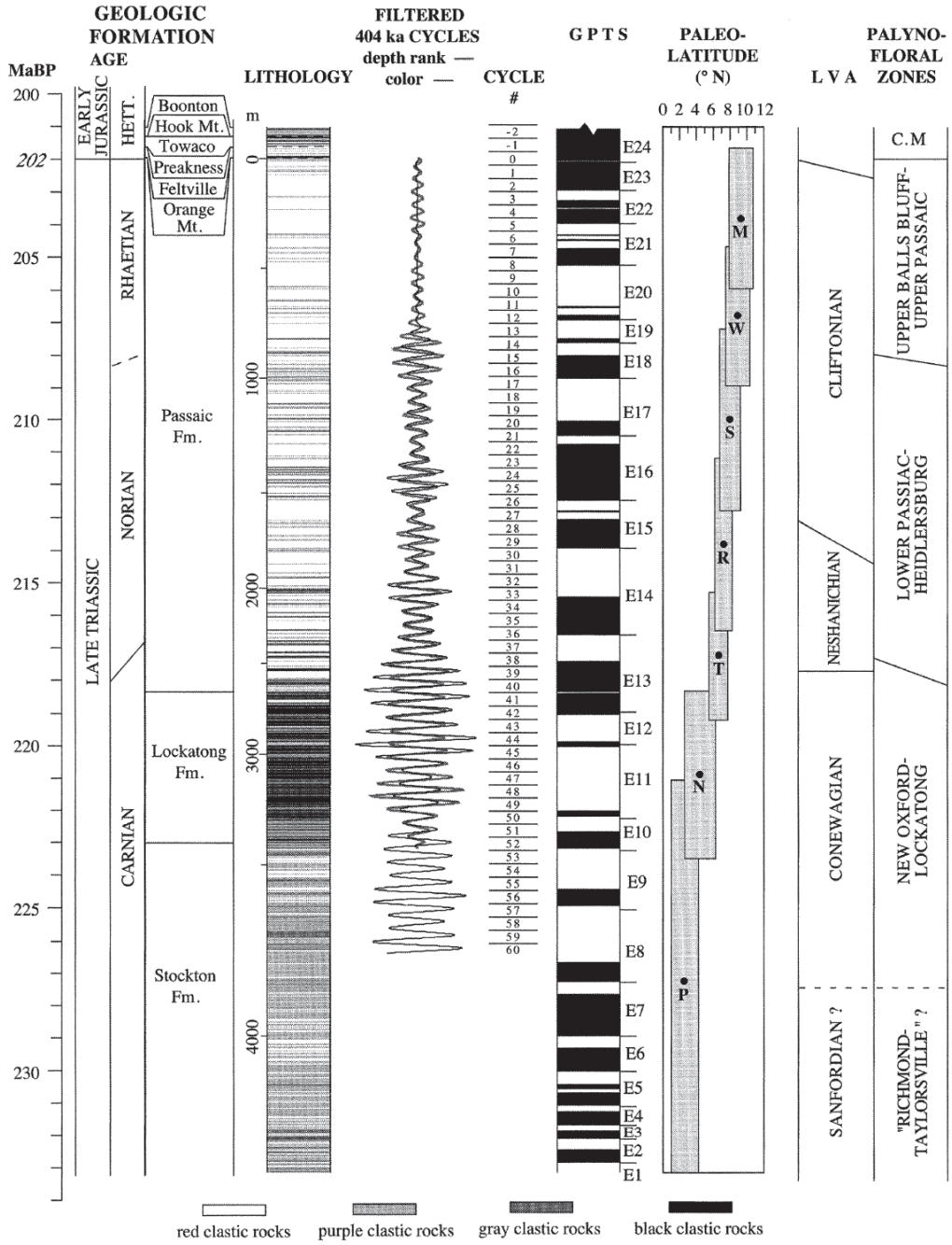

Figure 1.2: Newark Astrochronological Polarity Time Scale (APTS). From the left: formations and lithostratigraphy, cyclostratigraphy (McLaughlin cycles, 404 ky), magnetostratigraphy, paleolatitude of the cores, vertebrates and palynomorphs biostratigraphy. (from Olsen and Kent, 1999)

Newark magnetostratigraphy has been calibrated with the cyclostratigraphy by Kent et al. (1995), and then refined by Kent and Olsen (1999) and Olsen and Kent (1999), obtaining an Astrochronological Polarity Time Scale (APTS: or Astronomically-calibrated geomagnetic Polarity Time Scale, following the nomenclature of Olsen et al., 2011). Considering that the cyclostratigraphy starts from the Rock Raven Mb (upper Stockton Fm), the time calibration of the remaining part of the Stockton Fm was approximated by extrapolation of the average accumulation rate of the Raven Rock Mb (Olsen and Kent, 1999).

The potential of the Newark APTS as geochronological tool is huge. Fundamentally is a Geomagnetic Polarity Time Scale (GPTS), but the biostratigraphic-based chronostratigraphy is not clearly defined. In the Newark APTS, palynomorphs assemblages (e.g. Cornet, 1977, 1993; Fowell et al., 1994) are the mainly markers for the Stage boundaries, in association with conchostracans (Kozur and Weems, 2005, 2007, 2010). A great problem of palynomorphs is provincialism, as argued by Cornet (1993), Cornet and Olsen (1985), and Fowell and Olsen (1993). For example, taxa typical of Tethys are absent in parts of the boreal realm, regardless of age (Hochuli et al., 1989; Mørk et al., 1992; Hochuli and Vigran, 2010). Olsen et al. (2011) justify the provinciality of palynomorphs with the different climates between Newark area (tropical arid) and the alpine and central Europe (tropical humid to temperate), at least for Norian and Rhaetian, also recalling the provincialism of *Rhaetipollis germanicus*, typical of Rhaetian in Europe and extended to early Carnian in Siberia (likely corresponding to geographic North Pole in Late Triassic; e.g. Kozur and Weems, 2007). About conchostracans, the definition of Stages based on this continental fossils is limited by the lack of relations with marine fossils marking the same events, and normally considered as the main markers for Stage boundary definition due to their greater areal extension (e.g. the markers of Rhaetian Stage proposed by STS do not include continental taxa; Krystyn, 2010).

1.2.2 Newark APTS vs. marine sections: solving the Late Triassic geochronology

These problems restrict the direct use of the Newark APTS as GPTS, so since 1995 many authors have attempted a correlation between marine sections (in which the chronostratigraphy is well defined by fossils or other events) and the APTS. Obviously, correlating a marine section with a continental section using biostratigraphy is a hard endeavor, in particular if palynomorphs are excluded because of their provinciality. An easy way out is offered by the magnetostratigraphy, which potentially allows global correlations. However, the numerous attempts of magnetostratigraphic correlation

between marine sections (mostly of Tethyan realm) and the Newark APTS led to different (sometimes completely discordant) interpretations of the Late Triassic geochronology. Gallet et al. (2000) reconstructed a composite magnetostratigraphy of the Norian in Tethys, combining the magnetostratigraphy of Kavalaani (Turkey, Gallet et al., 2000), Kavur Tepe (Turkey, Gallet et al.. 1993), Scheiblkogel (Austria, Gallet et al., 1996), and Bolücektasi Tepe (Turkey, Gallet et al., 1992) sections. This Tethyan composite, calibrated with conodonts, have been visually compared with the Newark APTS, but any correlation was performed for a lacking of part of the Alaunian magnetostratigraphy and for the condensation of the considered marine sections, which can also preclude the detection of small reversals, as stated by Gallet et al. (2000). The earliest true correlation attempts between a Tethyan marine section and the Newark APTS was performed by Muttoni et al. (2001), with the basinal section of Pizzo Mondello (Italy), and by Channell et al. (2003), with the Silická Brezová section (Slovakia). In Muttoni et al. (2001) the Norian base was not clearly defined in Pizzo Mondello, and the Carnian/Norian boundary (CNB) was placed inside the E14r-E15r interval of the APTS, around ~213-216 Ma, near the CNB placed by Kent et al. (1995) in E13r at ~217-218. Later, Krystyn et al. (2002) integrate the composite Tethyan magnetostratigraphy by Gallet et al. (2000) with the magnetostratigraphy of Pizzo Mondello (Muttoni et al., 2001) to cover the Tuvalian missing in Bolücektasi Tepe (Gallet et al., 1992). Then a correlation with the Newark APTS was attempted, placing the CNB at the top of magnetozone E6r, at ~229 Ma. This correlation have been improved by Gallet et al. (2003), that confirm the position of the CNB in Newark E6r (Krystyn et al., 2002) and assign a Norian age to the Newark APTS up to E22n. Gallet et al. (2003) recalculated the Newark APTS assigning an age of ~200 Ma to the Jurassic base (Pálfy et al., 2000; Courtillot and Renne, 2003), considered coeval to the base of the Orange Mt. Basalts. In this case the Rhaetian falls at ~202 Ma (lasting ~2 My) and the CNB at ~227 Ma. However, this recalculation is not valid anymore after the radiometric age of 201.36±0.17 Ma for the base of the Hettangian stage (Wotzlaw et al., 2014). Channell et al. (2003) compared the more extended section of Silická Brezová (Tuvalian to Sevatian, calibrated with conodonts) with Pizzo Mondello (Tuvalian-Lacian), and then attempt a correlation with the Newark APTS. The greater extension of the Silická Brezová magnetostratigraphy allowed a more precise correlation with the APTS, placing the CNB within E7r, at ~227 Ma, resulting older than the CNB proposed for the Newark APTS (e.g. Kent et al., 1995; Kent and Olsen, 1999). The magnetostratigraphic correlations with the Newark was performed exclusively on

a visual base, comparing the pattern of reversals and chosing the correlation that fit best. Muttoni et al. (2004) extended the magnetostratigraphy of the Pizzo Mondello section up to the Sevatian. Having a continuous magnetostratigraphy from the end-Carnian to the end-Norian, Muttoni et al. (2004) compare the thickness of the Pizzo Mondello magnetozones to the duration of the Newark magnetozones, "moving" the Pizzo Mondello magnetostratigraphy along the entire APTS two magnetozones at time (to have always a comparison between magnetozones of the same polarity) and taking into account all the possible correlations. This kind of correlation is based on the assumption that in a basin the sedimentation rate is almost stable, so the thickness of the magnetozones is a proxy of time. Then the numerical thickness/duration comparison was evaluated with a linear regression and a Student t-test, and the correlations having the higher t value were considered the most reliable. Of 16 possible correlations, two resulted the most statistically reliable (significant at 95%). From these two options (Option #1 and Option #2), two age models have been derived to evaluate average sedimentation rates. Of the two options, preferred #2 has the highest t-value and smoother average values of sedimentation rates. Following this option, the CNB (refined by new conodont investigations) was placed within Newark magnetozone E7r at ~227-228 Ma, confirming the Norian age proposed by Channell et al. (2003).

The investigation of St. Audrie's Bay section (Hounslow et al., 2004) provided a magnetostratigraphy for the upper Norian/Rhaetian (calibrated with microfloral and palynomorphs) that show discontinuity around the Norian/Rhaetian boundary (NRB) for the presence of two unconformities. The NRB is approximated by the FO of dinoflagellate cyst *Rhaetogonyalux rhaetica*, at the top of the Blue Anchor Fm and at the base of magnetozone SA5n. Hence, the Rhaetian is characterized by a zone of prevalent normal polarity. The correlation with the Newark APTS constraint the Rhaetian in the E22-E23 interval.

Gallet et al. (2007) correlate the section of Oyuklu (Turkey), calibrated with conodonts, with the Tethyan composite of Gallet et al. (2003), constructing a Sevatian-Rhaetian Tethyan composite that was correlated with the Newark APTS. This correlation follows the one from Gallet et al. (2003), where the Rhaetian is about 2 My long, from E22r to E23r. The Rhaetian of Oyuklu is mostly normal polarity, as well as in St. Audrie's Bay (Hounslow et al., 2004), and that seems to confirm the correlation of Gallet et al. (2007), although in both sections part of the Rhaetian is missing. The absence of a correspondent magnetozone in Newark for Oyuklu magnetozone J- led Gallet et al. (2007) to conclude that a small part of the

Rhaetian in the Newark APTS is missing. The duration for the Rhaetian of ~2 My is based on the Triassic/Jurassic boundary (TJB) of Kozur and Weems (2005), placed inside the Preakness Basalts of Newark. Gallet et al. (2007) consider the possibility to include the Sevatian 2 as part of the Rhaetian (after Ogg, 2004). This means to include the *Misikella posthernsteini-bidentata* Zone in the Rhaetian. In this case the Rhaetian base is placed in upper E21n, obtaining a duration of this Stage of ~4.5 My (Gallet et al., 2007), considering the TJB by Kozur and Weems (2005). Using the TJB of Wotzlaw et al. (2014) the Rhaetian of Gallet et al. (2003) should last ~1 My ("Traditional Rhaetian") or ~3.2 My (including Sevatian 2). The idea of a missing Rhaetian in the Newark succession was early proposed by Van Veen (1995) and Kozur and Weems (2005) on a biostratigraphic basis. In the Newark, Cornet (1977) found Triassic pollens just below the TJB defined by *Classopollis meyeriana*, whereas these taxa disappear in the basal Rhaetian of Europe (Van Veen, 1995). Using conchostracans, Kozur and Weems (2005) show how in the Newark Supergroup the strata just below the Orange Mt Basalts reveal a quick transition from typical upper Sevatian conchostracans (*Shipingia olseni*) to typical upper Rhaetian assemblages. Following these interpretations, the Rhaetian in Newark should be condensed in a small interval. Anyway, the well-known provinciality of palynomorphs and the poor information about Rhaetian conchostracans make these hypotheses debatable.

Combining the marine sections with a well-calibrated magnetostratigraphy, Hounslow and Muttoni (2010) construct a time-calibrated composite of the Triassic magnetostratigraphy (Geomagnetic Polarity Time Scale – GPTS). The Late Triassic portion of the GPTS was partially calibrated using the Newark APTS (in particular with the Rhaetian). The comparison between the Norian to Rhaetian GPTS with the Newark APTS produced three options (Fig. 1.3):

- Option A follows the proposal of Muttoni et al. (2004), suggesting the NRB within E17 in the Newark APTS (as in Olsen and Kent, 1999), similar to the correlation of Channell et al. (2003). This option assumes an incomplete magnetostratigraphy at the E13-E14 interval.
- Option B follows the correlations of Krystyn et al. (2002), Gallet et al. (2003) and option 1 of Gallet et al. (2007). This option implies large sedimentation rates changes around the Norian/Rhaetian boundary. In Gallet et al. (2003) the NRB is placed in the E21r, while in Hounslow and Muttoni (2010) is placed around E19-E20.
- Option C follows the correlations of Hounslow et al. (2004) and option

2 of Gallet et al. (2007). This option is consistent with the hypothesis of a lack of Rhaetian sediments in the Newark APTS (e.g. Van Veen, 1995; Gallet et al., 2007). Following Hounslow et al. (2004), the NRB should fall within the E22-E23 interval but the previous biostratigraphic investigation of Orbell (1973), which place the FO of *Rhaetagonyalux rhaetica* lower in the Blue Anchor Fm, was not considered. Moreover, the *R. rhaetica* in alpine Tethyan sections (Krystyn et al., 2007b) is typical of upper-middle Rhaetian, suggesting a lower position of the NRB in St. Audrie's Bay, in the SA4r or lower.

Although any option is preferred to another, Option A seems the one less affected by stratigraphic inconsistencies (e.g. large variations of sedimentation rates,

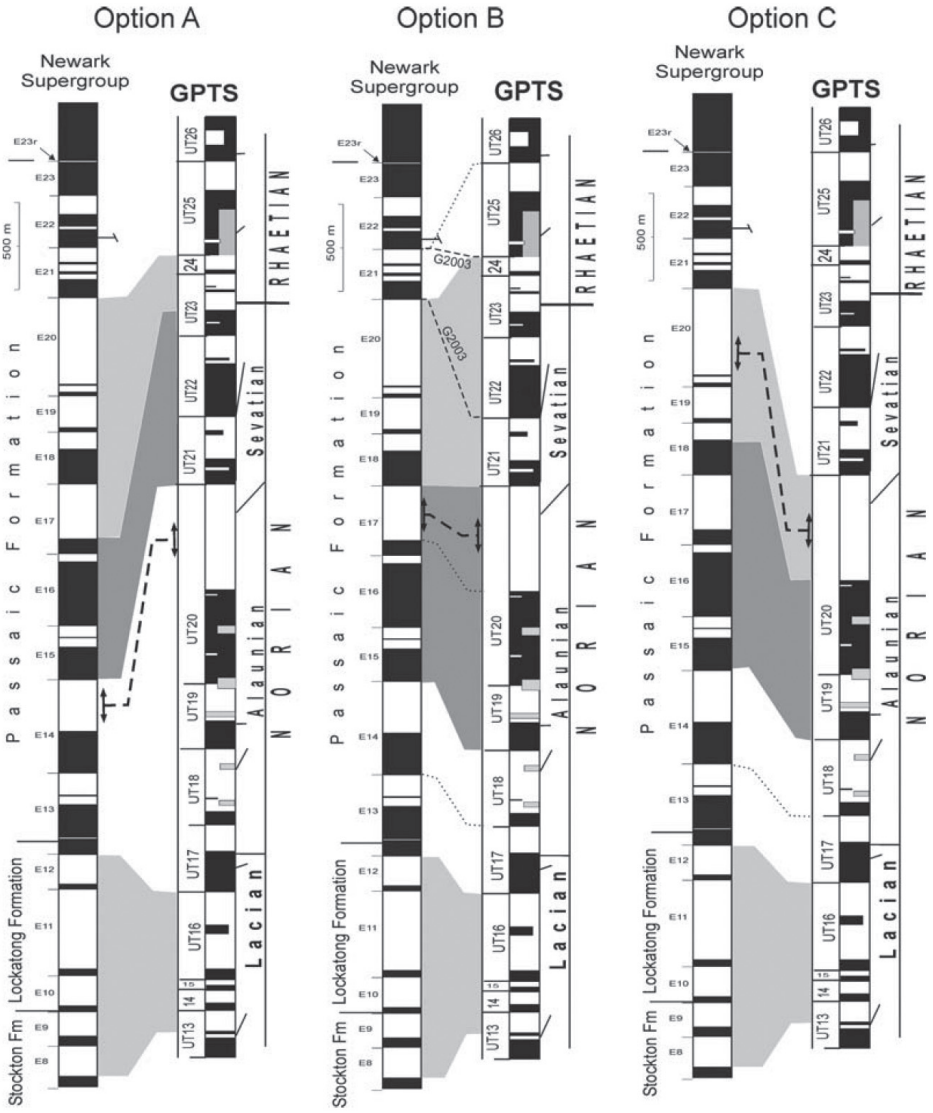

Figure 1.3: correlation options between the GPTS of Hounslow and Muttoni (2010) and the Newark APTS. (from Hounslow and Muttoni, 2010)

inconsistencies in biostratigraphic markers, etc.).

Recently, Hüsing et al. (2011) re-sampled the Steinbergkogel section, GSSP candidate for the Rhaetian Stage (Krystyn et al., 2007a, 2007b). The new magnetostratigraphy have been correlated with other Tethyan sections, including Pizzo Mondello (Muttoni et al., 2004). The astronomical cycles recognized in Pizzo Mondello (~1.75 My, Hüsing et al., 2011) was well correlated with the same cycles in the Newark APTS, confirming the proposed correlation of Steinbergkogel through Pizzo Mondello. The NRB, traced using the FO of conodont *Misikella hernsteini* instead of the younger *M. posthernsteini*, is correlated to the top of E16n, at ~209.8 Ma. This correlation is in agreement with Kent et al. (1995), Channell et al. (2003), and Muttoni et al. (2004).

Recently, the Geological Time Scale 2012 (Gradstein et al., 2012) propose two different options for the Stages of the Late Triassic (Fig. 1.4), based on the correlation between a magneto-biostratigraphic sequence (in which Stage boundaries are defined by ammonoid Zones) from the Tethys, and the Newark APTS (for both options, Carnian age is ~237 Ma and Hettangian age is ~201.3):

- **Long-Tuvalian option**: This option consider a hiatus of ~5 My in the Newark Supergroup, following the Late Triassic chronology proposed by Lucas et al. (2012). In the Newark Supergroup, strata just below the Orange Mt Basalts (oldest CAMP lava flows in the Newark Basin) show a quick transition from typical upper Sevatian (late Norian) conchostracans (*Shipingia olseni*) to typical upper Rhaetian assemblages (Kozur and Weems 2005, 2007, 2010). Anyway, conchostracans of lower Rhaetian are poorly described and the distribution of *S. olseni* could cover this interval up to the appearance of *Euestheria brodieana* (upper Rhaetian; Kozur and Weems, 2005). Lucas et al. (2012) justified this theory assuming that the Rhaetian should cover a large reversal polarity period, whereas in the Newark the conventional Rhaetian is mostly of normal polarity. Introducing the gap in the Newark APTS, the part of the magnetozone E24n included in the Passaic Fm is assigned to the uppermost Norian at ~206.5 Ma. Introducing the gap in the Rhaetian of the Newark Supergroup, the APTS has been recalculated and the Ladinian-Carnian boundary (~237 Ma; Mietto et al., 2012) corresponds to the Newark magnetozone E2r. The Rhaetian is placed at 205.5, apparently on the assumption that the Rhaetian base should be ~1 Myr younger than the Norian E24n (~206.5 Ma). The Carnian/Norian boundary is here placed at the top of E13r, at ~221 Ma, in agreement with the CNB placed with

palynomorphs (Olsen and Kent, 1999), and with the correlation Option #1 with the Pizzo Mondello section of Muttoni et al. (2004). Therefore, duration of the Stages are: Carnian ~16 My, Norian ~15.6 My and Rhaetian ~4.1 My long.

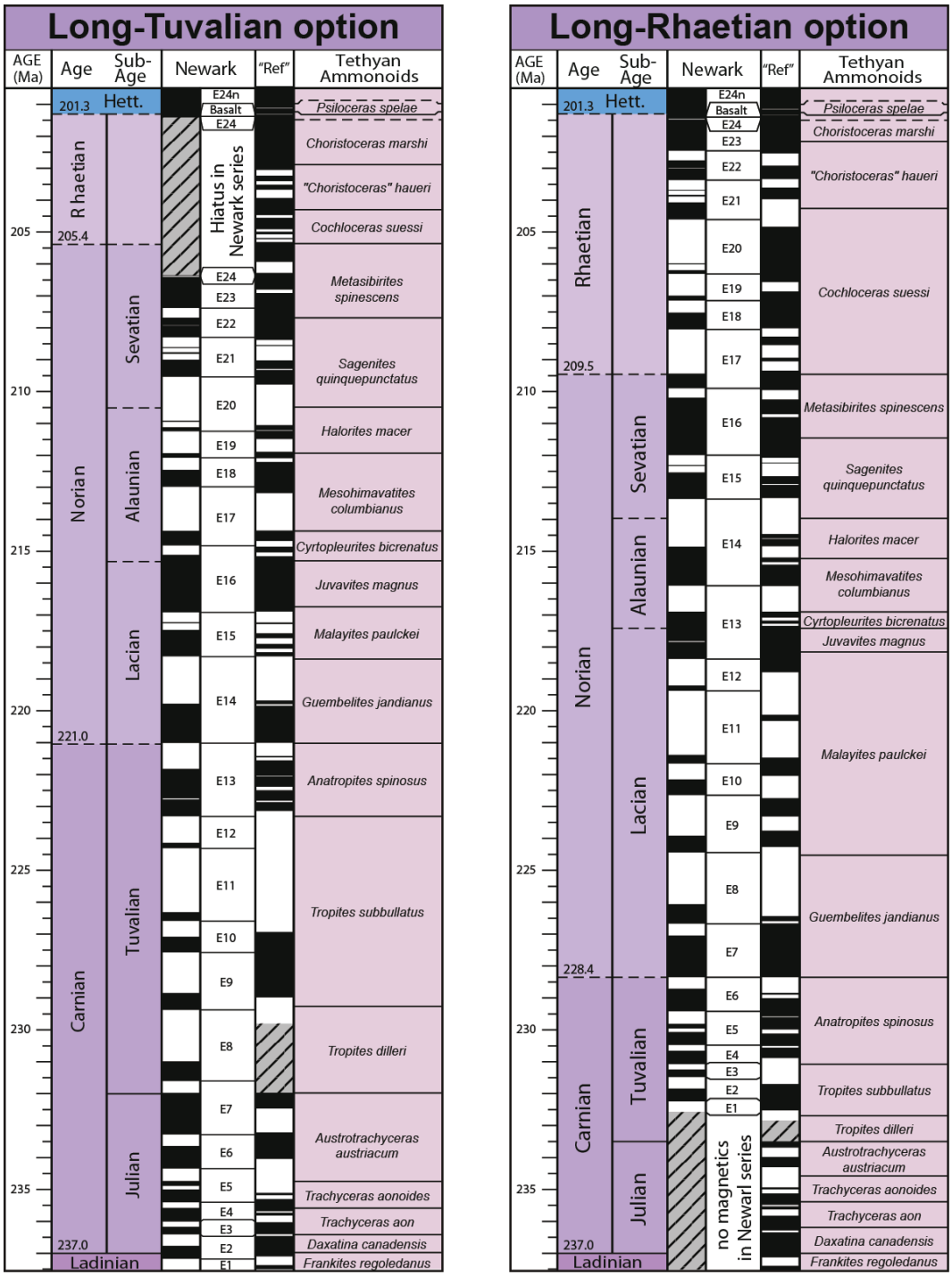

Figure 1.4: Long-Tuvalian and Long-Rhaetian options from the Geological Time Scale 2012 (Gradstein et al., 2012)

- **Long-Rhaetian option**: In this option, stratigraphy of the Newark Supergroup is considered as continuous. In facts, there is no lithostratigraphic evidences of a gap in the upper Passaic Formation (Gradstein et al., 2012) and coeval successions with cyclostratigraphy show same time span between the first CAMP basalt and the last reversal (~20 kyr) (Deenen, 2010; Deenen et al., 2010). The age of the Carnian-Norian boundary is assigned to the base of E7n (Channell et al., 2003; Muttoni et al., 2004), around 227-228 Ma. The base of the Rhaetian is placed at 209.5 Ma, at the base of E17r in the Newark, following Option A of Hounslow and Muttoni (2010) and the similar proposal of Hüsing et al. (2011). Summarizing, Carnian is ~8.6 My, Norian is ~18.9 My and the Rhaetian is ~8.2 My long.

The Long Rhaetian have been considered for the summary figures of the Geological Time Scale 2012. The choice is conditioned by the U/Pb radiometric ages from volcaninc tuffs in Nicola Group (British Columbia) that constraint the lower/middle Norian boundary at ~224 Ma (Diakow et al., 2011), an age inconsistent with the Long Tuvalian option.

Concluding, Late Triassic is constrained by radiometric ages at the top (201.36±0.17 Ma; Wotzlaw et al., 2014) and at its base (237.773±0.052 Ma; Mietto et al., 2012). Stage boundaries as Carnian/Norian and Norian/Rhaetian lacks of a formally accepted numerical age, because of many different proposals of correlations between the marine sections and the Newark APTS. To refine the Late Triassic geochronology further investigations are needed, focusing on biostratigraphic well-calibrated marine sections, which offer the possibilities to recognize clearly the markers of Late Triassic Stages and substages. The study of magnetostratigraphy in marine sections, as seen before, represent a valid tool to improve the Late Triassic chronology by the correlation with the Newark APTS.

1.3 A NEW PROPOSAL FOR LATE TRIASSIC CHRONOLOGY

The presence of (at least) two different geochronological options for the Late Triassic (Gradstein et al., 2012) lead to hardly assign an age or duration to the events occurring during this time period. To find a way out from this impasse is necessary to improve the integrated stratigraphy of the Late Triassic. Considering the importance of the Newark APTS as geochronological tool, the investigation of magnetostratigraphy is fundamental to attempt a correlation with stratigraphic succession recording clearly the chronological key marker.

To give a contribution to the Late Triassic chronology I investigate for

magnetostratigraphy a series of selected Tethyan sections covering the Norian-Rhaetian interval and the middle Carnian stage. The choice of these two intervals is strategical. The base of the Rhaetian is still debated so it is necessary to analyze the magnetostratigraphy of a section in which the Stage boundary is clearly defined and then attempt a correlation with the Newark APTS. The Pignola-Abriola section (Italy) is a perfect candidate because of a detailed conodont biostratigraphy, in association with radiolarians. The section was also investigated for organic carbon chemostratigraphy, obtaining a $\delta^{13}C_{org}$ curve. Moreover, I investigate the Rhaetian/Hettangian section of Mount Messapion (Greece) and the Norian/Rhaetian sequence of ODP Leg 122 - Hole 761C (Australia).

Also the Carnian Stage shows similar issues regarding its chronology. The Ladinian/Carnian boundary has been defined with a GSSP (Mietto et al., 2012) and the proposals of Carnian/Norian based on marine fossils are considered reliable (e.g. conodonts, ammonoids), but it is still debated the discrepancy with the Norian based on continental fossils (palynomorphs, conchostracans, vertebrates; Lucas et al., 2012). The Carnian/Norian boundary has a detailed magnetostratigraphy, which unfortunately is missing for the rest of the Carnian, characterized instead by the few sections affected by condensation or discontinuities like faults and disconformities/unconformities (e.g. Bolücektasi Tepe, Gallet et al., 1992). To improve the magnetostratigraphy of the middle Carnian I decided to investigate the Pignola-2 section in Southern Italy and the Dibona section in Northern Italy, both covering the middle Carnian, around the Julian/Tuvalian boundary. I also investigated the Carnian/Norian stratigraphic sequences of ODP Leg 122 - Holes 759B/760B (Australia).

Chapter II
ELEMENTS OF PALEOMAGNETISM

PART A
ROCK MAGNETISM

2.1 THE GEOMAGNETIC FIELD

As known, the Earth is wrapped by a magnetic field that protects the planet from the energy-charged particles of the solar wind. This "geomagnetic" field originates inside the Earth's Fe-Ni core, from the convection currents in the liquid outer core. The type of interaction is explainable by a self-exciting magnetohydrodynamic dynamo model. A self-exciting dynamo needs a moving electrical conductor (the

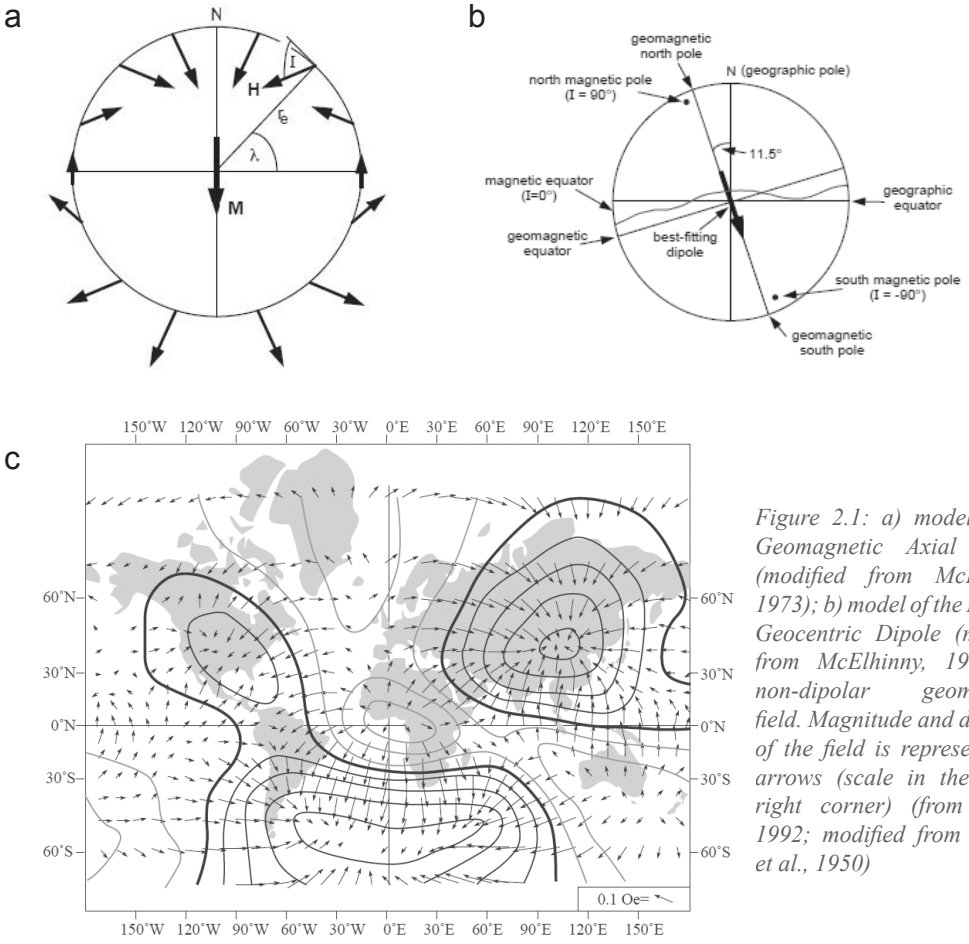

Figure 2.1: a) model of the Geomagnetic Axial Dipole (modified from McElhinny, 1973); b) model of the Inclined Geocentric Dipole (modified from McElhinny, 1973); c) non-dipolar geomagnetic field. Magnitude and direction of the field is represented by arrows (scale in the lower-right corner) (from Butler, 1992; modified from Bullard et al., 1950)

outer core) that generates a magnetic field, which in turn provide to the conductor the energy required to maintain the necessary rotation (by the Lorentz force) to feed the magnetic field itself. However, part of the energy is loss by electrical resistivity in the conductor and this energy must be supplied to keep the self-exciting dynamo active. Considering that the Earth has not been "roasted" yet by the solar wind, some kind of energy supply must be present. The most likely source of energy has been identified in the progressive cooling of the Earth's outer core, which can provide the estimated 10^{13} W necessary to sustain the geomagnetic field.
Theoretically, the geomagnetic field is approximated to a Geocentric Axial Dipole (GAD) (Fig. 2.1a), generated by a single dipole in the center of the planet and with the magnetic axis parallel to the rotation axis. Indeed, the real morphology of the geomagnetic field is quite different and the magnetic axis is inclined of about 11.5° respect to the rotation axis (Inclined Geocentric Dipole) (Fig. 2.1b). Assuming the IGD model as real, the inclined dipole axis must be coincident with the dip axis of the magnetic field lines, but this is not completely true. The Eccentric Dipole model (a dipole diverged from the center of the Earth) best fits the magnetic field in about the 80% of the Earth's surface, but in some areas the model does not fit. To explain this anomaly, a non-dipolar component of the magnetic field has been invoked (Fig. 2.1c), originating at the interface between the outer core and the lower mantle.

2.2 MAGNETIC PROPERTIES OF MINERALS

Most of the rocks in the Earth are characterized by magnetic properties and are able to retain a magnetization if they have been subjected to a magnetic field. The magnetic features of a rock are related to the content of magnetic minerals, which are characterized by different behaviors.

2.2.1 Behavior of the magnetic minerals

Magnetic minerals have been divided in three major categories: diamagnetic, paramagnetic and ferromagnetic minerals. Diamagnetic minerals do not acquire any magnetization if subjected to an external magnetic field, while the paramagnetics acquire a magnetization until the magnetic field is removed. Ferromagnetic minerals retain the magnetization even after the magnetic field is removed, showing a complicated behavior and at least three subcategories that are: ferromagnetic *sensu stricto*, antiferromagnetic and ferrimagnetic minerals. Ferromagnetic minerals *s.s.* are characterized by magnetic moments in minerals that are oriented parallel to the applied field (Fig. 2.2a), acquiring a strong residual magnetization. Minerals having

an antiferromagnetic behavior have magnetic moments oriented in both parallel and anti-parallel position respect to the applied field (Fig. 2.2b), with a resultant magnetization equals to zero; antiferromagnetic behavior pass to paramagnetic over the Nèel temperature (T_N). In ferrimagnetic minerals the magnetic moments are oriented parallel and anti-parallel too, but there is a dominant direction of magnetization (Fig. 2.2c); most of the magnetic minerals are ferrimagnetic. A ferromagnetic mineral become paramagnetic over the Curie temperature (T_C) and return ferromagnetic under the same temperature. There are also some special behaviors, like canted-antiferromagnetic and superparamagnetic.

A canted-antiferromangetic mineral differs from an antiferromangetic *s.s.* for a non-zero magnetization, due to canted magnetic moments that induce a preferred direction of the bulk magnetization vector.

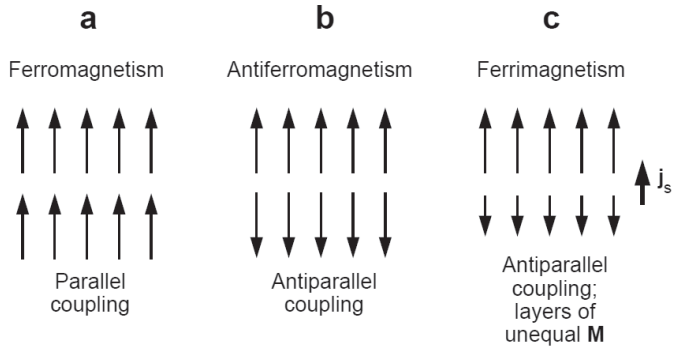

Figure 2.2: coupling of magnetic moments in a) ferromagnetic (s.s.), b) antiferromagnetic, c) ferrimagnetic minerals (from Butler, 1992).

Superparamagnetic minerals can acquire a magnetization from an applied magnetic field, but are characterized by a very short relaxation time (t_S, the period of time after which a magnetic mineral lose the acquired magnetization), so they lose their magnetization quickly; t_S is depending on temperature (Fig. 2.3) and its variation is characteristic for every magnetic mineral, so there are superparamagnetic materials at room-temperature and ferromagnetic minerals that become superparamagnetic at very high temperature (called blocking temperature, T_B).

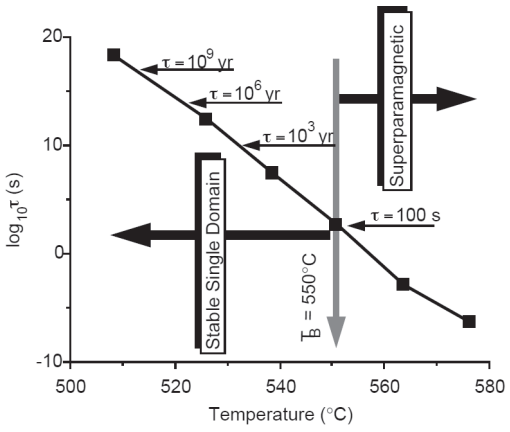

Figure 2.3: log plot of relaxation time of a single-domain magnetite as function of temperature. T_B is the blocking temperature (from Butler, 1992).

2.2.2 Main ferromagnetic minerals

Principal ferromagnetic minerals are the Fe-enriched phases of titanomagnetite and titanohematite solid solutions. Titanomagnetite is a solid solution between magnetite (Fe_3O_4) and ülvospinel (Fe_2TiO_4), where ülvospinel is paramagnetic at room-temperature (due to Ti-enrichment) and magnetite is ferromagnetic (T_C=580°C, J_S=4.5x10^5 A/m) (Fig. 2.4a). Titanohematite is a solid solution between hematite (αFe_2O_3) and ilmenite ($FeTiO_3$), where hematite is canted-antiferromagnetic (sometimes ferromagnetic *s.s.* due to structural defects) with a T_N=680°C (J_S=2x10^3 A/m) and ilmenite is paramagnetic at room-temperature (Fig. 2.4b). Minor ferromagnetic minerals are Fe-oxyhydroxides (e.g. goethite), maghemite and Fe-sulphurs (e.g. pyrrhotite).

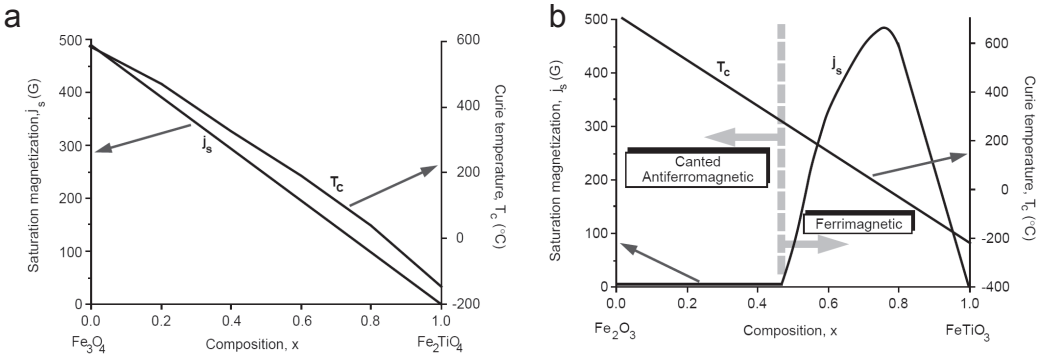

Figure 2.4: saturation magnetization and Curie temperature of the titanomagnetite series (a) and titanohematite series (b) (from Butler, 1992; modified from Nagata, 1961, and Stacey and Banerjee, 1974)

2.2.3 Magnetic domains

The acquired magnetization is also function of the grain structure. Crystals of magnetic minerals are characterized by magnetic domains, indicating the distribution of magnetic charge on the surface of the grain. In a single-domain (SD) crystal magnetic charge is equally distributed on the surface (Fig. 2.5a) and the acquired magnetization (J) is equal to the maximum acquirable magnetization (saturation magnetization, J_S). In a multi-domain (MD) grain there are more domains with different orientation and the magnetic charge is not equally distributed on the surface of the crystal (Fig. 2.5b); as a consequence, J is lower than J_S.

Grain size influence the develop of single or multiple domains, in particular small grains are characterized by single domains easily than large grains, which form usually multi-domains for energetic convenience. Is difficult to understand the exact grain size limit between SD and MD grains. In facts, a particular interval of grain size shows intermediate features between SD and MD. This situation refers to the pseudo-single-domain (PSD) grains. The PSD grains have a small number

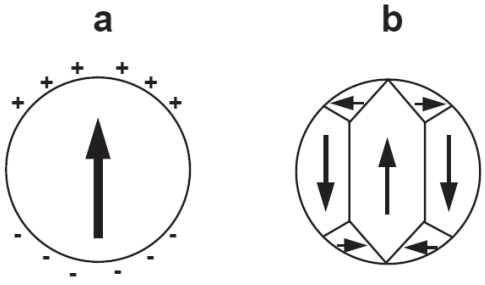

Figure 2.5: a) magnetic charge distributed on a single-domain spherical grain, b) magnetic domains in a spherical grain (arrows indicate direction of saturation magnetization j_s). From Butler (1992).

of domains inside and they also show a high coercivity and a relevant time stability of the magnetization. Most of the times, PSD grains are important carriers of remanent magnetism. Moreover, isotropic crystals are easily magnetizable than anisotropic ones, and anisotropic minerals are simply magnetizable along the long axis than the short one.

2.3 ACQUIRING THE MAGNETIZATION

Magnetization *in situ* of the rocks is the sum of the magnetization induced by the actual geomagnetic field and the Natural Remanent Magnetization (NRM). The NRM is necessary for paleomagnetic investigations and is recorded in rocks, contrary to the induced magnetization that is not preserved. The NRM results from the combination of a primary NRM (recorded during rock formation) and secondary NRM (acquired after the rock formation). The primary NRM is acquired mainly in three ways: cooling from high temperatures (ThermoRemanent Magnetization), deposition of magnetic minerals in detritus (Detrital Remanent Magnetization) and sometimes by growth of magnetic minerals below the T_C (Chemical Remanent Magnetization). A secondary NRM can be recorded in many ways, mainly by application of a relative weak magnetic field for a long time (Viscous Remanent Magnetization), chemical alteration of ferromagnetic minerals (secondary CRM) or by application of a very strong magnetic impulse (Isothermal Remanent Magnetization).

ThermoRemanent Magnetization (TRM)

The TRM, typical in magmatic rocks, is acquired during the cooling of a magnetic mineral subjected to a magnetic field, when the temperature of the system decreases below the T_C. In particular, TRM becomes stable below the T_B, at the passage between superparamagnetic and ferromagnetic behavior. The acquisition of the TRM is not instantaneous for the whole rock, but is acquired gradually when each phase reaches the T_B. The stability of TRM during time is strongly related to the grain size: small crystals have high probability to develop single domains, while large crystals are probably characterized by a multi-domain structure.

Detrital Remanent Magnetization (DRM)

The DRM is acquired during the deposition of sedimentary rocks. The DRM recorded by orientation of magnetic minerals in the moment of deposition is called depositional DRM (dDRM), while the DRM recorded successively to the deposition and before the lithification is called post-depositional DRM (pDRM). The classic model of DRM acquisition consider a complete, rapid alignment of the grains along the magnetic field direction, but is not what happens in reality. In many experiments (e.g. Verosub, 1977) grains showed a lower degree of alignment than expected and a shallowing in inclination respect to the magnetic field (Fig. 2.6a). In effect, during the deposition, grains rotate while laying down on the bottom (Fig. 2.6b). This phenomenon should induce an error in the recorded inclination, but the observations in nature are not coherent. Considering this, most of the recorded DRM is actually pDRM. The experiments of Verosub (1977) show that in water-rich sediment grains orient themselves exactly along the applied field (Fig. 2.6c) and that in the presence of a polarity inversion the grains in a 10-20 days old

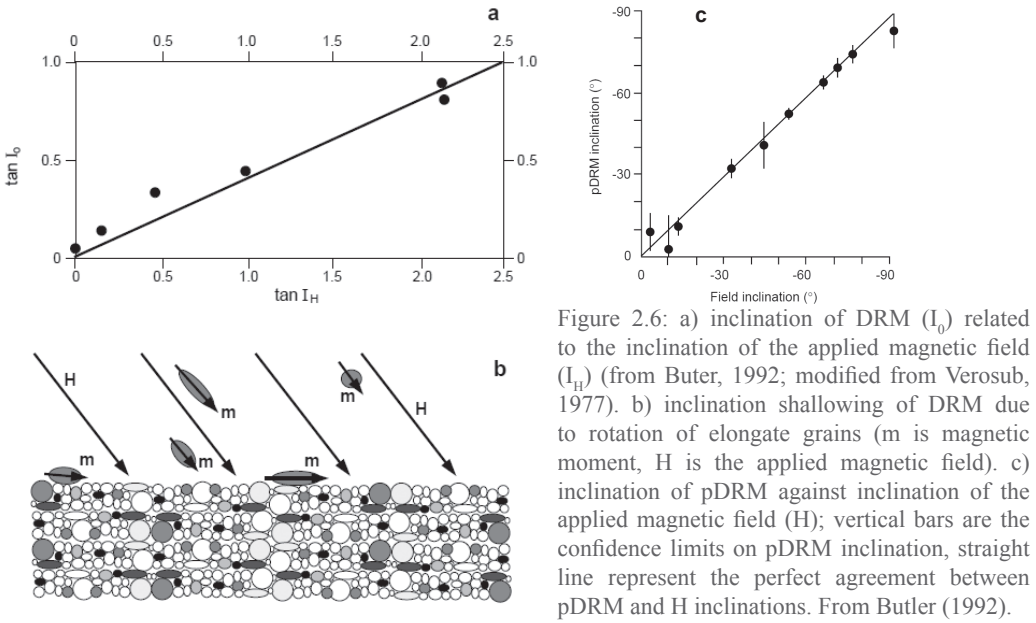

Figure 2.6: a) inclination of DRM (I_0) related to the inclination of the applied magnetic field (I_H) (from Buter, 1992; modified from Verosub, 1977). b) inclination shallowing of DRM due to rotation of elongate grains (m is magnetic moment, H is the applied magnetic field). c) inclination of pDRM against inclination of the applied magnetic field (H); vertical bars are the confidence limits on pDRM inclination, straight line represent the perfect agreement between pDRM and H inclinations. From Butler (1992).

sediment rotate to align themselves to the magnetic field. The pDRM is not the only contribution to the whole DRM, but dDRM is also present. The dDRM/pDRM ratio is function of many factors, mainly:

- grain size: small grains remain suspended in the water column longer than large grains, increasing the pDRM contribution.
- bioturbation: sediments reworked by biological activities record a pDRM.
- sedimentation rate: slow rates enhance the pDRM, increasing the residence

time of the magnetic particles in the high water content zone of the sediments. As mentioned before, grain size has also effects on the quantity of multi-, single- or pseudo-single-domain grains. Fine silt or clay has more SD (and PSD) particles than a coarse sand or silt, which are full of MD grains. SD and PSD grains retain a higher magnetization than MD grains, and the record is more stable. Moreover, coarse grains are more sensitive to mechanical energies that override the magnetic alignment of the particles, and the high permeability of coarse sediments enhance the chemical alteration of ferromagnetic minerals. For these reasons, fine-grained sedimentary rocks are preferable to coarse-grained for paleomagnetic analyses.

Chemical Remanent Magnetization (CRM)

If magnetic minerals form after chemical reaction and are subjected to a magnetic field, the acquired magnetization is called Chemical Remanent Magnetization (CRM). The magnetization is acquired during the growth of the crystals, and become stable after the crystals reach the blocking volume, allowing the formation of stable single domains. During alteration of minerals, if the crystal structure did not change (i.e. magnetite to maghemite), the direction of the CRM is controlled by the previous NRM. The acquisition of CRM can occur also from precipitation of magnetic minerals from a solution, or for postdepositional alteration. If the alteration occurs soon after the deposition, the CRM could be regarded as primary (i.e. oxidation reactions with formation of hematite; dehydration of goethite in hematite). Otherwise, if the alteration occurs long after deposition, the CRM is regarded as secondary (i.e. diagenetic production of sulfides).

Viscous Remanent Magnetization (VRM)

Magnetic minerals subjected to a weak magnetic field (i.e. the geomagnetic field) for a long time can acquire a secondary magnetization called Viscous Remanent Magnetization (VRM). Acquisition of VRM has a logarithmic growth in time, so normally is dominated by recent geomagnetic field. Moreover, the VRM is susceptible to the temperature and its intensity increase for high temperature. As argued before, the VRM is substantially related to time and SD grains with a short relaxation time are probably carrier of VRM. Different is the behavior of PSD and MD grains, where thermal energy is necessary to acquire the VRM, activating the domain walls motion. Magnetization of PSD and MD grains interacts with the applied field facilitating the domain walls motion, and the magnetization increases along the direction of the applied magnetic field. Furthermore, the lower is the coercivity of the PSD/MD grains, the higher is the VRM acquired.

Isothermal Remanent Magnetization (IRM)

After the rock is formed, strong magnetic fields (induced by natural or artificial sources) can remagnetize rocks completely, obliterating every remanent magnetism acquired before. This kind of remagnetization is called Isothermal Remanent Magnetization (IRM) and is acquired at room temperature. Rare in nature (acquired normally by effect of lightnings hitting the outcrops), IRM represents a valid analysis tool to reveal the main magnetic carrier in samples. Methods of IRM analyses are explained later.

PART B
METHODS

2.4 UNDERSTANDING THE ROCK MAGNETIC PROPERTIES

Rocks are made by an assemblage of minerals and some of them are magnetic. The magnetic properties of a rock sample reflect its content in magnetic minerals and are dominated by the most abundant phase. Knowing the properties of a magnetic mineral is fundamental in paleomagnetism, because it influences the preservation of the original magnetization during time. The reactions of magnetic minerals subjected to different conditions (external magnetic fields, heating, etc.) are unique, and many analytic techniques have been developed to quantify these reactions.

2.4.1 Analysis of Natural Remanent Magnetization (NRM)

To reveal the Natural Remanent Magnetization originally acquired during the formation of the rock, oriented samples are needed. Samples cored on the field are oriented using an orienter tool and a compass, then the orientation is marked on the sample with a line (Fig. 2.7) along z-axis, normally plunging into the outrcrop. Samples can be obtained also from oriented blocks, where the azimuth is derived adding 180° to the dip of the block, and the hade is 90-dip angle (Fig. 2.8). Most of

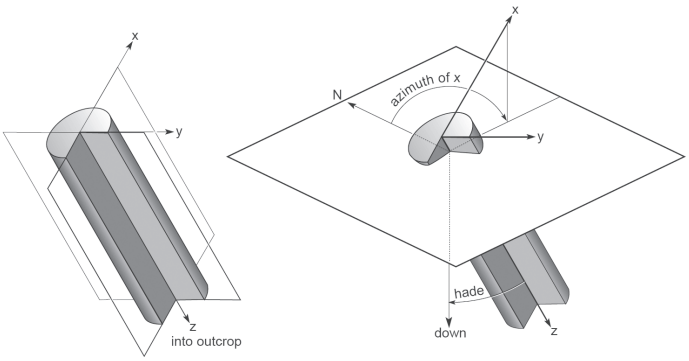

Figure 2.7: example of oriented core. Direction information are azimuth (the angle between the horizontal projection of the x-axis and the North) and hade (the angle from vertical). From Butler (1992)

the instruments fits with 1-inch diameter cores, 1 inch long.

The so-oriented samples are then demagnetized progressively. The magnetization retained by the magnetic minerals in the rock is removed by heating (thermal demagnetization) or by application of an alternate gradient magnetic field. The "soft" magnetic minerals (e.g. pyrrhotite, goethite, Ti-rich magnetite) are removed by low temperatures and fields, isolating the magnetization recorded by "hard" minerals (e.g. magnetite, hematite). For each step of demagnetization, the magnetometer detects the direction and the intensity of the magnetization vector, then plotted into an end-point vector diagram (Zijderveld, 1967) (Fig. 2.9).

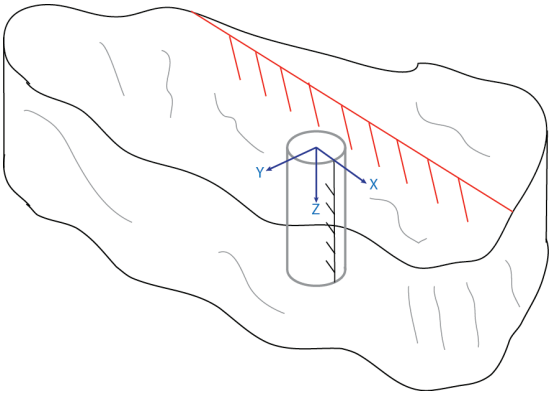

Figure 2.8: core obtained from an oriented block. Arrow on the block indicates the dip/dip-angle direction. The direction of the core is obtained by: Core Dip = dip+180°; Core Hade = 90°-dip angle

The diagram shows the projection of the magnetization vector on the horizontal (full symbols; Fig. 2.9a) and vertical (empty symbols; Fig. 2.9b) planes. When the magnetization component identified as characteristic of the sample (Characteristic NRM, ChRM; Fig. 2.10a) is isolated (Fig. 2.10b), the mean direction and intensity of this component are calculated using a Principal Component Analysis (PCA) (Fig. 2.10c). Once determined the direction of the characteristic component, the datum is interpreted paying attention to the values of azimuth and inclination. If the direction is unusual (e.g. north/up or south/down vectors in northern hemisphere, instead of north/down or south/up), orientation data of the samples should be checked and, in case, corrected or rejected.

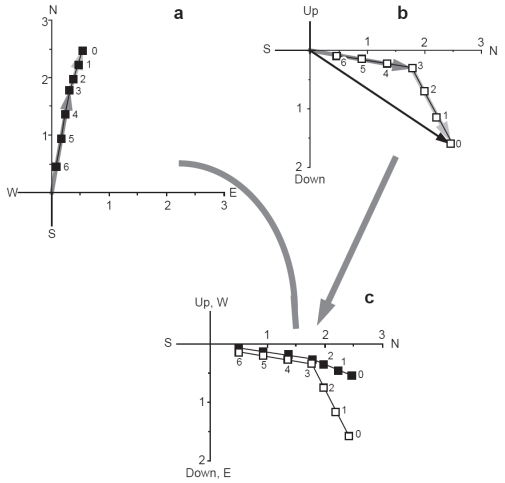

Figure 2.9: end-point vector diagram (Zijderveld, 1967). For each demagnetization step (numbers on dots), the diagram displays the horizontal (a; Declination) and the horizontal (b; Inclination) projections of the magnetization vector. The projections are plotted together (c), where inclination is marked by empty dots and declination by full dots.

Evaluation of paleomagnetic stability

Once derived the ChRM from a set of samples, is difficult sometimes to be sure that this component is primary or have been acquired lately. The application of paleomagnetic stability tests could

provide information about the origin and timing of the acquired magnetization. Here are presented the most common tests.

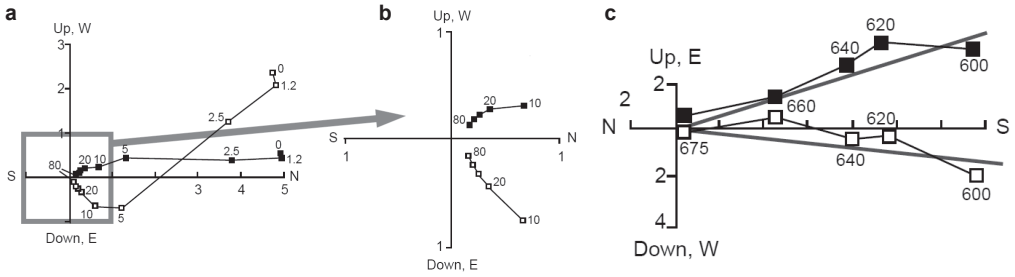

Figure 2.10: identification of ChRM in a sample (a) and its isolation (b). The mean direction of ChRM (c) is calculated applying a principal component analysis. The number on dots are demagnetization field (a, b) and temperatures (c) for each step. From Butler (1992).

Fold test

This test evaluates the time of the ChRM acquisition related with folding (obviously, this test does not work on homoclinal sections). If the ChRM is acquired before folding, the directions from the opposite limbs of the fold are dispersed, but they should converge after the application of the structural correction (Fig. 2.11). If the site pass the fold test (original ChRM) the structural corrected directions should be more clustered than before; on the contrary, if the fold test is failed, the corrected directions are more dispersed.

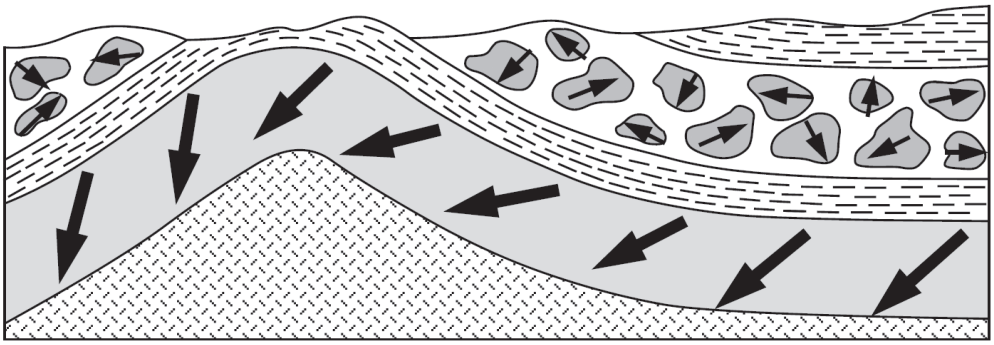

Figure 2.11: example of the fold and conglomerate tests. Arrows in fold limbs and conglomerate clasts are the magnetization directions. The random distribution of the directions in conglomerate suggest the acquisition of a primary ChRM, as well as the alignment of the directions in fold after structural correction. (from Butler, 1992)

Conglomerate test

If in a conglomerate the clasts acquired a ChRM before the deposition of the conglomerate (in the source rock), the ChRM directions should be randomly distributed (the site passed the conglomerate test) (Fig. 2.11). If the direction are consistent, the test is failed, which means that the ChRM have been acquired after the deposition of the conglomerate. This test usually works on interbedded

conglomerate to test the stability of the ChRM of the source rock in the same site.

Reversal test

As seen before (Chapter 2.1) the geomagnetic field is approximated by an axial dipole: this is true for a time-averaged geomagnetic field, both for normal or reverse polarity periods. Consequently, in a site the mean directions of primary normal and reverse components should differ of ~180°. Secondary components acquired later deviate the angular difference between the mean normal and reverse directions, resulting non-antiparallel (Fig. 2.12). If the reversal test is passed, it means that the secular variation of the geomagnetic field is well averaged and the ChRM is coherent with a primary acquisition. On the contrary, if the test is failed probably the ChRM is strongly contaminated by secondary magnetization, or the paleomagnetic data are not sufficient to average the secular variation of the geomagnetic field. This test is applicable to every dataset because any particular geological setting is required (as folding or conglomerates).

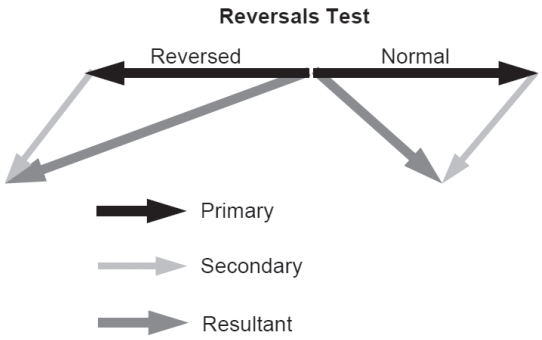

Figure 2.12: black arrows indicate the expected antiparallel configuration of the mean directions. In presence of a secondary component of magnetization (light gray arrows), the resultant mean directions (dark gray arrows) are non-antiparallel (from Butler, 1992). More the secondary component is relevant, less are the possibilities to pass the reversals test.

2.4.2 Isothermal Remanent magnetism (IRM): techniques

Magnetic characteristics of a rock are depending on the content in magnetic minerals. Each magnetic mineral has a different behavior if subjected to an induced magnetic field or if heated. By the application of different artificial IRM (Isothermal Remanent Magnetism) techniques is possible to understand the particular magnetic properties of a rock sample as a reflection of the dominant phases of magnetic minerals.

IRM acquisition curve

A magnetic field is applied increasing progressively the intensity of the field and the acquired magnetization is recorded after each step of treatment. When the sample reaches the maximum magnetization, it is saturated (Fig. 2.12). The minimum magnetic field necessary to reach saturation is the saturation field, which is diagnostic for magnetic minerals (e.g. magnetite saturates around 500 mT).

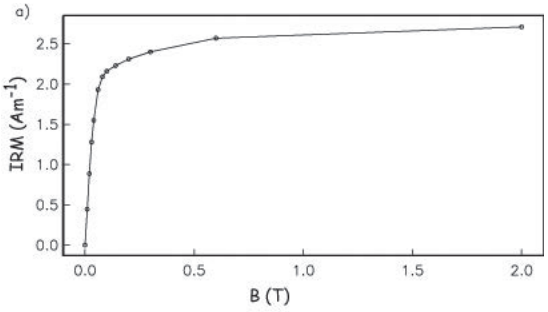

Figure 2.12: example of IRM acquisition curve. When the sample reach saturation, the curve flattens, maintaining the magnetization almost constant against the increase of field intensity. (from Tauxe, 1998)

Backfield curve

This technique is useful for the determination of the coercivity, or the minimum magnetic field necessary to delete completely the acquired magnetization of a mineral, after complete saturation. The magnetic coercivity measures the resistance of a ferromagnetic mineral to complete demagnetization. High-coercivity minerals (magnetically hard) are more difficult to demagnetize, or remagnetize, than low-coercivity minerals (magnetically soft). The experiment consists in saturate the sample by the application of a high magnetic field (usually >500 Mt), and then apply a gradient magnetic field until the total magnetic moment reaches zero (Fig. 2.13). Coercivity (H_c) is usually measured in A/m.

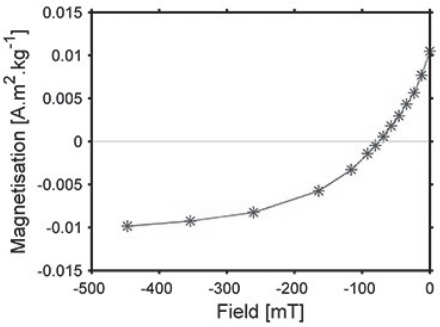

Figure 2.13: example of backfield IRM curve. The sample is saturated along a direction and then remagnetized progressively on the opposite direction until is saturated again. When the magnetization reaches zero (intersection of the curve with the applied field axis), the relative applied magnetic field is the coercivity (H_C). (from Lavallée et al., 2015)

Hysteresis loop

Once a ferromagnetic mineral is magnetized, it will not spontaneously come back to zero magnetization once the applied magnetic field is removed. It needs an external magnetic field in opposite direction to drive the magnetization to zero. Applying a gradient magnetic field to a mineral, the magnetization traces a closed curve called hysteresis loop (Fig. 2.14a). The magnetic hysteresis represents the lag between the magnetization curve (after application of a magnetic field) and the relaxation curve (once the magnetic field is removed), due to the presence of magnetic domains that need energy to be reoriented. The magnetization retained at zero-field is called remanence. In rock samples (representing a mixture of magnetic minerals),

the hysteresis loop reflects the content in SD, MD and PSD grains. SD grains start orienting along the magnetic field (Fig. 2.14b) direction until saturation, where they are all oriented (Fig. 2.14c). Once the field is removed, the magnetic moments orient along the long axis nearer to the magnetic field direction (remanence) (Fig. 2.14d). An opposite field is required to erase the magnetization (Fig. 2.14e). In MD grains, the application of an external field causes the growth of domains with magnetization parallel to the field. If the field is strong enough, the domain walls are destroyed and the grains saturate. Removing the field the domain walls regenerate, returning to initial conditions, but for the presence of imperfections in the grains they retain a weak remanence. The field required to drive the domain walls to original position is weak, reflecting the low coercivity force of MD grains. The PSD grains have a small number of domains, showing a behavior more similar to SD than MD.

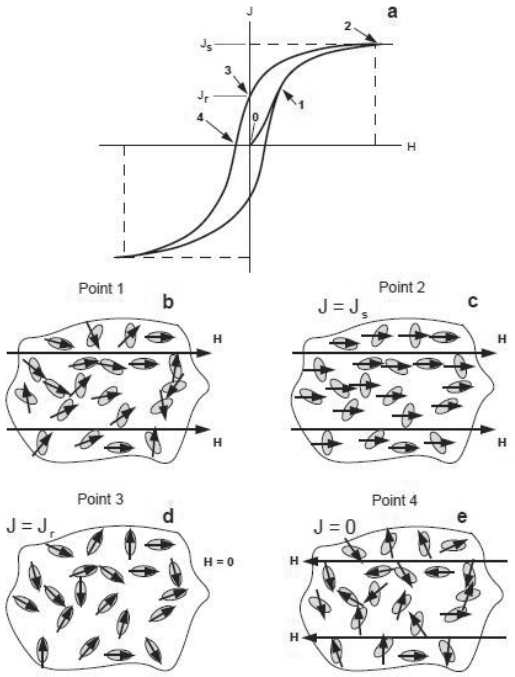

Figure 2.14: example of hysteresis loop (a). In case of SD grains: the magnetic moments, subjected to an applied magnetic field (H) are randomly oriented (b) until saturation-J_s (c); the field is removed and the magnetic moments orient along the long axis near to the direction of H (d), showing a remanent magnetization-J_r; an opposite magnetic field is necessary to erase J_r (e). (Butler, 1992)

Three-axial IRM

Magnetic minerals lose completely their magnetization if they reach the Curie temperature (T_C; for ferromagnetic s.s., ferromagnetic and canted-antiferromagnetic minerals) or the Néel temperature (T_N; for antiferromagnetic minerals). T_C and T_N are characteristics for each mineralogical phase and the three-axial IRM technique (Lowrie, 1990) has been developed to detect these temperatures. Samples are magnetized along X,Y,Z axes, saturating one axis (usually Z) at high magnetic force (2-2.5 T) and then magnetizing the others with lowest fields (e.g. X: 400 Mt; Y: 120 Mt). Then, the samples are thermally demagnetized increasing progressively

the temperature. After each step of temperature, the samples are analyzed in a magnetometer. The intensity of the resulting magnetic vector is then decomposed in X, Y and Z components (Fig. 2.15). The demagnetization curve reveals which category (magnetic hard or soft minerals) are dominant and at which temperature the samples lose magnetization, as a reflection of the magnetic minerals contained in the rock.

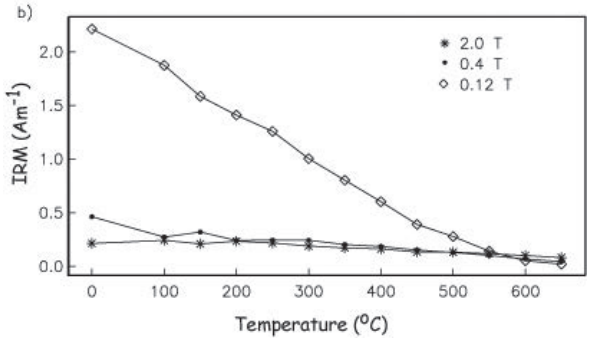

Figure 2.15: example of three-axial IRM. Three different demagnetization paths reflect different applied fields along x, y and z-axes. Along z-axis the sample is saturated, then other two weaker fields are applied along x and y to orient low-coercivity minerals. Then the sample is thermal demagnetized, and the path give information about the T_C and T_N of the magnetic minerals in the sample. (from Tauxe, 1998)

Thermomagnetic curve

In a constant external magnetic field, a sample subjected to a variation of temperature changes its magnetic moment. The decay curve of temperature represents the change of behavior (from ferromagnetic to paramagnetic or superparamagnetic) of the magnetic minerals inside the rock sample, depending on temperature (Fig. 2.16). If the analysis is performed in air, the curve could show the presence of neo-formed minerals by thermal oxidation of the original mineralogical phases (e.g. pyrite in magnetite, goethite in hematite, etc.), with increase of magnetization until the T_C (or T_N) of the neo-formed mineral is reached. If the new phase is stable, the magnetization at room temperature results higher than the starting magnetization.

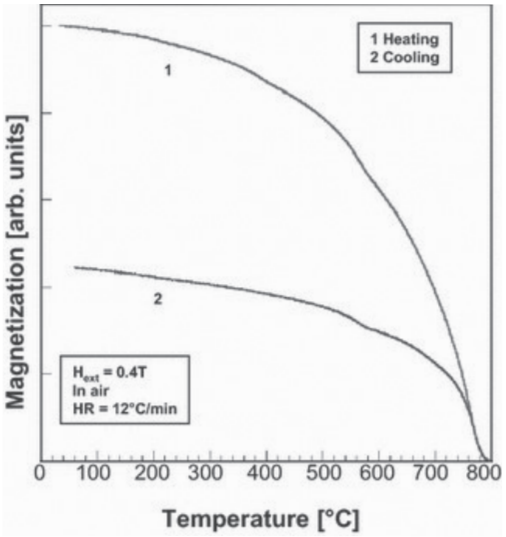

Figure 2.16: example of thermomagnetic curve. Magnetization is calculated in relation with the mass of the sample. The curve show an increase in magnetization at ~400°C, due to the presence of neo-forming minerals. This minerals decay at ~580°C, suggesting than it could be magnetite. The temperature of neo-formation is typical of oxidation of pyrite. (from Hoffman et al., 2011)

2.4.3 Instruments

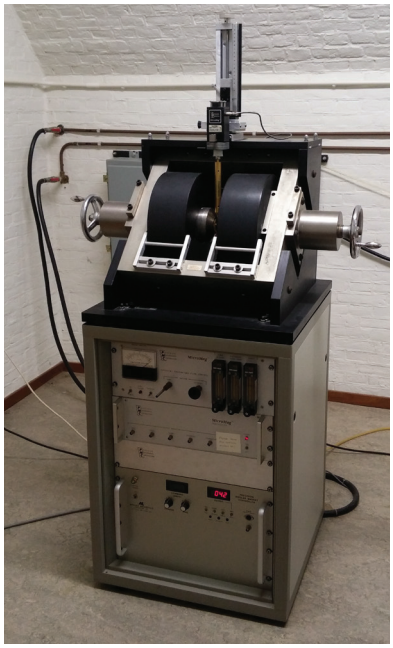

Figure 2.17: MicroMag AGM 2900

Alternate Gradient Field Magnetometer (AGM)
The AGM is based on the vibrating resonance of a magnetic material subjected to a DC (direct current) field and a small AC (alternating current) field gradient. The sample is put on a flexible stick, and then between two electromagnets generating a gradient magnetic field. The resonance vibrations are detected by a piezoelectric transducer (bimorph), connected to the sample/stick system, and then amplified. The sensibility of the instrument is attested at ~10^{-10}-10^{-11} Am^2, and the required mass for a single sample is very low (around 50 g). Example of AGM in Fig. 2.17.

Cryogenic Superconducting Quantum Interference Device (SQUID) Magnetometer
The SQUID magnetometer is made of a superconducting loop with one (RF-SQUID) or two (DC-SQUID) Josephson junctions inductively coupled with a series of superconducting coils (second-order gradiometer). To act as superconductors, the coils are maintained at a temperature of 4K using liquid Helium. The two Josephson junction are connected each other by a non-conducting (or low conducting) material. The coils are electrified (*I*), and if exposed to a magnetic field they are charged of an induced current *Is* (Josephson effect). The induced current has the same direction of the original current in one coil (total current $It = I/2 + Is$), and opposite in the other one ($It = I/2 - Is$). When the total currents in the coils exceed the critical current (*Ic*), an electric tension originates in the system. This tension is then transferred to a detector and translated into the induced magnetic field. In Fig. 2.18 a DC-SQUID cryogenic magnetometer.

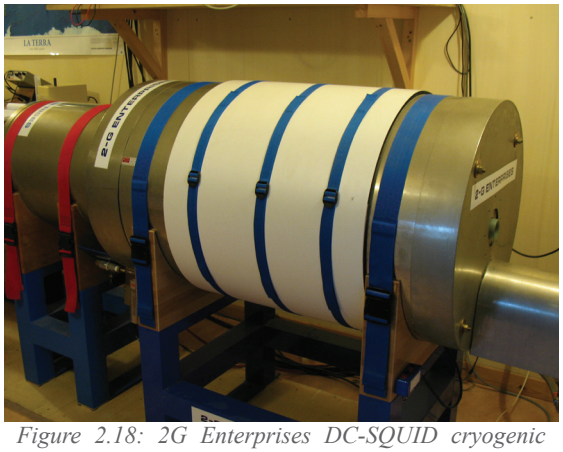

Figure 2.18: 2G Enterprises DC-SQUID cryogenic magnetometer

Thermal Demagnetizer

The thermal demagnetizer is a shielded cylindrical oven where the samples are progressively demagnetized by application of heat (Fig. 2.19). When a mineralogical phase reaches the Curie temperature (for all ferromagnetic materials) or the Néel temperature (for antiferromagnetic materials), the contribution of this phase in the total magnetism of the sample disappears. When the "softer" phases are removed (i.e. goethite, pyrrhotite, high-Ti titanomagnetite), the "hardest" remains (i.e. hematite, magnetite), revealing the original magnetism of the rock (usually preserved by hard minerals).

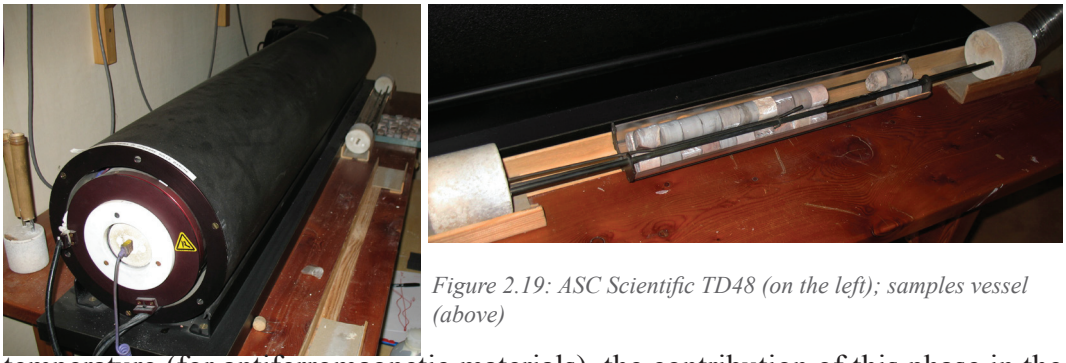

Figure 2.19: ASC Scientific TD48 (on the left); samples vessel (above)

Alternating Field (AF) Demagnetizer

The AF demagnetizer works with the application of a decaying alternating magnetic field to a sample. After each step of treatment, the sample is cleaned of any remanent magnetization of coercivity less than the peak of intensity of the applied field. A magnetic field is applied to the sample along the X, Y and Z orthogonal axes, randomizing the mobile magnetic domains. The applied field is decaying, so the amplitude of each half-cycle of the applied AF is smaller than the previous one. During each half-cycle, the domains with coercivities less than the applied field orient themselves along the field. A small percentage of these domains have a coercivity greater than the intensity of the following half-cycle, remaining fixed in the acquired direction. In this way, equal number of domains are oriented in positive and negative direction, resulting in a zero total field. Example of AF demagnetizer in Fig. 2.20.

Figure 2.20: 2G Enterprises AF demagnetizer

Curie Balance

The Curie Balance is a simple mechanic magnetic detector designed and built for the first time by Pierre Curie in 1895. Charles Cheneveau performed the most important improvement of the balance in 1930, introducing a torsion arm suspended by a fine wire from the torsion head. In the balance, the sample is placed on a torsion arm (Curie-Cheneveau balance) and exposed to a non-uniform magnetic field generated by an electromagnet, displacing the sample from its originary position. The balance

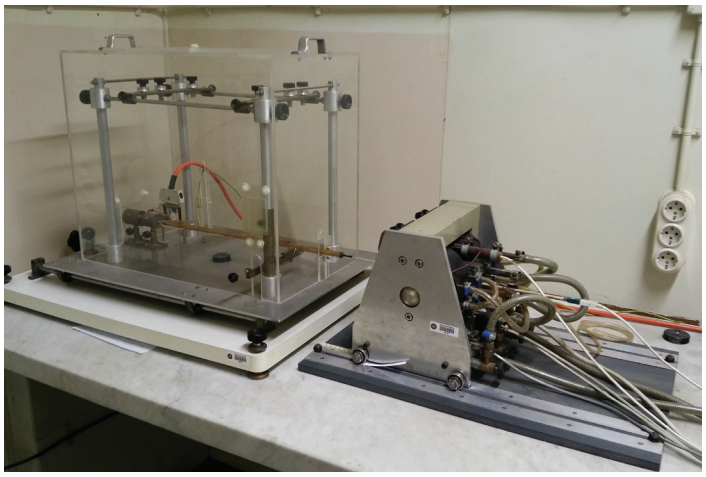

Figure 2.21: modified horizontal translation Curie balance

detect the torque/moment necessary to bring the specimen to the starting position. The magnitude of the torque is typical of a phase or a class of magnetic minerals. Using the Curie balance coupled to a furnace (example in Fig. 2.21) is possible to determine the behavior of the samples during heating or following a series of heating/cooling cycles.

Impulse Magnetizer

The Impulse Magnetizer generates a magnetic field for the artificial magnetization of samples. A capacitor is charged until the necessary tension is reached, then the tension is released in a coil generating a magnetic field inside it (Ampére's Law). The sample is placed inside the coil (or just in front of it) and magnetized along the axis parallel to the coil. Example of impulse magnetizer in Fig. 2.22.

Figure 2.22: ASC Scientific IM-10-30 with coils

Susceptibility Meter

This instrument is necessary to measure the capacity of a material of being magnetized if subjected to an external magnetic field. The measurement can be

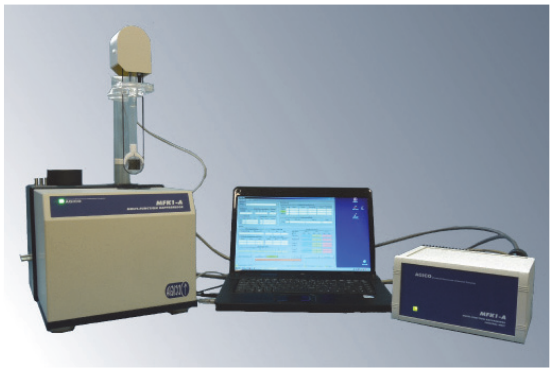

Figure 2.23: AGICO Kappabridge MFK-1

static (for analysis of bulk susceptibility) or dynamic (to determine the anisotropy of susceptibility) with the sample rotating along three orthogonal axes x, y and z. The sample is subjected to a non-uniform field of determined frequency, and then the instrument detects the intensity of the acquired magnetization. Example of susceptibility meter in Fig. 2.23.

2.5 USE OF THE PALEOMAGNETIC DATA

The data obtained from the analysis of the NRM provide the directions of the magnetic vector acquired by rocks during their formation. In the case of sedimentary rocks, it represents the magnetization acquired during the deposition and is normally in line with the direction of the magnetic field during that period. This information can be used to define the period of polarity inversions occurred during a particular period and recorded in a sedimentary sequence, or to extrapolate paleogeographic data from the position of the geomagnetic pole during the studied time interval.

2.5.1 Magnetostratigraphy

The sequence of paleomagnetic directions obtained by NRM analysis reflects the direction of the geomagnetic field in that time interval. For the northern hemisphere, northward declination and downward declination indicate normal polarity, whereas southward declination and upward inclination indicate reverse polarity. Obviously, in the southern hemisphere the situation is the opposite. A Virtual Geomagnetic Pole (VGP) can be derived from each direction datum using spherical trigonometric formulas (Fig. 2.24), and represents the position of the paleomagnetic pole in a location at one point in time (formulas are the same for each kind of magnetic pole).

To determine a VGP position (Lat_p; $Long_p$), we need the paleomagnetic direction (Inc_m; Dec_m) and site coordinates (Lat_s; $Long_s$). First, we need to obtain the magnetic colatitude (p), or the great-circle distance of the pole from our site:

$$p = \tan^{-1}\left(\frac{2}{\tan Inc_m}\right)$$

Then we derive the VGP latitude:

$$Lat_p = \sin^{-1}(\sin Lat_s \cos p + \cos Lat_s \cos Dec_m)$$

The difference of longitude between the pole and our site is given by β (positive to east):

$$\beta = \sin^{-1}\left(\frac{\sin p \sin Dec_m}{\cos Lat_p}\right)$$

Now, there are two kind of derivations for the pole longitude:

If: $\cos p \geq \sin Lat_s \sin Lat_p$, then: $Long_p = Long_s + \beta$

If: $\cos p < \sin Lat_s \sin Lat_p$, then: $Long_p = Long_s + 180° - \beta$

The latitude of a VGP places the paleomagnetic pole in the northern or southern hemisphere, indicating respectively normal and reverse polarity. Graphically, black and white bars represent the sequence of geomagnetic polarity inversions

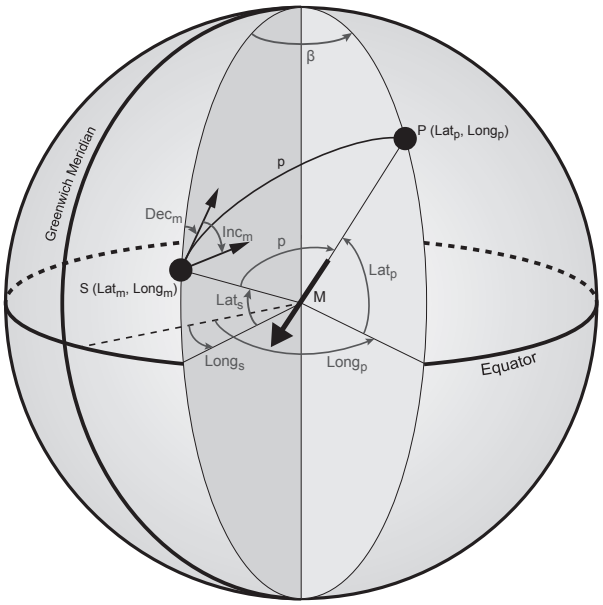

Figure 2.24: paleopole determination. S is the studied site, P the paleopole, and M the direction of the geomagnetic field. Magnetic colatitude is calculated from paleomagnetic inclination (Inc_m) and then used to determine the paleopole latitude (Lat_p). Lat_p and magnetic declination Dec_m are used to calculate β (the longitudinal difference between paleopole and site). β is used to calculate the palopole longitude $Long_p$. (modified from Butler, 1992)

respectively for normal and reverse polarity. A zone characterized by the same polarity is called magnetozone. Usually, inside a magnetozone some brief polarity

inversions occur and they are defined as submagnetozones. A magnetozone is named using an abbreviation followed by the sequence number and the polarity ("n" for normal, "r" for reverse; e.g. ID-1n or ID-1r); submagnetozones are named adding an extension to the name of the magnetozone following the same criteria (e.g. ID-1n.1r, ID-1n.2n, etc.). A sequence of magnetozones related to a stratigraphic succession is called magnetostratigraphy. The duration of a polarity inversion is not fixed, so the pattern of a sequence of polarity inversions is nearly unique. This is why magnetostratigraphy is a powerful tool to perform correlation between stratigraphic sections, considering also that the global range of the paleomagnetic record.

2.5.2 Paleogeography

As seen in the previous section, is possible to derive the position of a magnetic pole from the magnetic direction. Using the mean-site direction and the same formulas

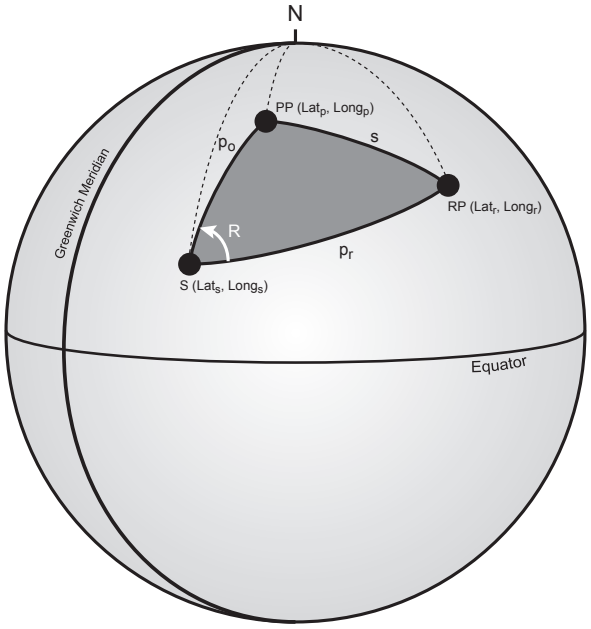

Figure 2.25: site rotation. S is the site position, RP the reference pole, and PP the site-mean paleomagnetic pole. Value of s (distance between PP and RP), pr (distance between S and RP), and pp (distance between S and PP) are calculated with spherical trigonometry. Then the angular rotation R is calculated. (modified from Butler, 1992)

of the VGP we can obtain the mean-site paleomagnetic pole. The mean-site paleomagnetic pole represents the position of the pole on the long time, eliminating the fast-changing (~3000 yr.) non-dipolar component of the geomagnetic field. A site-mean direction is usually associated to a circular confidence limit α_{95}. The α_{95} is transformed into an ellipse of confidence about the paleopole position. Along the great circle connecting the site to the pole, the semi-axis of the ellipse (dp) is calculated by:

$$dp = \alpha_{95}\left(\frac{1+3\cos^2 p}{2}\right)$$

The semi-axis perpendicular to the pole to site great circle (*dm*) is given by:

$$dm = \alpha_{95}\left(\frac{\sin p}{\cos Inc_m}\right)$$

In case of multiple site-mean poles, the paleomagnetic pole can be derived using a Fisher statistic, with a circular confidence limit A_{95}.

The mean paleomagnetic inclination (Inc_m) can be used to determine the paleolatitude (Lat_0) of the site:

$$Lat_0 = \tan^{-1}\left(\frac{\tan Inc_m}{2}\right)$$

Once determined the site-mean paleomagnetic pole (PP), is possible to calculate the rotation of the site (S) against a stable reference pole (RP) of the same period (Fig. 2.25). First, we need the distance S-RP (*pr*), S-PP (*pp*) and PP-RP (*s*), forming a spherical triangle on Earth surface:

$$p_r = \cos^{-1}\left[\sin Lat_r \sin Lat_s + \cos Lat_r \cos Lat_s \cos(Long_r - Long_s)\right]$$
$$p_p = \cos^{-1}\left[\sin Lat_s \sin Lat_p + \cos Lat_s \cos Lat_p \cos(Long_s - Long_p)\right]$$
$$s = \cos^{-1}\left[\sin Lat_r \sin Lat_p + \cos Lat_r \cos Lat_p \cos(Long_r - Long_p)\right]$$

Considering the rotation (*R*) as the angle at apex S of the triangle we can apply the law of cosines, solving for *R*:

$$R = \cos^{-1}\left(\frac{\cos s - \cos p_p \cos p_r}{\sin p_p \sin p_r}\right)$$

Chapter III
GEOLOGICAL FRAMEWORK OF THE CONCERNED AREAS

For my investigations of Late Triassic magnetostratigraphy, I considered four main areas: the Lagonegro Basin (Southern Italy), the Dolomites (Northern Italy), the Wombat Plateau (South-Western Australia) and the Pelagonian Domain (Greece).

3.1 LAGONEGRO BASIN (SOUTHERN ITALY)

3.1.1 Structural framework

The Lagonegro area is located in the Southern Apennines, near Potenza (Basilicata region, Southern Italy). The geological record is represented by the sediments of

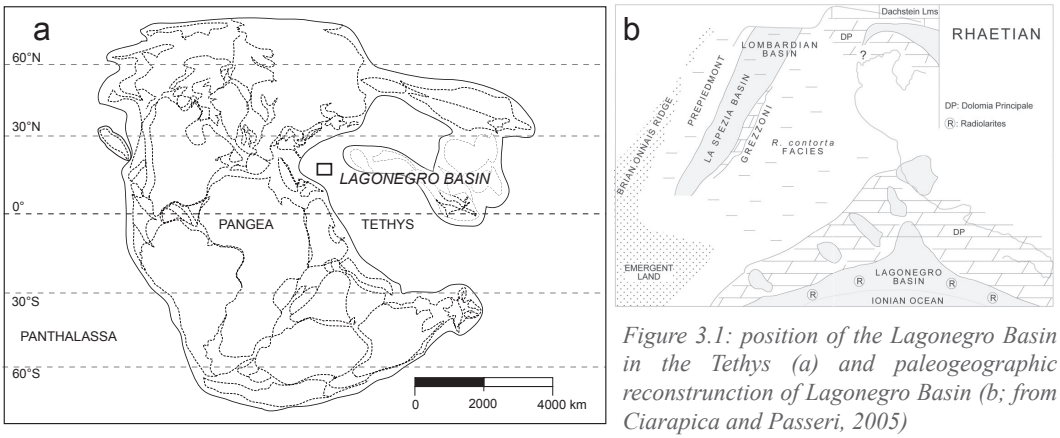

Figure 3.1: position of the Lagonegro Basin in the Tethys (a) and paleogeographic reconstrunction of Lagonegro Basin (b; from Ciarapica and Passeri, 2005)

the Lagonegro Basin, active since the Late Permian to the Miocene (Scandone, 1967; Finetti, 1982, 2005; Catalano et al., 2001; Ciarapica and Passeri, 2002, 2005; Argnani, 2005; Rigo et al., 2012a). The Lagonegro Basin belonged to the Ionian Ocean, a western branch of the Tethys (Fig. 3.1). The Ionian Ocean originated in the Late Permian/Early Triassic as continental rifting and probably evolved in ocean rifting (Catalano et al., 2001) during the Ladinian, coeval to the deposition of the radiolarites of the Monte Facito Formation (Ciarapica and Passeri, 2002, 2005).

The Lagonegro area is included in the southern part of the Apennines mountain range, an east-vergent fold and thrusted belt spanning through the Italian peninsula, from the Po valley to the Ionian Sea. The sedimentary sequences of the Lagonegro Basin are some of the tectonic units imbricated between the Apula platform (on

footwall) and the Apenninic platform (on headwall) in the Southern Apennines (Fig. 3.2). The Lagonegro Basin sequence was subdivided in two tectonic units (Scandone, 1967, 1972, 1975): the Lagonegro Unit I, including the more distal sequences, and the Lagonegro Unit II, represented by the more proximal facies. The Lagonegro Lower Sequence (Mostardini and Merlini, 1986; Ciarapica and

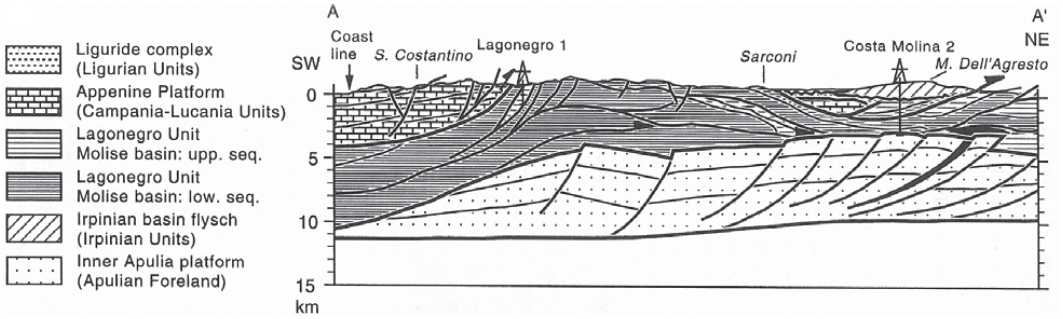

Figure 3.2: structural framework of the Southern Apennines. Lagonegro Upper and Lower sequences imbricated between Apulian and Apenninic platforms. (from Amodeo, 1999)

Passeri, 2005) includes, from the bottom, the Monte Facito Formation (Permian to Middle Triassic), the Calcari con Selce (Middle to Late Triassic), the Scisti Silicei (Late Triassic to Late Jurassic) and the Flysch Galestrino (Late Jurassic to Early Cretaceous) (Fig. 3.2). The Lagonegro Upper Sequence, always detached from the Lower Sequence (Mostardini and Merlini, 1986), includes the Flysch Rosso (Early Cretaceous to Early Miocene), the Flysch Numidico (Early Miocene to Middle Miocene) and the Flysch Irpini (Middle Miocene to Late Miocene).

3.1.2 Lithostratigraphy of the Late Triassic sequence

Focusing on the Late Triassic, the Carnian to Norian/Rhaetian is dominated by hemipelagic carbonatic sedimentation (Calcari con Selce), increasing in siliceous sedimentation around the Norian/Rhaetian boundary (Intervallo di Transizione-Transitional Interval; Miconnet, 1983) and passing to the Scisti Silicei in the Rhaetian/Hettangian (Fig. 3.3).

The Calcari con Selce is made of limestones and marly limestones, usually silicized towards the end of the succession, with chert nodules and bends, interbedded with dark, greenish or reddish shales. Limestones are mainly mudstone-wackestone (sometimes packstone) with radiolarians and bivalves (e.g. Rigo et al., 2012a). Thick banks of grey calcarenite are common in proximal successions, sometimes silicized, made of materials coming from near carbonate platforms, such as benthic foraminifera and fragments of echinoderms (e.g. Bazzucchi et al., 2005; Bertinelli et al., 2005). Micritic sediments might have been exported from neighbour platforms by currents in the nepheloid layer (Passeri et al., 2005), even if a major contributor

up to ca. 60 % to deep-water late Rhaetian carbonate hemipelagic lime-mudstones in western Tethys could have been derived from planktonic calcareous nannofossil (e.g. *Prinsiosphaera*) (Di Nocera and Scandone, 1977; Bown, 1987; Preto et al., 2012). Miconnet (1983) suggest a submarine delta as the main depositional environment of the carbonatic sequences of the Lagonegro. In facts, inside calcarenite is common to find fining-upward layers, similar to the *Ta* layers of a Bouma turbidity sequence. The boundary with the underlying Monte Facito Fm is not well defined and considered diachronous, from the upper Ladinian (Mietto and Panzanelli Fratoni, 1990; Rigo et al., 2007) to the lower-middle Carnian (Miconnet, 1983; Marsella et al., 1993). The passage to the overlying Scisti Silicei is gradual, with the increase of terrigenous sediments, with few cherty limestone layers and abundant red shales, red cherts and radiolarites (Transitional Interval; Amodeo, 1999). To explain this change of sedimentation many causes should be invoked: a decrease in carbonate supply from the nearby platforms, a deepening of the basin below the Calcite Compensation Depth (CCD), a rise of the CCD due to upwelling (Passeri et al., 2005), a bloom of siliceous organisms due to an increased nutrient supply (i.e. for volcanic activity; Giordano et al., 2011). Also the base of the Scisti Silicei is diachronous, from late Norian to Rhaetian (Amodeo, 1999; Rigo et al., 2015). Because of the difficulties to identify a sharp boundary between the Calcari con Selce and the Scisti Silicei, Miconnet (1982) introduced the "Transitional Interval" as the upper part of the Calcari con Sele, characterized by an increase of red radiolaritic intercalations, typical of the overlying Scisti Silicei (Amodeo 1999; Bertinelli et al. 2005a; Passeri et al. 2005; Reggiani et al. 2005; Rigo et al. 2012b). The Transitional Interval is included in the Calcari con Selce, as not official member (Amodeo, 1999). The base of the Transitional Interval is marked by a 2.5-4 m-thick interval of red shales (Amodeo 1999; Bertinelli et al. 2005b; Reggiani et al. 2005; Rigo et al. 2012b), Sevatian 1 in age (late Norian - *Mockina bidentata* Zone) (Rigo et al. 2005, 2012b). Deeper investigations on the Transitional Interval, mainly on

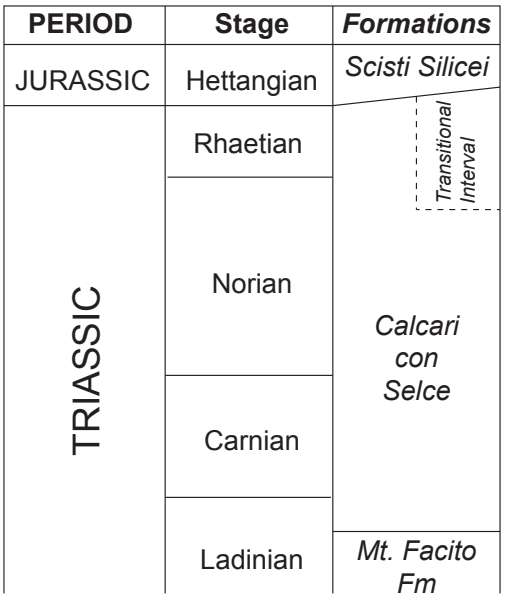

Figure 3.3: Stratigraphy of the Lagonegro Basin sequence

biostratigraphy (e.g. De Wever and Miconnet 1985; Bertinelli et al. 2005; Passeri et al. 2005; Reggiani et al. 2005; Rigo et al. 2005, 2012b), revealed atypical features in the Pignola-Abriola section, while it is easily recognized in the Mt. Volturino section.

3.1.3 Sections of interest

For my investigations I chose two sections from the Lagonegro Basin: the Pignola-Abriola section (Norian/Rhaetian) and the Pignola-2 section (Carnian).

The Pignola-Abriola section is a continuous succession of pelagic cherty limestone with interbedded shaley levels (Calcari con Selce), characterized by a detailed conodonts and radiolarians biostratigraphy. This section includes the Norian/Rhaetian boundary, well defined by the FO of conodont *Misikella posthernsteini* and supported by the concurrent radiolarian biostratigraphy (base of the *Proparvicingula moniliformis* Zone). Moreover, the low Conodont Alteration Index (CAI = 1.5; Giordano et al., 2010) indicate that the succession is preserved by thermal stress, that make the section suitable for paleomagnetic analyses. These characteristics make the Pignola-Abriola section very useful for my attempt of magnetostratigraphic integration of the Rhaetian.

The Pignola-2 section is a succession of pelagic cherty limestone (Calcari con Selce) covering the middle Carnian, at the passage from Julian to Tuvalian substages. The section is characterized by a detailed conodonts and palynomorphs biostratigraphy and by a low CAI (1.5; Rigo et al., 2007). The section records the Carnian Pluvial Event as a 5 m-thick green clayey and radiolaritic interval. Radiometric U/Pb age of 230.91±0.33 Ma was obtained from one of the ash-beds inside this green interval (Aglianico ash-bed; Furin et al., 2006). Considering the radiometric and biostratigraphic constraints, the paleomagnetic investigation of this section could provide a valid contribution to the magnetostraigraphy of the Carnian.

3.2 DOLOMITES (NORTHERN ITALY)

3.2.1 Structural Framework

The Dolomites are a mountain group covering the areas of Belluno, Trento and Bolzano (Northern Italy). Their name derives from the French geologist Déodat de Dolomieu, discoverer of the mineral dolomite in the Adige Valley, on the western Dolomites. The Dolomites rose rapidly during the Pliocene-Pleistocene because of the Alpine orogeny, and have been modelled and eroded quickly during the Pleistocene

glacial phases. Dolomites are located in the central part of the Southern Alps, a south-vergent belt not affected by metamorphism (e.g. Castellarin and Doglioni, 1985). This area is limited northward by the Insubric Line (dextral transpressive) and southward by the Valsugana Thrust (e.g. Doglioni, 1987; Castellarin et al., 1998). As the rest of the Alps, the Dolomites was part of the African continental margin in Tethys (Ziegler, 1988; Dercourt et al., 1993). Sedimentary record covers the Permian to Cretaceous interval and the slight deformation affecting the area did not disrupt most of the sedimentary frameworks (De Zanche et al., 1993; Gianolla et al., 1998a). The Late Triassic is well preserved and represented by carbonatic sedimentation in platform and basin in the very early part, that leads to a flatten topography in late Carnian and Norian (Fig. 3.4), with the development of anoxic intraplatform basins in the Norian and Rhaetian (e.g. De Zanche et al., 1993; Gianolla et al., 1998a; Neri et al., 2007).

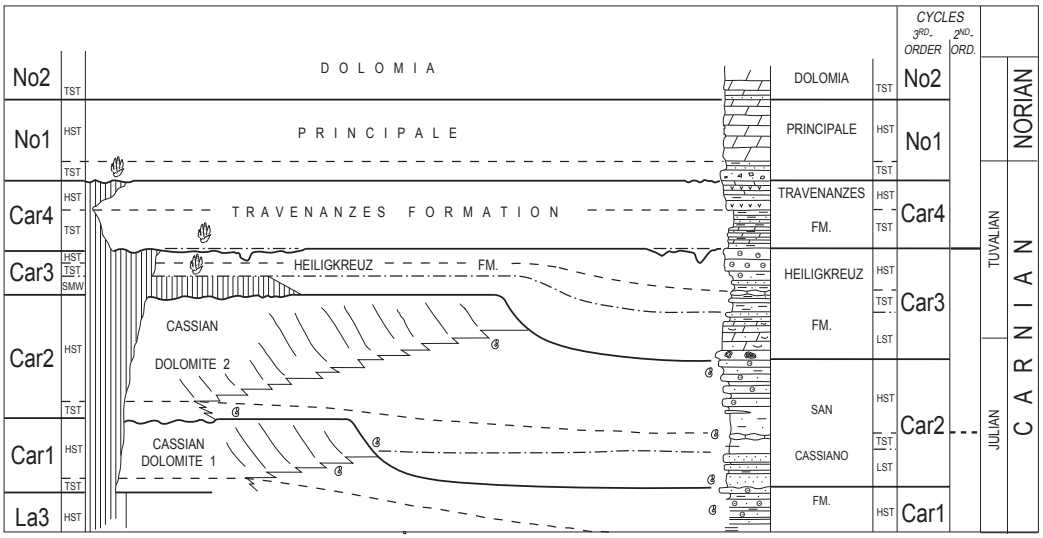

Figure 3.4: Triassic stratigraphic sequence in Dolomites. (from Gianolla et al., 1998a)

3.2.2 Lithostratigraphy of the Late Triassic sequences

The Late Triassic sequences in central Dolomites represent the recovery of the carbonate sedimentation after the Ladinian crisis due to intense volcanism (e.g. De Zanche et al., 1993).

Cassian platforms (e.g. Leonardi, 1968; Bosellini, 1984; De Zanche et al., 1993; Bosellini et al., 2003) are intensively dolomitized, but the depositional macro-structures (geometry, different paleoenvironments) are still well recognizable (e.g. Gianolla et al., 2008). Information about the characteristics of the platform margins derives from the deposits and the olistoliths in the coeval San Cassiano Formation (e.g. Gianolla et al., 2008). The platform margin was probably made of biogenic

reefs (boundstone dominated by microbialitic automicrite, with colonial corals) cross-bounded with calcarenitic shoals. The internal lagoon shows peritidal cycles with subtidal fine-grained carbonates alternated to stromatolites, tepees and pisolitic beds of supratidal environment.

The San Cassiano Formation is a basinal sequence of calcarenites, marls and volcanoclastic arenites (basal member) and a mostly carbonatic member in the upper part of the formation (De Zanche et al., 1993; Keim et al., 2006; Neri et al., 2007). The San Cassiano Formation is different from the underlying Wengen-La Valle Formation for the presence of carbonatic deposit transported from the coeval prograding Cassian platforms (i.e. oolithic-bioclastic turbidites). The quantity of volcaniclastic terrigenous mainly depends on the paleogeography: the higher contents of volcaniclastic sediments are near the old volcanic areas.

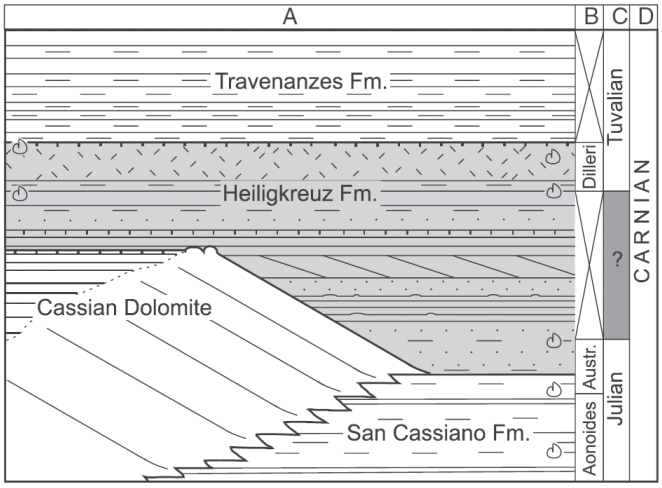

Figure 3.5: Lithostratigraphic scheme of the San Cassiano Fm to the Travenanzes Fm in the Cortina area (from Gattolin et al., 2015).

The overlying Heiligkreuz Formation (De Zanche et al., 1993; Preto and Hinnov, 2003; Neri et al., 2007; Breda et al., 2009; Gattolin et al., 2013, 2015) represents the beginning of the Cassian Basins closure (Fig. 3.5). The decreased subsidence led to a strong regression in all the Cassian Basins, and the carbonatic/terrigenous coastline starts prograding fast (as suggested by the decreasing of the platforms slope angle). The Heiligkreuz Fm is in concordance with the San Cassiano Fm and in onlap to the Cassian platforms, sometimes overlapping the platform top in discoformity (in this cases the platform top shows karst erosion). The Heiligkreuz Fm is divided in three members (Neri et al., 2007) (Fig. 3.6):

- Borca Member: dolomitic limestone, arenitic dolostone and arenites, commonly interbedded with thin shale layers. Limestones dominate the base of the member, whereas the top is made of well-stratified dolostones with marly layers in peritidal cycles (with stromatolites), ending with paleosoils.

- Dibona sandstones Member: conglomerates, sandstones and pelites, interbedded with limestones. Remains of plants are abundant, sometimes in thin coal layers.
- Lagazuoi Member: arenaceous dolostone, sandstones with carbonatic cement, oolithic-bioclastic dolomitic arenites/calcarenites.

The Travenanzes Formation (De Zanche et al. 1993, Neri et al. 2007, Breda and Preto 2011) deposited after the filling of the Cassian Basins in a low-gradient coastal environment (Breda and Preto, 2008) (Fig. 3.5). The Travenanzes Formation records the passage from a relative humid period (Heiligkreuz Formation) to an arid period. The contact with the underlying Heiligkreuz Formation is sharp, just above the Lagazuoi Mb. The Travenanzes Fm is made of mixed carbonatic-siliciclastic sediments, with marly levels at the base, passing to mainly siliciclastic sedimentations (shales, pelites, fine arenites) with levels of evaporites (mainly primary dolomite) indicating an arid lagoon environment (sabkha-type) (e.g. Breda et al., 2009; Breda and Preto, 2011). The passage to overlying Dolomia Principale is gradual, with an increase of carbonatic levels, dominated by dolomitic peritidal cycles of carbonate tidal-flat and shallow lagoon environments (e.g. Breda and Preto, 2011).

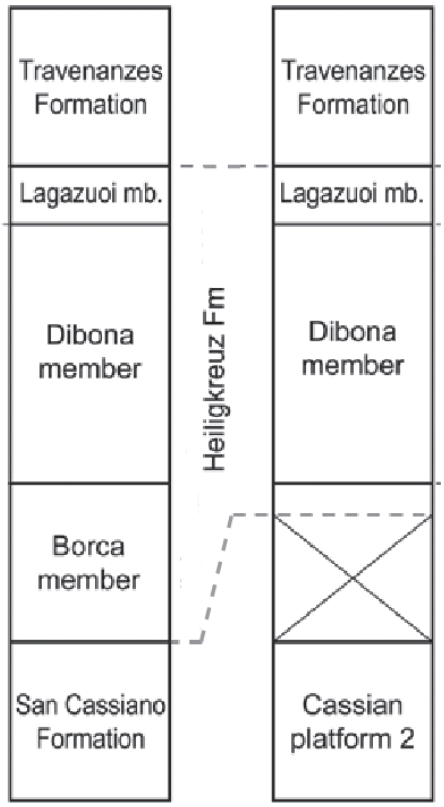

Figure 3.6: Sequence of the Carnian in the Tofane area, with the subdivision of the Heiligkreuz Fm in the Borca, Dibona sandstones and Lagazuoi Mbs (modified from Breda et al., 2009).

The Dolomia Principale is a very thick (max. 2000 m) sequence of dolostones and dolomitic limestones, outcropping from western Lombardy to western Slovenia (e.g. Bosellini and Hardie, 1988). The Dolomia Principale deposited in a shallow water environment, far away from coastline and controlled by constant subsidence persisting for several million years (in some areas for all the Norian). The sequence recorded peritidal cycles, made of grainstones with bivalves and gastropods passing to massive dolostones with *Megalodon* and *Worthenia* (subtidal facies), thin layers of stromatolitic dolostones (intertidal to supratidal facies), sometimes overlaid by a pedogenetic level with tepee structures (supratidal facies) (Gianolla et al., 1998a).

3.2.3 Section of interest

For paleomagnetic investigations I chose the Dibona section from the Dolomites, in order to check and integrate the magnetostratigraphy of the coeval Pignola-2 section. The Dibona section is a shallow-marine succession represented by limestones with fine to coarse-grained sandstones and shales (Heiligkreuz Fm), overlied by limestones with interbedded shales that pass quickly to a shale-dominant sequence with interbedded limestones and evaporites (Travenanzes Fm). The section is characterized by palynomorphs biostratigraphy, comparable with the Pignola-2 record.

3.3 WOMBAT PLATEAU (NORTHWESTERN AUSTRALIA)

3.3.1 Geological setting

The Wombat Plateau is located in the Indian Ocean (~453 km from the northwestern Australia coast), and was cored during a ODP (Oceanic Drilling Program) campaign in 1988. The mission was named Leg 122 and divided in six sites: 759, 760, 761, 764 from the Wombat Plateau (16°44'21.78"S; 115°29'12.3"E), and 762, 763 from the Exmouth Plateau (20°44'47.57"S; 112°31'26.45"E) (Fig. 3.7).

The sites 759, 760 and 761 cover a period from the Quaternary to the Lower-Upper

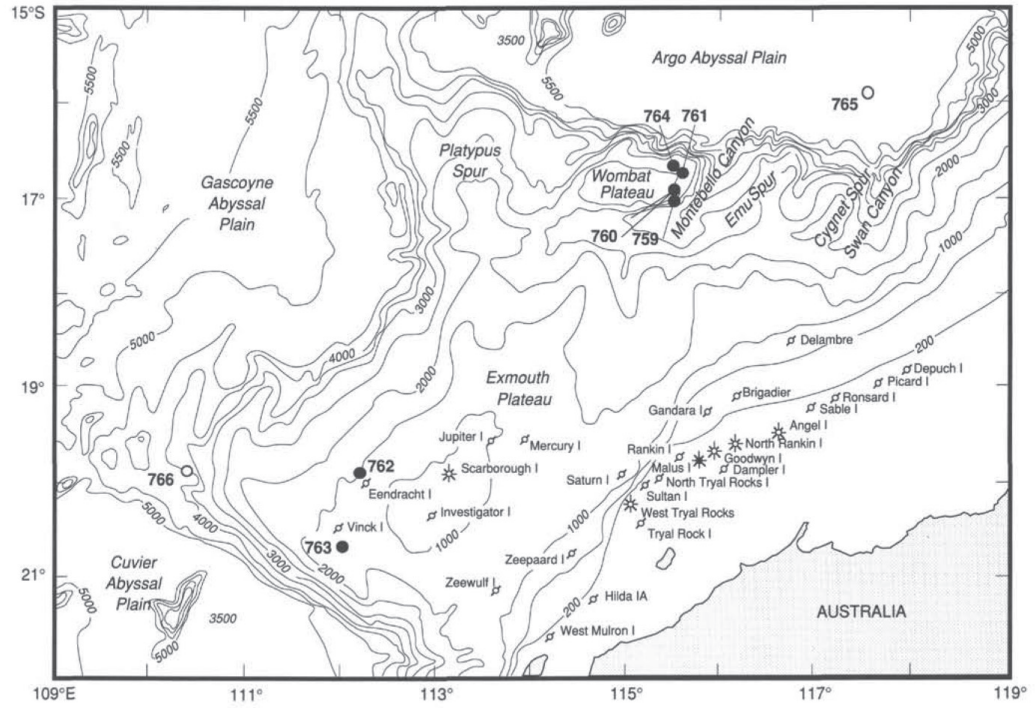

Figure 3.7: geographic position of Wombat Plateau (Sites 759-760-761-764) and Exmouth Plateau (Sites 762 and 763). From Haq et al. (1990).

Cretaceous, and then, after an unconformity, from Rhaetian to Carnian (Late Triassic). The variation in lithology reveals a passage between different environments, with facies typical of delta, shallow marine and tidal flat, where sedimentation is both carbonatic and siliciclastic.
The Late Triassic portions of the Leg 122 sites have a sufficient recovery in the Carnian and early Norian sediments, whereas in the late Norian and Rhaetian part most of the material has been lost. Here are briefly presented the features of Sites 759, 760 and 761, which will be discussed in detail in the respective chapters.

3.3.2 Sections of interest

In the Wombat Plateau I chose three Sites for my paleomagnetic analyses: 759, 760 and 761. These three sites cover the upper Carnian to middle Rhaetian interval, which means a potential magnetostratigraphic record for the great part of the Late Triassic.

Site 759 (Carnian/Norian):
Shales and siltstones, with some intercalations of arenite and limestone, are representative of the lower part of the site (Carnian). Moving upward, the limestone levels increase and become dominant in the upper part of the Norian portion of the site. Limestones are mainly mudstones and wackestones, sometimes packstones, containing peloids, calcareous lithoclasts, skeletal fragments (mollusk shells, echinoids ossicles, green algae), oncoids, and mudstone intraclasts. Also benthic foraminifers are present and often micritized. Most of the mudstones and wackestones show burrowing marks, responsible of the mottled color of these layers. Coal layers and coalified roots have been noticed in the terrigenous intervals. Diagenetic siderite ($FeCO_3$) is also present in the deepest cores (Carnian), in layers and surrounding the burrows.

Site 760 (Carnian/Norian):
This site is mostly siliciclastic, in particular in the Norian. The main lithology is black to dark gray claystones interbedded with dark greenish/gray clayey siltstones to silty sandstones, with occasional mollusk fragments, glauconite and coal. Fossiliferous limestones appear around the Carnian/Norian accompanied with siliciclastic dark claystones. Siliciclastic sediments become dominant in the Carnian, with dark silty claystones with minor greenish/gray silty sandstones. Molluscal shells and sideritic nodules are present.

Site 761 (Norian/Rhaetian):

In this site, limestones are concentrated in the youngest Rhaetian cores. White and pale brown limestones become dark grey/black in color in the lower Rhaetian, where rhythmical alternations with calcareous claystones are frequent. In the basal Rhaetian and upper Norian dark to black carbonaceous claystones are the main lithology, with subordinate crinoidal limestones in the Rhaetian. In the Norian silty claystones are also frequent, with coal levels.

3.4 PELAGONIAN DOMAIN (GREECE)

3.4.1 Geological setting

The Pelagonian Domain is an Early Permian to Late Jurassic sedimentary sequence, deposited on the metamorphic Pelagonia terrane, a Variscan crystalline basement of Late Carboniferous (Stampfli et al., 1998; Vavassis et al., 2000) and interpreted as a consequence of the rifting and spreading of the Maliac oceanic basin (De Bono et al., 2001). The Pelagonia was a part of the Africa/Apulian plate, along the south-western margin of the Tethys Ocean (e.g. Ciarapica and Passeri, 2002).

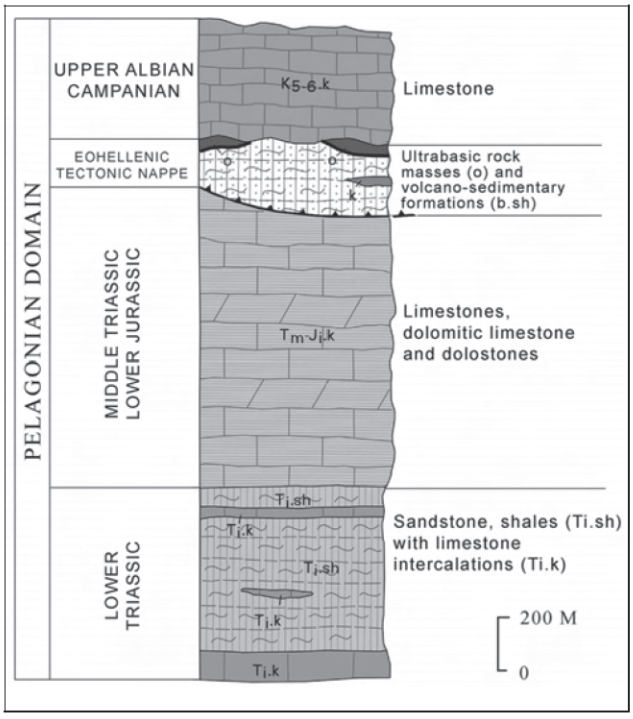

Figure 3.8: Stratigraphic sequence of Pelagonian Domain (from Romano et al., 2008)

Late Triassic is characterized by the emplacement of a wide carbonate platform that survived up to the Late Jurassic (e.g. Tataris et al., 1970; Celet and Ferrière, 1978; Celet et al., 1988), although in many areas is recorded until Early Jurassic (Pliensbachian) (e.g. Parginos et al., 2007) (Fig. 3.8). Large part of this platform has

been metamorphosed or intensely tectonized.

3.4.2 Section of interest

One of the few well-preserved Triassic/Jurassic portion of the platform is represented by the Mount Messapion section, located in the area of Chalkida, in the eastern part of central Greece. The section is a ~710 meters Late Triassic – Early Jurassic sequence of limestones, dolomitic limestones and dolomites (Fig. 3.9). The whole section is a pile of shallowing-upward peritidal cycles (Romano et al., 2008). The Mt. Messapion section has been subdivided in three units (A, B, C) based on sedimentary structures and fossil content (Fig. 3.9):

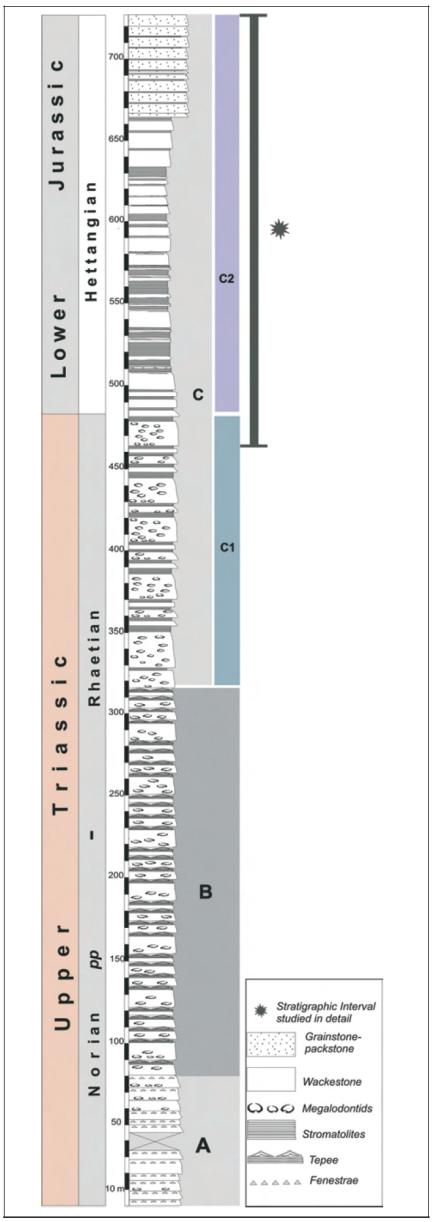

Figure 3.9: Stratigraphy of Mount Messapion section (from Romano et al., 2008). The bracketed bar represent the investigated area.

- Unit A – 70 meters: meter-scale shallowing upward peritidal cycles, bioclastic-intraclastic wackestones/ packstones with rare Megalodontids (subtidal) passing gradually into laminated loferites (supratidal) with irregular and laminoid fenestrae.
- Unit B – 230 meters: peritidal cycles similar to those described in Unit A. The differences are the tepee structure inside the supratidal levels.
- Unit C – 410 meters: peritidal cycles with tepee structures, and with well-developed microbial intervals in the inter-supratidal part of the cycles. Unit C is subdivided in subunits C1 (180 meters) and C2 (230 meters). Subunit C2 is different from C1 for the absence of Megalodontids and bioturbation, and for the gradual enrichment in oolitic bioclastic grainstones-packstones, with benthic foraminifera, green algae, gastropods and bivalves.

For my paleomagnetic investigations I considered the interval between subunits C1 and C2, around the Triassic/Jurassic boundary.

Chapter IV
INVESTIGATION ON SELECTED TETHYAN MARINE SECTIONS

4.1 RHAETIAN

As explained in Chapter 1, Rhaetian is affected by uncertainties about its base, mainly due to the different (and mostly discordant) markers used to place the Norian/Rhaetian boundary in stratigraphic sections. The following Tethyan marine sections have been analyzed for magnetostratigraphy in order to contribute to the resolution of this problem.

4.1.1 Pignola-Abriola section (*from Maron et al., 2015: GSA Bulletin, v. 127, p. 962-974; see Attached publications*)

Here are presented new biostratigraphic, magnetostratigraphic, and chemostratigraphic data from the Pignola-Abriola section of Italy. This section

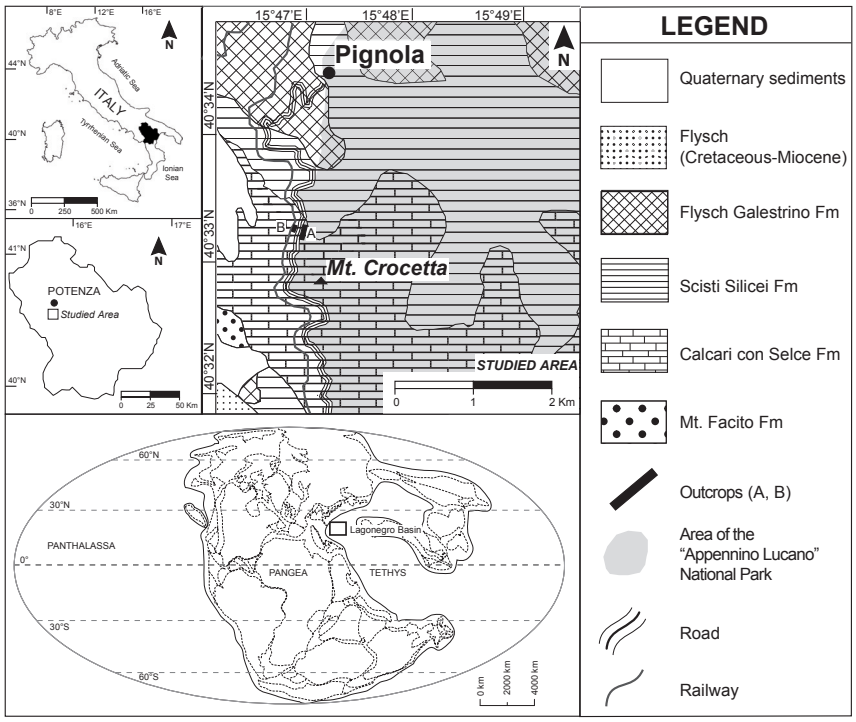

Figure 4.1: The Pignola-Abriola sections (A, B) are located in the southern Apennines, near Potenza (southern Italy). The main section (A) crops out on the western flank of Mount Crocetta, along the main road SP5 connecting the towns of Pignola and Abriola (40°33'23.50"N, 15°47'1.71"E), whereas the auxiliary subsection (B) crops out close to an unused railway tunnel located ~10 m below the SP5 road level (40°33'24.74"N, 15°46'59.59"E).

records the FAD of *Misikella posthernsteini*, occurring in the lower *Proparvicingula moniliformis* radiolarian zone (Giordano et al., 2010). I date these events by means of magnetostratigraphic correlation with the Newark APTS, while addressing in detail the taxonomic complexities vexing the use of the conodont *M. posthernsteini* as proxy for the Norian-Rhaetian boundary level. I also illustrate the occurrence of a prominent negative $\delta^{13}C_{org}$ excursion at meter level 44.5, ~0.5 m below the FAD of *M. posthernsteini* (within the base of the *P. moniliformis* zone), which serves as a useful geochemical proxy for the Norian- Rhaetian boundary level.

Geological Setting

The Pignola-Abriola section crops out on the western side of Mount Crocetta, along the road SP5 connecting the village of Pignola to Abriola (Potenza, southern Italy; Fig. 4.1, section A, coordinates: 40°33'23.50"N, 15°47'1.71"E). The road section is ~58 m thick (Fig. 4.2, left panel) and is complemented by an ancillary 7-m-thick subsection (Fig. 4.2, right panel) outcropping close to a unused railway tunnel located ~10 m below the SP5 road level (Fig. 4.1, section B, coordinates: 40°33'24.74"N, 15°46'59.59"E). The stratigraphic sequence is composed of the Calcari con Selce (i.e., Cherty Limestone) Formation, which was deposited in the Lagonegro Basin, a branch of the western Tethys Ocean characterized by pelagic sedimentation since the Permian (Finetti, 1982, 2005; Catalano et al., 2001; Ciarapica and Passeri, 2002, 2005; Argnani, 2005; Rigo et al., 2012a). The Calcari con Selce Formation consists of thinly bedded cherty hemipelagic to pelagic limestones (mudstones, wackestones, and rare packstones), interbedded with shales and marls, with common radiolarians, conodonts, and sporadic bivalves. The lower part of the section is dominated by cherty limestones, often dolomitized, intercalated with very thin marls or clayey levels (Fig. 4.2). The upper portion is instead dominated by an alternation of silicified limestones and black to brown or greenish, thinly laminated shales (Fig. 4.2), which are rich in organic matter, indicating deposition in dysoxic or anoxic conditions. Calcarenitic intercalations are also present through the section (Fig. 4.2). In particular, a 1.5-m-thick calcarenitic bank at ~35 m from the base of the measured section has been used as a lithostratigraphic marker to correlate the Pignola-Abriola road section (Fig. 4.2, left panel) to the railway tunnel subsection (Fig. 4.2, right panel).

Biostratigraphy

The fossil content of the Pignola-Abriola section consists mainly of conodonts

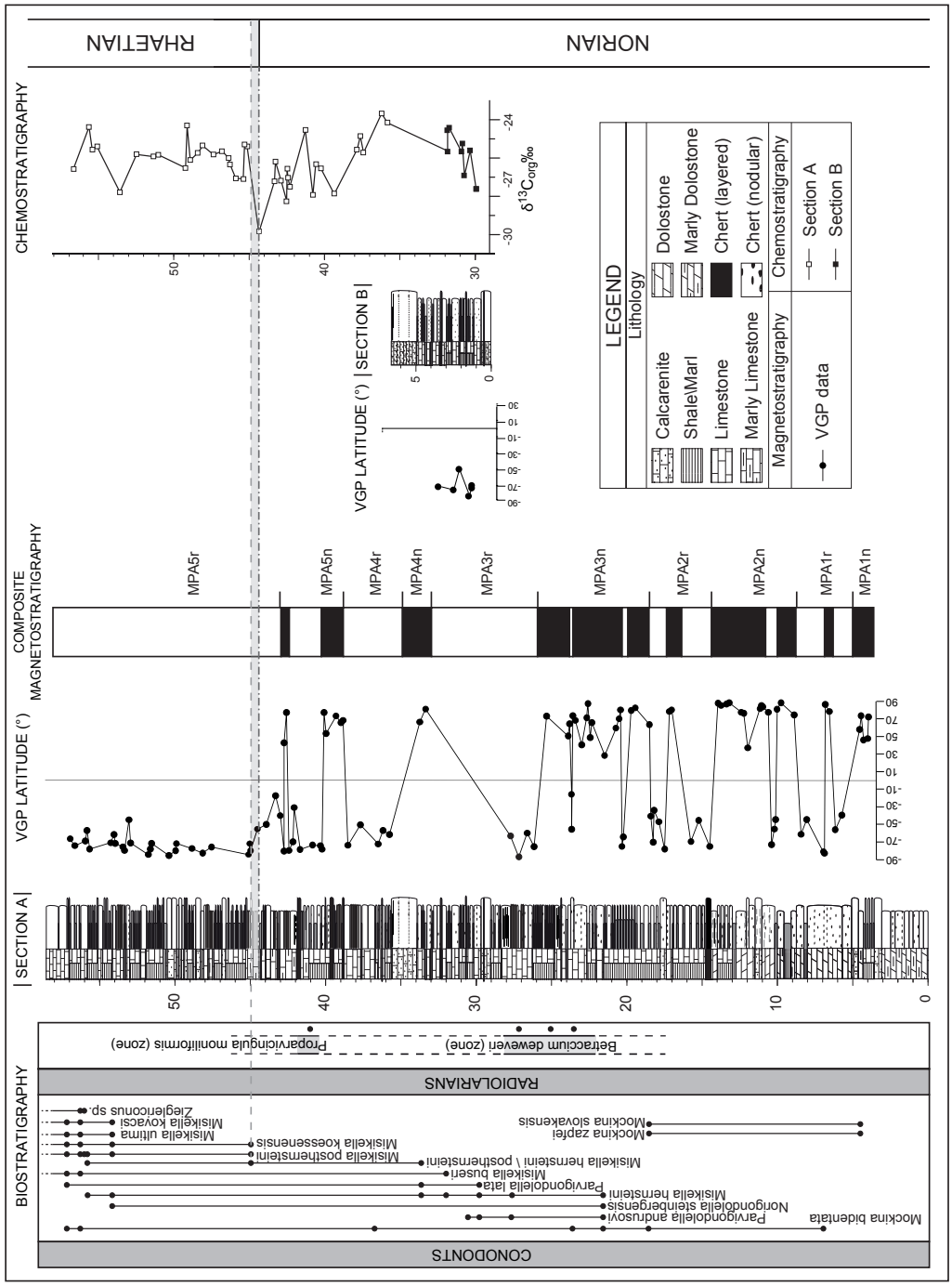

Figure 4.2: The Pignola-Abriola sections. From left to the right: conodont and radiolarian biostratigraphy (see Plate 4.1 for key species), lithostratigraphy, virtual geomagnetic pole (VGP) latitudes calculated from characteristic remanent magnetization (ChRM) component directions, and derived magnetostratigraphy and chemostratigraphy ($\delta^{13}C_{org}$) of the Pignola-Abriola section. To the right is lithostratigraphy and VGP latitudes of the auxiliary subsection B. Black is normal polarity, and white is reverse polarity. The levels containing the first appearance datum (FAD) of conodont Misikella posthernsteini *sensu stricto and the marked decrease in the $\delta^{13}C_{org}$ to ~–30‰ used to define the Norian-Rhaetian boundary are highlighted by dashed horizontal lines.*

and pyritized radiolarians. Here, I present an updated conodont and radiolarian biostratigraphy (Fig. 4.2) after recent biostratigraphic data published by Rigo et al. (2005), Bazzucchi et al. (2005), and Giordano et al. (2010).

Conodonts are well distributed along the entire section (representative specimens are shown in Plate 4.1) and are characterized by a conodont alteration index (CAI) of 1.5 (Epstein et al., 1977; Bazzucchi et al., 2005; Rigo et al., 2005). The following main events have been recognized (Fig. 4.2):

1. the first occurrence (FO) of *Mockina bidentata* at meter 7;
2. the FO of *Misikella hernsteini* at meter 21.5, associated with the FO of *Parvigondolella andrusovi*;
3. the FO of *the Misikella hernsteini/posthernsteini* morphocline at meter 33.5;
4. the FO of *Misikella buseri* at meter 32;
5. the FAD of *Misikella posthernsteini* at meter 45 in sample PIG24, in association with *Misikella koessenensis*; and
6. the FO of *Misikella ultima* at meter 54.

The radiolarian associations are well preserved and conform to the biozonation proposed by Carter (1993):

1. Sample PR14 at meter 25 yielded a radiolarian assemblage referable to the *Betraccium deweveri* zone (Carter, 1993) and consisting of *Betraccium deweveri* Pessagno and Blome, *Praemesotaturnalis gracilis* Kozur and Mostler, *Tetraporobrachia* sp. aff. T. composita Carter, *Ayrtonius elizabethae* Sugiyama, *Citriduma* sp. A sensu Carter (1993), *Globolaxtorum* sp. cf. *G. hullae* Yeh and Cheng, *Lysemela* sp. cf. *L. olbia* Sugiyama, *Livarella valida* Yoshida and *Livarella* sp. sensu Carter (1993) (Giordano et al., 2010); a similar assemblage was found also in sample PR15 at meter 23.5,

Plate 4.1: (following page) Scanning electron microscope (SEM) micrographs of Upper Norian and Rhaetian radiolarians and conodonts from the Calcari con Selce Formation, Pignola-Abriola section. Radiolarians: samples PR13, PR14, and PR15 are referred to the Betraccium deweveri *zone; sample PA25 is referred to the* Proparvicingula moniliformis *zone, assemblage 1. Scale bar = 100 μm for 1–2, 7, 9, 11–14; 112.5 μm for 3–5, 8; 150 μm for 6, 10 (after Bazzucchi at al., 2005; Giordano et al., 2010, modified). 1–2—*Betraccium deweveri *Pessagno and Blome, sample PR14. 3—*Praemesotaturnalis gracilis *(Kozur and Mostler), sample PR14. 4—*Tetraporobrachia *sp. aff.* T. composita *Carter, sample PR14. 5—*Ayrtonius elizabethae *Sugiyama, sample PR15. 6—*Citriduma *sp. A, sensu Carter (1993), sample PR13. 7—*Globolaxtorum *sp. cf.* G. hullae *(Yeh and Cheng), sample PR14. 8—*Lysemela *sp. cf.* L. olbia *Sugiyama, sample PR15. 9—*Livarella valida *Yoshida, sample PR15. 10—*Livarella *sp., sensu Carter (1993), sample PR14. 11—*Fontinella primitiva *Carter, section sample PA 25. 12—* Praemesosaturnalis *sp. cf.* P. sandspitensis *(Blome), sample PA25. 13—*Globolaxtorum hullae *(Yeh and Cheng), sample PA25. 14—*Livarella densiporata *Kozur and Mostler, sample PA25. Conodonts: Scale bar = 75 μm (after Bazzucchi at al., 2005; Giordano et al., 2010, modified): 15 (a, b, c)—*Mockina zapfei *(Kozur), sample PIG 0. 16 (a, b, c)—*Mockina slovakensis *(Kozur), sample PIG 0. 17 (a, b, c)—*Misikella hernsteini *(Mostler), sample PIG 16. 18 (a, b)—*Misikella posthernsteini *Kozur and Mock, sample PIG 24. 19 (a, b)—*Misikella kovacsi *Orchard, sample PIG 40. 20 (a, b, c)—*Misikella ultima *Kozur and Mock, sample PIG 40.*

PLATE 4.1

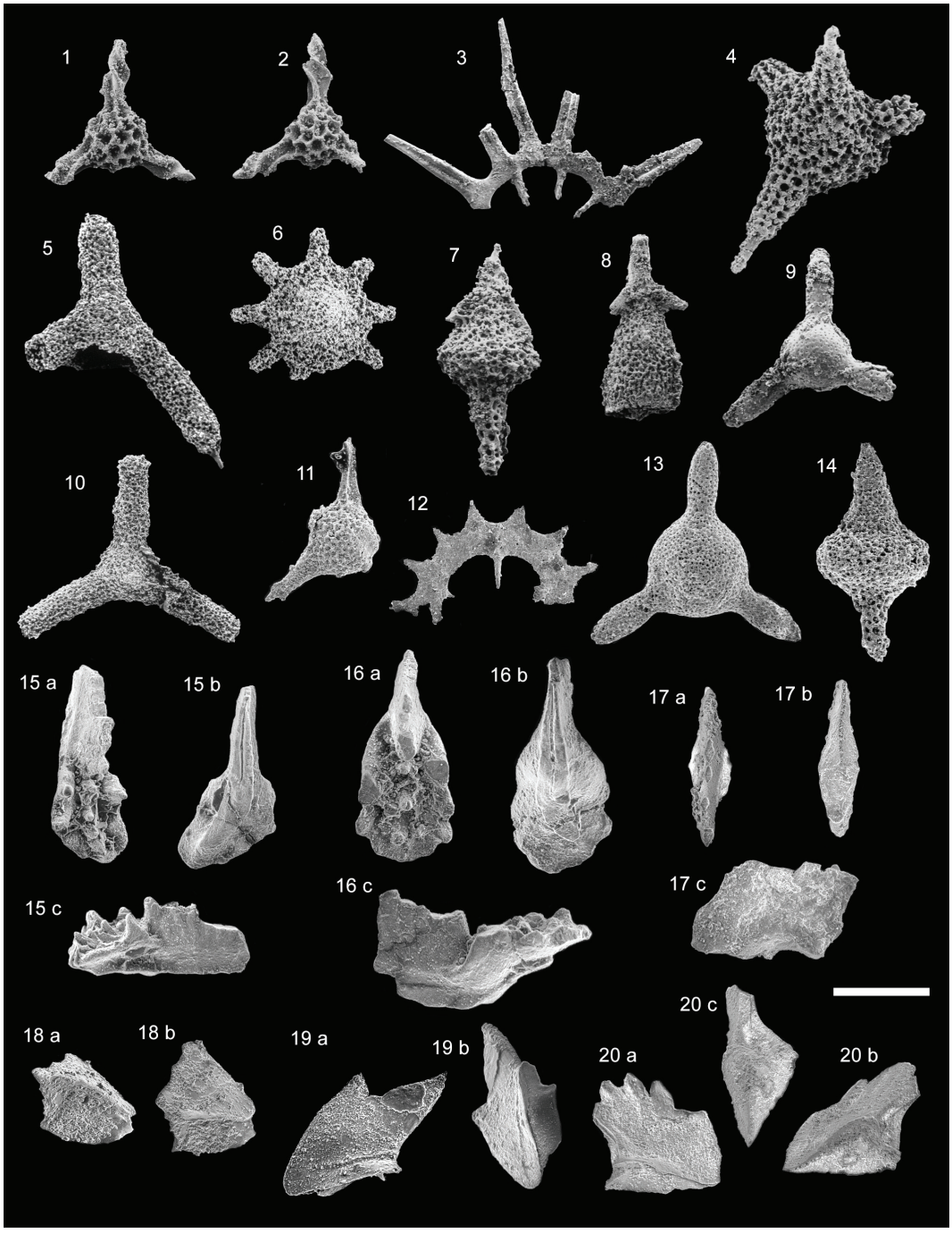

and sample PR13 at meter 27. The presence of *Globolaxtorum* sp. cf. *G. hullae* Yeh and Cheng in this assemblage is atypical, because the genus *Globolaxtorum* is usually referred only to the *Proparvicingula moniliformis* and *Globolaxtorum tozeri* zones (O'Dogherty et al., 2009).

2. Sample PA25 at meter 41 yielded a radiolarian assemblage referable to the *Proparvicingula moniliformis* zone assemblage 1 (U.A. 2–5 in Carter, 1993)

for the presence of *Fontinella primitiva* Carter, *Praemesosaturnalis* sp. cf. *P. sandspitensis* Blome, *Globolaxtorum* sp. cf. *G. hullae* Yeh and Cheng, and *Livarella densiporata* Kozur and Mostler (Bazzucchi et al., 2005; Giordano et al., 2010).

The Norian-Rhaetian boundary is conventionally placed in stratigraphic levels where the FAD of *Misikella posthernsteini* is documented (Krystyn, 2010), which is a phylogenetic descendent of *M. hernsteini* (e.g., Mostler et al., 1978; Kozur and Mock, 1991; Giordano et al., 2010). The transition from drop-shaped to heart-shaped basal cavity along with a reduction of the number of blade denticles characterize the evolution of the *M. hernsteini/posthernsteini* morphocline (Giordano et al., 2010). Specimens characterized by an evident furrow on the backside of the cusp and the associated inflection of the posterior margin of the basal cavity are here considered *Misikella posthernsteini* sensu stricto, as suggested by Giordano et al. (2010). At Pignola-Abriola, the presence of the *Misikella hernsteini/posthernsteini* morphocline, as well as the presence of the FAD of *M. posthernsteini* sensu stricto (m 45, sample PIG24) provide a reliable (and continuous) biostratigraphic signal. Furthermore, in the Pignola-Abriola section, the conodont *Misikella posthernsteini* sensu stricto appears 4 m above the base of radiolarian *Proparvicingula moniliformis* zone assemblage 1 (Fig. 4.2), which is commonly adopted to define the early Rhaetian (e.g., Carter, 1993; Bertinelli et al., 2005; Giordano et al., 2010).

Geochemistry

In total, 41 samples, mostly black to brown shales, from the upper portion of the Pignola-Abriola section (from meter 30 to the top of the section) were analyzed for $\delta^{13}C_{org}$ (data in Appendix A.1). The rock samples were pulverized and acid-washed with 10% HCl in a 70 °C water bath for 3 h, and the process was repeated at least three times to thoroughly remove pyrite and carbonates. The samples were subsequently neutralized with high-purity water, dried at 30°C overnight, and then wrapped in tin capsules and analyzed for their isotopic composition. The analyses were carried out using a GVI Isoprime continuous flow-isotope ratio mass spectrometer (CF-IRMS) at Rutgers University, adding multiple blank capsules and isotope standards for each batch of isotopic analyses (NBS 22 = –30.03‰; Coplen et al., 2006) plus a matrix matched in-house standard. Standard deviations for $\delta^{13}C_{org}$ standards during the period of analysis were better than σ= 0.2‰.

The $\delta^{13}C_{org}$ values of the Pignola-Abriola section are between –29.95‰ and –23.70‰ (Fig. 4.2). After a moderate increase in $\delta^{13}C_{org}$ (from ~–27.5‰ to –24‰ from meter

30 to 36), a large decrease to ~–30‰ was recorded for meter 36 to meter 44.5, immediately followed by a rapid return to higher values (~–25‰, ~20 cm above). A subsequent decrease of ~2‰ is recorded at meter 53.5 (close to the level containing the FO of *Misikella ultima*; Fig. 4.2). Notably, the low $\delta^{13}C_{org}$ of ~–30‰ at meter 44.5 is just below the level containing the FAD of *Misikella posthernsteini* sensu stricto, and within the base of the *Proparvicingula moniliformis* zone (Fig. 4.2).

Paleomagnetism

In total, 220 oriented core samples were collected from the Pignola-Abriola section and analyzed at the Alpine Laboratory of Paleomagnetism (Peveragno, Italy). Rock magnetic properties were studied on a representative set of samples by means of thermal decay of a three-component isothermal remanent magnetization (IRM)

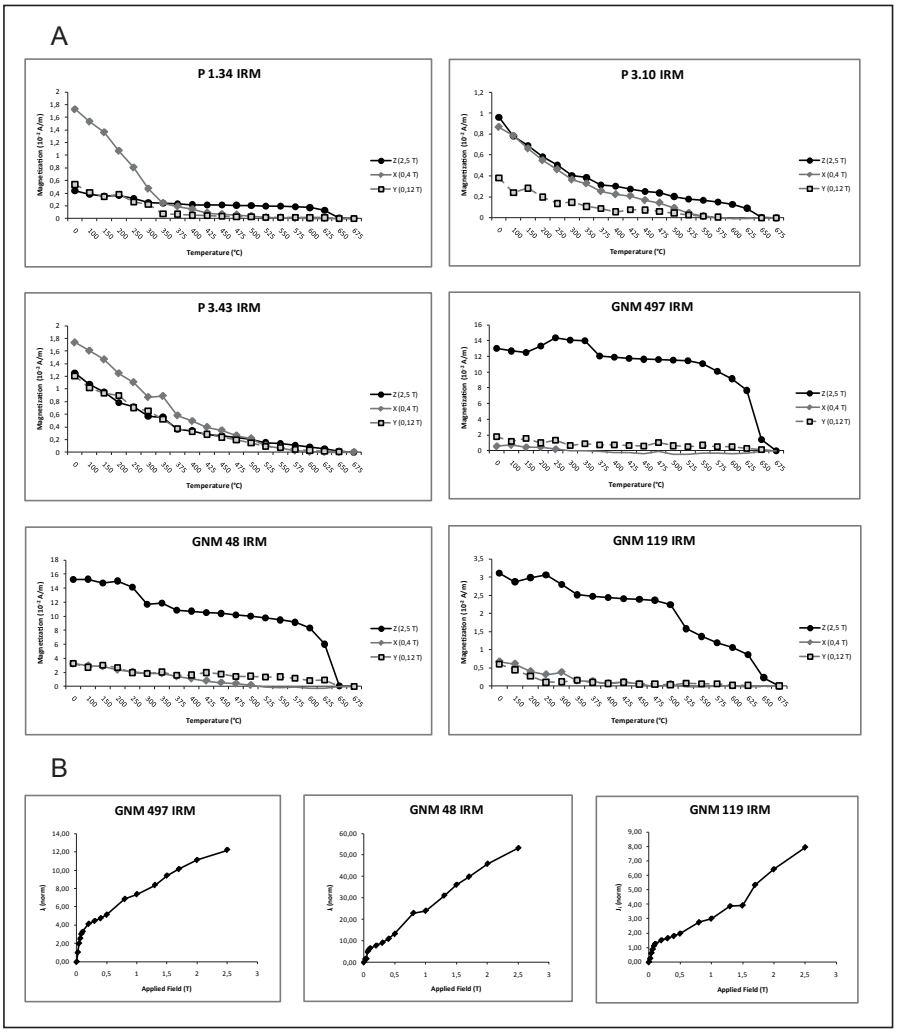

Figure 4.3: Thermal demagnetization of a three-component isothermal remanent magnetization (IRM) (A) and IRM acquisition curves (B) for representative samples from Pignola-Abriola showing the presence of a variable mixture of hematite and magnetite. See text for discussion.

imparted at fields of 2.5 T, 0.4 T, and 0.12 T (Lowrie, 1990) and IRM acquisition curves. The lower part of the section (samples P1.34, P3.10, P3.43; Fig. 4.3A) is characterized by a high-coercivity mineral with maximum unblocking temperatures (TB) of 650–675 °C, attributed to hematite, coexisting with a lower-coercivity mineral with TB of 525–575°C, interpreted as magnetite; an inflection at ~350°C in the 0.4 T curve observed in sample P1.34 suggests the presence of iron sulfides. Samples from the upper part of the section (GNM497 at 33 m; GNM48 at 43.5 m; GNM119 at 57 m) appear dominated by the high-coercivity hematite phase (Fig. 4.3A). IRM curves of these samples show no tendency to saturate even at applied fields of 2.5 T (Fig. 4.3B). The cumulative log-Gaussian (CLG) analysis (Kruiver et al., 2001) reveals the presence in these samples of two magnetic phases with contrasting coercivities: a high-coercivity phase with coercivity of remanence ($B_{1/2}$) = 1.6–2 T, which accounts for ~60%–85% of the IRM, and a subordinate low-coercivity phase with $B_{1/2}$ = 0.1 T, which accounts for the reminder of the IRM (Fig. 4.4). The presence of higher amounts of (detrital) hematite in the upper part of the section may correlate with the increase in terrigenous input (shales and marls) observed in the upper part of the section (Fig. 4.2).

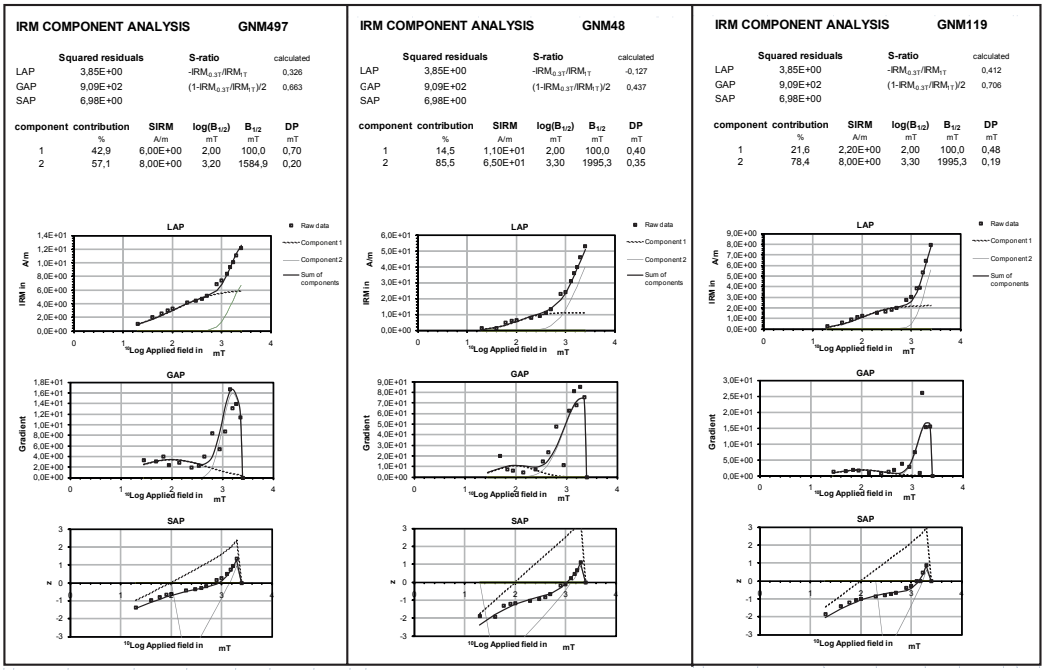

Figure 4.4: Cumulative log-Gaussian (CLG) IRM curves for samples GNM 497, 48, 119 (see text for details). The saturation magnetization (SIRM), the coercive force ($B_{1/2}$) and the dispersion parameter (DP) are listed for each magnetic component.

The natural remanent magnetization (NRM) of samples, measured on a 2G Enterprises DC- SQUID cryogenic magnetometer, is on average 0.08 mA/m. All

samples were thermally demagnetized in steps of 50 °C or 25 °C up to a maximum of 675 °C, and the component structure of the NRM was plotted on vector end-point demagnetization diagrams (Fig. 4.5; Zijderveld, 1967). After removal of spurious

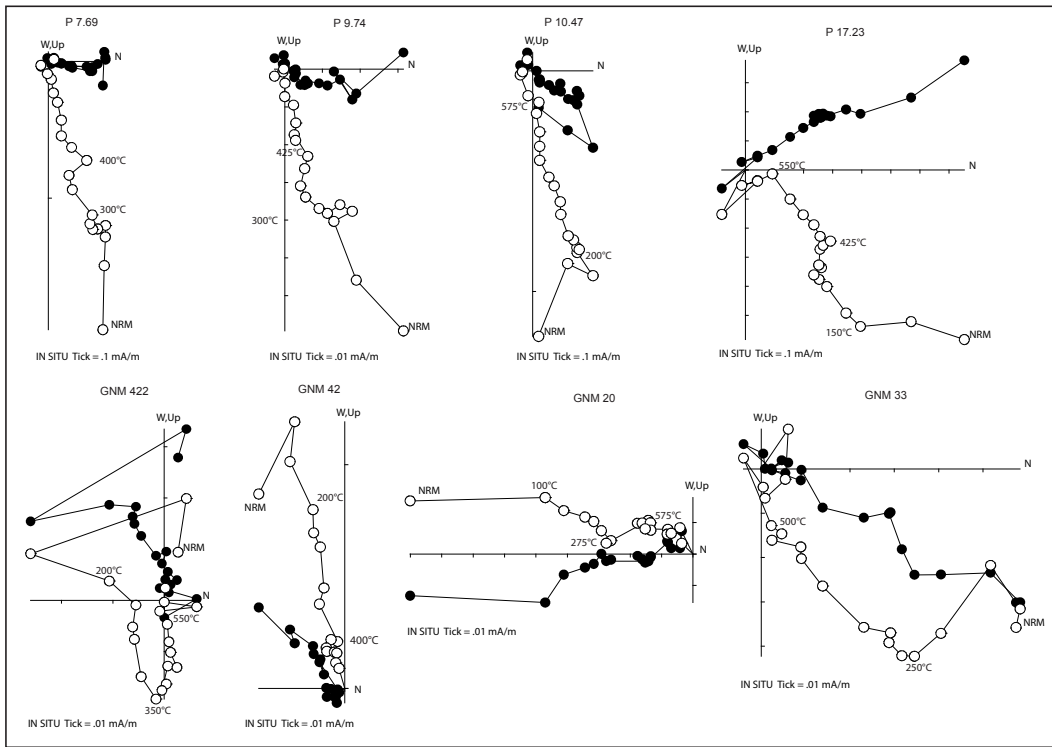

Figure 4.5: Vector end-point demagnetization diagrams for representative samples from Pignola-Abriola. Closed circles are projections onto the horizontal plane, and open circles are projections onto the vertical plane for in situ (geographic) coordinates. Temperatures are expressed in °C. NRM—natural remanent magnetization.

magnetizations between room temperature and ~100–300°C, a characteristic remanent magnetization (ChRM) was isolated up to 450–550°C (maximum of 625°C) in ~55% of the samples (N = 121; ChRM data in Appendix A.1) and found to be broadly oriented either N and down or S and up in tilt-corrected coordinates (Fig. 4.6). These ChRM component directions are distributed in tilt-corrected

TABLE 4.1: PALEOMAGNETIC DIRECTIONS AND POLE FROM THE PIGNOLA-ABRIOLA SECTION

Mean directions from the Pignola-Abriola section													
		IN SITU				TILT-CORRECTED							
Comp.	N	k	α_{95}	Dec.	Inc.	k	α_{95}	Dec.	Inc.	Inc.Corr.	Inc. Corr.		f
											max.	min.	
ChRM	121	8.2	4.8°	210°E	-71.5°	8.4	4.7°	195.9°E	-32.5°	47.7°	53.7°	39.0°	0.6

Paleomagnetic pole, paleolatitude and rotation from Tilt Corrected Filtered 'Ch' directions, corrected for inclination flattening						
Lat.	Long.	A_{95}	Paleolatitude	Paleolatitude		Rotation
				max.	min.	
72.5°N	143.0°E	4.0°	28.8°N	34.2°N	22.0°N	32.8° CW

Note:
Comp.: paleomagnetic component N: number of samples k, α_{95}: Fisher statistics parameters
Dec.: mean declination Inc.: mean inclination Inc. corr.: mean inclination corrected for inclination flattening
f: flattening factor Lat.: Latitude Long.: Longitude A_{95}: circular confidence limit Rotation: tectonic rotation of the site (relative to the 201 Ma Adria-Africa reference paleopole of Muttoni et al., 2013)

coordinates around an overall mean of Dec = 15.9°E, Inc = 32.5° (k = 8.4, α_{95} = 4.7°, N = 121; Table 4.1). No fold test could be performed because of the homoclinal bedding tilt of the section, whereas the reversal test (McFadden and McElhinny, 1990) was positive. Based on these results and the consistent magnetostratigraphic correlations with sections from the literature, as discussed later herein, we regard the ChRM component as primary in origin. I checked the ChRM component directions for sedimentary inclination shallowing due to sedimentary and/or compaction processes. The elongation/inclination (E/I) statistical method of Tauxe and Kent (2004) was applied to the ChRM directions, obtaining a flattening factor of f = 0.6 and a corrected mean inclination of 47.7° (min = 39.0°, max = 53.7°), corresponding to a paleolatitude for Pignola-Abriola of ~28.8°N (Table 4.1). A paleomagnetic pole was calculated for Pignola-Abriola using the tilt-corrected mean ChRM direction corrected for inclination shallowing (lat. = 72.5°N, long. = 143.0°E; Table 4.1) and compared to the 201 Ma Adria-Africa paleopole of Muttoni et al. (2013) located at lat. = 69.3°N, long. = 243.8°E. The Pignola-Abriola paleopole is displaced by ~32.8°

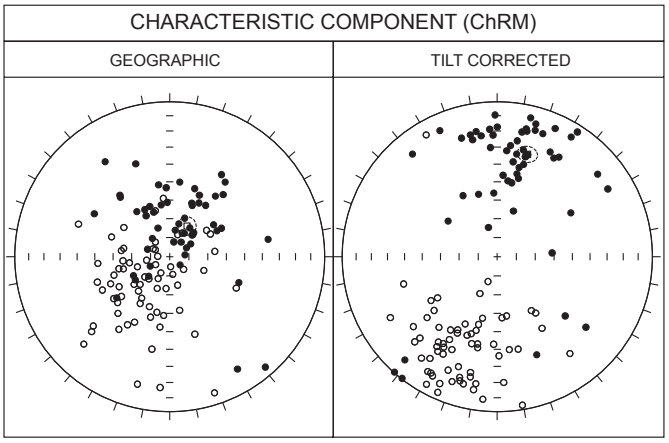

Figure 4.6: Equal-area projections for characteristic remanent magnetization (ChRM) component directions isolated at Pignola-Abriola for in situ (geographic) and tilt-corrected coordinates (see Table 4.1 for Fisher statistics parameters).

clockwise relative to the reference Adria-Africa paleopole, probably as a result of vertical-axis tectonic rotation of the sampling area during Apennine tectonics.

A virtual geomagnetic pole (VGP) was calculated for each ChRM component direction in tilt-corrected coordinates. The latitude of the sample VGP relative to the north pole of the paleomagnetic axis was used for interpreting the magnetic polarity stratigraphy, where VGP latitudes approaching +90° or –90° are attributed to normal or reverse polarity, respectively. An overall sequence of five polarity magnetozones, labeled from magnetozone MPA1 to MPA5, was established starting at the base of the section (Fig. 4.2). Each magnetozone was subdivided into a lower, predominantly normal and an upper, predominantly reverse portion, in which submagnetozones can be embedded. No obvious relation was observed between

magnetic polarity stratigraphy and the magnetic mineralogy of the samples. The FAD of *Misikella posthernsteini* sensu stricto falls within magnetozone MPA5r at ~45 m, while the new proposed Norian-Rhaetian boundary coincident with the $\delta^{13}C_{org}$ negative spike occurs inside the same magnetozone at ~44.5 m (Fig. 4.2).

Discussion

Correlations with Tethyan Sections from the Literature

The magnetostratigraphy of the Pignola-Abriola section is comparable with that of the Steinbergkogel section (Hüsing et al., 2011), which at present is the only global boundary stratotype section and point (GSSP) candidate for the base of the Rhaetian Stage (Krystyn et al., 2007a, 2007b), assuming that the occurrence of conodont *Misikella posthernsteini* at Steinbergkogel (plate 1 in Krystyn et al., 2007a) is equivalent to the FO of *Misikella hernsteini/posthernsteini* transitional forms at Pignola-Abriola (sensu Giordano et al., 2010). Hence, the main reversal portion of the Steinbergkogel magnetostratigraphy from magnetozone ST1/B– to magnetozone ST1/H– at Steinbergkogel STKA section (equivalent to ST2/B– to ST2/H– at Steinbergkogel STKB+C section), has been correlated to magnetozones MPA3r to MPA5r of the Pignola-Abriola section (Fig. 4.7). Also, part of the magnetostratigraphy of the Oyuklu section (Gallet et al., 2007), from magnetozone OyB– to OyD–, is comparable with MPA4r to MPA5r of the Pignola-Abriola section, and with ST/D– to ST/H– of the Steinbergkogel section (Fig. 4.7). Furthermore, the lower portion of the Pignola-Abriola section is magnetostratigraphically correlated with the upper part of the Pizzo Mondello section (Muttoni et al., 2004). Using the updated biostratigraphic calibration of the Pizzo Mondello magnetostratigraphy (Mazza et al., 2012), magnetozones MPA1n to MPA3n at Pignola-Abriola have been correlated to magnetozones PM-8n to PM-12n at Pizzo Mondello (Fig. 4.7). Moreover, data from Pignola-Abriola have been compared with the magnetobiostratigraphy of the Brumano and Italcementi Quarry sections (Lombardian Basin, southern Alps, Italy), which encompasses a portion of the Rhaetian (with specimens attributed to *Misikella*) up to the Triassic-Jurassic boundary as defined by pollens (Muttoni et al., 2010, 2014). Awaiting for a formal redefinition of the *Misikella* specimens in the Brumano section following the new definition of *Misikella posthernsteini* sensu stricto adopted in this study (after Giordano et al., 2010), we stress that all *Misikella* specimens at Brumano occur below the recovered magnetostratigraphy (Muttoni et al., 2010, 2014), and thus the sequence of Brumano-Italcementi Quarry magnetozones from BIT1n to

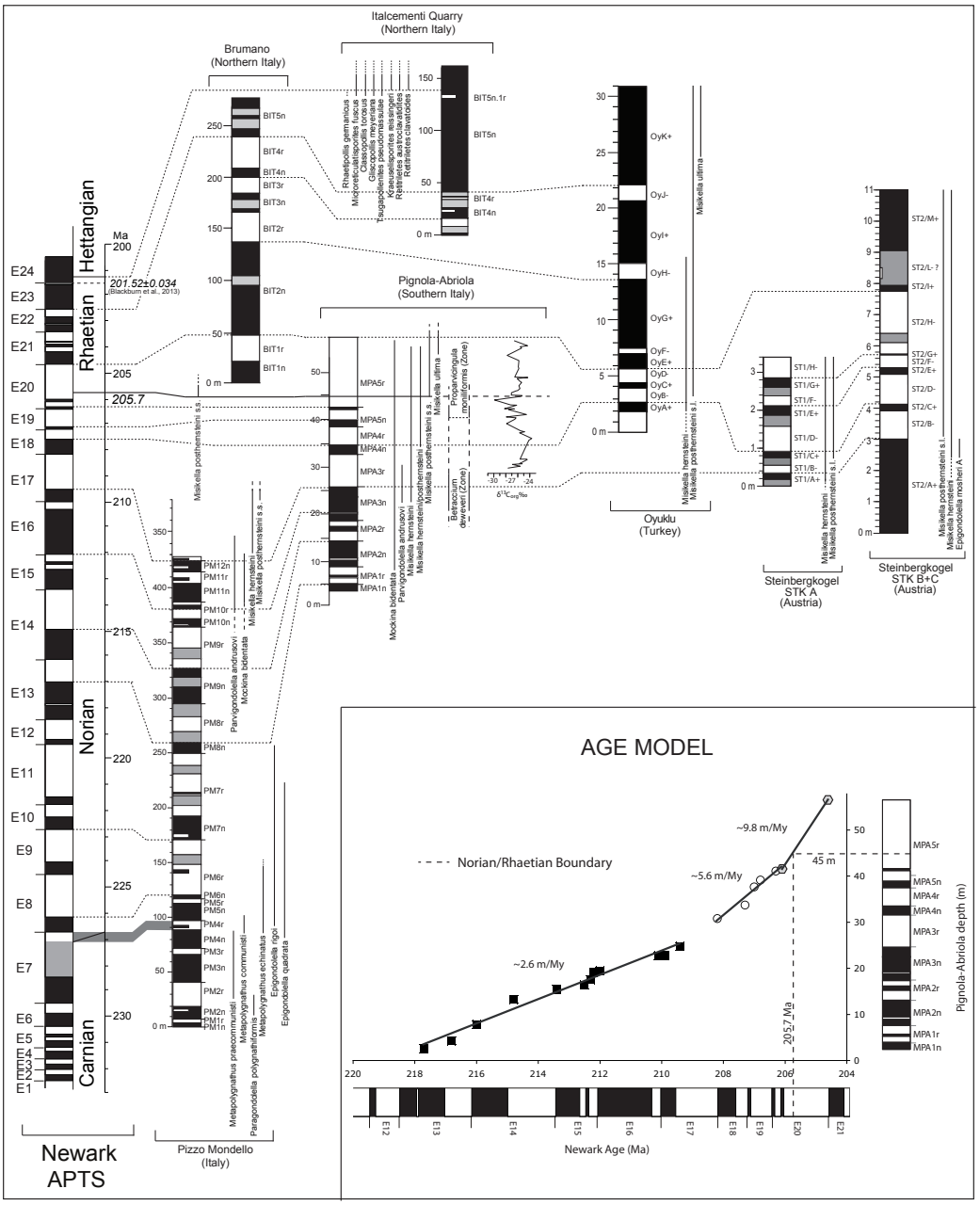

Figure 4.7: The Norian-Rhaetian magnetostratigraphy, biostratigraphy, and chemostratigraphy of the Pignola-Abriola section correlated to data from marine sections from the literature, such as Steinbergkogel (Hüsing et al., 2011), which is the current global stratotype section and point (GSSP) candidate for the Rhaetian Stage (Krystyn et al., 2007a, 2007b), Oyuklu (Gallet et al., 2007), Brumano-Italcementi Quarry (Muttoni et al., 2010, 2014), and Pizzo Mondello (Muttoni et al., 2004). In this work, specimens originally attributed to Misikella posthernsteini *at Steinbergkogel (Krystyn et al., 2007a, 2007b) are here considered* M. posthernsteini *sensu lato (s.l.) and attributed to the* M. hernsteini/posthernsteini *"transitional forms" (sensu Giordano et al., 2010). Key biostratigraphic events at Pizzo Mondello are after Mazza et al. (2012). The Pignola-Abriola section is correlated to the Newark astrochronological polarity time scale (APTS; left column) using preferred correlation option 7.1. The lower-right panel shows the derived age model of sedimentation for Pignola-Abriola with an increase in sedimentation rate in the upper part of the section where the terrigenous input is higher. The Norian-Rhaetian boundary, placed at a level coincident with a rapid decrease in $\delta^{13}C_{org}$ to ~–30‰, which virtually coincides with the level containing the first appearance datum (FAD) of conodont* Misikella posthernsteini *sensu stricto within the* Proparvicingula moniliformis *radiolarian zone, is traced within Newark magnetozone E20r at 205.7 Ma.*

BIT5n is regarded as largely younger than the Pignola-Abriola magnetostratigraphy (Fig. 4.7).

Correlation with the Newark APTS

The correlation between the Pignola-Abriola section and the Newark APTS was performed using the statistical approach proposed in Muttoni et al. (2004). Assuming that thickness is a linear proxy of time, the duration of Newark magnetozones was compared with the thickness of Pignola-Abriola magnetozones (Fig. 4.8). The Pignola-Abriola polarity reversal sequence in linear depth coordinates was placed alongside the top of the Newark APTS (at magnetozone E23r) in linear age coordinates. A linear correlation coefficient (R) relating the thickness of each of the N = 22 complete Pignola-Abriola magnetozones to the duration of the correlative Newark magnetozones was calculated, from which a t-value was derived, where $t = R*\mathrm{sqrt}([N - 2]/[1 - R^2])$, R is the linear correlation coefficient, and N is the number of matching magnetozones in the moving window, i.e. 22. The Pignola-Abriola sequence was then slid by two polarity zones along the Newark APTS (in order to maintain internal polarity consistency in correlation), R and t were recalculated, and the exercise was repeated until all 19 possibilities were explored (Fig. 4.8; statistical procedure with correlation options and analysis of t-values is reported in Appendix A.1).

For N = 22 (the number of matching reversals in moving window), each correlation has 20 degrees of freedom. A Student t-test shows that only correlation coefficients with a t-value larger than 1.725 are significant at the 95% level. According to the Student t-test, only correlation option 19 is reliable at more than 95% confidence level (Fig. 4.8), though it can be excluded on stratigraphic grounds. Precisely, option 19 places the Norian-Rhaetian boundary of the Pignola-Abriola section in the Carnian-Norian portion of the Newark sequence, as deduced from correlations of the Pizzo Mondello and Silická Brezová sections to the Newark APTS (Muttoni et al., 2004; Channell et al., 2003). For this reason, I decided to contemplate correlation options characterized by lower values of t (around 1). As a consequence, options 16 and 7 were considered as acceptable (Fig. 4.8). Option 16 is affected by the same problem as option 19 insofar as it places the Norian-Rhaetian boundary within the Norian Stage as implied by the Pizzo Mondello and Silická Brezová to Newark correlations discussed earlier. In addition, option 16 also implies sudden (and unexplained) variations in sediment accumulation rates of the Pignola-Abriola section.

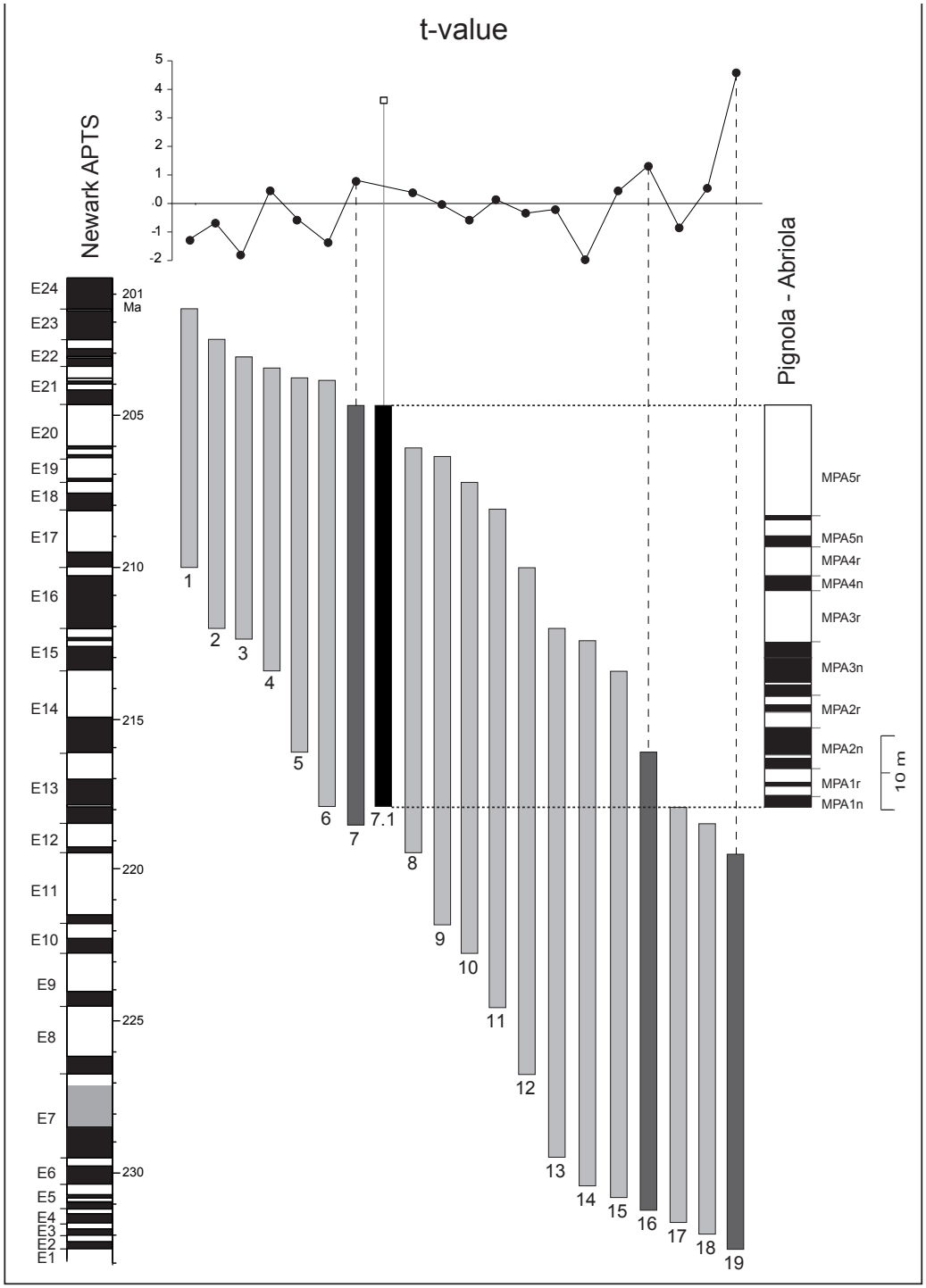

Figure 4.8: Pignola-Abriola geomagnetic reversal sequence in linear depth coordinates was slid aside the Newark astrochronological polarity time scale (APTS) in linear age coordinates maintaining the internal polarity coherency, and a t value was calculated for each of the 19 possible correlation options. Positive (negative) t-values refer to positive (negative) slopes of the linear function relating Pignola-Abriola magnetozone thickness to Newark magnetozone duration. Statistically significant options 16 and 19 were rejected for incoherence with the available stratigraphic data, whereas a modified version of correlation option 7, termed option 7.1, is considered the best solution that is in agreement with (or does not violate) the available stratigraphic data. See text for discussion.

Correlation option 7 results are more coherent with the available magneto-biostratigraphic correlations of Tethyan sections to the Newark APTS and will be investigated in detail. Option 7 links Pignola-Abriola magnetozone MPA1n with Newark E13n.1n at the base, and magnetozone MPA11r with E20r at the top (Fig. 4.8). However, this correlation implies sudden variations in sediment accumulation rates in the middle of the Pignola-Abriola section. Moreover, the lower part of Pignola-Abriola is considered Sevatian (late Norian) in age, but according to correlation 7, it should correspond to Newark magnetozones considered close to the Carnian-Norian boundary (Fig. 4.8; see also Muttoni et al., 2004).

In conclusion, no statistical correlation matches perfectly, and some "adjustments" are necessary. An alternative version of statistical correlation option 7, termed option 7.1 (black bar in Fig. 4.8), solves the problems outlined for option 7, increases statistical significance, and is coherent with the Pizzo Mondello and Pignola-Abriola magneto-biostratigraphies and correlations to the Newark APTS. Preferred option 7.1 is similar to statistical option 7 in range (MPA1n corresponding to E13n.1n, and MPA11r corresponding to E20r.2r) but differs from statistical option 7 in linking MPA1n with E13n.2n, MPA1r (0.1r, 0.1n, 0.2r) with E13r, MPA2n (0.1n, 0.1r, 0.2n) with E14n, and MPA11r with E20r, whereas magnetozones from MPA2r to MPA11n have been correlated with Newark magnetozones from E14r to E20n. Preferred correlation option 7.1 implies a correlation of the Steinbergkogel section to the Newark APTS from magnetozone E17n to E21n (Fig. 4.7) that is substantially equivalent to the correlation originally proposed by Hüsing et al. (2011). The correlation of the largely younger Brumano-Italcementi Quarry sections to the Newark APTS is the same of Muttoni et al. (2010, 2014), pending a formal redefinition of the *Misikella* specimens at Brumano (see also earlier discussion).

Using preferred correlation option 7.1, an age model for the Pignola-Abriola section can be derived. The age model shows a change in sedimentation rate from the lower to the upper part of the section (Fig. 4.7). From the base to meter 24.5, the mean sedimentation rate is of ~2.6 m/My, while from meter 24.5 to 40, the mean sedimentation rate increases to ~5.6 m/My. From meter 40 to the section top, the sedimentation rate increases further to ~9.8 m/My. This is coherent with the lithostratigraphy of the section, suggesting a general increase of terrigenous input in the upper part of the section. According to the proposed age model, the Norian-Rhaetian boundary defined by the level containing the FAD of *M. posthernsteini* sensu stricto at meter 45 should correspond to an estimated age of ca. 205.7 Ma

(Fig. 4.7), which is substantially equivalent to the age of the prominent negative $\delta^{13}C_{org}$ excursion to ~–30‰ observed at meter 44.5 (Fig. 4.7).

GSSP Proposal for the Base of the Rhaetian Stage

Based on my magneto-bio-chemostratigraphic study of the Pignola-Abriola section, coupled with the recognition of the taxonomic complexities concerning conodont *Misikella posthernsteini*, the current candidate species for the definition of the base of the Rhaetian Stage, I suggest an alternative option for the definition of the Norian-Rhaetian boundary. I favor placing the boundary at the prominent negative $\delta^{13}C_{org}$ spike observed in the Pignola-Abriola section at meter 44.5 (immediately below the level containing the FAD of *M. posthernsteini* sensu stricto and within the base of the radiolarian *Proparvicingula moniliformis* Zone). A similar $\delta^{13}C_{org}$ perturbation around the Norian-Rhaetian boundary was documented in Canada by Ward et al. (2001, 2004) and Whiteside and Ward (2011), coinciding with the disappearance of large *Monotis* (Ward et al., 2004), a typical proxy for the Norian-Rhaetian boundary (McRoberts et al., 2008). The stratigraphic level in the Pignola-Abriola section containing the ~–30‰ spike has been magnetostratigraphically correlated to Newark magnetozone E20r.2r at ca. 205.7 Ma. This age was obtained from the Newark astrochronology, calibrated with the new numerical age of 201.5 Ma from the base of the Orange Mountain Basalts in the Newark Supergroup (Blackburn et al., 2013). Assuming an age of ca. 201.3 Ma for the Triassic-Jurassic boundary (Guex et al., 2012), which is broadly consistent with previous estimates (Schoene et al., 2010), and a proposed age of ca. 205.7 Ma for the Norian-Rhaetian boundary, the Rhaetian Stage would have a duration of ~4.4 My (Fig. 4.7). Using a Carnian-Norian boundary at ca. 227 Ma (Muttoni et al., 2004), the Norian would be the longest stage of the Phanerozoic with a duration of ~21.3 My (but see Lucas et al., 2012). Using an approximated Ladinian-Carnian age of 238 Ma, derived from an uppermost Ladinian radiometric age of 237.77 ± 0.14 Ma (Mietto et al., 2012), the Carnian would have lasted almost 10 My According to these figures, the Late Triassic may have lasted ~36 My.

GSSP proposal for the Rhaetian Stage: an update (after Rigo et al., 2015)

The Pignola-Abriola section have been proposed as a GSSP (Global boundary Stratotype Section and Point) candidate for the Rhaetian Stage (Rigo et al., 2015). The other major candidate is the section of Steinbergkogel in Austria (Krystyn et al., 2007a, 2007b). The Steinbergkogel section is a basinal sequence of nodular

limestone, subdivided in three outcrops (Krystyn et al., 2007b): STK-A, ~4 meters thick; STK-B+C, ~9 meters thick; ST-4, ~23 meters thick. STK-A overlaps STK-B+C and the upper part of ST-4. The Norian/Rhaetian boundary is placed with the FAD of conodont *Misikella posthernsteini* at meter 2.2, in level 111A, of STK-A.
In the Pignola-Abriola section the FAD of *M. posthernsteini* approximates the Rhaetian base, that have been preferentially placed with the negative $\delta^{13}C_{org}$ peak of ~–30‰ at meter 44.5 (Rigo et al., 2015). Pignola-Abriola is more expanded than Steinbergkogel, covering the same time interval in ~60 meters instead of ~30. Moreover, the magnetostratigraphy is detailed as well as organic chemostratigraphy. The integrated statigraphy of Pignola-Abriola (litho-bio-chemo-magnetostratigraphy) is time constrained by the correlation with the Newark APTS, confirmed by radiometric age around the Norian/Rhaetian boundary from Peru (Wotzlaw et al., 2014). In addition to the ages of the FAD of *M. posthernsteini* and the negative $\delta^{13}C_{org}$ peak, already placed at ~205.7 Ma, Rigo et al. (2015) provided ages for other events recorded in Pignola-Abriola. The Alaunian/Sevatian boundary (FO of conodont *Mockina bidentata*) is dated at ~216.2 Ma, the Sevatian1/Sevatian2 boundary (FO of *Misikella hernsteini*) is at ~210.8 Ma. The base of the *Proparvicingula moniliformis* radiolarian Zone, considered one of the proxy of the Rhaetian (e.g. Giordano et al., 2010), is placed at ~206.2 Ma, while the FO of conodont *Misikella ultima* is dated ~204.7 Ma. Moreover, the FO of the *Misikella hernsteini/posthernsteini* transitional morphotype, associated to the older *Misikella posthersteini* specimens *sensu* Krystyn et al. (2007a) (Maron et al., 2015; Rigo et al., 2015), is dated ~207.6 Ma. The Pignola-Abriola section satisfies all the requirements to be proposed as GSSP candidate for the Rhaetian: the outcrop is well exposed and easily accessible; the section is minimal structured deformed and is continuous; is fossiliferous (conodonts and radiolarians); has a detailed magnetostratigraphy and $\delta^{13}C_{org}$ chemostratigraphy; the Norian/Rhaetian is well defined by bio-chemostratigraphy and time constrained after the magnetostratigraphic correlation with the Newark APTS and other marine sections.

Comparison with Previous Time Scales

I compared my solution with alternative proposals from the literature. Krystyn et al. (2002) used Carnian-Norian data from several Tethyan sections (Kavaalani, Kavur Tepe, Pizzo Mondello lower part, Bolücektasi Tepe, and Scheiblkogel; see references in Krystyn et al., 2002) to construct a Tethyan composite magneto-biostratigraphic sequence that was correlated to Newark magnetozones E3–E22

and used it to infer a duration of the Rhaetian of only ~2 My Later, Gallet et al. (2007) correlated data from Oyuklu, Pizzo Mondello (upper part), and the Tethyan composite sequence of Gallet et al. (2003) to the Newark APTS, suggesting that part of the Rhaetian is missing in the Newark sequence, and supporting the ~2 My duration of the Rhaetian as proposed by Krystyn et al. (2002). Muttoni et al. (2010) illustrated that middle Norian (Alaunian) magnetozones in the composite magneto-biostratigraphic sequence of Krystyn et al. (2002) may encompass Newark magnetozones ~E13–E15 rather than ~E13–E17, so that the overlying Sevatian magnetozones may correlate to Newark levels at and immediately above E15 rather than at and above E17 as proposed by Krystyn et al. (2002), thus supporting the existence of a longer (>2 My) Rhaetian.

Coming to more recent times, the long-Tuvalian option of the Geological Time Scale 2012 (Ogg, 2012), which is essentially based on data from Lucas et al. (2012), is characterized by a Carnian-Norian boundary placed at 221 Ma, a Norian-Rhaetian boundary at 205.4 Ma, and a large hiatus in the Newark Supergroup based on inferences from conchostracan biostratigraphy (Lucas et al., 2012, and references therein). According to this option, the preserved portion of the Rhaetian in the Newark Supergroup should have a duration of only ~0.2 My (Lucas et al., 2012). A duration of ~8 My for the Rhaetian, as proposed using marine-Newark magnetostratigraphic correlations by several authors (Channell et al., 2003; Muttoni et al., 2004, 2010; Hüsing et al., 2011), was rejected by Lucas et al. (2012) based on the inference that inserting 7.8 My of missing Rhaetian in the claimed Rhaetian gap of the Newark Supergroup (7.8 My = 8 My of total duration of Rhaetian – 0.2 My of preserved Rhaetian in the Newark) would produce an age for the base of the Newark Supergroup of 240.5 Ma; as Lucas et al. (2012) considered the base of the Newark Supergroup to coincide with the base of the Carnian (based on continental [palynomorphs, conchostracans, tetrapods] biostratigraphy), an age of 240.5 Ma is regarded as inappropriate because it would place the base of the Newark Supergroup close to the age of the Anisian-Ladinian boundary (Mundil et al., 2010). Therefore, a duration of ~8 My for the Rhaetian is considered unacceptable according to Lucas et al. (2012), who instead adopted a duration of ~4 My from Ogg (2004). Under the assumption of a 4 My duration for the Rhaetian and only 0.2 My of Rhaetian time preserved in the Newark Supergroup, Lucas et al. (2012) (and Ogg, 2012 in his long-Tuvalian option) estimated an age of 221.5 Ma for the Carnian-Norian boundary, based on continental biostratigraphy, by counting ~405 ky McLaughlin cycles of Newark astrochronology.

In my opinion, the Rhaetian gap of Lucas et al. (2012) at the basis of the long-Tuvalian option (Ogg, 2012) is flawed by lack of convincing correlations between terrestrial groups and marine-based stage boundaries. For example, conchostracans from the Weser Formation of the Germanic Basin are assigned an early Tuvalian age (late Carnian) because the Weser Formation is considered correlative with the Dolomie de Beaumont of France, which contains marine bivalves considered to be of such age (Lucas et al., 2012). As a further example, the conchostracan fauna from the Coburg Sandstein of the Germanic Basin is considered late Carnian, seemingly because it lies immediately below the beginning of a sporomorph association considered to be late Tuvalian. In general, I find difficult to decipher in Lucas et al. (2012) where and in which stratigraphic context a given continental association was found in direct association with stage-defining marine fossils.

The long-Rhaetian option of the Geological Time Scale 2012 (Ogg, 2012) is essentially based on magnetostratigraphic correlations between marine sections bearing stage-defining fossils and the Newark APTS assumed to be continuous in the Rhaetian (Channell et al., 2003; Muttoni et al., 2004, 2010; Hüsing et al., 2011), and it shows a Carnian-Norian boundary at ca. 228.4 Ma and a Norian-Rhaetian boundary at ca. 209.5 Ma. My new time scale for the Late Triassic could be considered an "update" of the long-Rhaetian option of (Ogg, 2012), with a Norian-Rhaetian boundary at 205.7 Ma based on data from this study and a Carnian-Norian boundary at ca. 227 Ma based on correlation of the Pizzo Mondello section with the Newark APTS (both numerical estimates obtained by rescaling the Newark APTS using an age of ca. 201.5 Ma for the base of the Orange Mountain Basalts in the Newark Supergroup; Blackburn et al., 2013). Moreover, my age of 205.7 Ma for the Norian-Rhaetian boundary is coherent with recent U/Pb ages of Wotzlaw et al. (2014) that constrain the Rhaetian base between 205.70 ± 0.15 Ma and 205.3 ± 0.14 Ma.

4.1.2 Mount Messapion section

The Mount Messapion is located near the city of Chalkida (Euboea), in the eastern part of Central Greece (Fig. 4.9). The section is situated along the street leading to the mountaintop, between two hairpin turns respectively at 38°27'52.92"N – 23°28'20.52"E and 38°27'40.2"N – 23°29'46.2"E (Fig. 4.9). The section was already sampled by Pasquale Tiano and Alberto Incoronato (University of Napoli "Federico II"), and I attempted a paleomagnetic analysis on the samples to cover the Rhaetian-Hettangian period as a continuation of the Rhaetian magnetostratigraphy

of Pignola-Abriola section.

Geological Setting

The section of the Mount Messapion is a ~710 m long carbonatic sequence covering the Norian to Hettangian interval, including the Triassic/Jurassic boundary (TJB) (see Fig. 3.9 in Chapter 3.4.1). The area investigated for magnetostratigraphy is only 23m long, covering the Rhaetian/Hettangian period. The studied interval is part of the

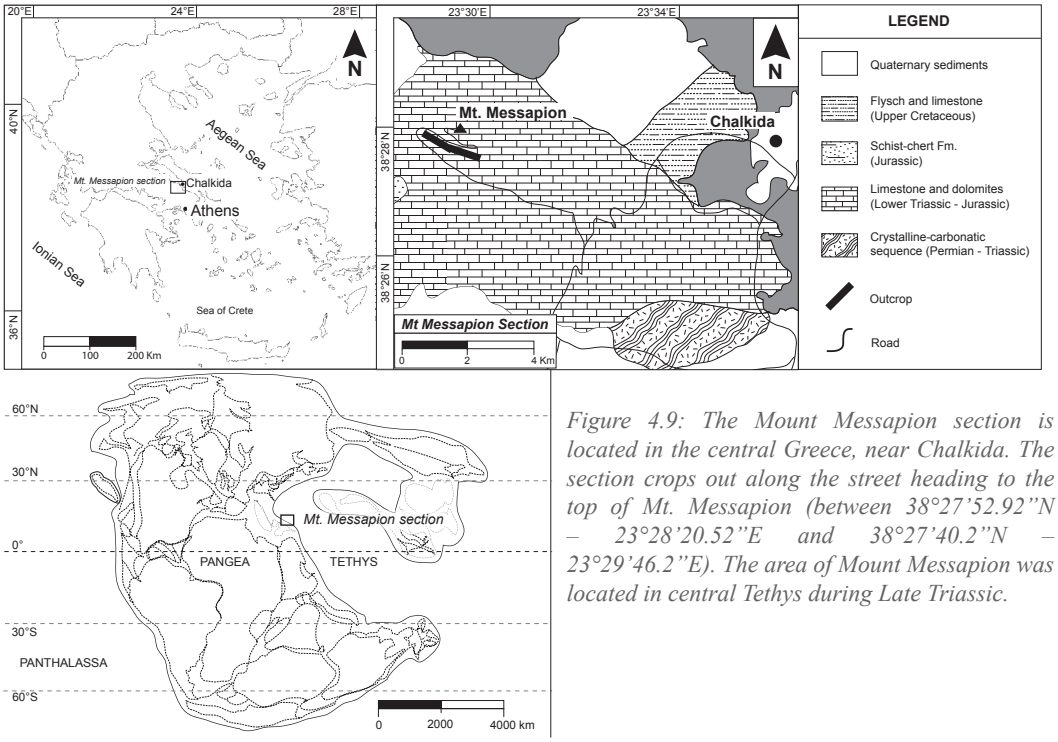

Figure 4.9: The Mount Messapion section is located in the central Greece, near Chalkida. The section crops out along the street heading to the top of Mt. Messapion (between 38°27'52.92"N – 23°28'20.52"E and 38°27'40.2"N – 23°29'46.2"E). The area of Mount Messapion was located in central Tethys during Late Triassic.

lithological unit C (Romano et al., 2008), made mainly of white limestone organized in peritidal cycles (Fig. 4.10). Below the T/J boundary, lithology is represented by supratidal microbialites alternated to subtidal bivalves rich wackestone (subunit C1). Above the T/J boundary, subunit C2 reveals the same peritidal cycles seen in subunit C1, but without Megalodontids. The upper part of C2 shows a passage to oolithic bioclastic grainstone/packstone, with abundant benthic foraminifera and green algae. The TJB is placed with the Last Occurrence of Megalodontids bivalves (Romano et al., 2008), at the limit between subunits C1 and C2 (Fig. 4.10).

Biostratigraphy

Romano et al (2008) distinguished three main associations based on the fossil content:

- Rhaetian association (Rh): is in the upper portion of C1 and is characterized

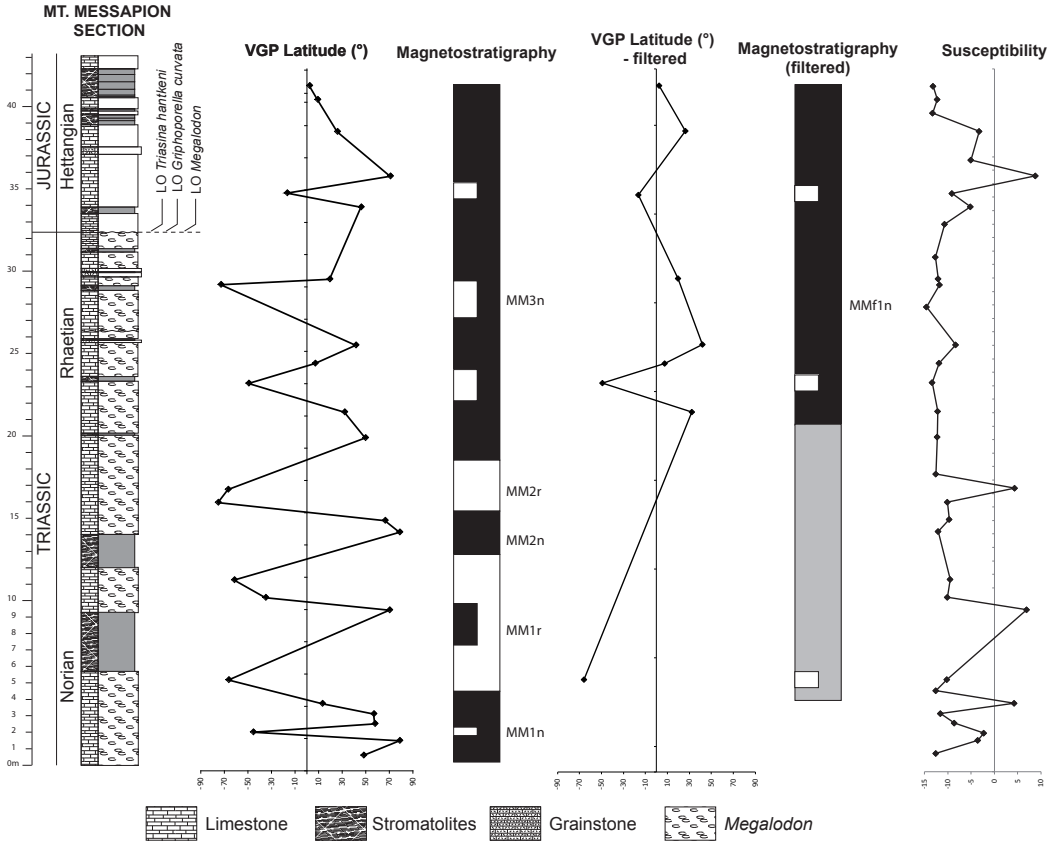

Figure 4.10: The Mount Messapion section. From left to the right: lithostratigraphy, main biostratigraphy (see text for discussion), virtual geomagnetic pole (VGP) latitudes calculated from non- filtered characteristic remanent magnetization (ChRM) component directions, and derived magnetostratigraphy. To the right, VGP latitude and magnetostratigraphy from filtered data (see text for details), and magnetic susceptibility. Triassic/ Jurassic boundary is placed with the LO of Triasina hantkeni*,* Griphoporella curvata*, and* Megalodon*.*

by the extremely abundance of Megalodontids, frequently in life position. Also microfossils are abundant, with small bivalves and gastropods, echinoid spines, foraminifers (e.g. *Triasina hantkeni*) and algae (e.g. Dasycladacea *Griphoporella curvata*).

- Lower Hettangian association (H1): is in the lower portion of C2 (130 m) and show the disappearance of Megalodontids, *T. hantkeni* and *G. curvata* (Fig. 4.10). Typical lower Hettangian association of foraminifera, cyanobacteria, bivalves and gastropods was found in these strata.
- Upper Hettangian association (H2): is in the middle-upper portion of C2 (100 m) and is characterized by the appearance of typical lower Jurassic Dasycladaceae. Other fossils are Jurassic palynomorphs, echinoids, corals (rare), and bivalves.

The age is constrained mainly by the distribution of foraminifera *Triasina hantkeni*, that appears into the *Paracochloceras suessi* ammonoid Zone (Gazdzicki, 1983), usually referred to Rhaetian (e.g. Moix et al., 2007; Rigo et al., 2015).

The vertical distribution of *T. hantkeni* is reported to reach and not overtake the end of *Choristoceras marshi* ammonoid Zone (De Castro, 1991), which upper limit is usually referred to the end-Triassic. The Last Occurrence of *T. hantkeni*, *Griphoporella curvata* and the megalodontids (Rh association) is linked to the end-Triassic extinction event (Romano et al., 2008). The fossils of H1 association are typical of Late Triassic and Early Jurassic, representing a post-extinction survival phase (Barattolo and Romano, 2005; Romano et al., 2008). The recovery of dasycladacean algae in H2 association suggests a late Hettangian age (Barattolo and Romano, 2005) for the upper C2, with a probably extension to the Sinemurian (Romano et al., 2008).

Paleomagnetism

Methods

A total of 34 samples from the Mount Messapion section have been analyzed for magnetostratigraphy at the "Alpine Laboratory of Paleomagnetism" in Peveragno (Italy). To isolate the characteristic component of the natural remanent magnetism (ChRM), the samples have been thermally demagnetized with an ASC TD48 furnace, and then measured with a 2G Enterprises DC-SQUID cryogenic magnetometer. Samples have been demagnetized by steps of 50°C from 100°C to 350°C, then 25°C until 675°C. Directions of magnetization for each step of demagnetization have been plotted on an end-point vector graph (Zijderveld, 1967), one for each sample. In case of samples with magnetization components represented by less than three end-points in sequence (equals to three subsequent demagnetization steps), these samples have been rejected. The low-field magnetic susceptibility (κ) of every sample was measured using an AGICO Kappabridge KLY-3 susceptibility meter. Considering the uniform lithology, only one sample (MES68.1) was treated for backfield IRM using an ASC IM-10-30 impulse magnetizer with a saturation field of 2.5 T.

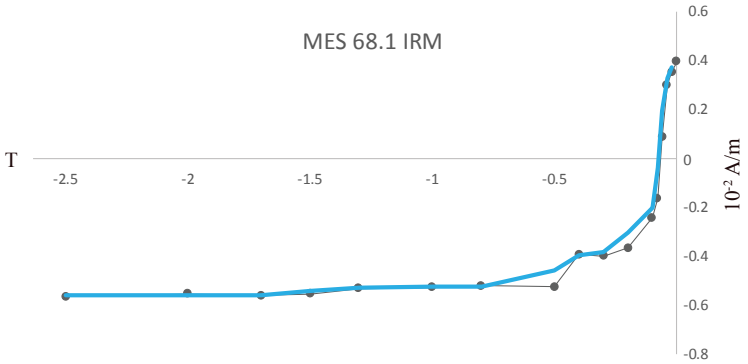

Figure 4.11: IRM back field curve of sample MES68.1. Blue line is the smoothed path of remagnetization. Coercivity is around 100 mT

Magnetic properties

Magnetic susceptibility (κ) along the Mt Messapion section is mostly negative (~ -10.2×10^{-6} SI), sometimes with peaks from 4.3×10^{-6} SI to 8.8×10^{-6} SI (Fig. 4.10). Negative susceptibility normally indicates a diamagnetic material, suggesting that any kind of magnetic mineral is present in the great part of the section. The hypothesis of an extremely low content of magnetic minerals inside the samples is more probable, with a bulk susceptibility too weak to be detected correctly by the instrument. Intensity of NRM at room temperature is weak, around 3×10^{-5} A/m, with few peaks of intensity reaching a maximum of 3×10^{-4} A/m.

IRM COMPONENT ANALYSIS **MES68.1**

	Squared residuals	S-ratio	calculated	measured
LAP	8.02E+00	$-IRM_{-0.3T}/IRM_{1T}$	0.938	
GAP	7.34E+00	$(1-IRM_{-0.3T}/IRM_{1T})/2$	0.969	
SAP	3.08E+01			

component	contribution	SIRM	log($B_{1/2}$)	$B_{1/2}$	DP
	%	A/m	mT	mT	mT
1	35.0	3.50E-03	1.90	79.4	0.20
2	50.0	5.00E-03	2.00	100.0	0.30
3	10.0	1.00E-03	1.00	10.0	0.50
4	5.0	5.00E-04	3.20	1584.9	0.10

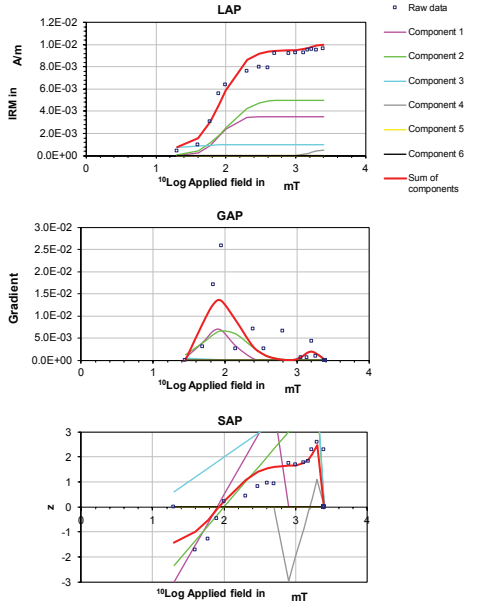

Figure 4.12: Cumulative log-Gaussian (CLG) IRM curves for sample MES68.1 (see text for details). The saturation magnetization (SIRM), the coercive force ($B_{1/2}$) and the dispersion parameter (DP) are listed for each magnetic component.

Sample MES68.1, showing negative susceptibility, has been analyzed for backfield IRM (Fig. 4.11). Total coercivity is low, around 60-100 mT, in line with most of the non-pure magnetic phases, while saturation is reached around 5×10^{-3} A/m after an applied field of 500 mT, which is quite low.

The cumulative log-gaussian (CLG) analysis (Kruiver et al., 2001) indicates four phases of magnetic minerals (Fig. 4.12), respectively with a coercivity of:

1. 100 mT at 50% of contribution
2. 80 mT at 35% o.c.
3. 10 mT at 10% o.c.
4. 1600 mT at 5% o.c.

The behavior of the acquisition path is complex near the saturation point, and is difficult to adapt the model to the data. The kind of magnetic minerals is difficult to determine, but the coercivity is not so low to justify the extremely weak NRM signal and the scattered magnetic vectors. These issues are more probably related to the scarcity of ferromagnetic minerals in the Mt. Messapion rocks.

Magnetostratigraphy

Direction obtained from NRM analysis are quite scattered, probably due to the weak magnetization acquired by the rocks. Only 27 on 34 samples revealed a characteristic component (ChRM), in a large range of temperature (ChRM data in Appendix A.2). In Zijderveld diagrams, directions are both north-down and south-up in *in situ* coordinates (Fig. 4.13), although some samples revealed north-

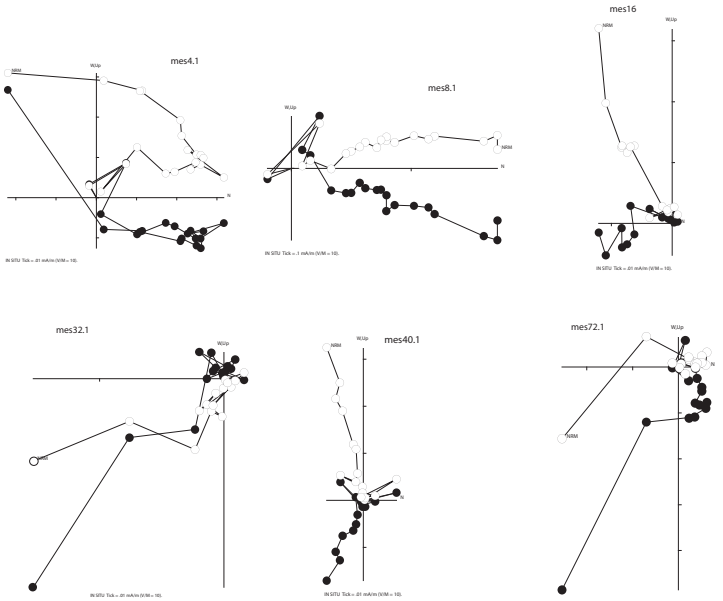

Figure 4.13: Vector end-point demagnetization diagrams for representative samples from Mount Messapion secrion. Closed circles are projections onto the horizontal plane, and open circles are projections onto the vertical plane for in situ (geographic) coordinates.

up or south-down directions not coherent with the area of deposition (northern hemisphere). In facts, filtering the component data for spurious directions, 17 of 27 data remains in *in situ* coordinates and 9 of 27 in tilt-corrected coordinates (Fig. 4.10). Equal-area projections show extremely scattered data both in *in situ* and *tilt-corrected* coordinates (Fig. 4.14). The scarcity of recovered data made difficult to obtain a reliable mean direction, which is Dec:12.2° Inc:-29.2° (k=2.8 α_{95}=20.8° N=27) in tilt-corrected coordinates. Fold test cannot be performed because the section in substantially homoclinal, but the reversals test (McFadden and McElhinny, 1990) has been applied, resulting indeterminated. Attempting to

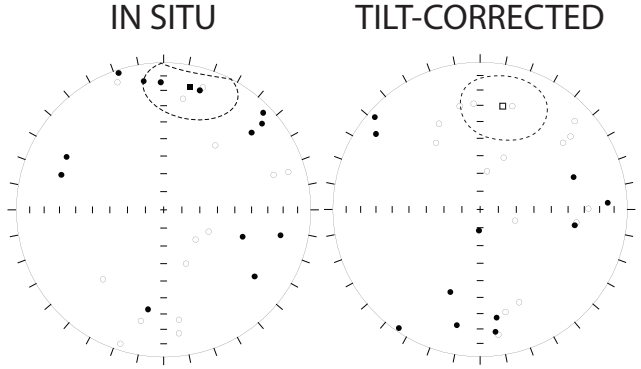

Figure 4.14: Equal-area projections for characteristic remanent magnetization (ChRM) component directions isolated at Mount Messapion for in situ (geographic) and tilt-corrected coordinates (see text for mean directions).

define the magnetostratigraphy with the few tilt-corrected ChRM data (filtered and non-filtered), Virtual Geomagnetic Poles (VGP) was calculated for each direction. From non-filtered data, five magnetozones have been identified and named MM, where one-point data have been indicated as partial inversions (Fig. 4.10). Using filtered ChRM data, only one large normal magnetozone have been identified (named MMf), with three partial reverse magnetozones and an uncertain polarity zone in the lower part of the section (Fig. 4.10).

Discussion

As seen before, paleomagnetic data from the Mt. Messapion reveal unusual directions of the characteristic component (Fig. 4.13). These directions are quite similar to the directions of the geomagnetic field lines in the southern hemisphere, with upward inclination for normal polarity and downward inclination for reverse polarity. Considering that the Greece in the Mesozoic is assumed as belonging to the northern hemisphere, these directions are not easy to explain. These samples have been sampled by P. Tiano and A. Incoronato (University of Napoli "Federico II") using a standard criteria for core orientation (as communicated before the analyses), which is clearly indicated by an arrow in every samples. The possibility of an error in orienting the samples correctly on the field has been considered, but this error should be present in all samples (collected by the same operator, with the same instruments), whereas some of them are oriented correctly. As seen, the filter applied to the ChRM directions eliminates these anomalous data, but only few components remain (9 on 27; Fig. 4.10). As obvious, these data-points are not enough to describe a pattern of polarity inversion that could be used for correlations. Without any assurance that the anomalous samples have been rotated during sampling, no changes in orientation data can be applied to obtain directions coherent with the hemisphere in which the sediments deposited. These issues affecting the Mt. Messapion paleomagnetism convinced me to renounce to continue the analyses on this section.

4.1.3 Leg 122: Site 761 (Hole C)

Site 761 of the Leg 122 is located in the Wombat Plateau (16°44'21.78"S; 115°29'12.3"E) (Fig. 4.15), subdivided in three Holes (761A, 761B and 761C). The paleomagnetic analyses provided in this work come from Hole 761C, in particular from the Rhaetian and the uppermost Norian. The core recovery for this Site is poor in the upper Rhaetian, while approaching the Norian/Rhaetian boundary the cores

are more complete (Fig. 4.16).

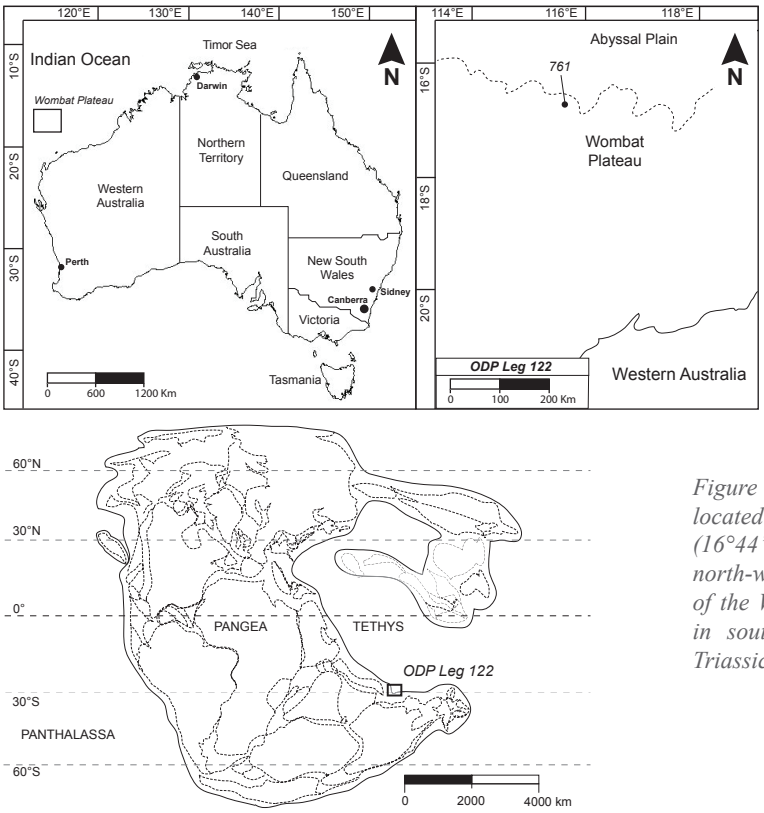

Figure 4.15: Site 761 is located in the Wombat Plateau (16°44'21.78"S; 115°29'12.3"E), north-western Australia. The area of the Wombat Basin was located in southern Tethys during Late Triassic.

Geological Setting

Lithostratigraphy

Hole 761C is represented by claystones in the Norian, passing gradually to limestones in the Rhaetian (Fig. 4.16). The top of the Triassic sediments depicts a major unconformity with the Cretaceous strata above.

The detailed lithology here presented (Leg 122 Initial Reports; Haq et al., 1990) is considered from the top to the base of the Late Triassic sediments, following the convention used by the ODP reports.

The first 78.8 m of Rhaetian are poorly recovered white limestones, with facies varying from grainstone to wackestone-packstone and mudstone, indicating littoral, subtidal or intertidal environment. Dissolution is common in cemented sediments, except for micrites that are affected instead by dolomitization and neomorphic replacement of calcite.

Below these white limestones, are present 61 m of carbonate mudstone, wackestone and packstone-grainstone, interbedded with calcareous to silty laminated claystones.

The last 23.1 m of the Rhaetian strata contains mainly calcareous and silty claystones with subordinate mudstone, wackestone-packstone and grainstone. Rare levels of

quartzose sandstones are present. The limit with the underlying Norian sediments is considered unconformable, with a hiatus of unknown duration marked by levels rich in crinoidal fragments.

The Norian is represented by 14.3 m of black and dark greenish laminated clayey siltstone, sometimes with pyrite nodules and coal levels.

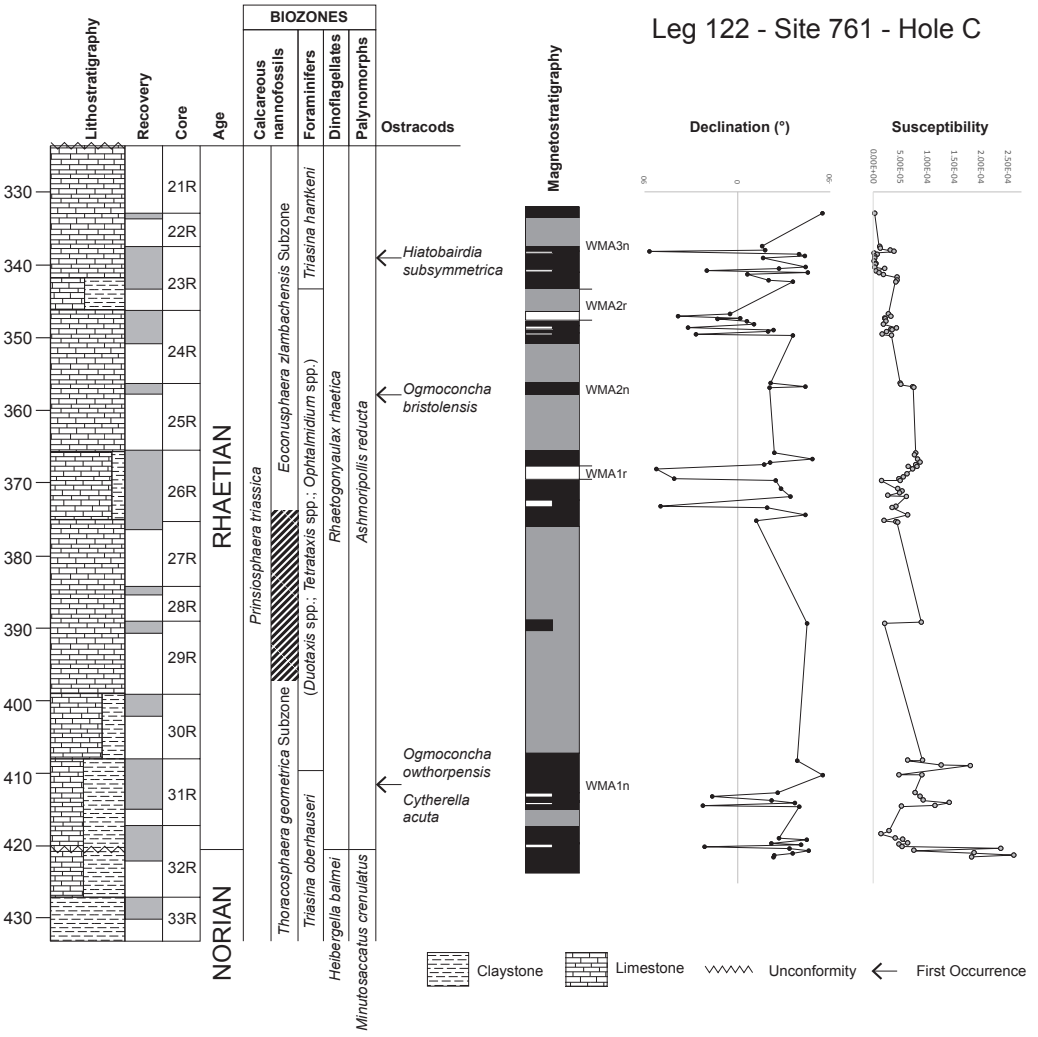

Figure 4.16: Hole 761C. From left to the right: lithostratigraphy, core recovery, main biostratigraphy (see text for discussion), magnetostratigraphy, virtual geomagnetic pole (VGP) latitudes calculated from characteristic remanent magnetization (ChRM) component directions, and magnetic susceptibility. Norian/Rhaetian boundary is placed with the beginning of Ashmoripollis reducta *palynomorph Zone and* Rhaetogonyaulax rhaetica *dinoflagellate Zone.*

Paleoenvironments

The sediments of the Norian suggest a deposition in a shallow-water coastal environment, dominated by clastic deposition. The abruptly overlain of open-marine strata of the lowermost Rhaetian suggest an intense deepening of the depositional

environment at the Norian/Rhaetian boundary, with an unconformable crinoid-rich pelagic level. The nature of this unconformity is unknown. The presence of quartz-rich sandstone, apparently from erosion of the Norian sediments, suggest that a portion of the Wombat Plateau still remain in high-relief and that the deepening in the Rhaetian is probably related to a rifting phase. The onset of carbonatic coastal facies in the upper Rhaetian suggests a restored shallow-water environment at this Site. At the top of the Rhaetian limestone an unconformity is present, passing immediately to Early Cretaceous (Berrasian-Valanginian) sediments. The cavities in uppermost Rhaetian limestone, filled with calcite cements, suggest different options to explain this unconformity. Possibilities include the uplift of the plateau until emersion and subsequent paleokarst, or dissolution after submersion and submarine cementation. The absence of Jurassic sedimentation in Site 761 could have been produced by uplift and subaerial erosion of Jurassic sediments, emersion of the plateau in the latest Triassic/earliest Jurassic followed by erosion or non-deposition, or subsidence and submarine condensation or non-deposition during the Jurassic.

Biostratigraphy

In Hole 761C, relevant fossils for biostratigraphy are calcareous nannofossils, foraminifera, palynomorphs, dinoflagellates, and ostracods (Haq et al., 1990; Brenner et al., 1992) (Fig. 4.16).

Depth is indicated in meters below sea floor (mbsf), thickness in meters.

Calcareous nannofossils

Nannoplankton of Site 761C, belonging to the *Prinsiosphaera triassica* Zone, shows a predominancy of *P. triassica* in association with *Crucirhabdus primulas*, *Thoracosphaera geometrica* and *Thoracosphaera wombatensis* (Bralower et al., 1992). These species extend from the meter 264 to the base of the recovered 761C. In the uppermost part of the sequence (from meter 375 to 264) *Eoconusphaera zlambachensis*, *Crucirhabdus minutus* and *Archaeozygodiscus koessenensis* have been found. These three species belong to the *Eoconusphaera zlambachensis* Subzone, exclusively Rhaetian in age (Bralower et al., 1992).

Foraminifera

In the lower part of the 761C (from the base to meter 410), genus *Triasina* (rare) and *Aulotortus* are present, where the occurrence of *T. oberhauseri* indicates a Norian age for these strata (Zaninetti et al., 1992). *Aulotortus* disappear in the middle part

of 761C (from meter 410 to 344) and diagnostic foraminifers (*Duotaxis birmanica*, genera *Ophthalmidium* and *Tetrataxis*) indicate a late Norian/early Rhaetian age (Zaninetti et al., 1992). In the upper part (from meter 344 to 264), genus *Aulotortus* reappears and *Triasina* species become abundant. The Rhaetian age is confirmed by the presence of *Triasina hantkeni* (Zaninetti et al., 1992).

Dinoflagellates

The presence of *Rhaetogonyaulax rhaetica* from meter 422 to 264 suggests a Rhaetian age for this portion (Brenner, 1992). Fossils typical of the *Heibergella balmei* Zone have been found from meter 422 to the base of the Hole (Brenner et al., 1992).

Palynomorphs

Most of the palynomorphs in Site 761C are poorly preserved and fragmented. For this Site the zonation is based mainly on the association with the *Rhaetogonyaulax rhaetica* dinoflagellate Zone. From ~340 to ~375 m and from ~400 to ~415 m palynomorphs typical of the *Ashmoripollis reducta* Zone (coeval to the *R. rhaetica* dinoflagellate Zone) (Brenner, 1992). The absence of *Corollina*/*Classopollis*-type palynomorphs (abundant at the top of the *A. reducta* Zone; e.g. Cirilli, 2010) suggests an early to middle Rhaetian age for this interval. From ~422 to ~430 m palynomorphs are typical of the *Minutosaccatus crenulatus* Zone (Norian) (Brenner, 1992). The absence of *R. rhaetica* dinoflagellates confirms the Norian age of this interval.

Ostracods

Samples from ~412 m contain ostracods *Ogmoconcha owthorpensis* (middle Rhaetian) and *Cytherella acuta* (upper Norian to middle Rhaetian) (Dépêche and Crasquin-Soleau, 1992). *Ogmoconcha bristolensis* (middle Rhaetian) was collected from meter ~370 and *Hiatobairdia subsymmetrica* (Rhaetian) from meter ~339 (Dépêche and Crasquin-Soleau, 1992).

Paleomagnetism

Methods

A total of 84 non-oriented ~10cc minicores and cubes from the Hole 761C have been analysed for paleomagnetism and rock magnetism. Samples have been provided by the Kochi Core Center (Kochi University, Japan) and analyzed at the “Fort

Hoofddijk" Paleomagnetic Laboratory (Utrecht University, Netherlands). Samples have been demagnetized progressively by application of an alternate gradient field (using a 2G Enterprises singe-axis AF demagnetizer) and measured using a 2G Enterprises RF-SQUID magnetometer. Samples have been demagnetized by steps of 5 mT until 50 mT, then steps of 10 mT until 100 mT. Single sample NRM directions for each step of demagnetization have been plotted on an end-point vector graph (Zijderveld, 1967), and only the magnetization components made of at least three subsequent end-points have been considered. Cores from Hole 761C are not geographically oriented, and the samples are oriented only respect of the cores. So only the magnetic inclination have been considered to determine the direction of magnetization. The low-field magnetic susceptibility (κ) was measured with an AGICO Kappabridge MFK1-A instrument on 86 samples. Rock magnetism experiments have been performed on selected samples to support the paleomagnetic interpretations. Thermomagnetic runs were performed on 3 samples (wba369001, wba3691401, wba3693801) using a modified horizontal translation Curie balance, measuring in air. Powdered samples (70-80 mg) was measured increasing temperature in several cycles, up to 580°C. Field cycles was between 100 and 300 mT, with heating-cooling rates of 10°C/min. Hysteresis cycles, IRM acquisition and backfield IRM have been performed using an alternate field gradient magnetometer (Princeton Measurement Corp. AGM 2900) on 23 samples fragments of about 50 mg (maximum field 500 mT, steps of 10 mT; exception for wba3669701 IRM: max. field 1200 mT, steps of 25 mT).

Magnetic properties

Susceptibility (κ) shows a general decrease from lowermost Rhaetian/uppermost Norian (~110×10^{-6} SI) to uppermost Rhaetian (~20×10^{-6} SI) strata (Fig. 4.16). The progressive decrease of κ could be related to the reduction of siliciclastic material in Hole 761C after the Norian/Rhaetian boundary (see "Paleoenvironments" paragraph, chapter 4.1.3, for details in environmental changing).

Thermomagnetic curves of samples wba3690001, 3691401 and 3693801 indicate a weak magnetization, where wba3693801 shows the most intense magnetization (max. ~0.063 Am^2/kg at 400°C) (Fig. 4.17). The curves show a huge increase in magnetization between 400 and 580°C (Fig. 4.17), probably due to the oxidation of a variable quantity of pyrite (FeS_2), in magnetite ($Fe^{3+}{}_2Fe^{2+}O_4$). Below 400°C there are no evidences of magnetic iron-sulfides (e.g. pyrrhotite – FeS) since the heating-cooling steps are totally reversible until this temperature and Curie temperature

for magnetic Fe-sulfides (~320°C) has not been reached (Fig. 4.17). The original magnetization is carried probably by magnetite but is impossible to differentiate the neo-formed magnetite to the original magnetite.

IRM acquisition curves show variable levels of saturation, from ~300 mT to

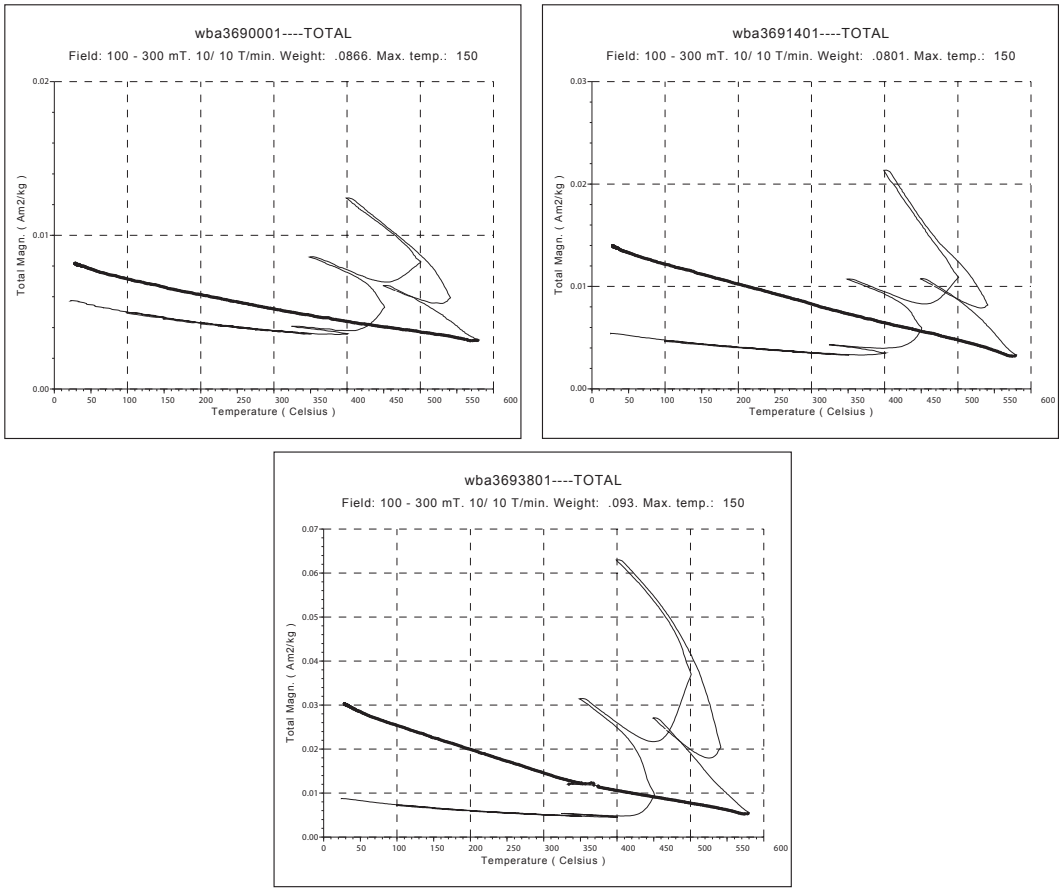

Figure 4.17: Thermomagnetic curves determined with a Curie balance of samples wba3690001, 3691401, and 3693801. The wba samples of Hole 761C reveal a mixture of different minerals, including magnetite, showing a magnetization increase above 400°C, coherent with the reaction of pyrite to magnetite.

~400 mT, coherent with the presence of magnetite; few samples saturate at field intensities higher than 500 mT (Fig. 4.18A). Samples subjected to backfield IRM are characterized by coercivity fields from 40 to 60 mT, except for two samples (wba3669701 and wba3670101) that reaches a coercivity of 200-300 mT (Fig. 4.18B). Lower coercivity fields could be associated to magnetite, while higher fields are probably related to magnetic iron-sulfides as pyrrhotite. Hysteresis cycles are pot-bellied shaped, suggesting a mixture of both single-domain (SD) and superparamagnetic (SP) magnetite (Tauxe et al., 1996) (Fig, 4.18C). Only one sample (wba3670101) has a wasp-waisted shaped hysteresis cycle, indicating a mixture SD/SP magnetite as pot-bellied, but with coarser SP grains (Tauxe et al., 1996) (Fig, 4.18C).

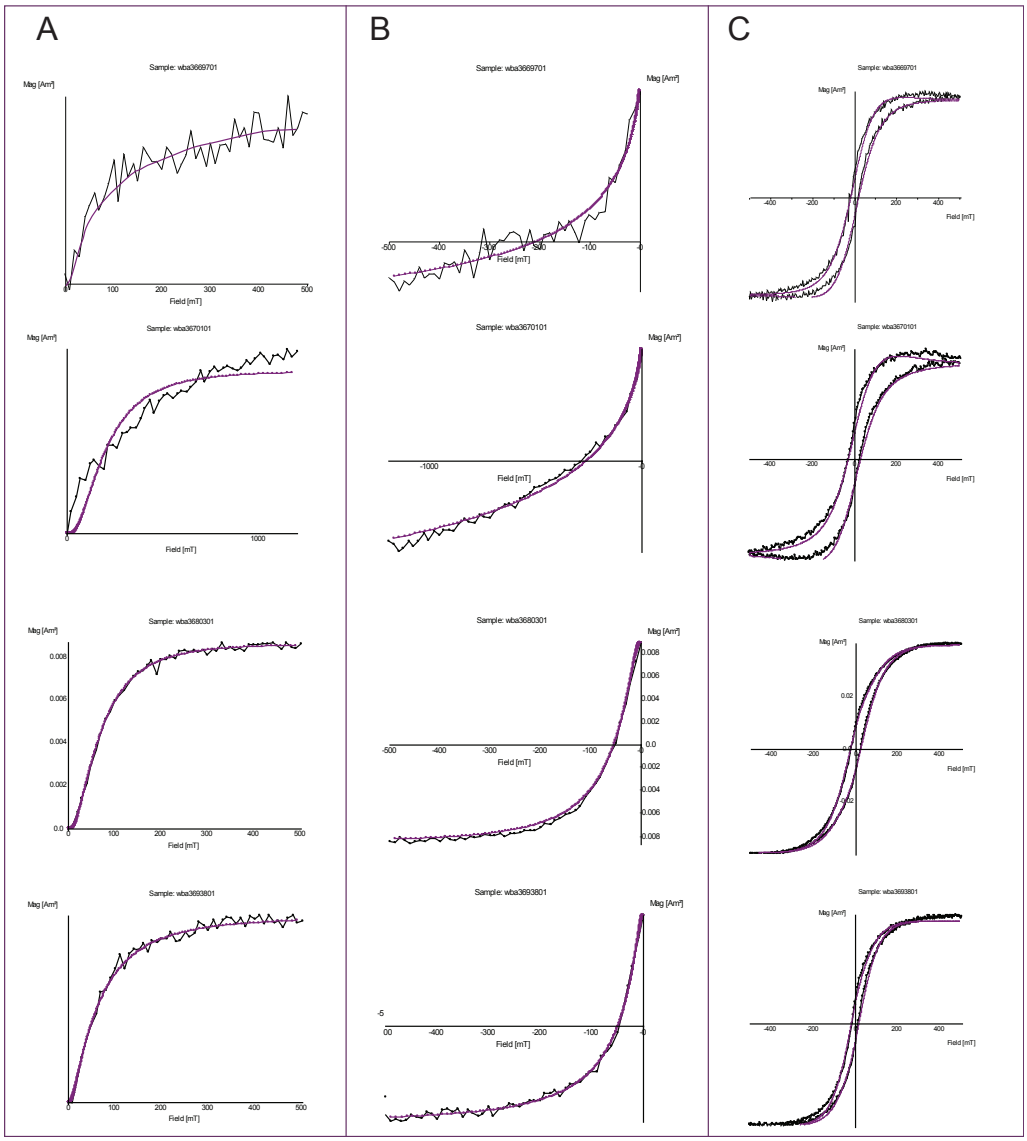

Figure 4.18: IRM acquisition curve (A), IRM backfield (B), and hysteresis cycles (C) of wba samples from Hole 761C (see discussion in text). Purple line is the data-fitting curve.

Magnetostratigraphy

Mean intensity of initial NRM is ~0.17 mA/m until meter 420.7, where the intensity increase to ~1.22 mA/m. The higher intensity is located in the Norian part of the hole, just below the Norian/Rhaetian boundary, where siliciclastic sediments are dominant and the magnetic susceptibility is elevated. Vector end-point demagnetization plots (Zijderveld, 1967) reveal a stable magnetic record, showing characteristic magnetization (ChRM) in 60 samples, in a variable range from min. 5 mT to max. 80 mT (Fig. 4.19; ChRM data in Appendix A.3). Equal area-projection for inclination-only data shows a substantial variability of inclinations, with a mean

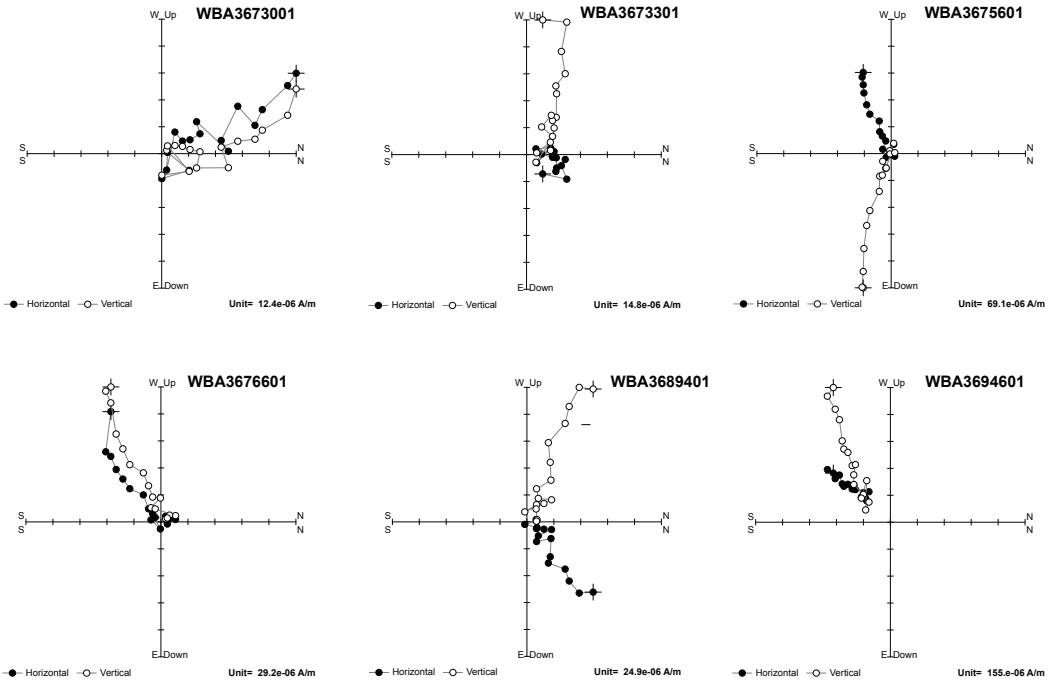

Figure 4.19: Vector end-point demagnetization diagrams for representative samples from Hole 761C. Closed circles are projections onto the horizontal plane, and open circles are projections onto the vertical plane for cores coordinates.

inclination value of 44.4°±7.2° (k=7.4, N=60; McFadden and Reid, 1982) (Fig. 4.20). The comparison with the Geomagnetic Axial Dipole inclination value at the latitude of the site (Inc_{GAD} = -31°) suggests that the paleomagnetic data of Hole 761C are not affected by contamination of VRM. The samples were not oriented geographically (only respect to the vertical axis of the cores), so the only way to determine the paleomagnetic polarity is to consider the magnetic inclination. During the Late Triassic, the Wombat Plateau was situated in the southern hemisphere, so I have to consider negative inclination as representative of normal polarity periods and positive inclination as reverse polarity periods. The stratigraphic sequence of ChRM inclinations provided 20 magnetic polarity reversals defining 5

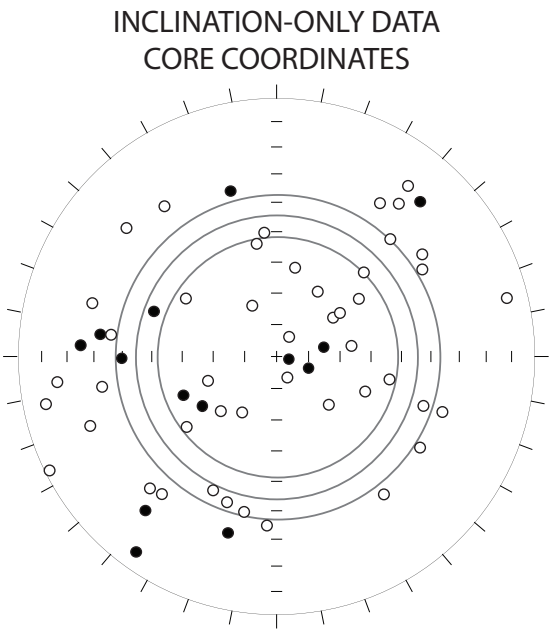

Figure 4.20: Equal-area projections for characteristic remanent magnetization (ChRM) component inclinations isolated at Hole 761C for core coordinates (see text for mean inclinations and discussion).

magnetozones named WMA1n to WMA3n (Fig. 4.16). Single data-points have been considered as partial reversals.

Discussion

The magnetostratigraphy of the Hole 761C is affected by many zones of unknown polarity, mainly due to the scarce recovery in those intervals. The biostratigraphy indicates that the strata from meter 422 to 264 are Rhaetian in age, and the strata below are upper Norian. The Norian/Rhaetian boundary is placed on an unconformity (Haq et al., 1990), suggesting a lack in uppermost Norian/lowermost Rhaetian sediments. The comparison between the discontinuous 761C magnetostratigraphy and the Norian/Rhaetian Tethyan sections of Pignola-Abriola (Maron et al., 2015; Rigo et al., 2015), Steinbergkogel STK A and STK B+C (Krystyn et al., 2007a, 2007b; Hüsing et al., 2011) and Brumano/Italcementi Quarry (Muttoni et al., 2010) seems to confirm a hiatus between Norian and Rhaetian strata at Hole 761C (Fig. 4.21). In facts, the Norian/Rhaetian boundary is placed within a long reverse magnetozone (see Chapter 4.1.1 and Maron et al., 2015), while in Hole 761C it falls within a long normal magnetozone and is indicated as an unconformable boundary (Fig. 4.16). Just above the unconformity the first Rhaetian strata show a partial reverse polarity zone, probably related to the large reversal containing the Rhaetian base. Magnetozones MPA5n of Pignola-Abriola, ST1/G+ of STKA, ST2/G+ of STK B+C and BIT1n of Brumano are considered coeval to the Norian portion of magnetozone WMA1n (below the unconformity; Fig. 4.21). The partial reverse magnetozone just above the unconformity (WMA1n.1r) could be coeval to the upper part of MPA5r (Pignola-Abriola), BIT1r (Brumano) ST1/H- of STK A and ST2/H- of STK B+C, while the remainder WMA1n is BIT2n and ST2/I+ of STK B+C (Fig. 4.21). The other magnetozones of 761C are difficult to correlate because biostratigraphy assigns a generic "Rhaetian Age" to this part of the Hole. Only the absence of palynomorphs *Classopollis*/*Corollina* constraints the Rhaetian strata of the Hole 760C to the early/middle Rhaetian. Probably, magnetozone WMA1r is coeval to BIT2r in Brumano, BIT3n could be correlated to WMA2n, BIT3r to WMA2r, and BIT4n to WMA3n (Fig. 4.21). A direct correlation with the Newark APTS is not possible because palynomorphs biostratigraphy is not comparable. An association could be made through the sections of Pignola-Abriola and Brumano/Italcementi Quarry, following correlations proposed respectively in Chapter 4.1.1 (and by Maron et al., 2015) and by Muttoni et al. (2010). Hence, the Newark magnetozone E19n should be coeval to the Norian WMA1n, while the Rhaetian

WMA1n is associated to E21n (the small WMA1n.1r should be the top of E20r) (Fig. 4.21). In this case, the estimated gap at the Norian/Rhaetian boundary in the Hole 761C is about 1.5 My. The remainder magnetozones WMA1r, 2n, 2r and 3n have been associated respectively to E21r, 22n.1n, 22n.1r and 22n.2n (Fig. 4.21). The unconformity at the top of the Rhaetian in Hole 761C obliterated the whole Jurassic and, following the correlation with the Newark APTS here proposed, at least 1.5 My of the upper Rhaetian.

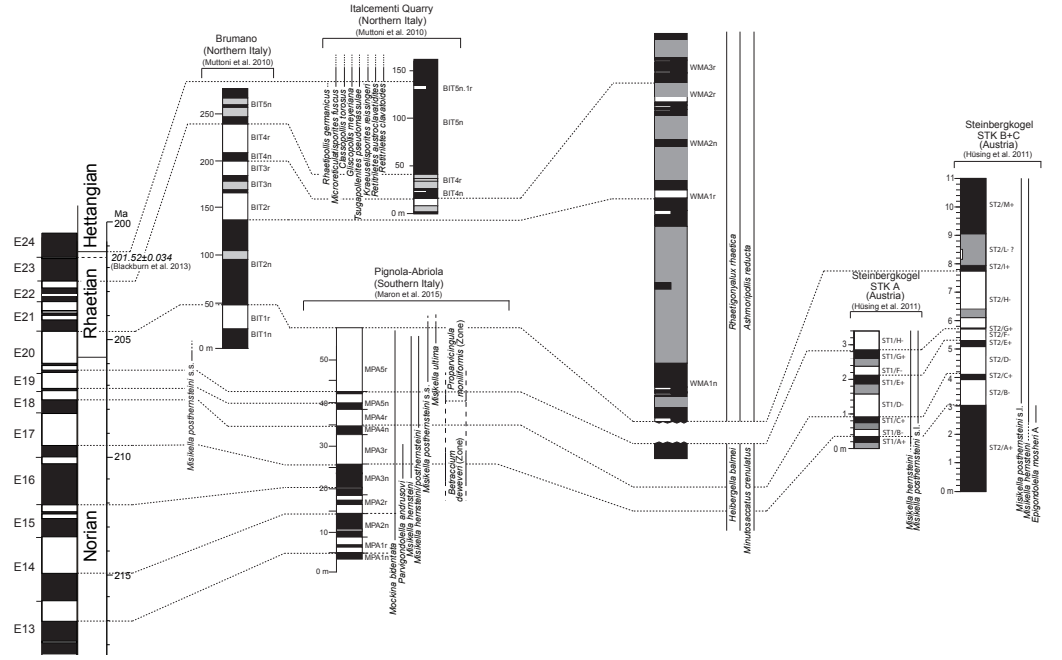

Figure 4.21: The Norian-Rhaetian magnetostratigraphy and biostratigraphy of Hole 761C correlated to data from marine sections from the literature, such as Steinbergkogel (Hüsing et al., 2011), Brumano-Italcementi Quarry (Muttoni et al., 2010, 2014), and Pignola-Abriola (Chapter 4.1.1; Maron et al., 2015; Rigo et al., 2015). The correlation with these sections seems to confirm the presence of a hiatus at the Norian/Rhaetian boundary in Hole 761C, recorded within a large reverse polarity zone in the other sections. Hole 761C is correlated to the Newark astrochronological polarity time scale (APTS) through the statistical correlation of Pignola-Abriola with the APTS (Chapter 4.1.1; Maron et al., 2015).

4.2 CARNIAN

The Carnian Stage has a detailed magnetostratigraphy around the Carnian/Norian boundary (e.g. Pizzo Mondello, Muttoni et al., 2004, and Silická Brezová, Channell et al., 2003) and at the Ladinian/Carnian boundary (e.g. Prati di Stuores/Stuores Wiesen, Broglio Loriga et al., 1999; Mietto et al., 2012), but in the remaining part the sections with magnetostratigraphy are affected by some stratigraphical issues. For example, the Bolücektasi Tepe section (Gallet et al., 1992) has a disconformity near the base and a fault that obliterate the lower Tuvalian.

The following Tethyan sections have been chosen for paleomagnetic investigation

to improve the magnetostratigraphy of the Carnian.

4.2.1 Pignola-2 and Dibona sections (*from Maron et al., submitted and in review: Newsletter on Stratigraphy; see Attached publications*)

Here I presented new magnetostratigraphic and biostratigraphic data from the Pignola-2 section of the Southern Apennines and the Dibona section of the Dolomites (both in Italy), which have been correlated to the Newark APTS in order to provide an independent control on the astrochronological ages of the older (Carnian) part of the Newark APTS (Kent and Olsen, 1999; Olsen and Kent, 1999).

Furthermore, I provide a numerical age estimation of a major event occurring in the Carnian, known as the Carnian Pluvial Event (CPE; Simms and Ruffell, 1989). The CPE is represented by a widespread deposition of siliciclastic materials recognized in most of the Carnian sections around the world (e.g., Ruffell et al., 2015). The CPE is attributed to a climatic shift to more humid conditions (Simms and Ruffell, 1989), triggered by the emplacement of the Large Igneous Province (LIP) of Wrangellia in North America (e.g., Furin et al., 2006; Rigo et al., 2007; Preto et al., 2010; Dal Corso et al., 2012; Xu et al., 2014) and consequent emission of greenhouse gasses

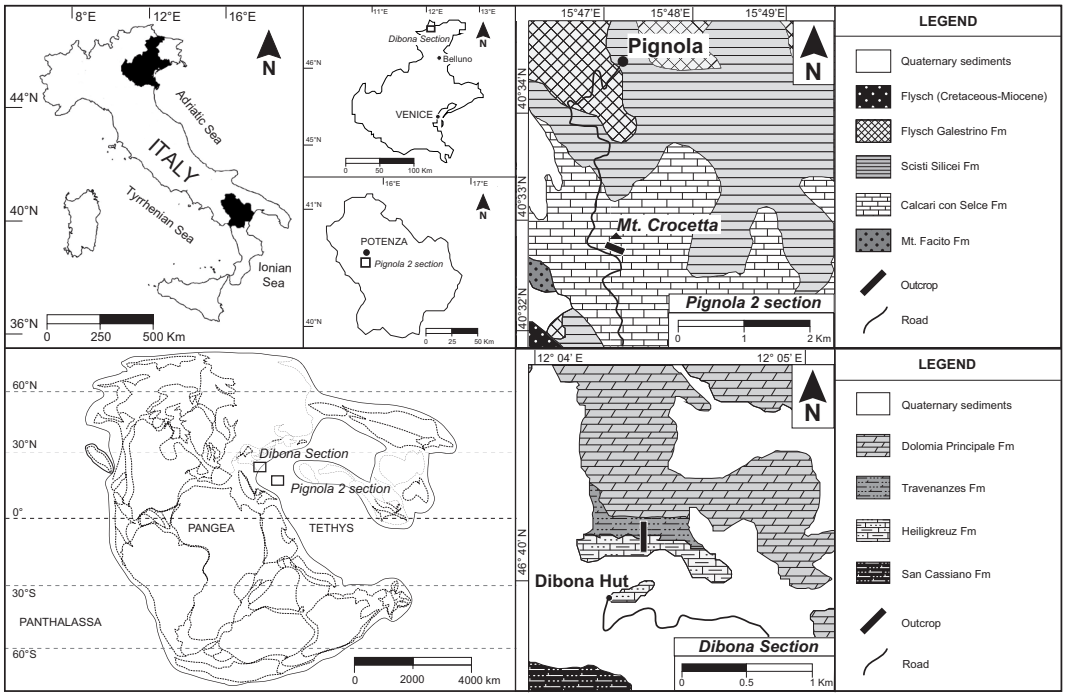

Figure 4.22: The Pignola-2 section (coord.: Lat: 40°32'51.44"N, Long: 15°47'17.43"E) is located in the Southern Apennines, near Potenza (Southern Italy). The outcrop is along the main road connecting Pignola to Abriola, on the southern side of the Mt Crocetta. The Dibona section (coord.: Lat: 46°32'2.50"N, Long: 12°04'21.68"E) is located in the Dolomites, near Cortina d'Ampezzo (Belluno, Northern Italy). The outcrop is on the southern side of the Tofane di Rozes. Pignola-2 and Dibona sections were located in central Tethys during the Late Triassic.

in the atmosphere, with temperature increase (Rigo and Joachimski, 2010; Rigo et al., 2012a; Trotter et al., 2015). The CPE is well expressed by the most siliciclastic intervals in both the Pignola-2 and Dibona sections.

Geological Setting

Pignola-2

The Pignola-2 section (Lat: 40°32'51.44"N, Long: 15°47'17.43"E) crops out in the Southern Apennines, south of the town of Potenza, along the road connecting the two Pignola and Abriola villages (Fig. 4.22). The section is comprised of a 40 m-thick succession of cherty limestones pertaining to the Calcari con Selce Formation Fm (Scandone, 1967; Miconnet, 1983; Amodeo, 1999; Rigo et al., 2012a), and encompassing the Julian/Tuvalian substage boundary (Carnian; Rigo et al., 2007, 2012). The section includes a ~5 m-thick (from meter 8 to 13) green shale and radiolaritic interval (the "green clay-radiolaritic horizon" of Rigo et al., 2007), representing the first documentation of the CPE in Tethyan basinal successions

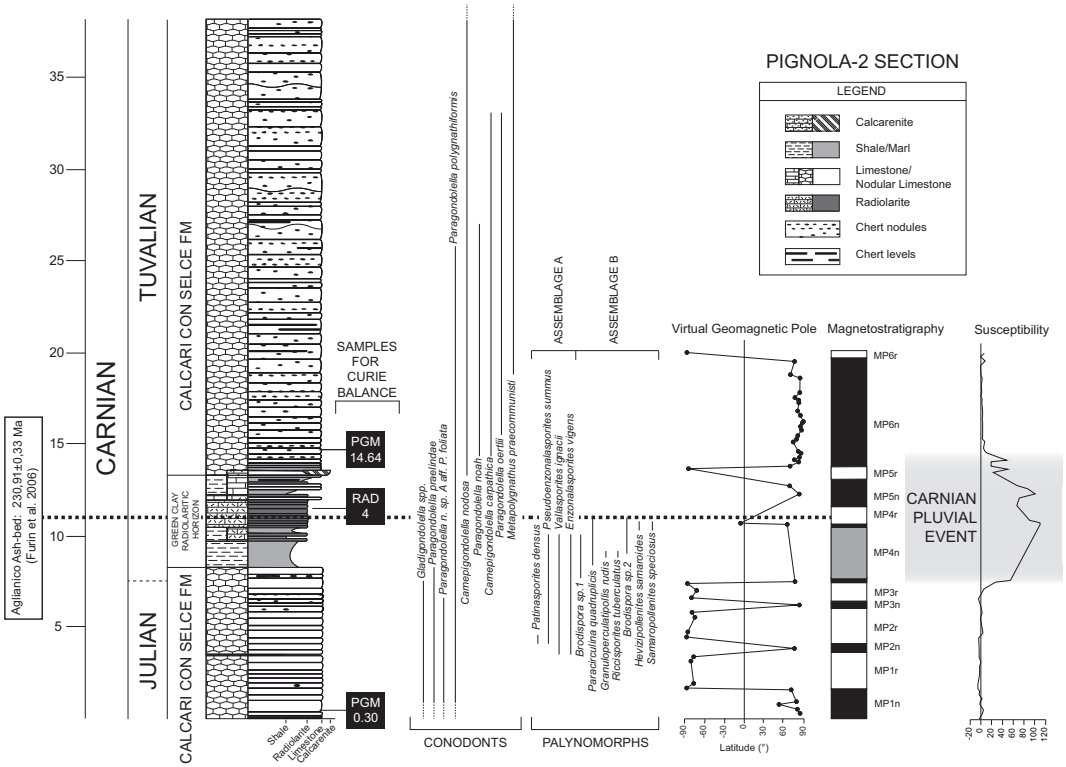

Figure 4.23: The Pignola-2 section. From left to right: lithostratigraphy, conodonts and palynomorphs biostratigraphy, Virtual Geomagnetic Pole (VGP) latitudes (from ChRM directions), magnetostratigraphy and magnetic susceptibility. In the magnetostratigraphy, black is normal polarity and white is reversed polarity. A total of 6 magnetozones have been identified, with a 5 meters interval of unknown polarity (grey shading) corresponding to the shales of the green clay-radiolaritic horizon (that could not be sampled). The U/Pb radiometric age of 230.91±0.33 Ma (Furin et al. 2006) comes from an ash-bed inside the green clay-radiolaritic horizon. Anomaly in the magnetic susceptibility around the "green horizon" represents the Carnian Pluvial Event in basinal environment (light-grey shaded interval).

(Rigo et al., 2007, 2012a). In the upper part of the "green clay-radiolaritic horizon" (hereafter "green horizon"), a tuff level, named "Aglianico ash-bed" (meter 12) provided a U/Pb radiometric age of 230.91±0.33 Ma (Furin et al., 2006) (Fig. 4.23). The "green horizon" has been interpreted as resulting from a transient rise of pCO_2 levels that triggered the shoaling of the calcite compensation depth (CCD). This inferred CCD shoaling is possibly coupled with increased detrital and nutrient input in the basin as a consequence of the CPE, a warm and humid period that fostered silicate weathering and runoff on land (Rigo et al., 2007, 2012b; Rigo and Joachimski, 2010; Trotter et al., 2015). A distinct rise of pCO_2 in the coupled ocean-atmosphere system may have been provided by the emplacement of the Wrangellia LIP (e.g., Furin et al., 2006; Rigo et al., 2007; Preto et al., 2010; Dal Corso et al., 2012; Xu et al., 2014), radiometrically dated with Ar/Ar between ~233 and ~222 Ma, with the most likely age comprised between ~230 and ~225 Ma (Greene et al., 2010). The oldest radiometric ($^{207}Pb/^{206}Pb$) age available for Wrangellia comes from gabbros in Yukon, associated to the Wrangellian effusions and dated at 232.2 ±1 Ma (Mortensen and Hulbert, 1992; see also Greene et al., 2010). This age interval includes the age of the CPE at Pignola-2 from the "Aglianico ash-bed" (Furin et al., 2006).

Dibona

The Dibona section (Lat: 46°32'2.50"N, Long: 12°04'21.68"E) is a ~370 m thick shallow-water sedimentary succession located in the Dolomites (Southern Alps), on the southern side of the Tofana di Rozes Mountain, near the Dibona Hut (Fig. 4.22). The section is characterized by mixed carbonate-siliciclastic deposits of shallow-marine (Heiligkreuz/Santa Croce Formation) to marginal-marine (Travenanzes Formation) environments (e.g. Breda et al., 2009). The ~160 m Heiligkreuz Fm. (De Zanche et al., 1993; Preto and Hinnov, 2003; Neri et al., 2007; Gattolin et al., 2013, 2015) is subdivided into three members, which from the base to the top are subsequently the Borca Mb., ~100 m-thick, consisting of limestones and arenites passing to dolostones; the Dibona Sandstones Mb., ~60 m-thick, consisting of arenites, conglomerates, pelites and limestones; the Lagazuoi Mb., ~30 m-thick, consisting mainly of strongly dolomitized oolitic limestones (Fig. 4.24). The shales and arenites of the Borca and Dibona Sandstones Mbs record the CPE in a coastal environment (Breda et al., 2009; Preto et al., 2010). A major negative $\delta^{13}C$ spike linked to the eruption of Wrangellia flood basalts has been observed at the base of the Heiligkreuz Fm., close to Dibona section, confirming the connection of

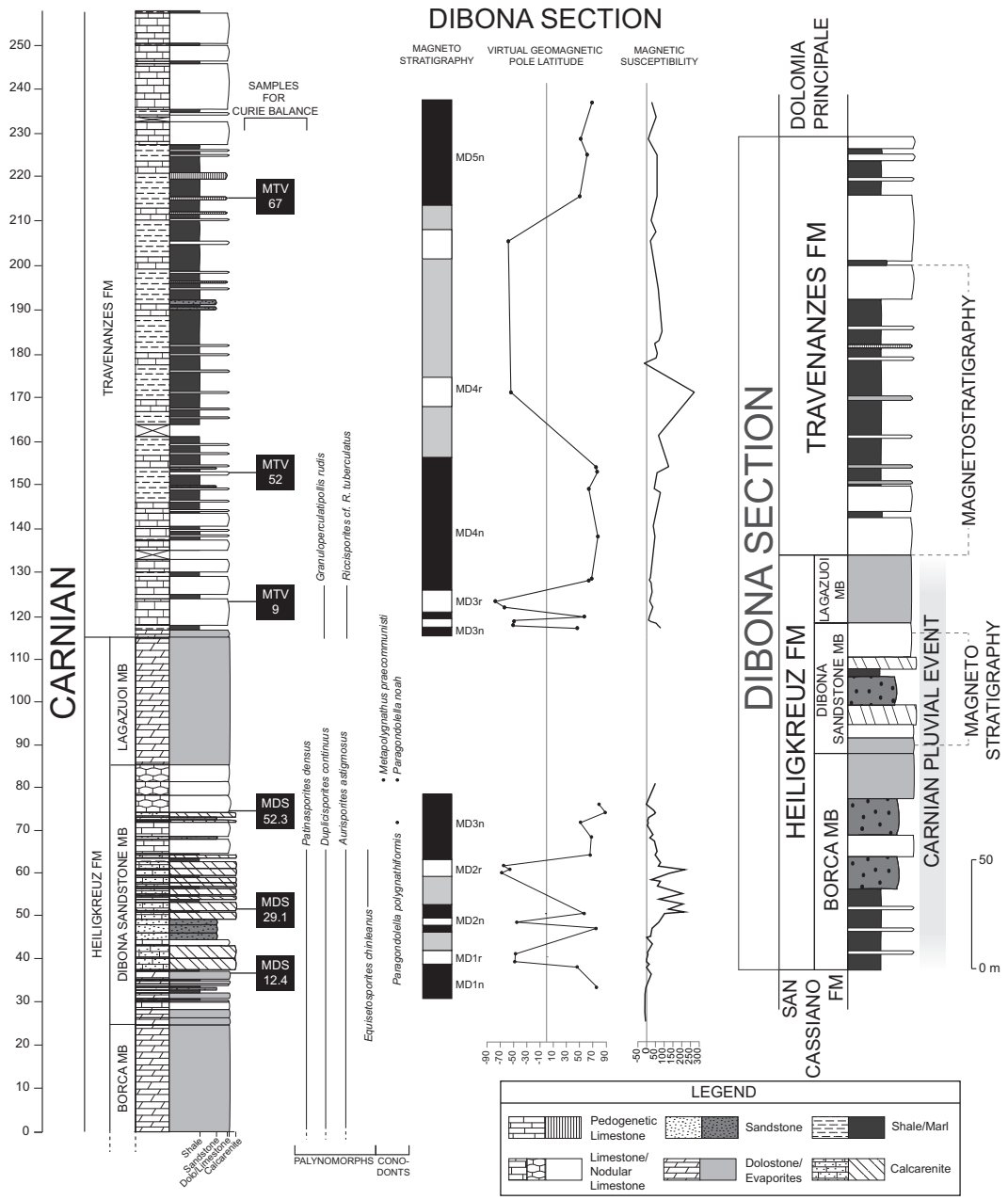

Figure 4.24: The Dibona section. From left to right: lithostratigraphy of the investigated portion, palynomorph and conodont biostratigraphy, magnetostratigraphy, Virtual Geomagnetic Pole (VGP) latitudes (from ChRM directions), magnetic susceptibility and lithostratigraphy of the whole Dibona section. In the magnetostratigraphy, black is normal polarity and white is reversed polarity. In the lower panel is the Dibona Sandstone Mb (Heiligkreuz Fm) site and in the upper panel is the Travenanzes Fm site. A total of 8 magnetozones have been identified, 5 from the Dibona Sandstones and 3 from the Travenanzes Fm. The large portion of unknown polarity (grey shading) in the Travenanzes portion is due to sparse seemingly robust paleomagnetic data (only three menaingful VGP points). Extension of the Carnian Pluvial Event is illustrated with the grey shaded area in the whole Dibona section lithostratigtaphy (on the right).

the clastic input to the CPE climatic event (Dal Corso et al., 2012). Above the Lagazuoi Mb., the ~180 m Travenanzes Fm. (De Zanche et al., 1993; Neri et al., 2007; Breda and Preto, 2011) starts with ~25 m of dark clays and aphanitic

dolostones passing upwards to multicolored clays with carbonatic and evaporitic intercalations deposited in sabkha-like environments. The top of the Travenanzes Fm. is dominated by dolomitic peritidal cycles of carbonate tidal-flat and shallow lagoon environments, with thin dark clay intercalations. It represents the transition to the overlying Dolomia Principale carbonate platform (Breda and Preto, 2011).

Biostratigraphy

Pignola-2

The Pignola-2 section has a detailed conodont and palynomorph biostratigraphy (Rigo et al., 2007, 2012). According to the conodont biostratigraphy, the Julian/Tuvalian (middle/late Carnian) boundary is placed at the base of the "green horizon". In fact, below the "green horizon" a typical Julian conodont association composed of *Paragondolella praelindae*, *P. polygnathiformis*, and *Gladigondolella* spp is present. Above the "green horizon", the section bears Tuvalian conodont species, i.e. *Carnepigondolella nodosa*, *C. carpathica*, *Paragondolella noah*, *P. oertlii*, and *Metapolygnathus praecommunisti* (Fig. 4.23) (Rigo et al. 2012a). Specifically, the Julian/Tuvalian boundary is placed at the level with the last occurrence (LO) of the *Gladigondolella* genus (Rigo et al., 2007). Palynomorphs from Pignola-2 have been grouped in two main assemblages (Rigo et al., 2007): Assemblage A is typical of the Julian/Tuvalian interval, while Assemblage B covers a narrower range in the upper Tuvalian (see Rigo et al. 2007 for additional details) (Fig. 4.23).

Dibona

The Dibona section has a detailed pollen and spore biostratigraphy (Roghi 2004, Roghi et al., 2010). The typical uppermost Julian-lower Tuvalian association with *Patinasporites densus*, *Aulisporites astigmosus* and *Duplicisporites continuus* (Borca Mb, Dibona Sandstones Mb) and *Equisetosporites chinleanus* (Dibona Sandstones Mb) is found in the Heilgkreuz Fm. It is followed by a Tuvalian association of *Granuloperculatipollis rudis* and *Riccisporites* cf. *R. tuberculatus*, found at the base

Plate 4.2: (following page) Conodonts from samples DIN2 and DIN6. The fauna illustrated in the plate includes Paragondolella polygnathiformis*,* Paragondolella noah*, transitional forms from* P. noah *to* Metapolygnathus praecommunisti*, and* M. praecommunisti*. The specimens of* M. praecommunisti *are basal, showing the accessorial node behind the cusp, the posterior prolongation of the keel and a quite centrally located pit, but no nodes on the anterior platform margins. The occurrence of basal representatives of this species in sample DIN6, together with advanced* P. noah*, suggests a lower Tuvalian age (Mazza et al. 2011; Mazza et al. 2012a). 1:* Paragondolella polygnathiformis *(Budurov and Stefanov 1965) (DIN2); 1c: the blade of the specimen got broken; 2:* Paragondolella noah *(Hayashi 1968) transitional to* Metapolygnathus praecommunisti *Mazza, Rigo and Nicora 2011 (DIN6); 3:* Metapolygnathus *cf.* praecommunisti *(DIN6) Figs b-c: the blade termination got broken; 4:* Metapolygnathus *cf.* praecommunisti *(DIN6); 5-7:* Metapolygnathus praecommunisti *(DIN6). a: view from above; b: lateral view; c: view from below. All the conodonts are at the same scale.*

PLATE 4.2

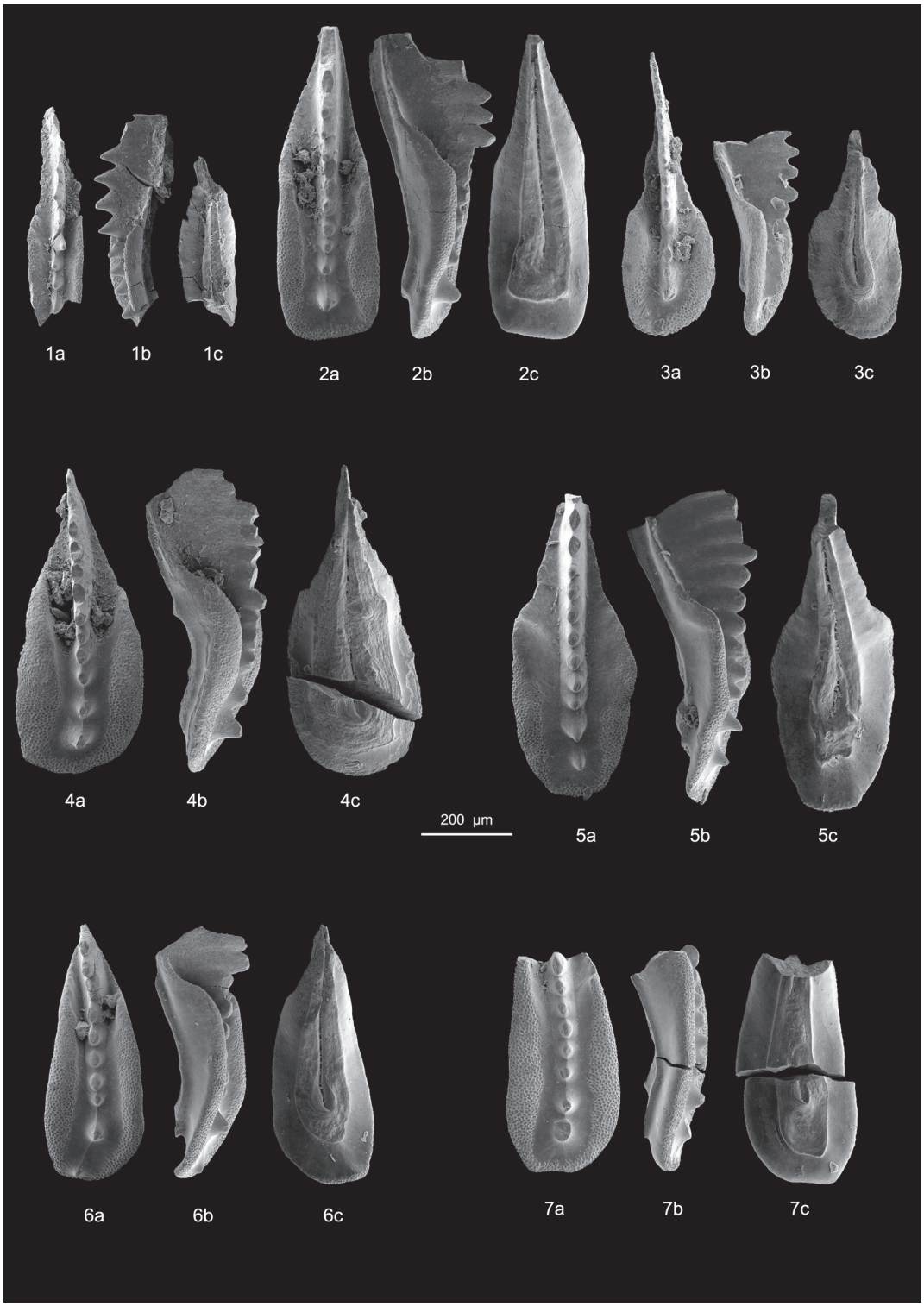

of the overlying Travenanzes Fm (Fig. 4.24). The former association, belonging to the *Granuloperculatipollis rudis* Assemblage of Roghi et al. (2006, 2010), is similar to Assemblage B found in the Pignola-2 section. Moreover, additional

sections coeval to the Dibona section reveal pollens and spores comparable with the biostratigraphic record of Pignola-2, e.g. the Cave del Predil section in the Southern Alps of Friuli (Roghi, 2004), and the Lunz (Köppen, 1997) and Rubland (Kraus, 1969) sections in the Northern Calcareous Alps of Austria. Six samples for conodont analysis have been collected from the Dibona section immediately below the base of the Lagazuoi Mb, in the last 10 meters of the Dibona Sandstones Mb. The conodont association consists of *Paragondolella polygnathiformis*, *Paragondolella noah*, transitional forms from *P. noah* to *Metapolygnathus praecommunisti*, and early representatives of *M. praecommunisti* (Fig. 4.24, Plate 4.2) attributed to the early Tuvalian age (Mazza et al. 2010, Mazza et al. 2011). Furthermore, the ammonoid *Shastites* cf. *pilari* has been found below the Lagazuoi Mb, in the nodular limestone corresponding to the upper portion of the Dibona Sandstone Mb of the Heiligkreuz Fm. (Gianolla et al., 1998b; De Zanche et al., 2000; Gattolin et al., 2015).

Paleomagnetism

Sampling and laboratory methods

A total of 63 oriented paleomagnetic core samples (~10cc) have been collected from the Pignola-2 section, 55 from limestones beds and 8 from the radiolaritic intervals within the "green horizon", with a stratigraphic interval of approximately 0.5 m (Fig. 4.23). The clayey intervals of the "green horizon" have not been sampled because they are both too thin and chipped. From the Dibona section a total of 45 cores have been collected from the upper Borca Mb. to the base of the Lagazuoi Mb. (Heiligkreuz Fm.), and 36 samples from the Travenanzes Fm. To isolate the ChRM, all samples have been thermally demagnetized (with an ASC TD48 furnace, residual field < 10 nT) and measured with a 2G Enterprises DC-SQUID magnetometer (magnetic moment noise level <10-12 Am^2) at the Alpine Laboratory of Paleomagnetism – ALP (Peveragno, Italy). Samples have been demagnetized by steps of 50°C from 100°C to 350°C, then 25°C until 675°C. Single sample directions of the magnetization vectors have been plotted on an end-point vector graph (Zijderveld 1967) for each step of demagnetization (Fig. 4.25). Samples showing magnetization components made of less than three end-points in sequence (representing three subsequent temperature steps) have been rejected.

The low-field magnetic susceptibility (κ) was measured with a AGICO Kappabridge KLY-3 instrument (sensitivity: 2×10^{-8} SI; at the ALP, Peveragno) for all samples. Further, to support the paleomagnetic interpretation, thermomagnetic runs were performed on a modified horizontal translation Curie balance (paleomagnetic

laboratory 'Fort Hoofddijk', Utrecht University, The Netherlands; noise level $5x10^{-9}$ Am^2, typical signals at least an order of magnitude higher; Mullender et al., 1993) for a subset of the samples. About 70-80 mg of powdered sample was measured in several cycles to increasingly higher temperature up to 670°C; the field was cycled between 100 and 300 mT, heating and cooling rates were 10°C/minute. Measurements were performed in air. Three samples from the Pignola-2 section were investigated and 6 from the Dibona section (3 from the Heiligkreuz Fm. and 3 from the Travenanzes Fm.).

Samples PGM0.30, RAD4 and PGM14.64 from the Pignola-2 section and samples MDS12.4, MDS29.1 and MDS52.3 from the Dibona section have been analyzed using the Curie balance.

Magnetic properties

Pignola-2

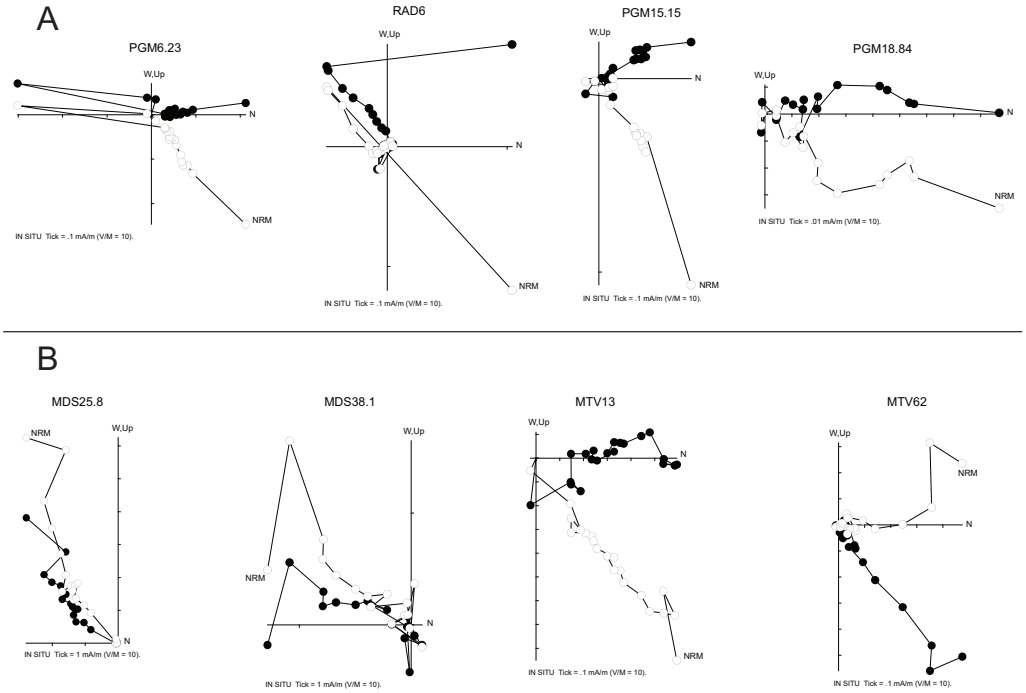

Figure 4.25: Vector end-point demagnetization diagrams (Zijderveld 1967) of the Pignola-2 section (panel A) and the Dibona section (panel B). Open circles are projections onto the vertical plane, and closed circle are projections onto the horizontal plane for in situ (geographic) coordinates.

The limestones of the Pignola-2 section reveal a very low κ, usually smaller than 5×10^{-6} SI (Fig. 4.23). In the "green horizon" the initial magnetic susceptibility is considerably higher (from ~70×10^{-6} to ~110×10^{-6} SI) than in the rest of the sampled interval, due to an increase of the terrigenous fraction (Fig. 4.23). Interestingly, magnetic susceptibility is high (from 25×10^{-6} to 55×10^{-6} SI) also in the carbonatic

strata delimiting the "green horizon" (~1 or 2 meters above and below), indicating a significant siliciclastic component we associate to the CPE.

The Curie balance results are shown in Fig. 4.26 and the stratigraphic position of the sample is in Fig. 4.23. The limestones of the Pignola-2 section (PGM0.30 and 14.64; Fig. 4.26A, 4.26C) are very weak, only slightly above instrumental noise level. Nonetheless there seems to be a marginally convex magnetization vs. temperature behavior between ~100-200 and ~450-500°C, that is reversible on intermittent cooling. The final cooling segment from 600°C back to room temperature, however, does not reveal that behavior. It is difficult to interpret this behavior that may be associated with titanomagnetite (*sensu lato*) with a varying Ti-content. However, a minute amount of magnetic sulfides cannot be excluded with certainty. The "green horizon" sample RAD4 (Fig. 4.26B) is much stronger (but still weak, it remains a sediment) and shows a Curie point (determined by the two-tangent method, Grommé et al. 1969) of ~350°C that is reversible on cooling after the final heating temperature of 600°C.

Dibona

The Dibona Sandstones Mb show a generally high susceptibility (κ), around ~43×10^{-6} SI, whereas in the more terrigenous part (meter ~50 to ~60) κ increases up to ~200×10^{-6} SI (Fig. 4.24). The Travenanzes Fm show higher κ values, around 50×10^{-6} SI, with a peak of ~270×10^{-6} SI around meter 170 (Fig. 4.24). The Dibona sandstones Mb samples (MDS12.4, Fig. 4.26D; MDS29.1, Fig. 4.26E; MDS52.3, Fig. 4.26F; stratigraphic position in Fig. 4.24) from the Dibona section all show a variable portion of non-magnetic pyrite (FeS_2) that is oxidized during the thermomagnetic analysis, first to magnetite and finally to hematite, explaining the occasionally huge increase in magnetization between 400 and 600°C. There are no indications for magnetic sulfides below 400°C since the analysis shows reversible heating and cooling segments in that temperature range and no Curie temperature of ~320°C. Plausibly traces of magnetite represent the original magnetic mineralogy but it is impossible to discriminate between left overs of neo-formed magnetite (most of it oxidizes further to hematite) and original magnetite. The three samples from the Travenanzes Fm (MTV9, Fig. 4.26G; MTV52, Fig. 4.26H; MTV67, Fig. 4.26I; stratigraphic position in Fig. 4.24) are all very weak, demonstrating paramagnetic behavior only. During the heating above 600°C a minute amount of magnetic minerals (presumably fine-grained magnetite) is formed because the final

cooling curves lie slightly above the corresponding heating curves.

Magnetostratigraphy

Pignola-2

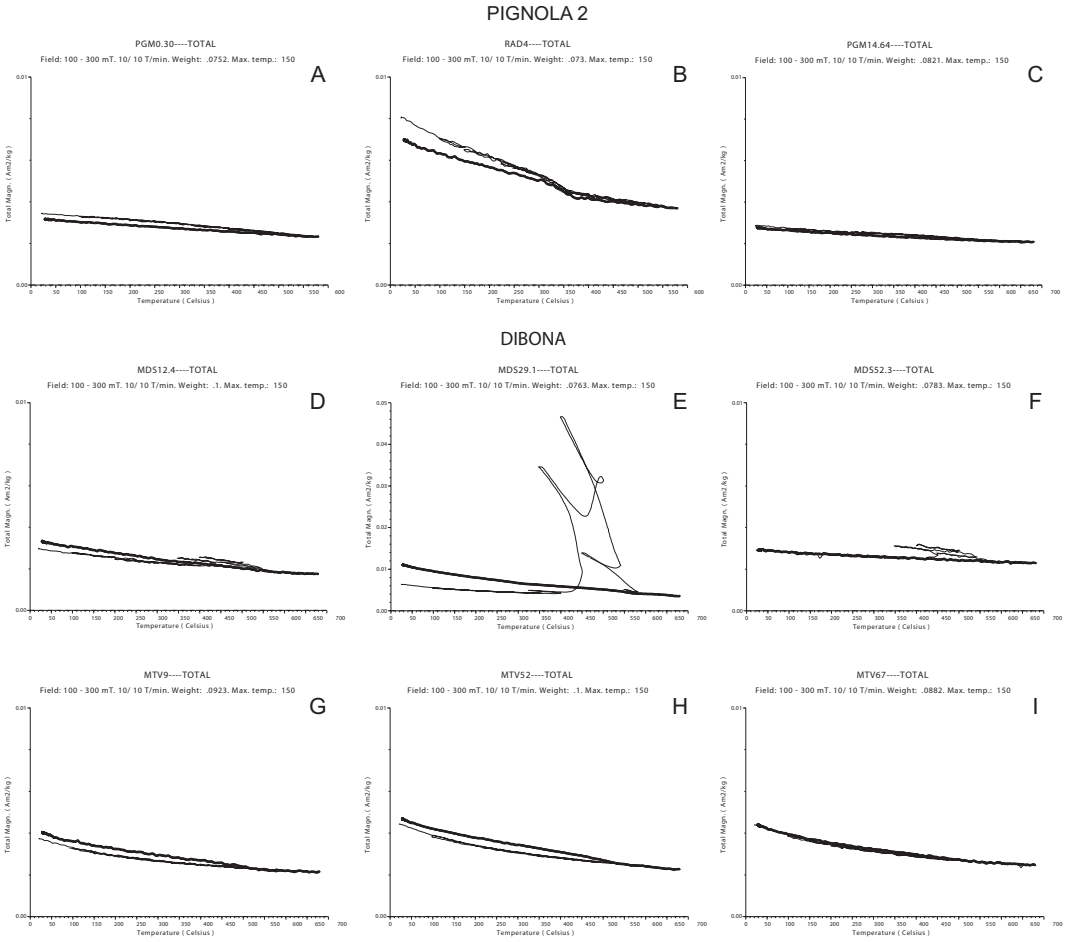

Figure 4.26: Thermomagnetic curves determined with a Curie balance of samples PGM (Pignola-2, Calcari con Selce Fm; panels A, C), RAD (Pignola-2, Green clay-radiolaritic horizon; panel B), MDS (Dibona, Heiligkreuz Fm; panels D, E, F), and MTV (Dibona, Travenanzes Fm; panels G, H, I). The PGM samples of Pignola-2 reveal a mixture of different minerals, including magnetite, in the cherty limestones, whereas in the green horizon (RAD sample) there is an increase in more Ti-rich magnetite. Samples MDS from the Heiligkreuz Fm in the Dibona section show a magnetization increase above 400-450°C, coherent with the reaction of pyrite to magnetite.

The mean intensity of the starting NRM is ~0.02 mA/m in the pelagic carbonates, ~0.06 mA/m in the radiolarites of the "green horizon", and ~0.2 mA/m in the carbonatic levels just above the "green horizon". Vector end-point demagnetization diagrams (Fig. 4.25A; Zijderveld, 1967) reveal the presence of spurious (viscous) magnetic components from room temperature to 250-300°C; at higher temperatures the characteristic component remanent magnetization (ChRM) direction is isolated (Fig. 4.25A). The demagnetization trajectory trends toward the origin up to a maximum temperature of 675°C. This behavior is observed in 47 samples (ChRM

data in Appendix A.4). Equal area stereographic projections reveal that the ChRM is bipolar being oriented north-and-down or south-and-up in *in situ* coordinates, and northwest-and-down or southeast-and-up after correction for bedding tilt (Fig. 4.27). The mean direction in tilt-corrected coordinates, calculated with standard Fisher statistics, is of Dec: 28.4°E; Inc: 39.6° (k=23.9; α_{95}=4.3°; N = 47; Table 4.2). No fold test could be performed because the bedding attitude trough the section is essentially the same. The reversals test (McFadden and McElhinny, 1990) is positive, suggesting that the ChRM is the original magnetization acquired during or shortly after deposition. The mean directions in *in situ* coordinates (Dec: 353.5°E; Inc: 59.7°; k: 24.1; α_{95}: 4.3°; Table 4.2) are similar to the inclination of the geomagnetic axial dipole (GAD Inc: ~59.8°), so we cannot exclude some contamination of the ChRM by VRM for normal polarity components. The latitudes of the Virtual Geomagnetic Poles, derived from the ChRM directions, provided a sequence of 12 magnetic polarity reversals defining 12 magnetozones labeled from MP1n to MP6r (Fig. 4.23). The shales of the "green horizon" were not sampled for magnetostratigraphy (see above).

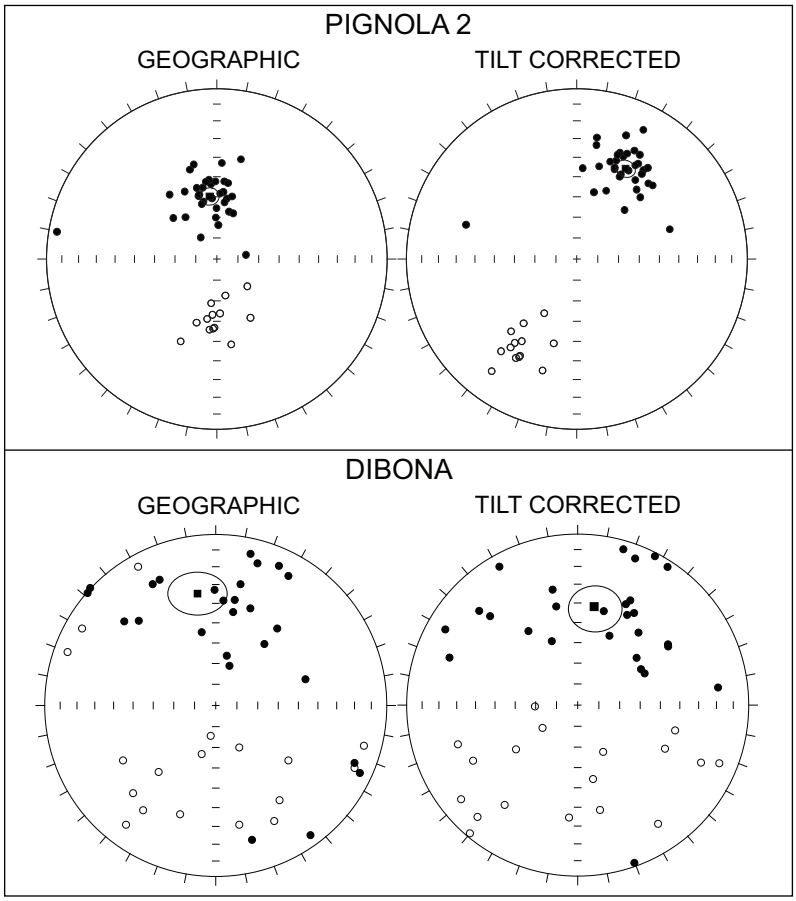

Figure 4.27: Equal area projections for ChRM (characteristic remanent magnetization) of the Pignola-2 (upper panel) and Dibona (lower panel). Mean directions in the text and in Table 4.2.

Dibona

The mean intensity of the samples from the Heiligkreuz Fm. is ~0.04 mA/m and in the Travenanzes Fm. is ~0.05 mA/m. The vector end-point diagrams (Fig. 4.25B; Zijderveld, 1967) reveal the ChRM between 200°C and 550°C in 25 of 45 samples of the Heiligkreuz Fm. (named MDS), and between 150°C and 400°C in 18 of 36 samples from the Travenanzes Fm (named MTV) (ChRM data in Appendix A.4). The diagrams shows both north-down and south-up directions, sometimes scattered (Fig. 4.25B) (typical MAD: ~11). The equal-area stereographic projection reveal fairly scattered directions (Fig. 4.27), failing the reversals test (McFadden and McElhinny, 1990). The mean directions in *in situ* coordinates (Dec: 350.5°E; Inc: 33.9°; k: 4.2; α_{95}: 11.8°; Table 4.2) differs to the inclination of the geomagnetic axial dipole (GAD Inc: ~62.8°), so the ChRM should not be contaminated by a VRM component. As for the Pignola-2 section, also here fold test cannot be performed due to homoclinality of the succession. The sequence of VGPs of the Dibona section shows nine magnetozones labeled MD, where MD1r, 2r and 4r are rather uncertain (grey intervals, Fig. 4.24), due to the poor preservation of NRM in these intervals (only three robust paleomagnetic directions).

TABLE 4.2 PALEOMAGNETIC DIRECTIONS FROM PIGNOLA-2 AND DIBONA SECTIONS

			IN SITU				TILT-CORRECTED			
Site	Comp.	N	k	α_{95}	Dec.	Inc.	k	α_{95}	Dec.	Inc.
Pignola-2	ChRM	47	24.1	4.3°	353.5°E	59.7°	23.9	4.3°	28.4°E	39.6°
Dibona	ChRM	46	4.2	11.8°	350.5°E	33.9°	4.2	11.8°	10.2°E	41.4°

LEGEND

Comp.: paleomagnetic component N: number of samples k, α_{95}: Fisher statistics parameters Dec.: mean declination Inc.: mean inclination

Discussion

Correlations between Tethyan sections

The Pignola-2 section is correlated with other coeval Tethyan sections from the literature containing conodonts to obtain a complete magneto-biostratigraphic record for the Carnian Stage (Fig. 4.28). The upper part of the Pignola-2 magnetostratigraphy (magnetozones MP2n to MP3r) is considered correlative to the basal portion of the Silická Brezová section (up to SB2r) (Channel et al., 2003) and the Pizzo Mondello section (up to PM2r) (Muttoni et al., 2004), whereas the entire Pignola-2 section is comparable with the Guri Zi section in Albania (up to GZ5r) (Muttoni et al., 2005, 2014) (Fig. 4.28). The conodont biostratigraphy of

Silická Brezová has been updated in this study by reclassifying the taxa illustrated in Figs. A1-A3 in Channell et al. (2003), using the new taxonomic criteria illustrated in Mazza et al. (2010, 2011, 2012a,b) (Fig. 4.28).

The magnetostratigraphy of the Dibona section straddling the Dibona Sandstones Mb. of the Heiligkreuz Fm. should be partially coeval with the magnetostratigraphy across the "green horizon" in the Pignola-2 section, as suggested by the first occurrence of conodont *Metapolygnathus praecommunisti* (Figs. 4.24, 4.28).

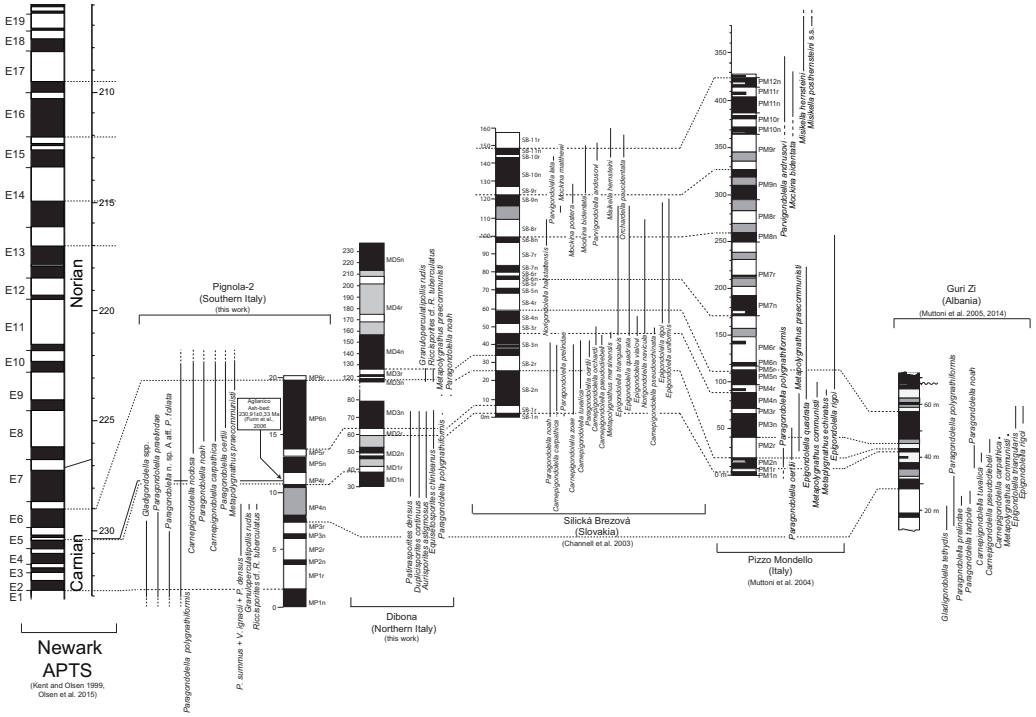

Figure 4.28: Correlations between Tethyan sections of Late Triassic and their calibration with the Newark Astrochronological Polarity Time Scale (APTS). The Norian to Rhaetian calibration and correlations are after Maron et al. (2015; see also Chapter 4.1.1). All correlations between Tethyan sections are based on integrated conodont bio-magnetostratigraphy. Biostratigraphy of Silická Brezová has been updated after Mazza et al. (2010, 2011, 2012a,b). Pignola-2 provides a chronological tie point with the Newark APTS (U/Pb age of 230.91±0.33 Ma; Furin et al., 2006) and part of the Dibona magnetostratigraphy (MD1n) covers the missing interval in Pignola-2. Correlation between Pignola-2 and the Newark APTS based on the statistical method of Muttoni et al. (2004) and Maron et al. (2015) (see Chapter 4.1.1).

Consequently, magnetozones MD1n-1r-2n-2r-3n at Dibona have been correlated to Pignola-2 magnetozones MP4n-4r-5n-5r-6n, respectively. Based on the first occurrence of *M. praecommunisti*, magnetozone MD3n is considered coeval to magnetozone SB2n at Silická Brezová and PM2n at Pizzo Mondello (Fig. 4.28).

The correlation between Pignola-2 and Dibona sections implies that the onset of the CPE at Dibona should fall in the lower part of the Heiligkreuz Fm. (basal Borca Mb, as suggested by Dal Corso et al., 2012) and its acme is reasonably represented by the terrigenous-rich levels of the Dibona Sandstone Mb (Fig. 4.24). The absence of strong biostratigraphic constraints does not allow a solid magnetostratigraphic

correlation between the upper Dibona section and other Tethyan sections.

Correlation with the Newark APTS

The Pignola-2 magnetostratigraphy has been compared with the Newark APTS (Kent and Olsen, 1999; see also Olsen et al., 2015) using the statistical approach described in Muttoni et al. (2004) and Maron et al. (2015; see also Chapter 4.1.1). The radiometric age of 230.91±0.33 Ma from the Aglianico ash-bed (Furin et al., 2006), comprised within the Pignola-2 magnetozone MP4r, has been taken into account for the correlation. The Dibona section was not considered for statistical correlation with the Newark APTS because of the unreliability of its magnetostratigraphy, due the variable sedimentation rate typical of shallow-water environments.

We compared the thickness of the Pignola-2 magnetozones with the duration of the magnetozones in the Newark APTS, testing the magnetostratigraphy of Pignola-2 along the APTS and obtaining 24 possible correlation options (Fig. 4.29). The interval of unknown polarity within the Pignola-2 "green horizon" is tentatively interpreted as dominated by normal polarity.

Each correlation is analyzed using linear regression, obtaining 24 t-test values; the higher the t-value, the more reliable the correlation. Only options 1, 2 and 24 pass the 95% confidence level threshold (Fig. 4.29) (statistical procedure with correlation options and analysis of t-values is reported in Appendix A.4). Option 24 is not considered because it is inconsistent with the U/Pb radiometric age of 230.91±0.33 Ma from the "green horizon" (Furin et al., 2006). Option 1 and 2 are consistent with this age. The main features of Option 1 and 2 are as follows:

Option 1:

- High t-value (~2.7).
- The radiometric age of Pignola-2 fits more closely (0.6 M.y. older) with the age provided by the Newark APTS for the equivalent stratigraphic level (Fig. 4.30).
- Fits with the correlation of Pizzo Mondello and the APTS. Specifically, magnetozones MP4r and MP5n of Pignola-2 are correlated respectively to E5r and E6n in Newark, as well as to the PM1r and PM2n in Pizzo Mondello. PMr1 and PM2n were correlated to the same Newark magnetozones by Muttoni et al. (2004) (Fig. 4.28).

Option 2:

- High t-value (~3.1)
- The correlation with the Newark APTS leads to a 0.9 M.y. discrepancy

between the radiometric age of Pignola-2 and the age of the APTS (Fig. 4.30).

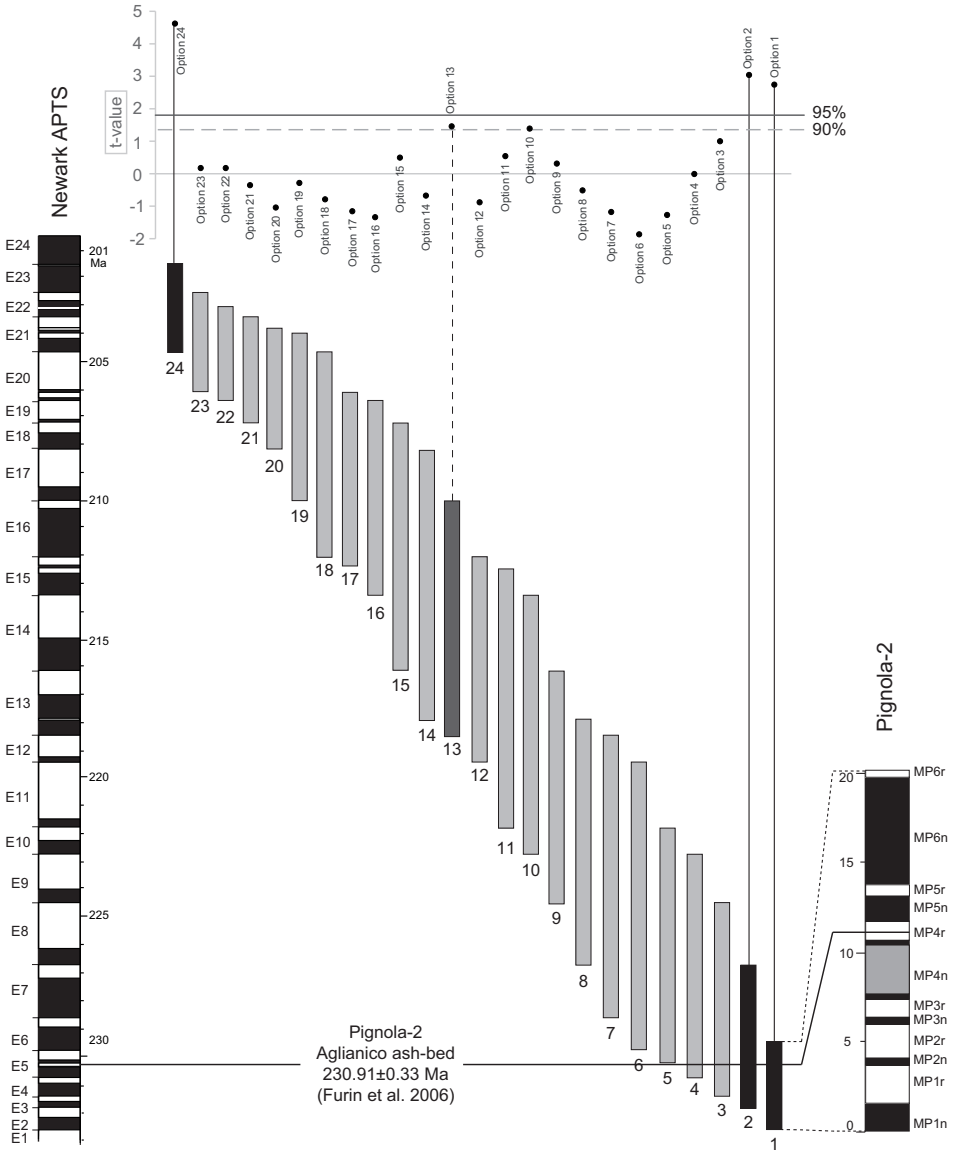

Figure 4.29: Sequence of 24 correlation options between the Pignola-2 section and the Newark APTS. Dark grey bars indicate the correlations that are reliable at the 90%, black bars are the correlations reliable at the 95%. Only three options are reliable at 95%: Options 1, 2 and 24. Option 24 was rejected because being inconsistent with the age of Pignola-2, while Options 1 and 2 both covers an interval consistent with the radiometric age of 230.91 Ma. In particular, preferred Option 1 is perfectly coherent with the time constraint in Pignola-2 and with the previous correlation between Pizzo Mondello section and the Newark APTS (Muttoni et al., 2004), performed using the same statistical method.

- This option does not fit with the previous correlation between Pizzo Mondello and the Newark APTS (Muttoni et al., 2004).

Option 1 implies only a minor discrepancy between the Pignola-2 U/Pb age and the Newark astrochronology, considering that in the lower Stockton Fm astrochronology is extrapolated from the upper Stockton and Lockatong Fms, where the 404 kyr

McLaughlin cycles are better expressed (Kent and Olsen, 1999; Olsen and Kent, 1999). Moreover, Option 1 is coherent with previous correlations from the literature (Pizzo Mondello; Muttoni et al., 2004) and is preferred over Option 2.

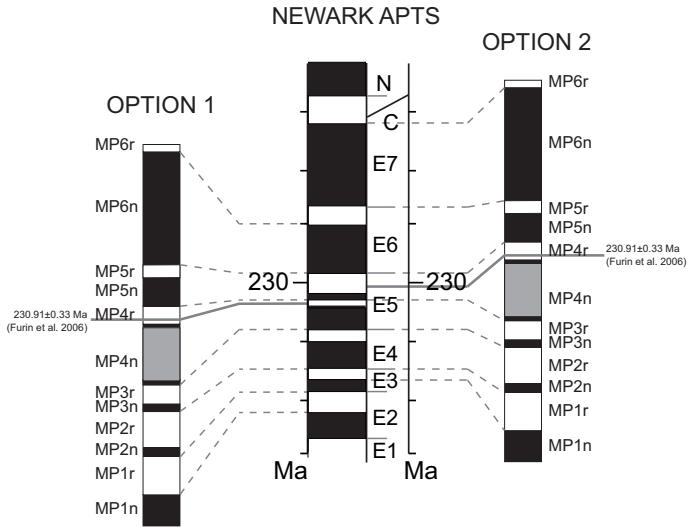

Figure 4.30: : Comparison between Option 1 and Option 2. Both Options 1 and 2 show a discrepancy between the radiometric age of 230.91 (Furin et al., 2006) and the corresponding level in the Newark APTS. In Option 1 is the age discrepancy (0.6 M.y.) is smaller than in Option 2 (0.9 M.y.). A possible cause of this age discrepancy is the absence of astronomic cycles recorded below E8n, and the age is presumed assuming sedimentation rates similar to the upper Lockatong Formation (Olsen and Kent, 1999).

We derived an age model from Option 1 that reveals a complex pattern of sedimentation rate along the Pignola-2 section (Fig. 4.31). In the cherty limestones, the sedimentation rate is mostly constant, except for a decrease just below and above the "green horizon". In the "green horizon" the sedimentation rate increases, probably due to an enhanced runoff of siliciclastic sediments from the continent caused by increased rainfall and weathering, in consequence of the intensification of the humid conditions at the CPE.

The age model derived from Option 1 (Fig. 4.31) suggests an age of ~230.7 Ma for the Julian/Tuvalian boundary, approximated in Pignola-2 by the LO of conodont *Gladigondolella* spp.. Assuming a Carnian/Norian boundary at ~227 Ma (Muttoni et al., 2004) and a Ladinian/Carnian boundary at ~237 Ma (Mietto et al., 2012), the Julian should be ~6.3 My-long and the Tuvalian ~3.7 My-long. Assuming the

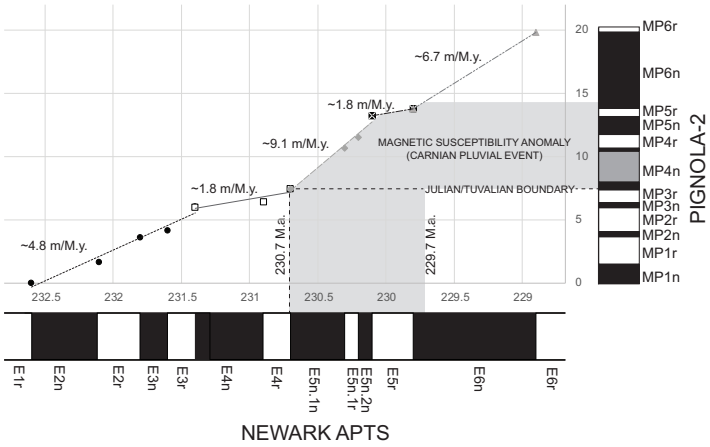

Figure 4.31: Age model based on Option 1. The inclination of the trend lines of the plot reflects the sedimentation rates, which decrease just after and before the "green clay-radiolaritic horizon". The model provides an age of ~230.7 Ma for the Julian/Tuvalian boundary and a duration of ~1 M.y. for the Carnian Pluvial Event.

magnetic susceptibility anomaly in Pignola-2 (covering the "green horizon" and the closest limestone beds) as expression of the CPE, its duration was about 1 My.

4.2.2 Leg 122: Site 759 (Hole B) and Site 760 (Hole B)

Sites 759 and 760 of the Leg 122 are located in the Wombat Plateau (16°44'21.78"S; 115°29'12.3"E) (Fig. 4.32). Sites are subdidived in Holes: 759A-759B; 760A-760B. The paleomagnetic analyses provided here come from Holes 759B and 760B, in particular from the Late Triassic portion. The core recovery in the Norian portion of Hole 759B is poor, while the Carnian portion is more available (Fig. 4.33). In Hole 760B the recovery is good for the entire Hole, and is greater in the Carnian portion (Fig. 4.34).

Geological Setting of the sites

Lithologies of Holes 759B and 760B show a transition from the siliciclastic sedimentation in the Carnian/lowermost Norian to an increased presence of carbonates in the middle Norian (Figs. 4.33, 4.34). In Hole 760B the siliciclastic sediments are more abundant and coarser than in Hole 759B. The detailed lithology here presented (Leg 122 Initial Reports; Haq et al., 1990) is considered from the

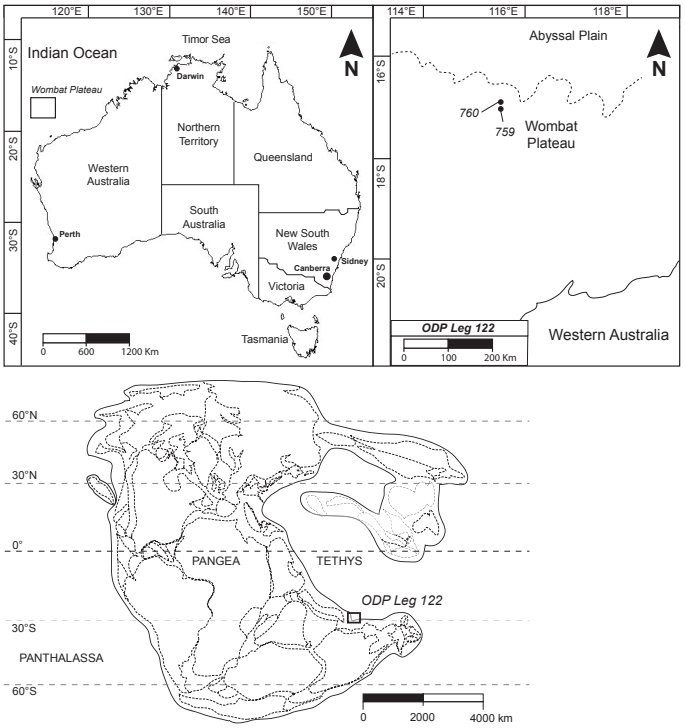

Figure 4.32: Sites 759-760 are located in the Wombat Plateau (16°44'21.78"S; 115°29'12.3"E), north-western Australia. The area of the Wombat Basin was located in southern Tethys during Late Triassic.

top to the base of the Late Triassic sediments, following the convention used by the ODP reports (depth is indicated in meters below sea floor – mbsf, thickness in meters).

Hole 759B

The first 95.4 m of sediments (Norian) are fossiliferous limestone (mudstone to wackestone, sometimes packstone) and dolomite, with interbedded silty claystone (Fig. 4.33). Minor lithologies associated with claystone are siltstone and fine-grained sandstone. In carbonates, oolitic/oncolitic grainstones are present, as well as calcarenites with variable amounts (1% to 20%) of siliciclastic component. Different degrees of dolomitization affect this interval, but they do not obliterate the

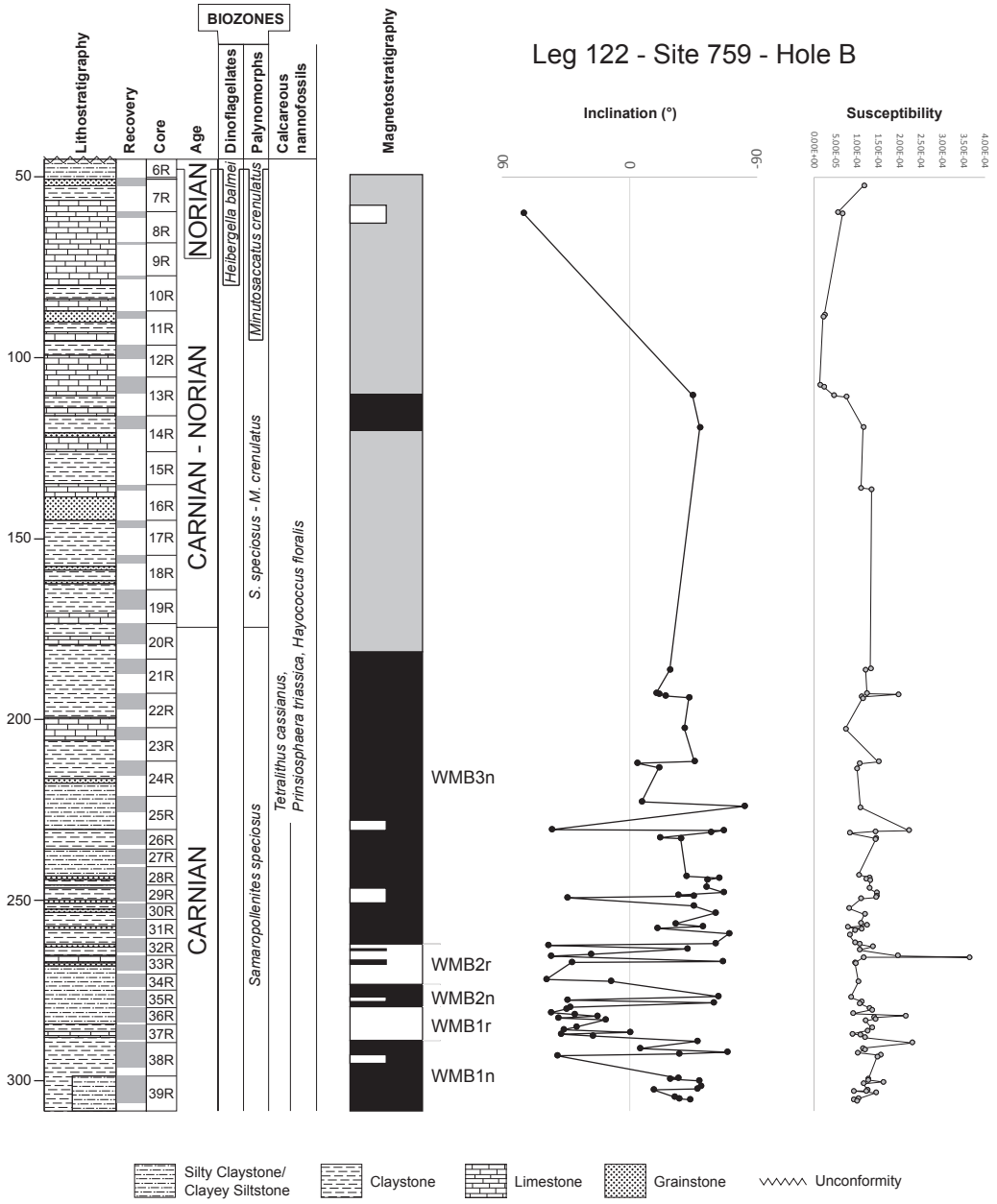

Figure 4.33: Hole 759B. From left to the right: lithostratigraphy, core recovery, main biostratigraphy (see text for discussion), magnetostratigraphy, virtual geomagnetic pole (VGP) latitudes calculated from characteristic remanent magnetization (ChRM) component directions, and magnetic susceptibility. Carnian/Norian boundary is placed with the beginning of Minutosaccatus crenulatus *palynomorph Zone.*

sedimentary features for most of the interval. The interbedded claystone become more abundant moving to the lowermost Norian. The boundary between the Late Triassic portion of the Hole and the overlying Cenozoic sediments is not recovered, so the type of stratigraphic contact is unknown.

The following 69 m (Carnian/early Norian) of sediments are dominated by parallel-laminated black silty claystone and clayey siltstone with disseminated pyrite nodules (Fig. 4.33). These lithologies are interbedded sometimes with coarse-grained levels of mixed siliciclastics and carbonates. Coarse-grained levels include a quartz-rich sandstones interval from ~140 to ~150 mbsf (sometimes fine-grained) and carbonate wackestone, packstone and grainstone.

The last 103 m (Carnian) are represented by alternation of silty claystone and clayey siltstone, with silty claystone becoming dominant in the lower part of the interval (Fig. 4.33). Minor lithologies are claystone (sideritic in part), sandy siltstone, coarse-grained quartz sandstone and pyrite nodules (decreasing downward).

Paleoenvironments

In the Carnian, the Wombat Plateau was characterized by a distal deltaic claystone sequence. The presence of pyrite/siderite, the absence of shelly faunas, the black color and the well-preserved lamination indicate restricted marine depositional conditions. The upward increase of carbonatic levels interbedded with claystone and sandstone indicates shallowing. The general coarsening upward trend in this interval is interpreted as marine regression and progradation of the delta. The presence of scattered pyrite, abundant carbonaceous matter in siltier levels and the lack of many faunas suggest oxygen-depleted, reducing conditions. The presence of quartz sandstone at ~140-150 mbsf marks the period of maximum marine regression. In the Norian sediments, the dominant carbonate-rich sediments suggest a marginal-marine, moderately low-energy environment. The presence of interbedded claystone and siltstone indicate carbonate banks formed in a coastal area with fluvial discharge. The acyclic repetition of carbonate and terrigenous claystone is related probably by change of terrigenous depocenter, consequent to the movement of distributary channels. These shifts could have driven the onset and the demise of the carbonate sedimentation in the Norian. The Norian sequence is truncated by a major unconformity beneath the Cenozoic pelagic sediments. The Jurassic and Cretaceous deposits have been eroded because of uplift, as well as the upper part of Late Triassic (upper Norian/Rhaetian). Reworked sands made of quartz, manganese fragments and early Miocene foraminifera (although they are

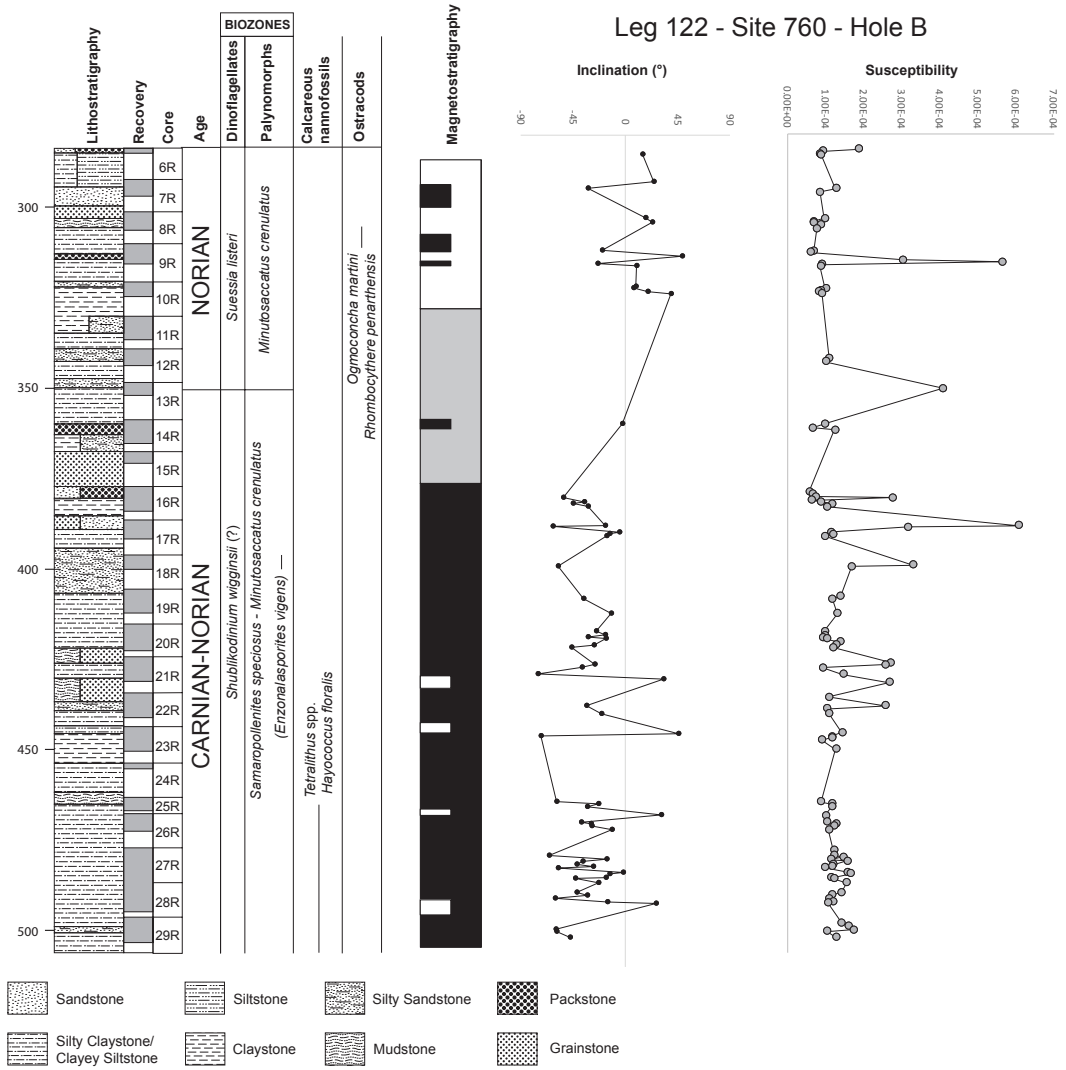

Figure 4.34: Hole 760B. From left to the right: lithostratigraphy, core recovery, main biostratigraphy (see text for discussion), magnetostratigraphy, virtual geomagnetic pole (VGP) latitudes calculated from characteristic remanent magnetization (ChRM) component directions, and magnetic susceptibility. Carnian/Norian boundary is placed with the beginning of Minutosaccatus crenulatus *palynomorph Zone and* Suessia listeri *dinoflagellate Zone.*

probably due to borehole contamination) overlie the erosive surface.

Hole 760B

Lithological information of Hole 760B starts from Core 6R (283 mbsf; Fig. 4.34), whereas the previous Cores were drilled only to reach the stratigraphic level corresponding to the end of the Hole 760A.

The first lithological unit of Hole 760B (179 m thick, Carnian-Norian) is characterized by interbedded carbonates and siliciclastic sedimentary rocks (Fig. 4.34). The main lithologies are dark gray clayey siltstone, black silty claystone, gray grainstone,

wackestone, mudstone, and quartz-rich silty sandstone. The carbonate rocks are abundant from 283 to 321 mbsf, 360 to 396 mbsf, and 416 to 464 mbsf (Fig. 4.34). Many of the carbonate rocks contains a high percentage of secondary dolomite.
Then, the second unit (42 m thick, Carnian) is dominated by black silty claystone, dark gray clayey siltstone, and dark greenish gray silty sandstone (Fig. 4.34). Coarser grained rocks are localized in the lower part of the unit, indicating a fining-upward trend. Sideritic levels are present, increasing with depth.

Paleoenvironments

Carnian sediments (lower unit) could have been deposited either in a distal prodelta environment, or in a protected shallow-water setting (i.e. tidal flat, estuarine bay). Chemically reducing conditions are locally present, with deposition of siderite and sulfurs.
The upper unit, around the Carnian/Norian boundary, shows lithologies and features typical of a marginal-marine environment, near the interfingering between siliciclastic and shallow-water carbonate depositional systems. Siliciclastic sediments were mostly deposited by currents and bioturbated. Carbonates contain peloidal and bioclastic components typical of a shallow to marginal-marine environment. Energy conditions were generally higher than in the lower unit.

Biostratigraphy

Hole 759B

In Hole 759B the more relevant fossils for biostratigraphy are calcareous nannofossils, dinoflagellates and palynomorphs (Haq et al., 1990; Brenner et al., 1992) (Fig. 4.33).

Calcareous nannofossils

An assemblage containing calcareous nannofossils *Tetralithus cassianus*, *Prinsiosphaera triassica* and *Hayococcus floralis* was found from ~230 mbsf to the bottom of the Hole. *T. cassianus* is a typical Carnian species, *H. floralis* is exclusively Norian and *P. triassica* is Norian/Rhaetian (see Tethyan palynology from Germany and Austria of Jafar, 1983) and they generally indicate a middle Late Triassic period. In some specimens of calcareous nannofossils Ca-carbonate have been replaced by siderite ($FeCO_3$).

Dinoflagellates

From ~41 to 45 mbsf, the dinoflagellates cysts *Heibergella balmei* and *Suessa listeri* indicate the *Heibergella balmei* Zone, which is late Norian in age (Brenner, 1992).

Palynomorphs

Palynomorphs assemblage belonging to the *Samaropollenites speciosus* Zone (Carnian) has been found in the lower part of the Hole, from ~175 mbsf to the bottom (Brenner, 1992; Brenner et al., 1992). The interval between ~41 mbsf and ~45 mbsf is in the *Minutosaccatus crenulatus* Zone (middle to late Norian), as confirmed by the coeval *Heibergella balmei* dinoflagellates Zone (Brenner, 1992). The interval between ~45 mbsf and ~175 mbsf provides a transitional assemblage between *S. speciosus* and *M. crenulatus* Zones. The presence of *Camerosporites secatus* and *Camerosporites pseudoverrucatus* suggests a Carnian age for the transition interval, whereas the permanent low abundance of *S. speciosus* indicates a Norian age (Brenner, 1992). Therefore, the *Samaropollenites speciosus*/*Minutosaccatus crenulatus* transition is considered late Carnian to early Norian in age.

Hole 760B

Main relevant fossils in Hole 760B are calcareous nannofossils, palynomorphs, dinoflagellates, and ostracods (Fig. 4.34).

Calcareous nannofossils

Main species are *Hayococcus floralis* and *Tetralithus* spp., found between 465 and 505 mbsf, in which calcite is often replaced by siderite. *H. floralis* indicates a Carnian age, whereas genus *Tetralithus* is usually identified as a Norian genus.

Palynomorphs

An assemblage typical of the *Minutosaccatus crenulatus* Zone has been found from ~350 to ~285 mbsf. The rest of the Hole 760B yielded palynomorphs indicating a transition zone between *Samaropollenites speciosus* and *M. crenulatus* (as seen also in Hole 759B). *Enzonalasporites vigens* is abundant from ~396 to ~400 mbsf, indicating a Carnian age (Brenner, 1992).

Dinoflagellates

First occurrence of dinoflagellates *Suessia listeri* and *Suessia swabiana* (*Suessia listeri* Zone; Helby et al., 1987) occurred at ~350 mbsf (at the base of the

Minutosaccatus crenulatus palynozone). The sporadic abundance of *Bartenia communis* suggest a middle-late Norian age for this interval (Helby et al., 1987), although the absence of *Heibergella balmei* suggest an early Norian age (although the presence or absence of *H. balmei* could be environmentally controlled). From ~350 mbsf to the bottom of the Hole, the absence of *Suessia listeria* and the presence of *Shublikodinium* spp. suggest the *Shublikodinium wigginsii* Zone. Unfortunately, the rare occurrence of *Shublikodinium* spp. and the absence of *Suessia swabiana* (typical of the upper *Shublikodinium wigginsii* Zone) indicate that dinoflagellates of this interval are environmentally controlled and that cannot be used for biostratigraphic investigations.

Ostracods

From ~305 to ~312 mbsf, the presence of ostracods *Ogmoconcha martini* and *Rhombocythere penarthensis* suggests a late Norian to Rhaetian age (Dépêche and Crasquin-Soleau, 1992). The age based on ostracods is in accordance with palynology (presence of middle-late Norian *Bartenia communis* in the *Minutosaccatus crenulatus* palynozone).

Paleomagnetism

Methods

A total of 90 non-oriented ~10cc minicores and cubes from the Hole 759B, and 103 from Hole 760B, have been analysed for paleomagnetism and rock magnetism. Samples have been provided by the Kochi Core Center (Kochi University, Japan) and analyzed at the "Fort Hoofddijk" Paleomagnetic Laboratory (Utrecht University, The Netherlands). Samples have been demagnetized progressively by application of an alternate gradient field (using a 2G Enterprises singe-axis AF demagnetizer) and measured using a 2G Enterprises RF-SQUID magnetometer. Samples have been demagnetized by steps of 5 mT up to 50 mT, then steps of 10 mT up to 100 mT. Single sample NRM directions for each step of demagnetization have been plotted on an end-point vector graph (Zijderveld, 1967), and only the magnetization components made of at least three subsequent end-points have been considered. Cores from Holes 759B and 760B are not oriented, and the samples are oriented only respect to the cores. So only the magnetic inclinations have been considered to determine the directions of magnetization. The low-field magnetic susceptibility (κ) was measured with an AGICO Kappabridge MFK1-A instrument on 87 samples from Hole 759B and on 84 samples from Hole 760B. Rock magnetism experiments have

been performed on selected samples to support the paleomagnetic interpretations. Thermomagnetic runs were performed on 8 samples from Hole 759B and 8 samples from Hole 760B, using a modified horizontal translation Curie balance (noise level $5x10^{-9}$ Am^2; Mullender et al., 1993), measuring in air. Powdered samples (70-80 mg) was measured increasing temperature in several cycles, up to 580°C. Field cycles was between 100 and 300 mT, with heating-cooling rates of 10°C/min.
Hysteresis cycles, IRM acquisition and backfield IRM have been performed on 23 samples from Hole 759B and on 19 samples from Hole 760B, using an alternate field gradient magnetometer (Princeton Measurement Corp. AGM 2900) on rock fragments of about 50 mg (maximum field 500 mT, steps of 10 mT).

Magnetic properties

Hole 759B

Susceptibility (κ) is almost constant (~125×10^{-6} SI) up to 110 mbsf, where it decreases abruptly (~46×10^{-6} SI) (Fig. 4.33). The sudden decrease of κ could be related to a strong reduction of siliciclastic material in carbonate levels (usually contaminated by terrigenous from fluvial discharge), probably due to one of the frequent movement of distributary channels (for details in environmental changing see "Paleoenvironments" paragraph, Chapter 4.2.3).
Thermomagnetic curves of samples wbb3709801, 3711801, 3713201, 3714901, 3716501, 3720701, 3722201 and 3722901 indicate a weak magnetization (frequently below 0.02 Am^2/kg), in particular for wbb3713201 that does not reach 0.005 Am^2/kg (Fig. 4.35). The curves of samples wbb3709801 (~165 mbsf), 3720701, 3722201 and 3722901 (from ~262.1 to ~299 mbsf) show an increase in magnetization between 400 and 580°C (followed by a gentle increase during cooling, until room temperature is reached) (Fig. 4.35), probably due to the oxidation of a variable quantity of pyrite (FeS_2) and siderite ($FeCO_3$) in magnetite ($Fe^{3+}_2Fe^{2+}O_4$). Probably pyrite is the dominating magnetite-forming mineral in wbb3709801, while the stratigraphic interval containing the other three samples is rich in siderite (but also pyrite is present). Below 400°C there are no evidences of magnetic iron-sulfides (e.g. pyrrhotite – FeS), since the heating-cooling steps are totally reversible up to this temperature, and the Curie temperature for magnetic Fe-sulfides (~320°C) has not been reached (Fig. 4.35). The original magnetization is carried probably by magnetite but is impossible to differentiate the neo-formed magnetite to the original magnetite. Samples wbb3711801, 3713201, 3714901 and 3716501 (from ~186.3 to ~246.6 mbsf) show a similar behavior, but the increase

is very (sometimes extremely) slight (Fig. 4.35). This difference with the other samples is probably due to a smaller amount of magnetite-forming minerals (in this interval pyrite is common).

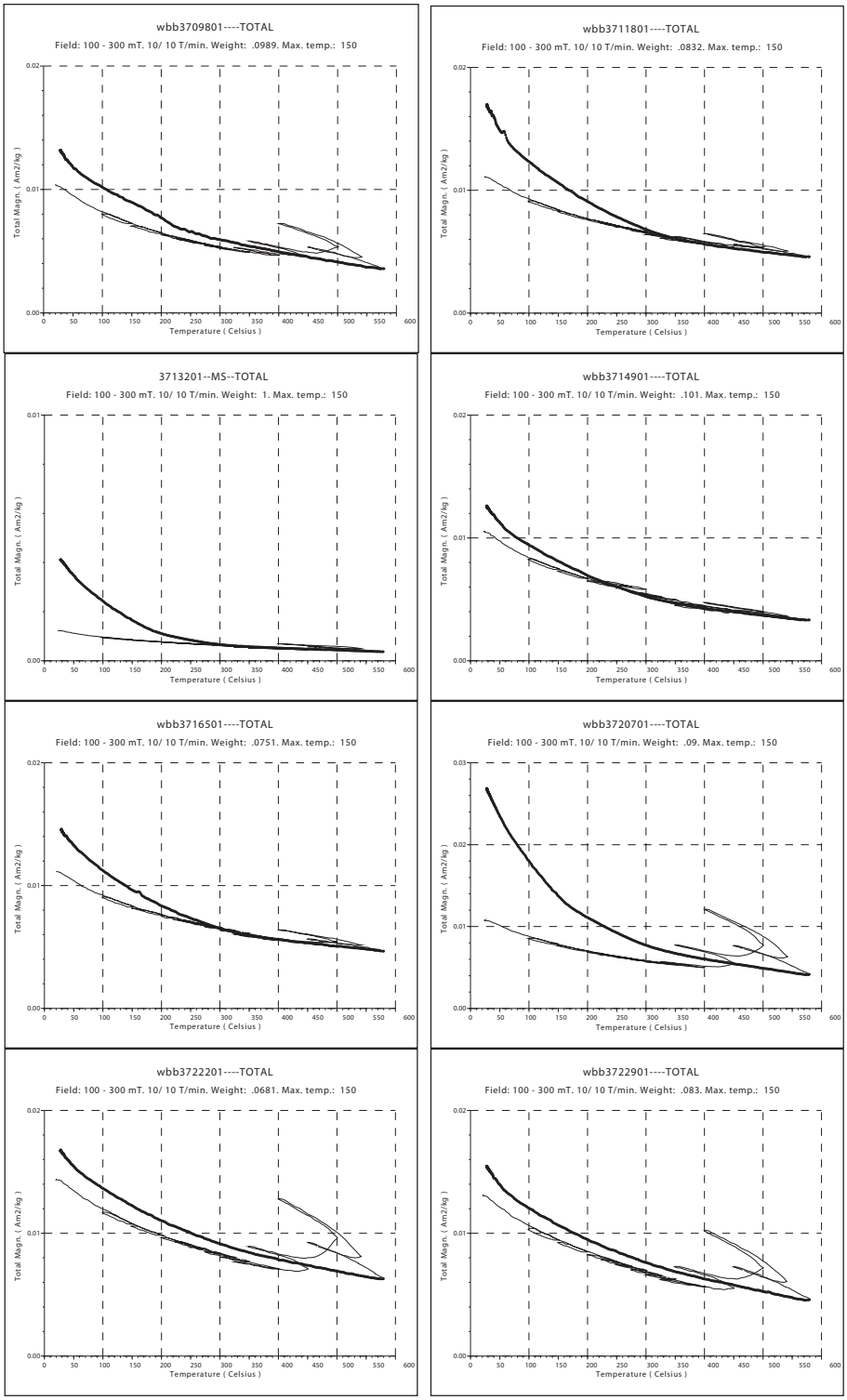

Figure 4.35: Thermomagnetic curves determined with a Curie balance of samples wbb709801, 3711801, 3713201, 3714901, 3716501, 3720701, 3722201 and 3722901. See text for discussion.

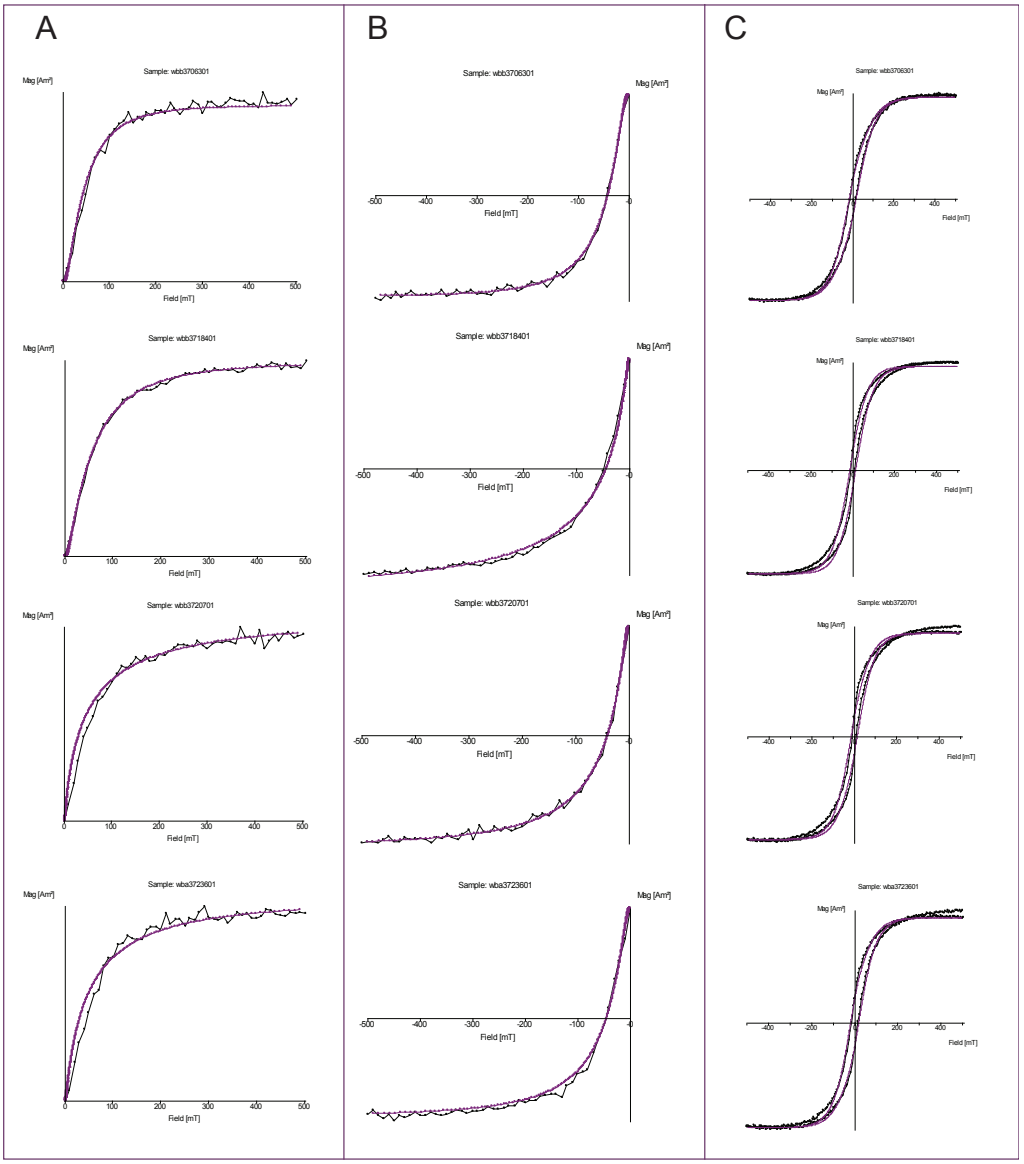

Figure 4.36: IRM acquisition curve (A), IRM backfield (B), and hysteresis cycles (C) of wba samples from Hole 759B (see discussion in text). Purple line is the data-fitting curve.

IRM acquisition curves show variable levels of saturation, from ~300 mT to ~500 mT, coherent with the presence of magnetite (Fig. 4.36A). Samples subjected to backfield IRM are characterized by coercivity fields from 40 to 60 mT, associated to magnetite (Fig. 4.36B). Hysteresis cycles are pot-bellied shaped (Fig. 4.36C), suggesting a mixture of single-domain (SD) and superparamagnetic (SP) magnetite (Tauxe et al., 1996).

Hole 760B

Susceptibility (κ) is normally around 100×10^{-6} SI, increasing to ~250×10^{-6} SI from ~426 to ~440 mbsf and to ~300×10^{-6} SI from ~380 to ~400 mbsf (Fig. 4.34). Two

major peaks of 550-600×10^{-6} SI at ~387 mbsf and at ~316 mbsf are present, as well as a minor peak of 400×10^{-6} SI at ~350 mbsf (Fig. 4.34). The higher values of κ seem localized in the more carbonatic levels, probably related to the presence of

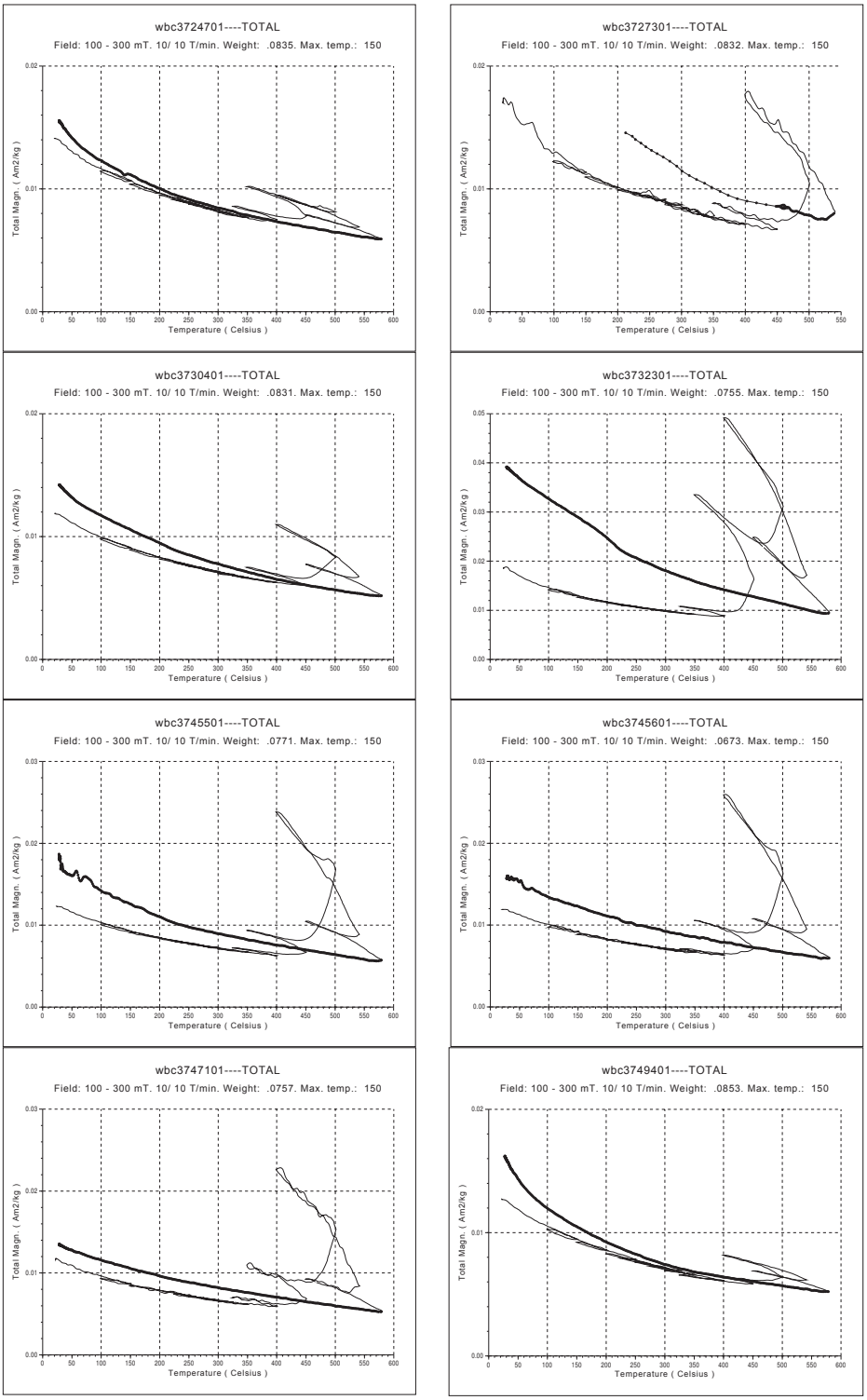

Figure 4.37: Thermomagnetic curves determined with a Curie balance of samples wbc3724701, 3727301, 3730401, 3732301, 3745501, 3745601, 3747101 and 3749401. See text for discussion.

siderite.

Thermomagnetic curves of samples wbc3724701, 3727301, 3730401, 3732301, 3745501, 3745601, 3747101 and 3749401 indicate a weak magnetization, normally below 0.02-0.03 Am^2/kg (only sample wbc3732301 reach 0.05 Am^2/kg) (Fig. 4.37). The curves of samples wbc3727301 (~323 mbsf), 3732301 (~392 mbsf), 3745501, 3745601 (from ~440 to ~441 mbsf) and 3747101 (~465 mbsf) show an increase in magnetization between 400 and 580°C, and then a smooth increase in cooling curve until room temperature (Fig. 4.37). This behavior is probably due to the oxidation of pyrite (or siderite, in the lower part of the Hole) in magnetite. Magnetic iron sulfides (e.g. pyrrhotite) seems not to be present since the heating-cooling steps are

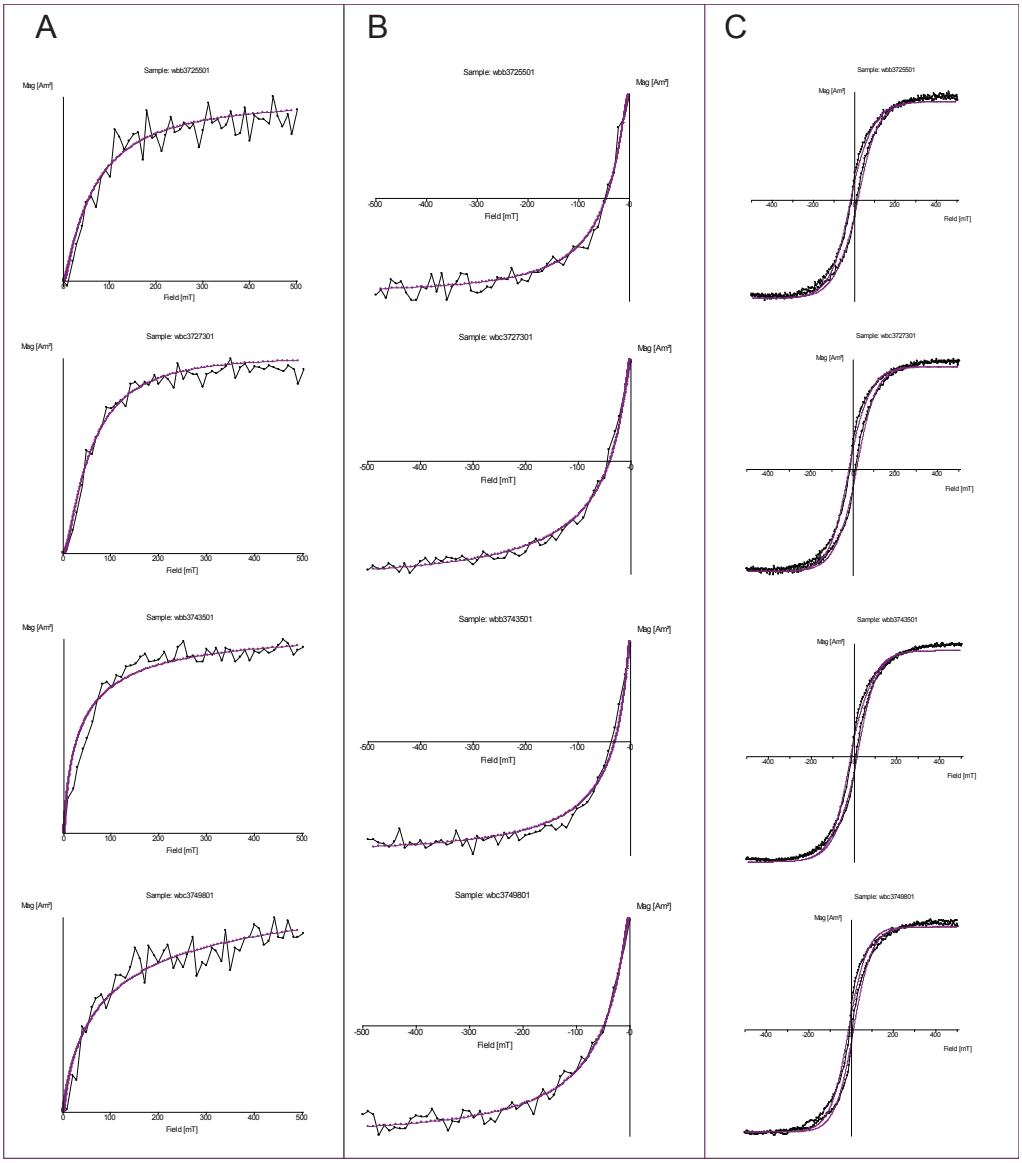

Figure 4.38: IRM acquisition curve (A), IRM backfield (B), and hysteresis cycles (C) of wba samples from Hole 760B (see discussion in text). Purple line is the data-fitting curve.

reversible until 400°C and Curie temperature for magnetic Fe-sulfides (~320°C) has not been reached (Fig. 4.37). A small amount of primary magnetite is present, but it cannot be differentiated from the neo-formed magnetite. The behavior of samples wbc3724701 (~285 mbsf), 3730401 (~363 mbsf), and 3749401 (~492 mbsf) is similar, but the increasing in magnetization after 400°C is less intense (Fig. 4.37). These small differences are probably related to the different amount of pyrite (or siderite, probably in sample wbc3747101) in the rocks, which seems not to be controlled by lithology. More likely, the various pyrite content is related to temporary reducing conditions.

Sample subjected to IRM acquisition show variability in saturation field, generally from ~300 mT to ~500 mT (Fig. 4.38A), coherent with the presence of magnetite. Few samples seems not to reach saturation above 500 mT. Backfield IRM curves revealed coercivity fields from 40 to 80 mT, ascribed to magnetite (Fig. 4.38B). The shape of hysteresis cycles is pot-bellied (Fig. 4.38C), typical of single-domain (SD) and superparamagnetic (SP) magnetite mixture (Tauxe et al., 1996).

Magnetostratigraphy

Hole 759B

Mean intensity of initial NRM is ~0.58 mA/m, lower in the upper part (~0.07

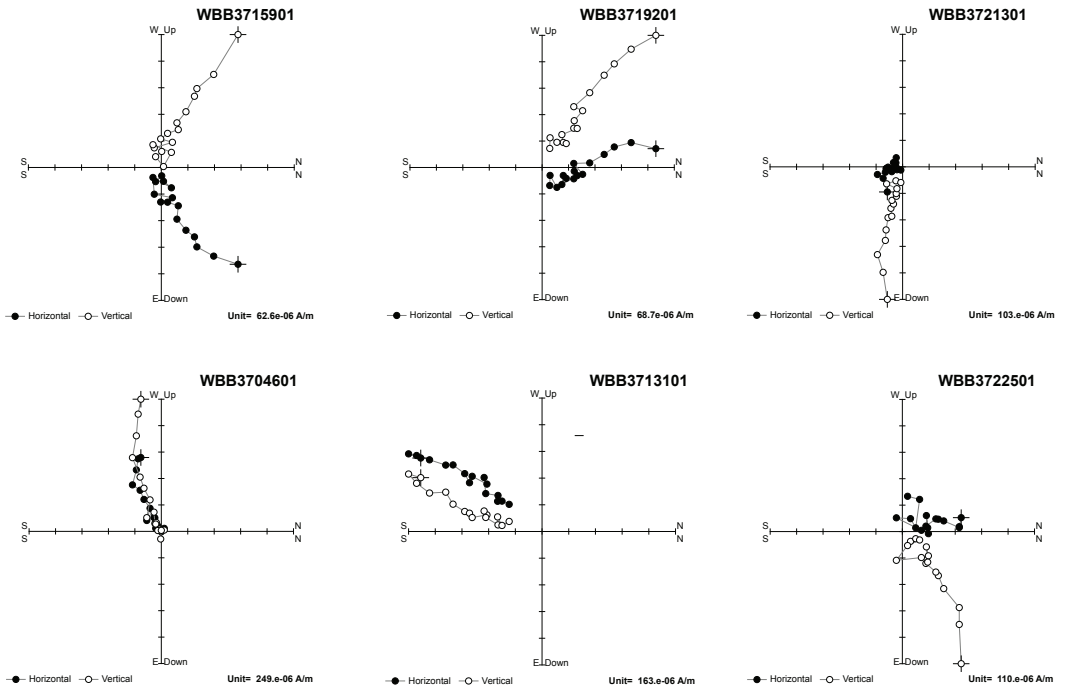

Figure 4.39: Vector end-point demagnetization diagrams for representative samples from Hole 759B. Closed circles are projections onto the horizontal plane, and open circles are projections onto the vertical plane for cores coordinates.

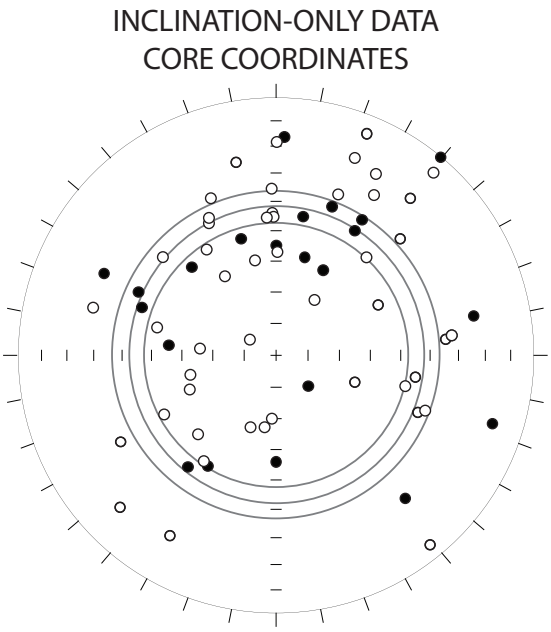

Figure 4.40: Equal-area projections for characteristic remanent magnetization (ChRM) component inclinations isolated at Hole 759B for core coordinates (see text for mean inclinations and discussion).

mA/m; 52 to 90 mbsf) and higher in the middle (~1.1 mA/m; 186 to 243 mbsf). The lower intensities are located around the Norian carbonate, where the siliciclastic input decreased. Characteristic magnetization (ChRM) have been identified in 71 samples, mainly above 15-20 mT and maximum until 100 mT (ChRM data in Appendix A.3), resulting stable in vector end-point demagnetization plots (Zijderveld, 1967) (Fig. 4.39). Equal-area projection for inclination-only data show a substantial variability of inclinations, mainly localized around 30°-50° (Fig. 4.40). This is confirmed by the calculation of the mean inclination: 42.2°±5.4° (k=10.4, N=71; McFadden and Reid, 1982). The mean inclination of 759B differs from the Geomagnetic Axial Dipole (GAD) inclination value at the latitude of the site (Inc_{GAD} = -31°), suggesting

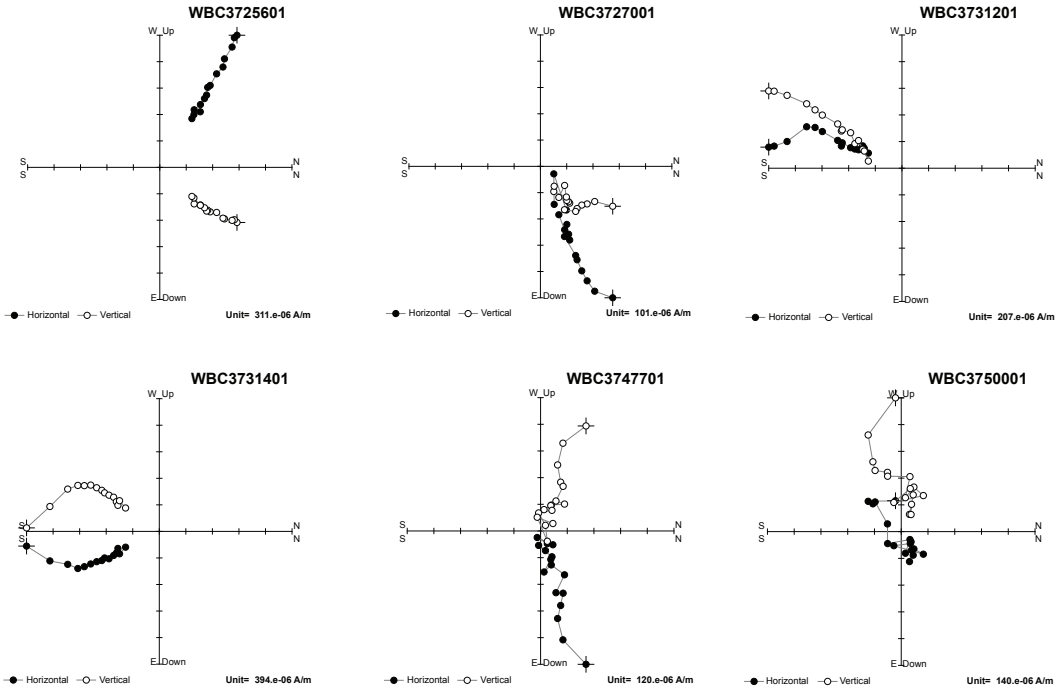

Figure 4.41: Vector end-point demagnetization diagrams for representative samples from Hole 760B. Closed circles are projections onto the horizontal plane, and open circles are projections onto the vertical plane for cores coordinates.

that the paleomagnetic data of the Hole are not affected by contamination of VRM. Samples have no geographic orientation, so the paleomagnetic polarity must be derived from the magnetic inclination. In Late Triassic, the Wombat Plateau was in the southern hemisphere, hence positive inclination means normal polarity and negative inclination means reverse polarity. The sequence of ChRM inclinations define 17 polarity inversions, grouped in 5 magnetozones named WMB1n to WMB3n, where single data-points have been considered as partial reversals (Fig. 4.33).

Hole 760B

The mean intensity of initial NRM is ~0.67 mA/m, and is higher between 380 and 420 mbsf (~1.21 mA/m). A characteristic NRM magnetization (ChRM) has been recognized in 67 samples generally between 10 and 60 mT (maximum until 100 mT; ChRM data in Appendix A.3), as shown in vector end-point demagnetization diagrams (Zijderveld, 1967) (Fig. 4.41). Paleomagnetic inclinations ditribution in equal-area projection show a certain variability (Fig. 4.42), with a mean inclination of 31.5°±5.6° (k=10.5, N=67; McFadden and Reid, 1982). Mean inclination of Hole 760B is dramatically similar to the GAD inclination at the latitude of the Site (Inc_{GAD} = -31°), which means that there is a probable contamination of VRM. As for Hole 759B, only the magnetic inclination must be considered to define the polarity inversions, following the criteria for the southern hemisphere. The stratigraphic sequence of ChRM inclinations shows 16 normal/reverse polarity shifts, defining two long magnetozones named WMC1n and 1r; 8 single data points define likewise partial inversions (Fig. 4.34).

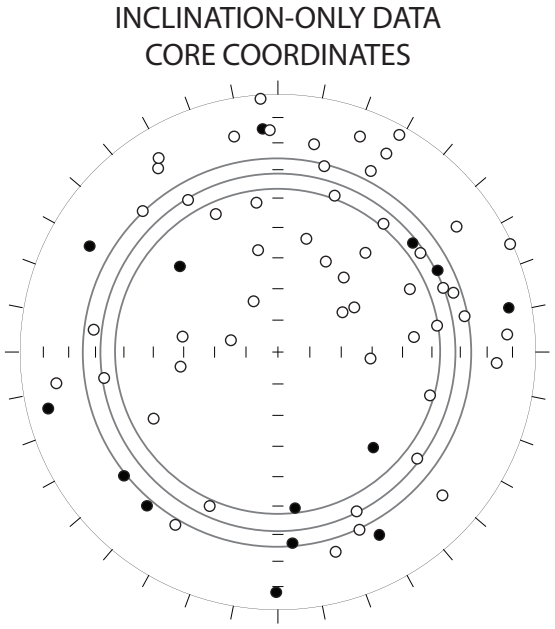

Figure 4.42: Equal-area projections for characteristic remanent magnetization (ChRM) component inclinations isolated at Hole 760B for core coordinates (see text for mean inclinations and discussion).

Discussion

The magnetostratigraphy of Holes 759B and 760B have been compared with other

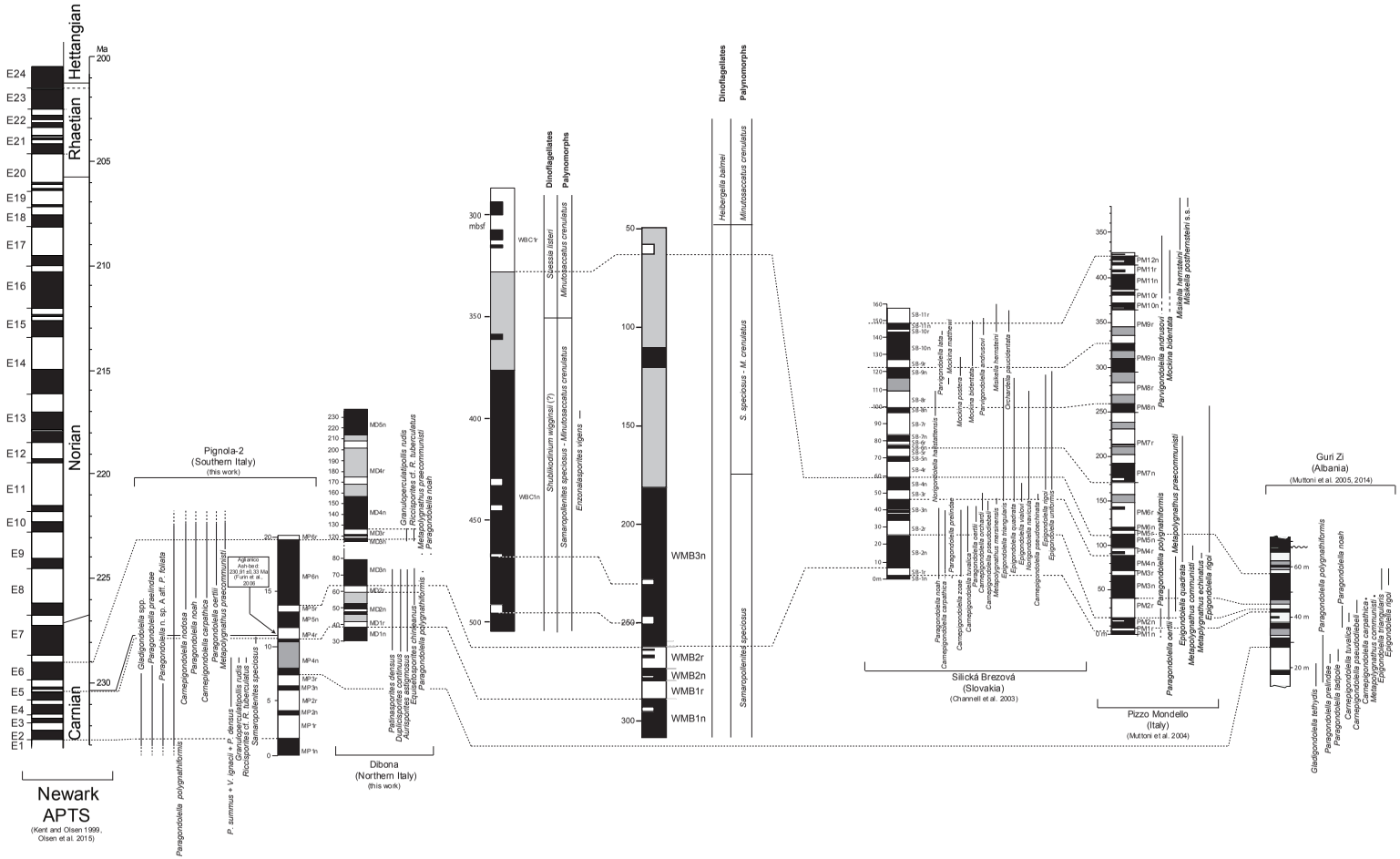

Figure 4.43: The Carnian-Norian magnetostratigraphy and biostratigraphy of Holes 759B and 760B, correlated to data from marine sections from the literature, such as Pignola-2, Dibona (Chapter 4.2.1), Silická Brezová (Channell et al., 2003), Pizzo Mondello (Muttoni et al., 2004), and Guri Zi (Muttoni et al., 2005, 2014). Holes 759B and 760B are correlated to the Newark astrochronological polarity time scale (APTS) through the statistical correlation of Pignola-2 with the APTS (Chapter 4.2.1).

Carnian/Norian sections, as Pignola-2, Dibona, Silická Brezová (Channell et al., 2003), Pizzo Mondello (Muttoni et al., 2004) and Guri Zi (Muttoni et al., 2005, 2014) (Fig. 4.43). The palynomorph biozonation places the magnetozones WMB1n to 3n in the Carnian (see paragraph "Palynomorphs", Chapter 4.2.3; Fig. 4.33), whereas the unknown polarity zone covers mainly the transitional Carnian/Norian interval (*Samaropollenites speciosus*/*Minutosaccatus crenulatus* transitional Zone). The partial reverse magnetozone between Cores 759B-7R and 759B-8R is considered Norian in age, following the palynomorphs and dinoflagellates biozonation (Fig. 4.33). In Hole 760B, palynomorphs and dinoflagellates diagnostic for Norian age have been found in WMC1r, while the large normal magnetozone below (WMC1n) is considered Carnian to Norian (Fig. 4.34). Using these calibrations, is reasonable to think that partial reversals WMB3n.1r and WMB3n.2r are coeval respectively to WMC1n.1r and WMC1n.2r (Fig. 4.43). Moreover, the palynomorph *Samaropollenites speciosus* is found also in Pignola-2 section, in correspondence of the transition to magnetozones MP4n and MP4r (Fig. 4.43). Magnetozone WMB1n should correspond to MD1n (Dibona), MP4n (Pignola-2) and GZ3n (Guri Zi); WMB1r to MD1r, MP4r and GZ3r; WMB2n to MD2n, MP5n, GZ4n, SB-1n (Silická Brezová) and PM1n (Pizzo Mondello); WMB2r to MD2r, MP5r, GZ4r, SB-1r and PM1r; WMB3n and WMC1n to MD3n, MP6n, GZ5n, SB-2n and PM2n (Fig. 4.43). Magnetozone WMC1r is considered middle-late Norian for the abundance of dinoflagellate *Bartenia communis* (coherent with the founding of upper Norian ostracod *Ogmoconcha martini*), so is reasonable to think that the base of this magnetozone should be coeval to the base of SB-4r in Silická Brezová, of PM5r in Pizzo Mondello, and of GZ6r in Guri Zi (Fig. 4.43). Partial reversals within WBC1r could be part of the normal magnetozones included in the mainly reverse interval SB-4r/SB8r in Silická Brezová (coeval to PM5r/PM8r interval in Pizzo Mondello) (Fig. 4.43).

Following the correlation between the Carnian/Norian sections here considered and the Newark APTS (see paragraph "Correlation with the Newark APTS" in Chapter 4.2.1), the magnetostratigraphy of Holes 759B and 760B should cover the interval E5n to E8r (~6 My), although it could be more extended, considering that probably the partial reversal within WBC1r could be the normal magnetozones E9n and above (Fig. 4.43).

Chapter V
A GEOMAGNETIC POLARITY TIME SCALE FOR THE LATE TRIASSIC

5.1 BRIEF HISTORY OF THE GPTS

A Geomagnetic Polarity Time Scale (GPTS) assigns a duration to each magnetozone in a sequence of geomagnetic polarity reversals. Using a GPTS is possible to assign an age to the events (biologic, climatic, geodynamic, etc.) calibrated to the magnetostratigraphy of the same period.

The first attempts to construct a GPTS for the Triassic started in 1960s-1970s, but they were fragmentary and poor-detailed. Khramov (1963) proposed the first GPTS for Early-Middle Triassic, based on the Moscow Basin and correlated with other studies from literature. Later, other authors (McElhinny and Burek, 1971; Pergament et al., 1971; Pechersky and Khramov, 1973; Molostovsky et al., 1976) proposed their version of GPTS for the entire Triassic. Contrary to the Late Jurassic to Pleistocene magnetostratigraphic record, mainly derived from linear magnetic anomalies of the sea floor, Triassic magnetostratigraphy was derived mainly from sedimentary successions in which the magnetization was very low-preserved. After the introduction of the more sensitive SQUID magnetometer in the late 1980s, paleomagnetic analyses provided more detailed magnetostratigraphic investigations. The integrations of detailed magnetostratigraphic studies with detailed biostratigraphies, mostly based on ammonoids, conodonts, palynomorphs and radiolarians, paved the way to the construction of a precise GPTS. In 2010, Hounslow and Muttoni proposed a GPTS for the Triassic, based on marine sections with biostratigraphically calibrated magnetostratigraphy, focusing on the Stage boundaries that are fixed points in the geochronology. To accommodate the differences in sedimentation rates, the magnetostratigraphy of the considered sections has been stretched (or shrinked), creating a Triassic composite magnetostratigraphy in a pseudo-height scale, which permits a graphic correlation. Marine sections were preferred for their greater chances to confirm correlations using different constraints (biostratigraphic, chemostratigraphic, etc.). To reshape the Triassic composite magnetostratigraphy in a GPTS, the metric length scale have been converted in a time scale (Hounslow and Muttoni, 2010) using linear interpolation

or radiometric ages from Induan (first Stage of the Triassic) to Carnian. The Newark APTS ages (Olsen and Kent, 1999) has been applied to calibrate the Rhaetian, using the Triassic/Jurassic boundary age of ~201.6 Ma (Schaltegger et al., 2008) as a tie-point. Problems remain for the Norian Stage, which is poorly constrained by radiometric ages and the correlation with the Newark APTS was not certain.

5.2 A NEW PROPOSAL OF GPTS

The correlations between the Carnian/Norian sections proposed in Chapter 4.2.1 (Pignola-2 and Dibona, Fig. 4.28), in association with the correlations between the Norian/Rhaetian sections in Chapter 4.1.1 (Pignola-Abriola, Fig. 4.7), allow to assemble a composite magnetostratigraphy of Tethyan sections valid for the Late Triassic. The magnetostratigraphy of Leg 122 (Sites 759-760, Chapter 4.2.2; Site 761, Chapter 4.1.3) is not included in the Late Triassic composite, because of the extended stratigraphic discontinuities and poor bio- and chemostratigraphic constraints. Similarly, magnetostratigraphy of Mt. Messapion (Chapter 4.1.2) is excluded for its scarce reliability. This long-time extended composite magnetostratigraphy includes many reversals (Fig. 5.1; high-definition version in Appendix B), defining a unique pattern that allows a more precise correlation with the Newark APTS. The chance to build a Geomagnetic Polarity Time Scale for the Late Triassic, connecting our composite polarity scale to the Newark APTS, is given by radiometric constraints. In facts, the Carnian magnetostratigraphy of the Pignola 2 section is constrained at 230.91±0.33 Ma (Furin et al., 2006) and the age of the Rhaetian at Pignola-Abriola is confirmed by the U/Pb ages around the Norian/Rhaetian boundary in Peru (Wotzlaw et al., 2014). The Pignola-2 section is correlated confidently with the Pizzo Mondello section, and the correlation with the Newark APTS of which (Muttoni et al., 2004; Hounslow and Muttoni, 2010) was confirmed by the correlation of Norian/Rhaetian sections proposed in Chapter 4.1.1. Using the radiometric age of Pignola-2 (Furin et al., 2006) was possible to constrain the magnetostratigraphy of the Carnian in the lower APTS, strictly correlating magnetozone MP2r of Pignola-2 section with E5n.1r of the APTS (Fig. 5.1) using statistics (Fig. 4.29), while for the upper APTS the Rhaetian was constrained by the correlation between MPA5r in Pignola-Abriola and E20r of the APTS. Therefore, the Tethyan magnetostratigraphy of the Late Triassic is both anchored at the bottom (at 230.91 Ma) and the top of the APTS (at 205.7 Ma). The magnetostratigraphy of the APTS older than 230.9 Ma is associated to a composite of Dibona, Pignola-2, Guri Zi (Muttoni et al., 2005, 2014) and Bolücektasi Tepe

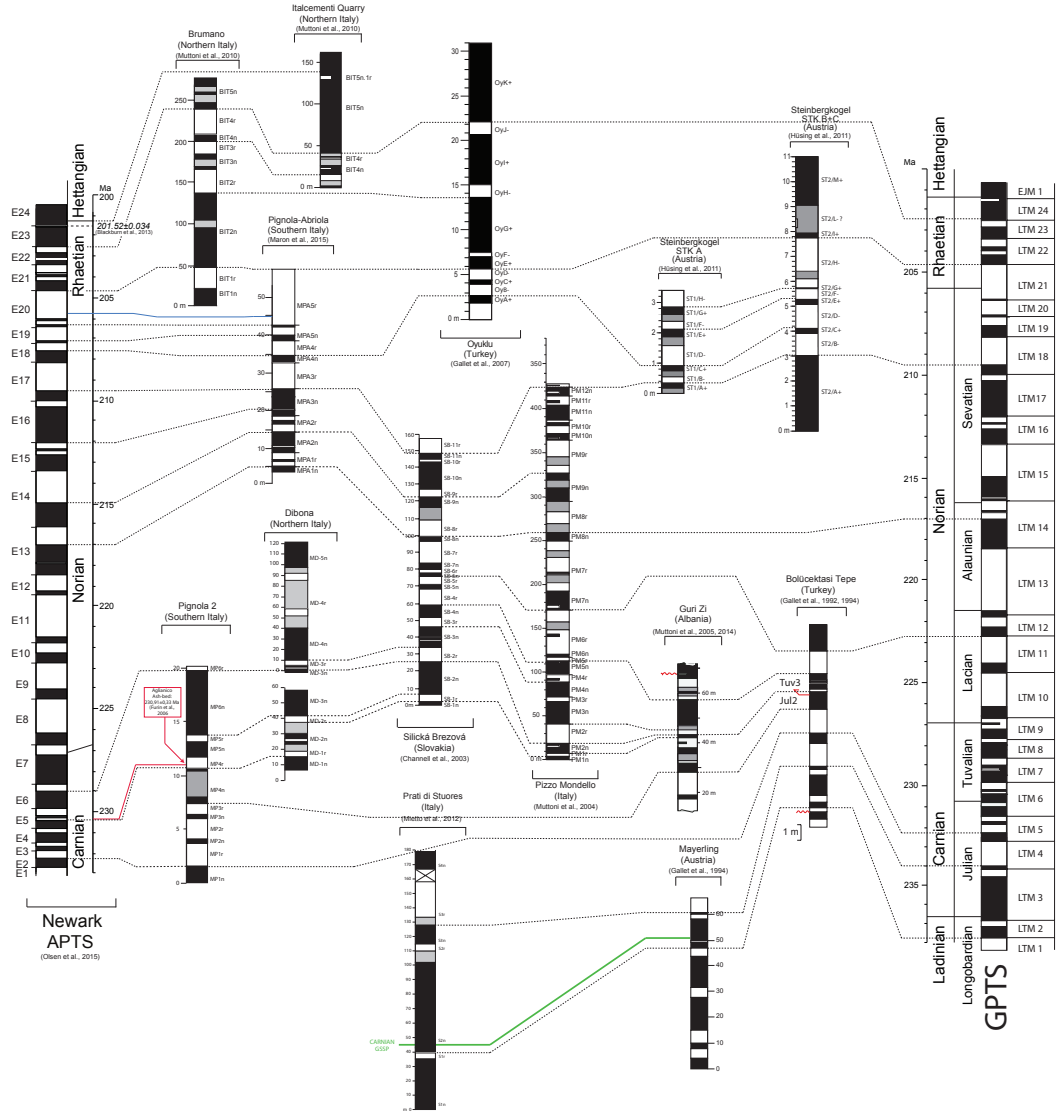

Figure 5.1: The composite magnetostratigraphy of the intercorrelated Tethyan marine sections here considered, covering the entire Late Triassic, has been time-calibrated with the Newark Astrochronological Polarity Time Scale (on the left), obtaining a Geomagnetic Polarity Time Scale (GPTS; on the right). The magnetochronozones of the GPTS are named LTM.

(Gallet et al., 1992) sections until ~233 Ma, as explained in Chapter 4.1.1. The Late Triassic composite magnetostratigraphy here proposed defines a pattern of geomagnetic polarity reversals coherent with the Newark magnetostratigraphy, confirming the correlations between the considered Tethyan marine sections and the Newark APTS as proposed in the previous Chapters (4.1.1 and 4.2.1).

Since the Newark APTS does not record sediments younger than lower Tuvalian (upper Carnian), the magnetostratigraphy of the Mayerling (Gallet et al., 1994) and the Prati di Stuores/Stuores Wiesen (Mietto et al., 2012) have been integrated for the lowermost Carnian time interval. The duration of these magnetozones have been derived considering a basin with constant sedimentation rate and a radiometric

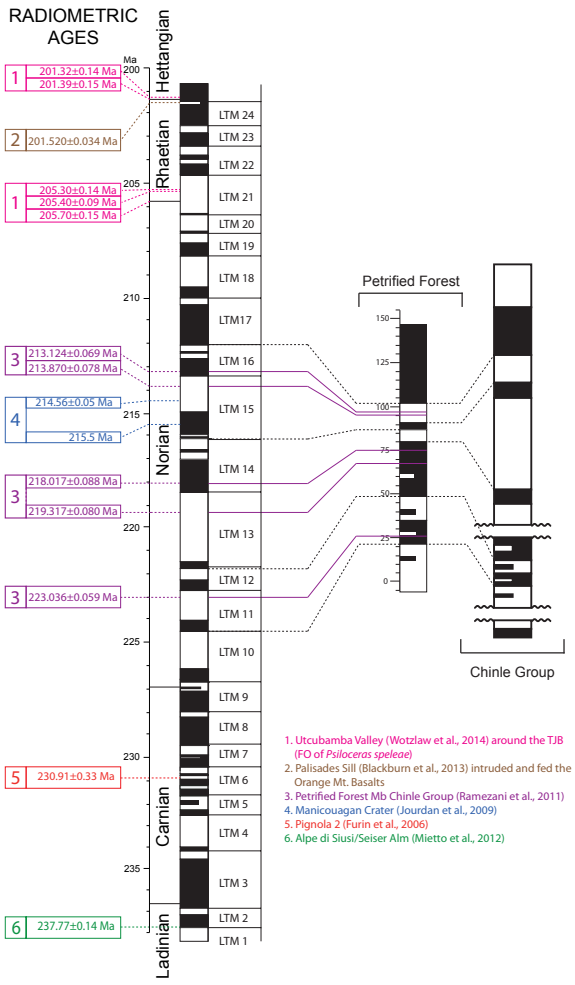

Figure 5.2: events with radiometric ages have been calibrated with the GPTS. The Chinle Group magnetostratigraphy have been compared to the GPTS through the radiometric ages of Ramezani et al. (2011) from the Petrified Forest.

age around the Ladinian/Carnian boundary of 237.77±0.14 Ma (Mietto et al., 2012). The 233-238 interval is thus represented by the sections of Bolücektasi Tepe, Mayerling and Prati di Stuores/ Stuores Wiesen (that includes the GSSP of the Carnian). The duration of the magnetozones of Bolücektasi Tepe was derived extending the duration/thickness ratio of magnetozone BT5n, tied to E2n of the APTS, to the other magnetozones, up to ca. 234.5 Ma. The duration of the magnetozones of Mayerling and Prati di Stuores has been calculated comparing the duration and thickness of the whole interval between the beginning of magnetozone MY5n.2n/S2n.2n and the radiometric age of 237.77±0.14 Ma, and then assigning duration to each magnetozone proportionally to its thickness.

Furthermore, magnetostratigraphic correlation between the Tethyan GPTS and the continental section of Chinle Group have been attempted using the radiometric ages of the Petrified Forest (Ramezani et al., 2011) (Fig. 5.2). The magnetostratigraphy of the Petrified Forest (Steiner and Lucas, 2000) is partially inconsistent with the GPTS and the APTS, as well as with coeval sections of the Chinle Group, in particular in the Sonsela Sandstone Mb (Zeigler and Geissmann, 2012; Lucas and Spielmann, 2013). In facts, the magnetostratigraphy of the Poleo Fm (Zeigler et al., 2005) shows a large interval of reversal polarity (~30 m) that is considered time equivalent with the less extended Sonsela Sandstone Mb (~5 m; Steiner and Lucas, 2000). Lucas and Spielmann (2013) propose a composite magnetostratigraphy of the Chinle Group, including the Petrified Forest and relative radiometric ages, which appear more coherent with the APTS and the GPTS. After these considerations,

the GPTS of the Tethys is confirmed also by sections of other realms, as the ones belonging to the Chinle Group.

The potential of the Late Triassic GPTS is to assign an age or a duration to each event calibrated with the magnetostratigraphy occurring in this time interval. Virtually, the events of every realm could be calibrated with the GPTS, using markers of global extension (i.e. fossil markers as radiolarians, geochemical curves or magnetostratigraphy itself). There are many advantages of the GPTS against the APTS, for instance the full Late Triassic coverage (from Ladinian/Carnian to Rhaetian/Hettangian) and the clear definition of the Stage boundaries. In facts, the GPTS includes the Ladinian/Carnian GSSP of Prati di Stuores/Stuores Wiesen (Mietto et al., 2012) that is the only ratified Stage boundary in the Late Triassic. Regarding the Carnian/Norian boundary, the Stage is placed with the FO of the conodont *Carnepigondolella gulloae* (Pizzo Mondello section), proposed as a primary biomarker for the Norian base (Mazza et al., 2012a). The Norian/Rhaetian boundary is proposed with a negative $\delta^{13}C_{org}$ spike (Maron et al., 2015; Rigo et al., 2015; Chapter 4.1.1) and approximated by the FAD of conodont *Misikella posthernsteini* (Pignola-Abriola section), proposed as one of the primary biomarkers for the Rhaetian Stage (i.e. Krystyn, 2010; Ogg, 2012). The Triassic/Jurassic

Table 5.1: Main Events

Event	Stage	Substage	Section	Age
LO of *Gladigondolella* spp.	Carnian	Julian	Pignola-2	~230.8 Ma
Carnian Pluvial Event	Carnian	Julian to Tuvalian	Pignola-2 Dibona	~229.7 Ma to ~230.7 Ma
FO of *Metapolygnathus communisti*	Norian	Lacian	Pizzo Mondello	~227.3 Ma
FO of *Epigondolella rigoi*	Norian	Lacian	Pizzo Mondello Silická Brezová	~227 Ma ~226.6 Ma
FO of *Carnepigondolella gulloae*	Norian	Lacian	Pizzo Mondello	~226.6 Ma
FO of *Mockina tozeri*	Norian	Alaunian	Pizzo Mondello	~221.5 Ma
FO of *Mockina bidentata*	Norian	Sevatian	Pignola-Abriola	~216.2 Ma
FO of *Misikella hernsteini*	Norian	Sevatian	Pignola-Abriola	~210.8 Ma
Proparvicingula moniliformis Zone	Norian	Sevatian	Pignola-Abriola	~206.2 Ma
FO of *Misikella posthernsteini*	Rhaetian	----------	Pignola-Abriola	~205.7 Ma
Negative $\delta^{13}C_{org}$ spike	Rhaetian	----------	Pignola-Abriola	~205.7 Ma
FO of *Misikella ultima*	Rhaetian	----------	Pignola-Abriola	~204.7 Ma

Table 5.1: Ages of the main Late Triassic events. Here are reported the events defining the Stage and substage boundaries, as well as the Carnian Pluvial Event, the largest climatic episode occurred in the Late Triassic before the End Triassic Extinction event.

boundary (TJB) is placed in the GPTS using the palynomorphs biostratigraphy of Brumano/Italcementi Quarry section (Muttoni et al., 2010), obtaining an age of about 201.3-201.4 Ma that is coherent with the radiometric age of TJB relative to the FO of ammonoid *Psiloceras spelae* (201.36±0.17 Ma; Wotzlaw et al., 2014) (Fig. 5.2). The age of substages is approximated by conodonts biostratigraphy in the considered sections. The Julian/Tuvalian boundary (Carnian) is placed with the LO of *Gladigondolella* spp. in the Pignola-2 section (Rigo et al., 2007), just below the "green clay-radiolaritic horizon", where the typical Tuvalian conodonts was found only above this horizon. The base of the Alaunian (Norian) can be placed with the FO of *Mockina tozeri* in Pizzo Mondello (Mazza et al., 2012a), and the Sevatian is normally defined by the FO of *Mockina bidentata* in Pignola-Abriola (Maron et al., 2015; Rigo et al., 2015). The ages of the events here reported are presented in Table 5.1.

Chapter VI
CONCLUSIONS

6.1 RHAETIAN

6.1.1 Pignola-Abriola (*from Maron et al., 2015: GSA Bulletin, v. 127, p. 962-974; see Attached publications*)

Paleomagnetic data obtained from the Pignola-Abriola section provided a sequence of 22 polarity reversals grouped in 10 magnetozones. The correlation between the Pignola-Abriola section and additional Norian and Rhaetian Tethyan marine sections from the literature (Steinbergkogel, Oyuklu, Brumano, Italcementi Quarry, and Pizzo Mondello) reveals significant internal consistency.

To provide numerical age constraints on the Pignola-Abriola section, I applied a statistical correlation to the Newark APTS, which is assumed to be continuous in its younger part (contra Lucas et al., 2012). Three out of a total of 19 explored correlation options produced statistically reliable results, and after a thorough analysis, one option (7.1) is considered as the most reliable. According to this option, the Pignola-Abriola section correlates to Newark magnetozones E13n to E20r. I place the Norian-Rhaetian boundary at Pignola-Abriola at a level coincident with a rapid decrease in $\delta^{13}C_{org}$ to ~–30‰, which virtually coincides with the level containing the FAD of conodont *Misikella posthernsteini* sensu stricto within the *Proparvicingula moniliformis* radiolarian zone. This level is traced within Newark magnetozone E20r at 205.7 Ma.

Assuming an age of ca. 201.3 Ma for the Triassic-Jurassic boundary (Schoene et al., 2010; Guex et al., 2012; Wotzlaw et al., 2014), our study shows that the Rhaetian is ~4.4 m.y. long. Assuming a Carnian-Norian boundary age of ca. 227 Ma (Muttoni et al., 2004, 2014, and references therein), our study shows that the Norian is ~21.3 m.y. long.

6.1.2 Mount Messapion

Paleomagnetic analysis of the Mt. Messapion sample provided only a very small number of reliable data. The resulting magnetostratigraphy consisting only of few data points, which made impossible to define clearly the magnetozones. The possibility of a bad-preserved signal was suggested by the extremely low

susceptibility, mostly negative, although the demagnetization path suggest that some kind of magnetization is retained by rock. Unfortunately, in the great part of the samples the directions are unusual, mirroring the typical directions of the southern hemisphere (whereas the site was in the northern hemisphere in the Late Triassic). Filtering the data for these strange directions, the final dataset resulted too small to attempt a magnetostratigraphy of this section.

6.1.3 Leg 122 – Hole 761C

The paleomagnetic analysis on the Hole 761C of the Wombat Plateau provided a sequence of 5 magnetozones, showing discontinuity because of the scarce recovery in some of the Cores. The magnetostratigraphy is constrained in the uppermost Norian to middle Rhaetian by calcareous nannofossils, ostracods, foraminifera, dynoflagellates and palynomorphs biostratigraphy. The correlation with the Norian/Rhaetian sections of Pignola-Abriola, Brumano/Italcementi Quarry and Steinbergkogel seems to confirm the partial magnetostratigraphy of Hole 761C, as well as a lack of sediments around the Norian/Rhaetian boundary. By a comparison with the Newark APTS the hiatus should be ~1.5 My. The Rhaetian strata in Hole 761C are in unconformity with overlying Lower Cretaceous (Berriasian/Valanginian) strata. The whole Jurassic and the upper Rhaetian is missed, probably by erosion or condensation/non-deposition (at least 1.5 My of missing Rhaetian, by comparison with the Newark APTS). Hence, at least ~57.5 My of Late Triassic/Jurassic sediments are missing in the Wombat Plateau.

6.2 CARNIAN

6.2.1 Pignola-2 and Dibona (*from Maron et al., submitted and in review, Newsletter on Stratigraphy; see Attached publications*)

The paleomagnetic analyses of the Carnian sections of Pignola-2 (Southern Apennines, Italy) and Dibona (Dolomites, Italy) provided respectively a sequence of 12 and 8 magnetozones.

The correlation with other Tethyan sections of the same time interval (Pizzo Mondello, Silická Brezová, Guri Zi) reveals a virtually continuous magnetostratigraphic record for the Carnian, constrained by a radiometric age of 230.91±0.33 Ma.

Using a statistical approach, I performed a correlation between the Pignola-2 section and the Newark APTS that led to three statistically relevant options. Only two of them (Options 1 and 2) appear to be broadly consistent with both the radiometric age

of the Pignola-2 ash-layer and their correlative ages in the Newark APTS. Although Option 2 was statistically slightly more robust, Option 1 is provisionally preferred as it shows the highest matching between radiometric and astrochonologic age estimates of the Pignola-2 ash-layer and does not violate the correlation between the Newark APTS and the Pizzo Mondello section as proposed by Muttoni et al (2004) using the same statistical method adopted in this study. Ages of the main events of the Pignola-2 and Dibona sections were calculated using a model derived from Option 1. The level containing the Julian/Tuvalian boundary defined by conodonts is now calibrated at ~230.7 Ma, and the levels attributed to the Carnian Pluvial Event should have deposited between ~229.7 and 230.7 Ma.

6.2.2 Leg 122 – Holes 759B and 760B

Paleomagnetic analysis of Holes 759B and 760B (Wombat Plateau) provided respectively a sequence of 5 and 2 magnetozones. Due to poor recovery and bad-preserved ChRM, magnetostratigraphy of the upper part of Hole 759B and middle part of Hole 760B is considered as unknown polarity. Calcareous nannofossils, palynomorphs, dinoflagellates and ostracods biostratigraphy constraint Holes 759B/760B into the Carnian to middle Norian. Although some parts of Holes 759B/760B magnetostratigraphy are missing or have a low resolution, it seems confirmed by the correlation with the Carnian/Norian sections of Pignola-2, Dibona, Silická Brezová, Pizzo Mondello and Guri Zi. The comparison with the Newark APTS, obtained through the correlations between the APTS and Pignola-2, Dibona, Pizzo Mondello and Silická Brezová sections (see Chapter 4.2.1 and references within), suggest that the stratigraphic record of Holes 759B/760B covers ~6 My, straddling the Carnian/Norian boundary.

6.3 LATE TRIASSIC GPTS

A composite magnetostratigraphy have been obtained combining the Late Triassic Tethyan marine sections of Pignola-Abriola (Norian/Rhaetian), Brumano/Italcementi Quarry (Rhaetian/Hettangian), Pizzo Mondello (Carnian/Norian), Silická Brezová (Carnian/Norian), Pignola-2 (Carnian), Dibona (Carnian), Guri Zi (Carnian), Bolücektasi Tepe (Carnian), Mayerling (Ladinian/Carnian), and Prati di Stuores/Stuores Wiesen (Ladinian/Carnian). Through the statistical correlation between the Newark APTS of Pizzo Mondello (Muttoni et al., 2004), Pignola-Abriola (Chapter 4.1.1; Maron et al., 2015), and Pignola-2/Dibona (Chapter 4.2.1),

the Tethyan magnetostratigraphic composite has been calibrated with the APTS, also using the radiometric age of 230.91±0.33 Ma from Pignola-2 (Aglianico ash-bed) as a tie point. The part of GPTS not covered by the Newark APTS, which is the portion of late Ladinian/early Carnian represented by lower Bolücektasi Tepe, Mayerling and Prati di Stuores/Stuores Wiesen magnetostratigraphy, is time-calibrated using the radiometric age of 237.77±0.14 Ma for the lattermost Ladinian (Mietto et al., 2012) as a tie-point. The time-calibration of the magnetozones in this interval is calculated assuming a mostly constant sedimentation rate within sections, using the thickness of the magnetozones as a proxy of their duration. The resulting sequence of magnetochrons of the GPTS have been named LTM 1 to LTM 25. Using the GPTS is possible to assign an age to the events occurring in the Late Triassic that are calibrated with magnetostratigraphy. Ages of key events have been reported as obtained from the GPTS.

REFERENCES

Ager, D.V., 1987. A defense of the Rhaetian Stage. *Albertiana*, v. 6, p. 4-13.

Amodeo, F., 1999. Il Triassico terminale-Giurassico del Bacino Lagonegrese. Studi stratigrafici sugli Scisti Silicei della Basilicata (Italia meridionale). *Mémoires de Géologie (Lausanne)*, v. 33, p. 121.

Argnani, A., 2005. Possible record of a Triassic ocean in the southern Apennines. *Bollettino della Società Geologica Italiana*, v. 124, p. 109–121.

Balini, M., Bertinelli, A., Di Stefano, P., Guaiumi, C., Levera, M., Mazza, M., Muttoni, G., Nicora, A., Preto, N., and Rigo, M., 2010. The Late Carnian-Rhaetian succession at Pizzo Mondello (Sicani Mountains). *Albertiana*, v. 39, p. 36-57.

Barattolo, F., and Romano, R., 2005. Some bioevents at the Triassic-Liassic boundary in the shallow water environment. *Bollettino della Società Geologica Italiana*, v. 124, p. 123-142.

Bazzucchi, P., Bertinelli, A., Ciarapica, G., Marcucci, M., Passeri, L., Rigo, M., and Roghi, G., 2005. The Late Triassic-Jurassic stratigraphic succession of Pignola (Lagonegro-Molise Basin, southern Apennines), Italy. *Bollettino Società Geologica Italiana*, v. 124, p. 143–153.

Bertinelli, A., Ciarapica, G., De Zanche, V., Marcucci, M., Passeri, L., Rigo, M., and Roghi, G., 2005. Stratigraphic evolution of the Triassic-Jurassic Sasso di Castalda succession (Lagonegro basin, southern Apennines, Italy). *Bollettino Società Geologica Italiana*, v. 124, p. 161–175.

Bittner, A., 1892. Was ist norisch? *Geologische Reichsanstalt Jahrbuch*, v. 42, p. 387-396.

Blackburn, T.J., Olsen, P.E., Bowring, S.A., McLean, N.M., Kent, D.V., Puffer, J., McHone, G., Rasbury, E.T., and Et-Touhami, M., 2013. Zircon U-Pb geochronology links the end-Triassic extinction with the Central Atlantic magmatic province. *Science*, v. 340, p. 941–945.

Bosellini, A., 1984. Progradation geometries of carbonate platforms: examples from the Triassic of the Dolomites, Northern Italy. *Sedimentology*, v. 32, p. 1–24.

Bosellini, A., and Hardie, L.A., 1988. Facies e cicli della Dolomia Principale delle Alpi Venete. *Memorie della Società Geologica Italiana*, v. 30, p. 245–266.

Bosellini, A., Gianolla, P., and Stefani, M., 2003. The Triassic carbonate platforms of the Dolomites (northern Italy): their evolution and stratigraphic framework. *Memorie di Scienze Geologiche*, v. 54, p. 111-114.

Bown, P.R., 1987. Taxonomy, biostratigraphy, and evolution of late Triassic-early Jurassic calcareous nannofossil. *Special Papers in Paleontology*, v. 38, p. 1-118.

Broglio Loriga, C., Cirilli, S., De Zanche, V., Di Bari, D., Gianolla, P., Laghi, G.F., Lowrie, W., Manfrin, S., Mastandrea, A., Mietto, P., Muttoni, G., Neri, C., Posenato, R., Reichichi, M., Rettori, R., and Roghi, G., 1999. The Prati di Stuores/Stuores Wiesen Section (Dolomites, Italy): a candidate Global Stratotype Section and Point for the base of the Carnian stage. *Rivista Italiana di Paleontologia e Stratigrafia*, v. 105, p. 37-78.

Bralower, T.J., Bown, P.R., and Siesser, W.G., 1992. Upper Triassic calcareous nannoplankton biostratigraphy, Wombat Plateau, Northwest Australia. *In* Von Rad, U., Haq, B.U., Kidd, R.B., O'Connell, S., eds.: *Proceedings of the Ocean Drilling Program, Scientific Results*, v. 122, p. 437-451.

Breda, A, and Preto, N., 2008. A continental/siliciclastic to shallow-marine/carbonate system in the Upper Triassic of Dolomites (Travenanzes Formation, N Italy). *Rendiconti della Società Geologica Italiana*, v. 2, p. 51–56.

Breda, A., and Preto, N., 2011. Anatomy of an Upper Triassic continental to marginal-marine system: the mixed siliciclastic-carbonate Travenanzes Formation (Dolomites, Northern Italy). *Sedimentology*, v. 58, p. 1613-1647.

Breda, A., Preto, N., Roghi, G., Furin, S., Meneguolo, R., Ragazzi, E., Fedele, P., and Gianolla, P., 2009. The Carnian Pluvial Event in the Tofane Area (Cortina d'Ampezzo, Dolomites, Italy). *Geo.Alp*, v. 6, p. 80-115

Brenner, W., 1992. First results of Late Triassic palynology of the Wombat Plateau, Northwestern Australia. *In* Von Rad, U., Haq, B.U., Kidd, R.B., O'Connell, S., eds.: *Proceedings of the Ocean Drilling Program, Scientific Results*, v. 122, p. 413-426.

Brenner, W., Bown, P.R., Bralower, T.J., Crasquin-Soleau, S., Dépêche, F., Dumont, T., Martini, R., Siesser, W.G., and Zaninetti, L., 1992. Correlation of Carnian to Rhaetian palynological, foraminiferal, calcareous nannofossil, and ostracode biostratigraphy, Wombat Plateau. *In* Von Rad, U., Haq, B.U., Kidd, R.B., O'Connell, S., eds.: *Proceedings of the Ocean Drilling Program, Scientific Results*, v. 122, p. 487-495.

Butler, R.F., 1992. Paleomagnetism: Magnetic Domains to Geologic Terranes. *Blackwell Scientific Publications, Boston*, p. 319.

Callegaro, S., Rigo, M., Chiaradia, M., and Marzoli, A., 2012. Latest Triassic marine Sr isotopic variations, possible causes and implications. *Terra Nova*,

v. 24, p. 130–135.

Carter, E.S., and Orchard, M.J., 2007. Radiolarian-Conodont-Ammonoid intercalibration around the Norian-Rhaetian boundary and implications for trans-Panthalassan correlation. *Albertiana*, v. 36, p. 149-163.

Castellarin, A., and Doglioni, C., 1985. A geologic schematic cross-section of the Southern Alps. *Rendiconti della Società Geologica Italiana*, v. 8, p. 35-36.

Castellarin, A., Selli, L., Picotti, V., and Cantelli, L., 1998. La tettonica delle Dolomiti nel quadro delle Alpi Meridionali orientali. *Memorie della Società Geologica Italiana*, v. 53, p. 133-143.

Catalano, R., Doglioni, C., and Merlini, S., 2001. On the Mesozoic Ionian Basin. *Geophysical Journal International*, v. 144, p. 49–64.

Celet, P., and Ferrière, J., 1978. Les Hellénides internes: Le Pélagonien. *Eclogae Geologicae Helvetiae*, v. 71, p. 467-495.

Celet, P., Clément, B and Ferrière, J., 1988. Evolution géodynamique de la plate-forme pélagonienne au Mésozoïque. *Bulletin of the Geological Society of Greece*, v. 20, p. 215-222.

Channell, J.E.T., Kozur, H.W., Sievers, T., Mock, R., Aubrecht, R., and Sykora, M., 2003. Carnian-Norian biomagnetostratigraphy at Silická Brezová (Slovakia): correlation to other Tethyan sections and to Newark Basin. *Palaeogeography, Palaeoclimatology, Palaeoecology*, v. 191, p. 65-109.

Ciarapica, G., and Passeri, L., 2002. The palaeogeographic duplicity of the Apennines. *Bollettino della Società Geologica Italiana*, v. 121, no. 1, p. 67-75.

Ciarapica, G., and Passeri, L., 2005. Ionian Tethydes in the Southern Apennines. *In* Finetti I.R., ed.: Crop Project: Deep Seismic Exploration of the Central Mediterranean and Italy. *Elsevier, Amsterdam*, p. 209-224.

Cirilli, S., 2010. Upper Triassic-lowermost Jurassic palynology and palynostratigraphy: a review. *In* Lucas, S.G., ed.: The Triassic Timescale. *Geological Society, London, Special Publications*, v. 334, p. 285-314.

Cohen, A.S., and Coe, A.L., 2007. The impact of the Central Atlantic magmatic province on climate and on the Sr- and Os-isotope evolution of seawater. *Palaeogeography, Palaeoclimatology, Palaeoecology*, v. 244, p. 374–390.

Coplen, T.B., Brand, W.A., Gehre, M., Gröning, M., Meijer, H.A.J., Toman, B., and Verkouteren, R.M., 2006. New guidelines for $\delta^{13}C$ measures. *Analytical Chemistry*, v. 78, p. 2439–2441.

Cornet, B., 1977. The palynostratigraphy and age of the Newark Supergroup. *Ph.D.*

thesis, University Park, Pennsylvania, Pennsylvania State University, p. 504.

Cornet, B., 1993. Applications and limitations of palynology in age, climatic, and paleoenvironmental analyses of Triassic sequences in North America. *In* Lucas, S.G., and Morales, M., eds.: The nonmarine Triassic. *New Mexico Museum of Natural History and Science Bulletin*, v. 3, p. 75–93.

Cornet, B., and Olsen, P.E., 1985. A summary of the biostratigraphy of the Newark Supergroup of eastern North America with comments on Early Mesozoic provinciality. *III Congresso Latinoamericano de Paleontologia, Mexico, Simposio sobre floras del Triasico Tardio, su Fitogeografia y Paleoecologia, Memoria*, p. 67-81.

Courtillot, V., and Renne, P., 2003. On the ages of flood basalt event. *Comptes Rendus Geoscience*, v. 335, p. 113-140.

Dal Corso, J., Mietto, P., Newton, R.J., Pancost, R.D., Preto, N., Roghi, G., and Wignall, P.B., 2012. Discovery of a major negative $\delta^{13}C$ spike in the Carnian (Late Triassic) linked to eruption of Wrangellia flood basalts. *Geology*, v. 40, p. 79-82.

De Bono, A., Martini, R., Zaninetti, L., Hirsch, F., Stampfli, G.M., and Vavassis, I., 2001. Permo-Triassic stratigraphy of the pelagonian zone in central Evia island (Greece). *Eclogae Geologicae Helvetiae*, v. 94, p. 289-311.

De Castro, P., 1991. Mesozoic. *In* Barattolo, F., De Castro, P., and Parente, M., eds.: 5th International Symposium on Fossil Algae - Field Trip Guide Book. *Giannini, Napoli*, p. 21-38.

De Wever, P., and Miconnet, P., 1985. Datations directes des radiolarites du bassin de Lagonegro (Lucanie, Italie méridionale). Implications et consequences. *Revista Española de Micropaleontologia*, v. 17, p. 373-402.

De Zanche, V., Gianolla, P., Mietto, P., Siorpaes, and C. Vail, P.R., 1993. Triassic sequence stratigraphy in the Dolomites (Italy). *Memorie di Scienze Geologiche*, v. 45, p. 1–27.

De Zanche, V., Gianolla, P., and Roghi, G., 2000. Carnian stratigraphy in the Raibl/ Cave del Predil area (Julian Alps, Italy). *Eclogae Geologicae Helvetiae*, v. 93, p. 331-347.

Deenen, M.H.L., 2010. A new chronology for the Late Triassic to Early Jurassic. *Geologica Utraiectina*, v. 323, p. 216.

Deenen, M.H.L., Ruhl, M., Bonis, N.R., Krijgsman, W., Kuerschner, W.M., Reitsma, M., and van Bergen, M.J., 2010. A new chronology for the end-Triassic

mass extinction. *Earth and Planetary Science Letters*, v. 291, p. 113-125.

Dépêche, F., and Crasquin-Soleau, S., 1992. Triassic marine ostracodes of the Australian margin (Holes 759B, 760B, 761C, 764A, 764B). *In* Von Rad, U., Haq, B.U., Kidd, R.B., O'Connell, S., eds.: *Proceedings of the Ocean Drilling Program, Scientific Results*, v. 122, p. 453-462.

Dercourt, J., Ricou, L.E., and Vrielynck, B., 1993. Atlas Tethys Palaeoenvironmental Maps. Explanatory Notes. *Gauthier-Villars, Paris*, p. 307.

Di Nocera, S., and Scandone, P., 1977. Triassic nannoplankton limestones of deep basin origin in the Central Mediterranean region. *Palaeogeography, Palaeoclimatology, Palaeoecology*, v. 21, p. 101-111.

Diakow, L., Orchard, M.J., and Friedman, R., 2011. Absolute ages for the Norian Stage: A contribution from southern British Columbia, Canada. *21st Canadian Paleontological Conference, Vancouver, Canada, August 19-22, 2011*.

Doglioni, C., 1987. Tectonics of the Dolomites (Southern Alps-Northern Italy). *Journal of Structural Geology*, v. 9, p. 181-193.

Epstein, A.G., Epstein, J.B., and Harris, L.D., 1977. Conodont Color Alteration: An Index to Organic Metamorphism. *US Geological Survey Professional Paper*, v. 995, p. 1–27.

Finetti, I.R., 1982. Structure, stratigraphy and evolution of central Mediterranean. *Bollettino di Geofisica Teorica e Applicata*, v. 24, p. 247–315.

Finetti, I.R., 2005. CROP Project, Deep Seismic Exploration of the Central Mediterranean and Italy. *Elsevier, Amsterdam*, v. 1, p. 794.

Fowell, S.J., and Olsen, P.E., 1993. Time calibration of Triassic/Jurassic microfloral turnover, eastern North America. *Tectonophysics*, v. 222, p. 361 - 369.

Fowell, S.J., Cornet, B., and Olsen, P.E., 1994. Geologically rapid Late Triassic extinctions: Palynological evidence from the Newark Supergroup. *In* Klein, G.D., ed.: Pangea: paleoclimate, tectonics, and sedimentation during accretion, zenith and breakup of a supercontinent. *Geological Society of America Special Paper*, v. 228, p. 197-206.

Furin, S., Preto, N., Rigo, M., Roghi, G., Gianolla, P., Crowley, J.L., and Bowring, S.A., 2006. High-precision U-Pb zircon age from the Triassic of Italy: Implications for the Triassic time scale and the Carnian origin of calcareous nannoplankton and dinosaurs. *Geology*, v. 34, p 1009-1012.

Gallet, Y., Besse, J., Krystyn, L., Marcoux, J., and Théveniaut, H., 1992. Magnetostratigraphy of the late Triassic Bolücektasi Tepe section

(southwestern Turkey): implications for changes in magnetic reversal frequency. *Physics of Earth and Planetary Interior*, v. 73, p. 85-108.

Gallet, T., Besse, J., Krystyn, L., Théveniaut, H., and Marcoux, J., 1993. Magnetostratigraphy of the Kavur Tepe section (south western Turkey): a magnetic polarity time scale for the Norian. *Earth and Planetary Science Letters*, v, 117, p. 443–456.

Gallet, Y., Besse, J., Krystyn, L., Théveniaut, H., and Marcoux, J., 1994. Magnetostratigraphy of the Mayerling section (Austria) and Erenkolu Mezarlik (Turkey) section: Improvement of the Carnian (late Triassic) magnetic polarity time scale. *Earth and Planetary Science Letters*, v. 125, p. 173-191.

Gallet, T., Besse, J., Krystyn, L., and Marcoux, J., 1996. Norian magnetostratigraphy from the Scheiblkogel section, Austria: constraints on the origin of the Antalya Nappes, Turkey. *Earth and Planetary Science Letters*, v. 140, p. 113–122.

Gallet, Y., Besse, J., Krystyn, L., Marcoux, J., Guex, J., and Théveniaut, H., 2000. Magnetostratigraphy of the Kavaalani section (southwestern Turkey): consequences for the origin of the Antalya Calcareous Nappes (Turkey) and for the Norian (Late Triassic) magnetic polarity timescale. *Geophysical Research Letters*, v, 27, p. 2033–2036.

Gallet, Y., Krystyn, L., Besse, J., and Marcoux, J., 2003. Improving the Upper Triassic numerical timescale from cross-correlation between Tethyan marine sections and the continental Newark Basin sequence. *Earth and Planetary Science Letters*, v. 212, p. 255–261.

Gallet, Y., Krystyn, L., Marcoux, J., and Besse, J., 2007. New constraints on the End-Triassic (Upper Norian-Rhaetian) magnetostratigraphy. *Earth and Planetary Science Letters*, v. 225, p. 458-470.

Gazdzicki, A., 1983. Foraminifers and biostratigraphy of Upper Triassic and Lower Jurassic of the Slovakian and Polish Carpathian. *Acta Palaeontologica Polonica*, v. 44, p. 109-169.

Gazdzicki, A., Kozur, H., and Mock, R., 1979. The Norian-Rhaetian boundary in the light of micropaleontological data. *Geologija*, v. 22, p. 71-112.

Gattolin, G., Breda, A., and Preto. N., 2013. Demise of Late Triassic carbonate platforms triggered the onset of a tide-dominated depositional system in the Dolomites, Northern Italy. *Sedimentary Geology*, v. 297, p. 38-49.

Gattolin, G., Preto, N., Breda, A., Franceschi, M., Isotton, M., and Gianolla, P.,

2015. Sequence Stratigraphy after the demise of a high-relief carbonate platform (Carnian of the Dolomites): sea-level and climate disentangled. *Palaeogeography, Palaeoclimatology, Palaeoecology*, v. 423, p. 1-17.

Gianolla, P., De Zanche, V., and Mietto, P., 1998a. Triassic sequence stratigraphy in the Southern Alps (northern Italy): definition of sequences and basin evolution. *In* de Graciansky, P.-C., Hardenbol, J., Jacquin, T., and Vail, P.R., eds.: Mesozoic and Cenozoic sequence stratigraphy of European basins. *SEPM Special Publications*, v. 60, p. 719-747

Gianolla, P., Ragazzi, E., and Roghi, G., 1998b. Upper Triassic amber from the Dolomites (Northern Italy). A paleoclimatic indicator? *Rivista Italiana di Paleontologia e Stratigrafia*, v. 104, p. 381-39.

Gianolla, P., Micheletti, C., Panizza, M., and Viola, F., 2008. Nomination of the Dolomites for Inscription on the World Natural Heritage List Unesco. *Artimedia, Trento*, p. 367.

Giordano, N., Rigo, M., Ciarapica, G., and Bertinelli, A., 2010. New biostratigrphical constraints for the Norian/Rhaetian boundary: data from Lagonegro Basin, Southern Apennines, Italy. *Lethaia*, v. 43, p. 573-586.

Giordano, N., Ciarapica, G., Bertinelli, A., and Rigo, M., 2011. The Norian-Rhaetian interval in two sections of the Lagonegro area: the transition from carbonate to siliceous deposition. *Italian Journal of Geosciences*, v. 130, p. 380-393.

Gradstein, F.M., Ogg, J.G., Schmitz, M., and Ogg, G., 2012. The Geologic Time Scale 2012. *Elsevier, Amsterdam*, p. 1142.

Greene, A.R., Scoates, J.S., Weis, D., Katvala, E.C., Israel, S., and Nixon, G.T., 2010. The architecture of oceanic plateaus revealed by the volcanic stratigraphy of the accreted Wrangellia oceanic plateau. *Geosphere*, v. 6, p. 47-73.

Grommé, C.S., Wright, T.L., and Peck, D.L., 1969. Magnetic Properties and Oxidation of Iron-Titanium Oxide Minerals in Alae and Makaopuhi Lava Lakes, Hawaii. *Journal of Geophysical Research*, v. 74, p. 5277-5293.

Guex, J., Bartolini, A., Atudorei, V., and Taylor, D., 2004. High-resolution ammonite and carbon isotope stratigraphy across the Triassic-Jurassic boundary at New York Canyon (Nevada). *Earth and Planetary Science Letters*, v. 225, p. 29-41.

Guex, J., Schoene, B., Bartolini, A., Spangenberg, J., Schaltegger, U., O'Dogherty, L., Taylor, D., Bucher, H., and Atudorei, V., 2012,. Geochronological constraints on post-extinction recovery of the ammonoids and carbon cycle perturbations during the Early Jurassic. *Palaeogeography,*

Palaeoclimatology, Palaeoecology, v. 346–347, p. 1–11.

Gümbel, C.W.v., 1859. Über die Gleichstellung der Gesteinsmachen in den nordöstlichen Alpen mit außeralpinen Flötzschichten. *Verhandlungen der Gesellschaft Deutscher Naturforscher und Ärtze*, v. 54, p. 80-88.

Haq, B.U., von Rad, U., O'Connell, S., et al., 1990. Proceedings of the Ocean Drilling Program, Initial Reports. *College Station, Texas (Ocean Drilling Program)*, v. 122.

Hardenbol, J., Thierry, J., Farley, M.B., Jacquin, T., de Graciansky, P.-C., and Vail, P.R., 1998. Mesozoic and Cenozoic sequence chronostratigraphic framework of European basins. *In* de Graciansky, P.-C., Hardenbol, J., Jacquin , T., and Vail, P.R., eds.: Mesozoic-Cenozoic Sequence Stratigraphy of European Basins. *SEPM Special Publication*, v. 60, p. 3-13, 763-781.

Helby, R., Morgan, R., and Partridge, A.D., 1987. A palynological zonation of the Australian Mesozoic. *In* Jell, P.A., ed.: Studies in Australian Mesozoic Palinology. *Memoirs of the Association of the Australasian Paleontologists*, v. 4, p. 1-94.

Hillebrandt, A.v., Krystyn, L., Kürschner, W.M., Bonis, N.R., Ruhl, M., Richoz, S., Schobben, M.A.N., Urlichs, M., Bown, P.R., Kment, K., McRoberts, C.A., Simms, M., and Tomasovych, A., 2013. The Global Stratotype Sections and Point (GSSP) for the base of the Jurassic System at Kuhjoch (Karwendel Mountains, Northern Calcareous Alps, Tyrol, Austria). *Episodes – Newsmagazine of the International Union of Geological Sciences*, v. 36, p. 162-198.

Hochuli, P.A., and Vigran, J.O., 2010. Climate variations in the Boreal Triassic – Inferred from palynological records from the Barents Sea. *Palaeogeography, Palaeoclimatology, Palaeoecology*, v. 290, p. 20–42.

Hochuli, P.A., Colin, J.P., and Vigran, J.O., 1989. Triassic biostratigraphy of the Barents Sea area. *In* Collinson, J.D., ed.: Correlation in Hydrocarbon Exploration. *Springer, Netherlands*, p. 131–153.

Hoffman, V.H., Hochleitner, R., Torii, M., Funaki, M., Mikouchi, T., Kaliwoda, M., Jenniskens, P., and Shaddad, M.H., 2011. Magnetism and mineralogy of Almahata Sitta polymictic ureilite (= asteroid 2008 TC_3): Implications for the ureilite parent body magnetic field. *Meteoritics and Planetary Science*, v. 46, p. 1551-1564.

Hounslow, M.W., and Muttoni, G., 2010. The geomagnetic polarity timescale for the Triassic: linkage to stage boundary definitions. *In* Lucas, S.G., ed.: The

Triassic Timescale. *Geological Society, London, Special Publications*, v. 334, p. 61-102.

Hounslow, M.W., Posen, P.E., and Warrington, G., 2004. Magnetostratigraphy and biostratigraphy of the Upper Triassic and lowermost Jurassic succession, St. Audrie's Bay, UK. *Palaeogeography, Palaeoclimatology, Palaeoecology*, v. 213, p. 331-358.

Hüsing, S.K., Deenen, M.H.L., Koopmans, J.G., and Krijgsman, W., 2011. Magnetostratigraphic dating of the proposed Rhaetian GSSP at Steinbergkogel (Upper Triassic, Austria): Implications for the Late Triassic time scale. *Earth and Planetary Science Letters*, v. 302, p, 203-216.

Jafar, A.S., 1983. Significance of Late Triassic calcareous nannoplankton from Austria to Southern Germany. *Neues Jahrbuch für Geologie und Paläontologie Abhandlungen*, v. 166, p. 218-259.

Jourdan, F., Renne, P.R., and Reimold, W.U., 2009. An appraisal of the ages of terrestrial impact structures. *Earth and Planetary Science Letters*, v. 286, p. 1-13.

Keim, L., Spötl, C., and Brandner, R., 2006. The aftermath of the Carnian carbonate platform demise: a basinal perspective (Dolomites, Southern Alps). *Sedimentology*, v. 53, p. 361–386.

Kent, D.V., and Olsen, P.E., 1999. Astronomically tuned geomagnetic polarity time scale for the Late Triassic. *Journal of Geophysical Research*, v. 104, p. 12831–12841.

Kent, D.V., Olsen, P.E., and Witte, W.K., 1995. Late Triassic-earliest Jurassic geomagnetic polarity sequence and paleolatitudes from drill cores in the Newark rift basin, eastern North America. *Journal of Geophysical Research*, v. 100, p. 14965-14998.

Khramov, A.N., 1963. Paleomagnetic study of Upper Permian and Lower Triassic sections in the north and east of Russian platform. *In* Khramov, A.N., ed.: Paleomangetic Stratigraphic Investigations. *Gostoptechizdat Press, Leningrad*, p. 145-174.

Köppen, A., 1997. Faziesentwicklung in der frühen Obertrias Mitteleuropas – ein sequenzstratigraphischer Vergleich. *Gaea Heidelbergensis*, v. 2, p. 1-233.

Kozur, H., 1973. Beitrage zur Stratigraphie von Perm und Trias. *Geologisch-Paläontologische Mitteilungen*, v. 3, p. 1-31.

Kozur, H., 2003. Integrated Permian ammonoid, conodont and radiolarian zonation of the Triassic. *Hallesches Jahrbuch für Geowissenschaften*, v. 25, p. 49–79.

Kozur, H., and Mock, R., 1974. Misikella posthernsteini n. sp., die jüngste Conodontenart der tethyalen Trias. *Càsopis pro Mineralogii a Geologii*, v. 19, p. 245-250.

Kozur, H., and Mock, R., 1991. New middle Carnian and Rhaetian conodonts from Hungary and the Alps. Stratigraphic importance and tectonic implications for the Buda Mountains and adjacent areas. *Jahrbuch der Geologischen Bundesanstalt*, v. 134, p. 271–297.

Kozur, H., and Weems, R.E., 2005. Conchostracan evidence for a late Rhaetian to early Hettangian age for the CAMP volcanic event in the Newark Supergroup, and a Sevatian (late Norian) age for the immediately underlying beds. *Hallesches Jahrbuch Geowissenschaft*, v. 27, p. 21-51.

Kozur, H., and Weems, R.E., 2007. Upper Triassic conchostracan biostratigraphy of the continental rift basins of eastern North America: its importance for correlating Newark Supergroup events with the Germanic basin and the international geologic time-scale. *New Mexico Museum for Natural History and Science Bulletin*, v. 41, p. 137-188.

Kozur, H., and Bachmann, G.H., 2010. The Middle Carnian Wet Intermezzo of the Stuttgart Formation (Schilfsandstein), Germanic Basin. *In* Kustatscher, E., Preto, N., and Wignall, P., eds.: Triassic Climates. *Palaeogeography, Palaeoclimatology, Palaeoecology*, v. 290, p. 107-119.

Kozur H., and Weems R.E., 2010. The biostratigraphic importance of conchostracans in the continental Triassic of the northern hemisphere. *In* Lucas, S.G., ed.: The Triassic Timescale. *Geological Society, London, Special Publications*, v. 334, p. 315-417.

Kraus, O., 1969. Die Raibler Schichten des Drauzunges (Südliche Kalk-alpen). Lithofazielle, sedimentpetrographische un paläogeographische Untersuchungen. *Jahrbuch der Geologischen Bundesanstalt*, v. 112, p. 81-152.

Kruiver, P.P., Dekkers, M.J., and Heslop, D., 2001. Quantification of the magnetic coercivity by the analysis of acquisition curves of isothermal remanent magnetization. *Earth and Planetary Science Letters*, v. 189, p. 269-276.

Krystyn, L., 1980. Stratigraphy of the Hallstatt region. Guidebook, Abstracts, Second European Conodont Symposium-ECOS II. *Abhandlungen der Geologischen Bundesanstalt*, v. 35, p. 69–98.

Krystyn, L., 1990. A Rhaetian stage-chronostratigraphy, subdivision and their intercontinental correlation. *Albertiana*, v. 8, p. 15–24.

Krystyn, L., 2010. Decision report on the defining event for the base of the Rhaetian stage. *Albertiana*, v. 38, p. 11–12.

Krystyn, L., Gallet, Y., Besse, J., and Marcoux, J., 2002. Integrated Upper Carnian to Lower Norian biochronology and implications for the Upper Triassic magnetic polarity time scale. *Earth and Planetary Science Letters*, v. 203, p. 343–351.

Krystyn, L., Bouquerel, H., Kürschner, W., Richoz, S., and Gallet, Y., 2007a. Proposal for a candidate GSSP for the base of the Rhaetian Stage. *In* Lucas, S.G., and Spielman, J.A., eds.: The Global Triassic. *New Mexico Museum of Natural History and Science Bulletin*, v. 41, p. 189-199.

Krystyn, L., Richoz, S., Gallet, Y., Bouquerel, H., Kürschner, W.M., and Spötl, C., 2007b. Updated bio- and magnetostratigraphy from Steinbergkogel (Austria), candidate GSSP for the base of the Rhaetian stage. *Albertiana*, v. 36, p. 164-172.

Kuroda, J., Hori, R.S., Suzuki, K., Grocke, D.R., and Ohkouchi, N., 2010. Marine osmium isotope record across the Triassic-Jurassic boundary from a Pacific pelagic site. *Geology*, v. 38, p. 1095–1098.

Lavallée, Y., Wadsworth, F.B., Vasseur, J., Russell, J.K., Andrews, G.D.M., Hess, K.U., von Aulock, F.W., Kendrick, J.E., Tuffen, H., Biggin, A.J., and Dingwell, D.B., 2015. Eruption and emplacement timescales of ignimbrite super-eruptions from thermo-kinetics of glass shards. *Frontiers in Earth Science*, v. 3, A. 2, p. 1-10.

Leonardi, P., 1968. Le Dolomiti. Geologia dei Monti dall'Isarco al Piave. *Manfrini, Rovereto*, p. 1019.

Lowrie, W., 1990. Identification of ferromagnetic minerals in a rock by coercivity and unblocking temperature properties. *Geophysical Research Letters*, v. 17, p. 159-162.

Lucas, S.G., and Huber, P., 1993. Revised internal correlation of the Newark Supergroup Triassic, eastern United States and Canada. *In* Lucas, S.G., and Morales, M., eds.: The Non-Marine Triassic. *New Mexico Museum of Natural History and Science Bulletin*, v. 3, p. 311–319.

Lucas, S.G., and Spielmann, J.A., 2013. Magnetostratigraphy of the Upper Triassic Chinle Group in New Mexico: an appraisal of 40 years of analysis. *In* Tanner, L.H., Spielmann, J.A., and Lucas, S.G., eds.: The Triassic System. *New Mexico Museum of Natural History and Science Bulletin*, v. 61, p. 375-381.

Lucas, S.G., Tanner, L.H., Kozur, H.W., Weems, R.E., and Heckert, A.B., 2012. The Late Triassic timescale: Age and correlation of the Carnian-Norian boundary. *Earth-Science Reviews*, v. 114, p. 1-18.

Marsella, E., 1988. Un modello deposizionale per i terreni triassico-giurassici nel lagonegrese a nord della congiungente Villa d'Agri-Paterno. *Atti del 74° Congresso Nazionale della Società Geologica Italiana*, sec. A, p. 375-382.

Maron, M., Rigo, M., Bertinelli, A., Katz, M.E., Godfrey, L., Zaffani, M., and Muttoni, G., 2015. Magnetostratigraphy, biostratigraphy and chemostratigraphy of the Pignola-Abriola section: New constraints for the Norian-Rhaetian boundary. *Geological Society of America Bulletin*, v. 127, p. 962-974.

Marzoli, A., Renne, P.R., Piccirillo, E.M., Ernesto, M., Bellieni, G., and De Min, A., 1999. Extensive 200-Million-Year-Old Continental Flood Basalts of the Central Flood Basalts of the Central Atlantic Magmatic Province. *Science*, v. 284, p. 616-618.

Marzoli, A., Bertrand, H., Knight, K.B., Cirilli, S., Buratti, N., Vérati, C., Nomade, S., Renne, P.R., Youbi, N., Martini, R., Allenbach, K., Neuwerth, R., Rapaille, C., Zaninetti, L., and Bellieni, G., 2004. Synchrony of the Central Atlantic magmatic province and the Triassic-Jurassic boundary climatic and biotic crisis. *Geology*, v. 32, p. 973-976.

Marzoli, A., Jourdan, F., Puffer, J.H., Cuppone, T., Tanner, L.H., Weems, R.E., Bertrand, H., Cirilli, S., Bellieni, G., and De Min, A., 2011. Timing and duration of the Central Atlantic magmatic province in the Newark and Culpeper Basin, eastern U.S.. *Lithos*, v. 122, p. 175–188.

Mazza, M., Furin, S., Spötl, C., and Rigo, M., 2010. Generic turnovers of Carnian/Norian conodonts: Climatic control or competition?. *In* Kustatscher, E., Preto, N., and Wignall, P., eds.: Triassic Climates. *Palaeogeography, Palaeoclimatology, Palaeoecology*, v. 290, p. 120-137.

Mazza, M., Rigo, M., and Nicora, A., 2011. A new Metapolygnathus platform conodont species and its implications for Upper Carnian global correlations. *Acta Palaeontologica Polonica*, v. 56, p. 121-131.

Mazza, M., Rigo, M., and Gullo, M., 2012a. Taxonomy and biostratigraphic record of the Upper Triassic conodonts of the Pizzo Mondello section (western Sicily, Italy), GSSP candidate for the base of the Norian. *Rivista Italiana di Paleontologia e Stratigrafica*, v. 118, n. 1, p. 85-130.

Mazza, M., Cau, A., and Rigo, M., 2012b. Application of numerical cladistic analyses to the Carnian–Norian conodonts: a new approach for phylogenetic

interpretations. *Journal of Systematic Palaeontology*, v. 10, p. 401-422.

McElhinny, M.W., and Burek, P.J., 1971. Mesozoic palaeomagnetic stratigraphy. *Nature*, v. 232, p. 98-102.

McFadden, P.L., and McElhinny, M.W., 1990. Classification of the reversal test in palaeomagnetism. *Geophysical Journal International*, v. 103, p. 725–729.

McFadden, P.L., and Reid, A.B., 1982. Analysis of paleomagnetic inclination data. *Geophysical Journal of the Royal Astronomical Society*, v. 69, p. 307-319.

McLaughlin, D.B., 1933. A note on the stratigraphy of the Brunswick Formation (Newark) in Pennsylvania. *Michigan Academy of Science, Arts, and Letters*, v. 18, p. 59–74.

McRoberts, C.A., 2007. The halobid bivalve succession across a potential Carnian/Norian GSSP at Black Bear Ridge, Williston Lake, northeast British Columbia, Canada. *Albertiana*, v. 36, p. 142-145.

McRoberts, C.A., Krystyn, L., and Shea, A., 2008. Rhaetian (Late Triassic) *Monotis* (Bivalvia: Pectinoida) from the eastern Northern Calcareous Alps (Austria) and the end-Norian crisis in pelagic faunas. *Palaeontology*, v. 51, p. 721-735.

Miconnet, P., 1983. La région de Lagonegro (Italie méridionale): évolution géologique d'un bassin dans son cadre alpin. *PhD Thesis, III cycle, Université des Sciences et Techniques de Lille*, p. 185.

Mietto, P., and Panzanelli Fratoni, R., 1990. Conodonts from the Monte Facito Formation and from the base of the Monte Sirino Formation (Lagonegro sequence). *Bollettino della Società Geologica Italiana*, v. 109, no. 1, p. 165-169.

Mietto, P., and Manfrin, S., 1999. A debate on the Ladinian-Carnian boundary. *Albertiana*, v. 22, p. 23-27.

Mietto, P., Manfrin, S., Preto, N., Rigo, M., Roghi, G., Furin, S., Gianolla, P., Posenato, R., Muttoni, G., Nicora, A., Buratti, N., Cirilli, S., Spötl, C., Ramezani, J., and Bowring, S.A., 2012. The Global Boundary Stratotype Section and Point (GSSP) of the Carnian Stage (Late Triassic) at Prati di Stuores/Stuores Wiesen Section (Southern Alps, NE Italy). *Episodes – Newsmagazine of the International Union of Geological Sciences*, v. 35, p. 414-430.

Moix, P., Kozur, H.W., Stampfli, G.M., and Mostler, H., 2007. New paleontological, biostratigraphical and paleogeographic results from the Triassic of the Mersin Mélange, SE Turkey. *In* Lucas, S.G., and Spielmann, J.A., eds.:

The Global Triassic. *New Mexico Museum of Natural History and Science Bulletin*, v. 41, p. 282-311.

Mojsisovics, E., 1869. Über die Gliederung der oberen Triasbildungen der östlichen Alpen. *Jahrbuch Geologischen Reichsanstalt*, v. 19, p. 91-150.

Mojsisovics, E., 1892. Die Hallstatter Entwicklunung der Trias. *Sitzungsberichte Akademie Wissenschaften Wien*, v. 101, p. 769-780.

Mojsisovics, E., Waagen, W.v., and Diener, C., 1895. Entwurf einer Gliederung der pelagischen Sedimente des Trias-Systems. *Sitzunberichte Akademie Wissenschaften Wien*, v. 104, p. 1271-1302.

Molostovsky, E.A., Pevzner, M.A., and Pechersky, D.M., 1976. Phanerozoic magnetostratigraphic scale and regime of magnetic field reversals. *In* Geomagnetic Investigations. *Radio i Svyaz', Moscow*, p. 45-52.

Mørk, A., Vigran, J.O., Korchinskaya, M.V., Pchelina, T.M., Fefilova, L.A., Vavilov, M.N., and Weitschat, W., 1992. Triassic rocks in Svalbard, the Arctic Soviet islands and the Barents Shelf: Bearing on their correlations. *In* Vorren, T.O., Bergsager, E., Dahl-Stamnes, O.A., Holter, B., Johansen, B., Lie, E., and Lund, T.B., eds.: Arctic geology and petroleum potential. *Norwegian Petroleum Society, Special Publication*, v. 2, p. 457–79.

Mortensen, J.K., and Hulbert, L.J., 1992. A U-Pb zircon age for a Maple Creek gabbro sill, Tatamagouche Creek area, southwestern Yukon Territory, in Radiogenic age and isotopic studies: Report 5. *Geological Survey of Canada Paper*, v. 91, p. 175–179.

Morton, N., and Hesselbo, S., 2008. Details of voting on proposed GSSP and ASSP for the base of the Hettangian Stage and Jurassic System. *International Subcommission on Jurassic Stratigraphy Newsletter*, v. 35, p. 76.

Mostardini, F., and Merlini, S., 1986. Appennino centro-meridionale. Sezioni geologiche e proposta di modello strutturale. *Memorie della Società Geologica Italiana*, v. 35, p. 177-202.

Mostler, H., Scheuring, B., and Urlihs, M., 1978. Zur Mega-Mikrofauna und Mikroflora der Kössener Schichten (alpine Obertrias) vom Weissloferbach in Tirol unter besonderer Berücksichtigung der in der suessi- und marshi-Zone auftretenden Conodonten. *Schriftenreihe der Erdwissenschaftlichen Kommissionen*, v. 4, p. 141–174.

Mullender, T.A.T., van Velzen, A.J., and Dekkers, M.J., 1993. Continuous drift correction and separate identification of ferrimagnetic and paramagnetic contributions in thermomagnetic runs. *Geophysical Journal International*,

v. 114, p. 663-672.

Mundil, R., Pálfy, J., Renne, P.R., and Brack, P., 2010. The Triassic time scale: New constraints and a review of geochronological data. *In* Lucas, S.G., ed.: The Triassic Timescale. *Geological Society, London, Special Publications*, v. 334, p. 41–60.

Muttoni, G., Kent, D.V., Di Stefano, P., Gullo, M., Nicora, A., Tait, J., and Lowrie, W., 2001. Magnetostratigraphy and biostratigraphy of the Carnian/Norian boundary interval from the Pizzo Mondello section (Sicani Mountains, Sicily). *Palaeogeography, Palaeoclimatology, Palaeoecology*, v. 166, p. 383-399.

Muttoni, G., Kent, D.V., Olsen, P.E., Di Stefano, P., Lowrie, W., Bernasconi, S.M., and Hernandez, F.M., 2004. Tethyan magnetostratigraphy from Pizzo Mondello (Sicily) and correlation to the Late Triassic Newark astrochronological polarity time scale. *Geological Society of America Bulletin*, v. 116, p. 1043-1058.

Muttoni. G., Meço, S., and Gaetani, M., 2005. Magnetostratigraphy and biostratigraphy of the Late Triassic Guri Zi section, Albania: constraint on the age of the Carnian-Norian boundary. *Rivista Italiana di Paleontologia e Stratigrafia*, v. 111, p. 233-245.

Muttoni, G., Kent, D.V., Jadoul, F., Olsen, P.E., Rigo, M., Galli, M.T., and Nicora, A., 2010. Rhaetian magneto-biostratigraphy from the Southern Alps (Italy): constraints on Triassic chronology. *Palaeogeography, Palaeoclimatology, Palaeoecology*, v. 399, p. 246-259.

Muttoni, G., Dallanave, E., and Channell, J.E.T., 2013. The drift history of Adria and Africa from 280 Ma to present, Jurassic true polar wander, and zonal climate control on Tethyan sedimentary facies. *Palaeogeography, Palaeoclimatology, Palaeoecology*, v. 386, p. 415–435.

Muttoni, G., Mazza, M., Mosher, D., Katz, M.E., Kent, D.V., and Balini, M., 2014. A Middle-Late Triassic (Ladinian-Rhaetian) carbon and oxygen isotope record from the Tethyan Ocean. *Palaeogeography, Palaeoclimatology, Palaeoecology*, v. 399, p. 246-259.

Nagata, T., 1961. Rock Magnetism. *Maruzen Ltd., Tokyo*, p. 350.

Neri, C., Gianolla, P., Furlanis, S., Caputo, R., and Bosellini, A., 2007. Note illustrative della Carta Geologica d'Italia alla scala 1:50000, foglio 029 Cortina d'Ampezzo. *APAT, Rome, Italy*, p. 200.

Nicora, A., Balini, M., Bellanea, A., Bowring, S.A., Di Stefano, P., Dumitrica,

P., Guaiumi, C., Gullo, M., Hungerbuehler, A., Levera, M., Mazza, M., McRoberts, C.A., Muttoni, G., Preto, N., and Rigo, M., 2007. The Carnian/Norian boundary interval at Pizzo Mondello (Sicani Mountains, Sicily) and its bearing for the definition of the GSSP of the Norian Stage. *Albertiana*, v. 36, p. 102-129.

O'Dogherty, L., Carter, E.S., Dumitrica, P., Goričcan, Š., and De Wever, P., 2009. An illustrated and revised catalogue of Mesozoic radiolarian genera—Objectives, concepts and guide for users. *Geodiversitas*, v. 31, p. 191–212.

Ogg,, J.C., 2004. Status of divisions of the International Geological Time Scale. *Lethaia*, v. 37, p. 183–199.

Ogg, J.G., 2012. Triassic. *In* Gradstein, F.M., Ogg, J.G., Schmitz, M., and Ogg, G., eds.: The Geological Time Scale 2012. *Elsevier, Amsterdam*, v. 2, p. 681–730.

Olsen, P.E., 1980. The latest Triassic and Early Jurassic formations of the Newark Basin (Eastern North America, Newark Supergroup): Stratigraphy, structure, and correlation. *New Jersey Academy of Science Bulletin*, v. 25, p. 25-51.

Olsen, P.E., 1986. A 40-million year lake record of early Mesozoic orbital climatic forcing. *Science*, v. 234, p. 842–848.

Olsen, P.E., and Kent, D.V., 1999. Long-period Milankovitch cycles from the Late Triassic and Early Jurassic of eastern North America and their implications for the calibration of the Early Mesozoic time-scale and the long-term behaviour of the planets. *Royal Society of London Philosophical Transactions*, v. 357, p. 1761–1786.

Olsen, P.E., and Sues, H.D., 1986. Correlation of the continental Late Triassic and Early Jurassic sediments, and patterns of the Triassic-Jurassic tetrapod transition. *In* Padian, K., ed.: The Beginning of the Age of Dinosaurs, Faunal Change Across the Triassic-Jurassic Boundary. *Cambridge, UK, Cambridge University Press*, p. 321–351.

Olsen, P.E., Kent, D.V., Cornet, B., Witte, W.K., and Schlische, R.W., 1996. High-resolution stratigraphy of the Newark rift basin (early Mesozoic, eastern North America). *Geological Society of America Bulletin*, v. 108, p. 40-77.

Olsen, P.E., Kent, D.V., and Whiteside, J.H., 2011. Implications of the Newark Supergroup-based astrochronology and geomagnetic polarity time scale (Newark-APTS) for the tempo and mode of the early diversification of the Dinosauria. *Earth and Environmental Science Transactions of the Royal Society of Edinburgh*, v. 101, p. 201-229.

Olsen, P.E., Reid, J.C., Taylor, K.B., Whiteside, J.H., and Kent, D.V., 2015. Revised stratigraphy of Late Triassic age strata of the Dan River Basin (Virginia and North Carolina, USA) based on drill core and outcrop data. *Southeastern Geology*, v. 51, p. 1-31.

Orchard, M.J., 2007. A proposed Carnian-Norian Boundary GSSP at Black Bear Ridge, northeast British Columbia, and a new conodont framework for the boundary interval. *Albertiana*, v. 36, p. 130-160.

Orchard, M.J., 2010. Triassic conodonts and their role in stage boundary definitions. *In* Lucas, S.G., ed.: The Triassic Timescale. *Geological Society, Special Publication*, v. 334, p. 139-161.

Orchard, M.J., Zonneveld, J.P., Johns, M.J., McRoberts, C.A., Sandy, M.R., Tozer, E.T., and Carrelli, G.G., 2001. Fossil succession and sequence stratigraphy of the Upper Triassic of Black Bear Ridge, northeast British Columbia, a GSSP prospect for the Carnian-Norian boundary. *Albertiana*, v. 25, p. 10-22.

Pálfy, J., Smith. P., and Mortensen, J., 2000. A U-Pb and $^{40}Ar/^{39}Ar$ time scale for the Jurassic. *Canadian Journal of Earth Sciences*, v. 37, p. 923-944.

Palmer, A.R., 1983. Geologic Time Scale. *Decade of North American Geology (DNAG), Geological Society of America, Boulder (CA)*.

Parginos, D., Mavrides, A., Bornovas, I., Mettos, A., Katsikatsos, G., Koukis, G., Christodoulou, G., Tsaila-Monopolis, St., Skourtis-Koroneou, B., Ioakim, Ch., Dimou-Honianaki, E., and Kanaki-Mavridou, F., 2007. Geological Map of Greece 1:50000, sheet "Halkida". *IGME, Athens*.

Passeri, L., Bertinelli, A., and Ciarapica, G., 2005. Paleogeographic meaning of the late Triassic–Early Jurassic Lagonegro units. *Bollettino della Società Geologica Italiana*, v. 124, p. 231-245.

Pearson, D.A.B., 1970. Problems of Rhaetian stratigraphy with special reference to the lower boundary of the stage. *Journal of the Geolocigal Society of London*, v. 146, p. 125-150.

Pechersky, D.M., and Khramov, A.N., 1973. Mesozoic palaeomagnetic scale of the USSR. *Nature*, v. 244, p. 499-501.

Pergament, M.A., Pechersky, D.M., and Khramov, A.N., 1971. On the Paleomagnetic Timescale of the Mesozoic. *Izvestiya of the Academy of Sciences of the USSR, Geological Series*, v. 10, p. 3-11.

Preto, N., and Hinnov, L.A., 2003. Unraveling the origin of carbonate platform cyclothems in the Upper Triassic Durrenstein Formation (Dolomites, Italy). *Journal of Sedimentary Research*, v. 73, p. 774-789.

Preto, N., Kustatscher, E., and Wignall, P.B., 2010. Triassic climates – State of the art and perspectives. *Paleaeogeography, Palaeoclimatology, Palaeoecology*, v. 290, p. 1-10.

Preto, N., Rigo, M., Agnini, C., Bertinelli, A., Guaiumi, C., Borello, S., and Westphal, H., 2012. Triassic and Jurassic calcareous nannofossils of the Pizzo Mondello section: a SEM study. *Rivista Italiana di Paleontologia e Stratigrafia*, v. 118, p. 131-145.

Ramezani, J., Hoke, G.D., Fastovsky, D.E., Bowring, S.A., Therrien, F., Dworkin, S.I., Atchley, S.C., and Nordt, L.C., 2011. High-precision U-Pb zircon geochronology of the Late Triassic Chinle Formation, Petrified Forest National Park (Arizona, USA): Temporal constraints on the early evolution of dinosaurs. *Geological Society of America Bulletin*, v. 123, p. 2142-2159.

Reggiani, L., Bertinelli, A., Ciarapica, G., Marcucci, M., Passeri, L., Ricci, C., and Rigo, M., 2005. Triassic–Jurassic stratigraphyof the Madonna del Sirino succession (Lagonegro basin, Southern Apennines, Italy). *Bollettino della Società Geologica Italiana*, v. 124, p. 281-291.

Rigo, M., Preto, N., Roghi, G., Tateo, F., and Mietto, P., 2007. A rise in the Carbonate Compensation Depth of western Tethys in the Carnian (Late Triassic): deep-water evidence for the Carnian pluvial event. *Paleaeogeography, Palaeoclimatology, Palaeoecology*, v. 246, p. 188-205.

Rigo, M., and Joachimski, M.M., 2010. Palaeoecology of Late Triassic conodonts: constraints from oxygen isotopes in biogenic apatite. *Acta Palaeontologica Polonica*, v. 55, p. 471-478.

Rigo, M., Preto, N., Franceschi, M., and Guaiumi, C., 2012a. Stratigraphy of the Carnian-Norian Calcari con Selce Formation in the Lagonegro Basin, Southern Apennines. *Rivista Italiana di Paleontologia e Stratigrafia*, v. 118, p. 143- 154.

Rigo M, Trotter, J.A., Preto, N., and Williams, I.S., 2012b. Oxygen isotopic evidence for Late Triassic monsoonal upwelling in the northwestern Tethys. *Geology*, v. 40, p. 515-518.

Rigo, M., Bertinelli, A., Concheri, G., Gattolin, G., Godfrey, L., Katz, M.E., Maron, M., Mietto, P., Muttoni, G., Sprovieri, M., Stellin, F., and Zaffani, M., 2015. The Pignola-Abriola section (southern Apennines, Italy): a new GSSP candidate for the base of the Rhaetian Stage. *Lethaia*. doi: 10.1111/let.12145

Roghi, G., 2004. Palynological investigations in the Carnian of the Cave del Predil area (Julian Alps, NE Italy). *Review of Palaeobotany and Palynology*, v.

132, p. 1-35.

Roghi, G., Gianolla, P., Minarelli, L., Pilati, C., and Preto, N., 2010. Palynological correlation of Carnian humid pulses throughout western Tethys. *Paleaeogeography, Palaeoclimatology, Palaeoecology*, v. 290, p. 89-106.

Romano, R., Masetti, D., Carras, N., Barattolo, F., and Roghi, G., 2008. The Triassic/Jurassic boundary in a peritidal carbonate platform of the Pelagonian Domain: the Mount Messapion section (Chalkida, Greece). *Rivista Italiana di Paleontologia e Stratigrafia*, v. 114, no. 3, p. 431-452.

Ruffell, A., Simms, M.J., and Wignall, P.B., 2015. The Carnian Humid Episode of the Late Triassic: a review. *Geological Magazine*, doi: 10.1017/S0016756815000424

Scandone, P., 1967. Studi di geologia lucana: la serie calcareo-silicomarnosa. *Bollettino della Società dei Naturalisti in Napoli*, v. 76, p. 117-119.

Scandone, P., 1972. Studi di geologia lucana: nota illustrativa della carta dei terreni della serie calcareo-silico-marnosa. *Bollettino della Società dei Naturalisti in Napoli*, v. 81, p. 225-300.

Scandone, P., 1975. Triassic seaways and the Jurassic Tethys Ocean in the central Mediterranean area. *Nature*, v. 256, p. 117-119.

Schaltegger, U., Guex, J., Bartolini, A., Schoene, B., and Ovtcharova, M., 2008. Precise U-Pb age constraints for end-Triassic mass extinction, its correlation to volcanism and Hettangian post-extinction recovery. *Earth and Planetary Science Letters*, v. 267, p. 266-275.

Schlager, W., and Schöllnberger, W., 1974. Das Prinzip stratigraphischer Wenden in der Schichtenfolge der Nördlichen Kalkalpen. *Mitteilungen der Österreichischen Geologischen Gesellschaft, Wien*, v. 66/67, p. 165-193.

Schoene, B., Guex, J., Bartolini, A., Schaltegger, U., and Blackburn, T.J., 2010. Correlating the end-Triassic mass extinction and flood basalt volcanism at the 100 ka level. *Geology*, v. 38, p. 387–390.

Silberling, N.J., and Tozer, E.T., 1968. Biostratigraphic classification of the marine Triassic in North America. *Geological Society of America Special Paper*, v. 10, p. 1-63.

Simms, M.J., and Ruffell, A.H., 1989. Synchroneity of climatic change and extinction in the Late Triassic. *Geology*, v. 17, p. 265-268.

Slavin, V.I., 1961. Stratigraphic position of the Rhaetian Stage. *Sovyetskaya Geologiya*, v. 3, p. 68-78.

Slavin, V.I., 1963. Au sujet du Rhétian. *Bureau Recherches Géologie et Minieres*

Memoir, v. 15, p. 29-32.

Stacey, F.D., and Banerjee, S.K., 1974. The Physical Principles of Rock Magnetism. *Elsevier, Amsterdam*, p. 195.

Stampfli, G.M., Mosar, J., De Bono, A, and Vavassis, I., 1998. Late Paleozoic, Early Mesozoic Plate Tectonics of the Western Tethys. *Bulletin of the Geological Society of Greece*, v. 32, p. 113-120.

Steiner, M.B., and Lucas, S.G., 2000. Paleomagnetism of the Late Triassic Petrified Forest Formation, Chinle Group, western United States: Further evidence of "large" rotation of the Colorado Plateau. *Journal of Geophysical Research*, v. 105, p. 25791-25808.

Tataris, A., Kounis, G., Maragoudakis, N., Christodoulou, G., Bizon, G., and Tsaila-Monopolis, St., 1970. Geological Map of Greece 1:50000, Sheet "Thivai". *I.G.S.R., Athens*.

Tauxe, L., 1998. Paleomagnetic principles and practice. *Kluwer Academic, Dordrecht*, p. 301.

Tauxe, L., and Kent, D.V., 2004. A simplified statistical model for the geomagnetic field and the detection of shallow bias in paleomagnetic inclinations: Was the ancient magnetic field dipolar?. *In* Channel, J.E.T., ed.: Timescales of the Paleomagnetic field. *American Geophysical Union Geophysical Monograph*, v. 145, p. 101–115.

Tauxe, L., Mullender, T.A.T., and Pick, T., 1996. Potbellies, wasp-waists, and superparamagnetism in magnetic hysteresis. *Journal of Geophysical Research*, v. 101, p. 571-583.

Tozer, E.T., 1967. A standard for Triassic time. *Geological Survey of Canada Bulletin*, v. 156, p. 104.

Tozer, E.T., 1984. The Trias and its Ammonites: The evolution of a time scale. *Geological Survey of Canada Miscellaneous Report,* v. 35, p. 171.

Tozer, E.T., 1994. Canadian ammonoid faunas. *Geological Survey of Canada Bulletin*, v. 467, p. 1-663.

Trotter, J.A., Williams, I.S., Nicora, A., Mazza, M., and Rigo, M., 2015. Long-term cycles of Triassic climate change: a new $\delta^{18}O$ record from conodont apatite. *Earth and Planetary Science Letters*, v. 415, p. 165-174.

Van Houten, F.B., 1964. Cyclic lacustrine sedimentation, Upper Triassic Lockatong Formation, central New Jersey and adjacent Pennsylvania. *In* Mermaid, O.F., ed.: Symposium on cyclic sedimentation. *Kansas Geological Survey Bulletin*, v. 169, p. 497–531.

Van Houten, F.B., 1969. Late Triassic Newark Group, northcentral New Jersey and adjacent Pennsylvania and New York. *In* Subitzki, S., ed.: Geology of selected areas in New Jersey and eastern Pennsylvania and guidebook of excursions, New Brunswick, New Jersey (Geological Society of America, Field Trip 4). *Atlantic City, New Jersey, Rutgers University Press*, p. 314–347.

Van Houten, F.B., 1980. Late Triassic part of Newark Supergroup, Delaware River section, west central New Jersey. *In* Manspeizer, W., ed.: Field studies of New Jersey geology and guide to field trips: New York State Geological Association, 52nd Annual Meeting. *Newark, New Jersey, Rutgers University*, p. 264–269.

Van Veen, P.M., 1995. Time calibration of Triassic/Jurassic microfloral turnover, eastern North America-comment. *Tectonophysics*, v. 245, p. 93-95.

Vavassis, L., De Bono, A., Stampfli, G.M., Giorgis, D., Valloton, A., and Amelin, Y., 2000. U-Pb and Ar-Ar geochronological data from Pelagonia basement in Evia (Greece): geodynamic implications for the evolution of Paleotethys. *Schweizerische mineralogische und petrographische Mitteilungen*, v. 80, p. 21-43.

Verosub, K.L., 1977. Depositional and post-depositional processes in the magnetization of sediments. *Reviews of Geophysics and Space Physics*, v. 15, p. 129-143.

von Alberti, F.A., 1834. Beitrag zu einer Monographie des Bunten Sandsteins, Muschelkalks und Keupers und die Verbindung dieser Gebilde zu einer Formation. *Verlag der J.G. Cotta'schen Buchhandlung, Stuttgart und Tübingen*, p. 326.

Ward, P.D., Haggart, J.W., Carter, E.S., Wilbur, D., Tippert, H.W., and Evans, T., 2001. Sudden productivity collapse associated with the Triassic-Jurassic boundary mass extinction. *Science*, v. 292, p. 1148–1151.

Ward, P.D., Garrison, G.H., Haggart, J.W., Kring, D.A., and Beattie, M.J., 2004. Isotopic evidence bearing on Late Triassic extinction events, Queen Charlotte Islands, British Columbia, and implications for the duration and cause of the Triassic/Jurassic mass extinction. *Earth and Planetary Science Letters*, v. 224, p. 589–600.

Whiteside, J., and Ward, P.D., 2011. Ammonoid diversity and disparity track episodes of chaotic carbon cycling during the early Mesozoic. *Geology*, v. 39, p. 99–102.

Witte, W.K., Kent, D.V., and Olsen, P.E. , 1991. Magnetostratigraphy and paleomagnetic poles from Late Triassic–earliest Jurassic strata of the Newark basin. *Geological Society of America Bulletin*, v. 103, p. 1648–1662.

Wotzlaw, J.F., Guex, J., Bartolini, A., Gallet, Y., Krystyn, L., McRoberts, C.A., Taylor, D., Schoene, B., and Schaltegger, U., 2014. Towards accurate numerical calibration of the Late Triassic: high precision U-Pb geochronology constraints on the duration of the Rhaetian. *Geology*, v. 42, p. 571-574.

Xu, G., Hannah, J.L., Stein, H.J., Mørk, A., Vigran, J.O., Blingen, B., Schutt, D.L., and Lundschien, B.A., 2014. Cause of Upper Triassic climate crisis revealed by Re-Os geochemistry of Boreal black shales. *Palaeogeography, Palaeoclimatology, Palaeoecology*, v. 395, p. 222-232.

Zaninetti, L., Martini, R., and Dumont, T., 1992. Triassic foraminifers from sites 761 and 764, Wombat Plateau, Northwest Australia. *In* Von Rad, U., Haq, B.U., Kidd, R.B., and O'Connell, S., eds.: *Proceedings of the Ocean Drilling Program, Scientific Results*, v. 122, p. 427-436.

Zapfe, H., 1974. Die Stratigraphie der Alpin-Mediterranen Trias. *Schriftenreihe der Erdwissenschaftlichen Kommissionen, Österreichische Akademie der Wissenschaften*, v. 2, p. 137-144.

Zapfe, H., 1983. Das Forschungsprojekt "Triassic of the Tethys Realm" (IGCP Project 4) (Abschlussbericht). *Schriftenreich Erdwissenschaftlichen Komitee 5. Wien: Oesterreiche Akademie der Wissenschaft*.

Zeigler, K.E., and Geissman, J.W., 2012. Magnetostratigraphy of the Upper Triassic Chinle Group of New Mexico: Implications for regional and global correlations among Upper Triassic sequences. *Geosphere*, v. 7, p. 802-809.

Zeigler, K.E., Geissman, J.W., and Lucas, S.G., 2005. Paleomagnetism and magnetostratigraphy of the Upper Triassic Petrified Forest and Poleo Formations, North-Central New Mexico, and the Bluewater Creek and lower Petrified Forest Formations, central New Mexico. *New Mexico Geological Society, Guidebook*, v. 56, p. 115-128.

Ziegler, P.A., 1988. Evolution of the Arctic-North Atlantic and Western Tethys. *AAPG Memoires*, v. 43, p. 198.

Zijderveld, J.D.A., 1967. A.C. demagnetization of rocks: analysis of results. *In* Collinson, D.W., Creer, K.M., and Runcorn, S.K., eds.: Methods in Paleomagnetism. *Elsevier, Amsterdam*, p. 254–286.

APPENDIX A

ChRM DATA AND STATISTICS

APPENDIX A.1
PIGNOLA-ABRIOLA SECTION

ORGANIC CARBON

meter	Sample	$\delta^{13}C_{org}$
30.00	GNI 1	-27.68
30.40	GNI 2	-25.66
30.65	GNI 3	-26.95
30.80	GNI 4	-25.30
30.95	GNI 5	-25.72
31.70	GNI 6	-24.45
31.80	GNI 7	-24.58
31.80	GNI 8	-25.67
35.80	GNI 9	-24.19
36.20	GNI 10	-23.70
37.40	GNI 11	-25.76
37.60	GNI 12	-24.90
37.80	GNI 13	-25.58
39.45	GNP 1	-27.93
40.29	GNM 35B	-26.55
40.60	GNI156	-26.33
40.80	GNM 37	-27.97
41.30	GNI155	-24.59
42.38	GNM 41A	-27.55
42.39	GNI 154	-27.05
42.41	GNI 153	-26.62
42.45	GNP 2	-28.28
42.90	GNI152	-27.24
43.29	GNI151	-26.22
43.40	GNP 3	-27.26
44.45	GNM 52	-29.95
45.25	GNI 150	-25.33
45.33	GNI 14	-25.42
45.40	GNI 15	-27.13
45.90	GNI 16	-27.10
46.40	GNI 17	-26.37
46.55	GNI 18	-26.05
46.90	GNI 19	-25.68
47.50	GNI 19B	-25.86
48.10	GNI 20	-25.40
48.50	GNI 21	-25.77
49.00	GNI 22	-26.15
49.10	GNI 23	-24.36
49.20	GNI 24	-26.56
51.00	GNM 85	-25.86
51.30	GNI 25	-25.97
52.50	GNI 26	-25.85
53.70	GNM 102	-27.83
55.10	GNI 27	-25.40
55.45	GNI 28	-25.63
55.75	GNI 29	-24.41
56.85	GNM 117	-26.61

LEGEND	
Comp.	Type of component
N	Number of demagnetization steps used to define the magnetic component
A/F	Magnetic component anchored to origin (A) or free from origin (F)
MAD	Mean Angular Deviation of the magnetic component
%VAR	Percentage of Variance
Dec	Declination of the magnetic component
Inc	Inclination of the magnetic component

CHARACTERISTIC COMPONENTS OF MAGNETIZATION (ChRM)

						Core		Geographic		Tilt-Corrected				
Sample	Comp.	N	A/F	MAD	%VAR	Dec	Inc	Dec	Inc	Dec	Inc	Treatment min-max (°C)		Magnetization (10^{-2}A/m)
p0.51	ChRM	7	A	12.4	95.4	226.8	47.1	68.6	55.9	37.2	26.1	100	375	0.0098
p0.56	ChRM	8	A	11.9	95.8	219.3	59.8	70	56.2	37.6	26.8	320	550	0.0025
p0.84	ChRM	8	A	12.6	95.2	119.2	72.7	96.6	36.1	68	27.8	150	400	0.0062
p1.00	ChRM	6	A	9.9	97.1	219.2	26	33.4	50.1	21.9	9.9	100	450	0.0037
p1.10	ChRM	12	A	2.1	99.9	172.6	-0.7	230.2	75.4	343.4	54.5	100	550	0.0215
p2.27	ChRM	5	A	6.5	98.7	82.5	1.1	175.4	-3.9	173.4	39.6	0	250	0.0022
p2.71	ChRM	3	A	9.6	97.2	330.8	-63.2	288.9	-57.5	229.6	-45.6	100	200	0.0009
p2.83	ChRM	5	F	9.5	97.3	105.5	28.7	156.9	27.9	125.7	62.9	150	475	0.0018
p3.10	ChRM	4	A	19.8	88.6	210.3	27.6	53.9	61.4	26.8	25.3	100	250	0.0012
p3.37	ChRM	11	A	21.1	87	195.4	25.6	26.3	75.5	9.3	32.6	300	675	0.0017
p3.43	ChRM	12	A	4.1	99.5	1.3	-44.9	226.4	-66.1	200.7	-27.3	150	575	0.0083
p3.49	ChRM	8	A	6.2	98.8	13.7	-48.7	217.3	-62.1	199	-21.8	150	475	0.0046
p3.56	ChRM	3	F	18.9	89.5	64	14.8	136	-15.2	135.9	15.8	100	200	0.0006
p3.62	ChRM	5	F	21.9	86.1	243.6	-17	354.5	13.3	353.6	-30.2	225	350	0.0008
p4.21	ChRM	4	F	21	87.1	332.5	-15.9	22.6	-61.9	153.1	-70.4	150	300	0.0005
p4.60	ChRM	5	A	11.2	96.2	354.6	-6	60.8	-65.5	145.7	-53.8	225	350	0.0007
p4.71	ChRM	3	F	6	98.9	293.5	2.9	5.5	-22.5	9.8	-66.2	150	250	0.0011
p4.98	ChRM	7	A	7.1	98.5	334.9	8.3	29.4	-52.5	122.2	-71.4	150	500	0.0035
p5.06	ChRM	3	F	10.8	96.5	190.7	-83.6	271.1	-3.7	268.9	-1.8	100	200	0.001
p5.42	ChRM	6	A	12	95.7	173.5	29.2	112.5	79.9	16.9	48.7	250	450	0.0007
p6.30	ChRM	10	A	13.1	94.8	205.1	39.8	2.7	69.9	2.4	26	100	500	0.0031
p6.56	ChRM	6	A	10.8	96.5	204.6	18.7	19.3	60.6	11	17.6	350	570	0.0012
p6.66	ChRM	4	A	3.1	99.7	329.4	1.6	353.6	-58.9	201	-76.2	150	350	0.0053
p6.74	ChRM	5	A	9.3	97.4	333.7	-2.2	345.7	-63.7	204	-70.2	150	350	0.0041
p6.93	ChRM	3	A	14.1	94	10	-49.4	239.8	-56.6	212.6	-23.4	100	200	0.0011
p7.03	ChRM	5	F	6.5	98.7	341.9	-31.7	294.6	-68	215.1	-50	100	300	0.0016
p7.14	ChRM	8	A	7.3	98.4	213	33.8	27.9	51.6	18.1	10.2	300	600	0.0023
p7.51	ChRM	10	A	6.6	98.7	198.5	23.8	21.1	68.3	9.8	25.2	300	600	0.0041
p7.60	ChRM	19	A	4.3	99.4	189.3	17.7	20.8	78.8	6.7	35.4	150	650	0.0045
p7.69	ChRM	16	A	3.5	99.6	194.8	14	7.3	74.7	3.9	30.8	200	600	0.0127
p8.50	ChRM	11	A	13.7	94.4	216.8	3.4	330.5	48.5	341.7	8.6	200	525	0.0013
p8.65	ChRM	8	A	15.9	92.5	190.7	-17.3	263	50.3	308.4	38.8	150	475	0.0017
p8.76	ChRM	5	A	12.4	95.4	219.1	44.9	20.2	51.4	13.5	8.8	275	400	0.001
p8.93	ChRM	7	A	7.7	98.2	171.9	33.5	132.6	82.7	11.1	50.5	200	375	0.0017
p9.02	ChRM	6	A	15.5	92.8	180.9	12.2	267.9	80.2	348.3	46	100	375	0.0019
p9.50	ChRM	4	A	19.7	88.7	337.3	-0.9	40.3	-65.4	149	-62	250	400	0.0014
p9.74	ChRM	13	A	4.3	99.4	193.6	24.8	27.2	76.5	9.1	33.6	250	575	0.004
p9.91	ChRM	10	A	5.9	98.9	195.6	28	23.9	74.7	8.8	31.6	100	500	0.0036
p10.27	ChRM	15	A	11.8	95.8	189.6	29.5	48.2	73	16.9	33.3	225	600	0.0021
p10.33	ChRM	10	A	16.3	92.1	189.1	37.5	57.4	68.9	22.8	31.9	0	450	0.0024
p10.47	ChRM	15	A	3.4	99.6	192.8	33.6	34.5	75.3	11.7	33.2	200	575	0.0086
p10.88	ChRM	3	A	3.7	99.6	268.6	-65	283.6	-20.2	265.7	-22	200	275	0.0014
p11.01	ChRM	4	F	13.8	94.3	349.7	-23.7	315.3	-79.3	195.4	-52.6	225	300	0.0005
p11.13	ChRM	9	A	12.7	95.2	248.4	7.2	336.4	22.7	337.4	-17.3	100	500	0.0024
p11.75	ChRM	4	A	16.2	92.2	317.5	-74	280.7	-24.5	260.4	-23	200	320	0.0003
p12.10	ChRM	8	A	11.2	96.2	221.4	-4.5	325.8	44.2	336.9	5.9	300	525	0.0018
p12.26	ChRM	5	A	14.9	93.3	10.2	-32	132.5	-80.2	172.6	-39.4	100	300	0.002
p12.42	ChRM	3	F	11.1	96.3	83	-56.4	231	-16.3	230.3	13.8	0	150	0.0038
p13.36	ChRM	6	A	18.4	90	186.5	6.7	286.8	71.6	339	38.9	0	300	0.0044
p13.45	ChRM	2	A	.8	100	232.1	-3.7	339.9	35.4	344.2	-6	275	300	0.0022
p13.54	ChRM	5	A	19.2	89.2	179.4	23.9	83.2	82	13.4	44.3	200	425	0.002
p13.69	ChRM	15	A	9.2	97.4	202.5	28.6	34.3	58.9	19.1	18.2	0	570	0.0043
p14.00	ChRM	5	F	9.4	97.3	355.2	-30.5	305.2	-82.2	192.6	-49.9	100	275	0.0093
p14.22	ChRM	9	F	18	90.5	324.3	-70.1	262.8	-39.4	237.5	-21.6	0	350	0.0014
p14.38	ChRM	12	F	4.5	99.4	359	-15.1	83.2	-66.1	148	-44.7	0	525	0.0819
p14.58	ChRM	5	F	25.3	81.7	317.2	-45	299.5	-46.9	247.8	-47.8	200	300	0.0006
p14.70	ChRM	8	F	8.9	97.6	308.1	-50.8	289.6	-37.6	253.8	-37.2	150	475	0.0049
p14.76	ChRM	8	A	6.4	98.7	351.8	-41.6	267.5	-63.4	216.8	-38.3	150	475	0.0078
p14.92	ChRM	5	A	6.7	98.7	51	-27.2	167.2	-46.2	171.9	-3.3	350	475	0.0027
p15.01	ChRM	11	A	6.1	98.9	213.2	7.1	331.5	55.3	344.7	14.7	0	500	0.0088
p15.46	ChRM	14	A	6	98.9	220.6	34.1	0.5	54.5	1.3	10.7	200	625	0.0064
p15.95	ChRM	8	A	9	97.5	201.4	28.6	11.8	70.3	5.8	26.6	300	550	0.0047
p16.22	ChRM	13	A	6.7	98.6	207.7	53	26.1	56.9	15.6	14.9	225	600	0.0028
p16.39	ChRM	11	A	14.5	93.7	282.6	50.4	30.9	14.6	32.8	-24.1	250	525	0.0028
p16.73	ChRM	4	A	16.7	91.8	28.2	-44.6	213.9	-64.7	196.4	-23.5	100	250	0.0027
p16.83	ChRM	13	A	18.9	89.5	39.1	-29.2	187.9	-52.2	185.8	-8.5	0	500	0.0061
p16.92	ChRM	10	A	9.5	97.3	227.6	44.2	32.8	52.3	20.7	11.8	100	500	0.0044
p17.02	ChRM	13	A	9.6	97.2	242.3	46	359.2	48.3	0.2	4.4	100	575	0.0051
p17.15	ChRM	10	A	12.1	95.6	43.1	-41.9	185.6	-57.1	184.2	-13.2	225	525	0.002
p17.23	ChRM	9	F	10.6	96.6	214.3	8.4	325.4	52.1	340.2	13.3	350	550	0.0371
p17.84	ChRM	8	A	12.1	95.6	86.8	-65.3	230	-35.3	219.4	-2.1	200	500	0.0049
p17.98	ChRM	13	F	7.9	98.1	169.9	-2.8	232.3	52	301.3	57.4	0	550	0.0225
p18.22	ChRM	10	F	21.5	86.6	164.2	21.3	211	71.1	343.4	61.4	0	450	0.0027
p18.31	ChRM	5	A	21.2	86.9	222.3	14.1	342.1	49	349	6.7	0	250	0.003
p18.83	ChRM	12	A	7.4	98.3	211.8	5	322.1	55.6	339.8	17.2	100	550	0.0045
p18.93	ChRM	10	A	14	94.2	159.2	1	229.2	47.5	292.2	58.4	275	525	0.0042
p19.08	ChRM	7	F	30.9	73.6	192	45.1	335.5	81.2	357.3	38.1	0	400	0.0013
p19.16	ChRM	18	A	9	97.6	209.6	23.3	359.7	63	1.1	19.1	0	650	0.0142
p19.49	ChRM	13	A	2.2	99.9	233	-0.7	324.3	27	328.5	-9.2	0	550	0.0756
p19.92	ChRM	15	A	9.8	97.1	207.2	22.9	336.7	64.3	350.6	22.2	0	600	0.005
p20.02	ChRM	18	A	10.5	96.7	205.8	15.3	356.8	65.1	359.9	21.3	100	650	0.0089
p20.08	ChRM	17	A	5.4	99.1	210.3	19.2	359.3	61.5	0.8	17.6	100	600	0.0046
p20.16	ChRM	6	A	19.4	89	106.1	-70.6	224.5	-22.1	221.8	11.7	150	350	0.0017
gnm418	ChRM	7	A	6.3	98.8	195	-45.2	148.9	16.5	131.1	41.5	225	450	0.0012

p20.29	ChRM	9	A	19	89.3	225.2	33.9	331.6	53.7	344.3	13.2	100	500	0.0021
p20.39	ChRM	7	A	15.9	92.5	229.6	12.6	314.7	41.3	328.3	7.1	200	500	0.0042
gnm419	ChRM	7	A	15.8	92.6	145.8	5	319.9	40.2	332.7	5	0	350	0.0027
gnm420	ChRM	5	A	10.9	96.4	172.1	7.7	356.5	50.1	1	7.7	0	225	0.0013
gnm422	ChRM	9	A	7.2	98.4	148.2	41.3	272.8	66.6	333.1	41.3	350	550	0.0021
gnm423	ChRM	7	A	9.1	97.5	31.2	-29	239.3	-58.9	209.1	-29	200	375	0.0027
gnm424	ChRM	5	A	7.2	98.4	46.8	1.1	233.3	-26.4	225.7	1.1	250	425	0.017
m50	ChRM	6	A	2.8	99.8	188.6	17.5	316.3	76.8	86	61	400	525	0.0058
m51	ChRM	3	F	5.5	99.1	196.4	29.6	6.2	74.9	78.2	49.7	425	475	0.0012
gnm426	ChRM	4	F	19.7	88.6	335.4	-38.8	111.9	-70.7	167.3	-38.8	200	275	0.0003
m54	ChRM	9	A	7.3	98.4	134.2	55.6	238.4	63.6	145.7	64.2	300	525	0.004
m55	ChRM	12	F	10.7	96.6	181.1	22.3	240.3	68.3	135	63.8	300	600	0.0062
gnm01	ChRM	7	F	8.8	97.7	350.7	9.6	256.8	-68.8	271.6	-31.2	100	320	0.001
gnm5	ChRM	3	A	5.3	99.2	29.2	-35.2	251.3	-63.7	216.1	-35.2	150	250	0.0012
gnm6	ChRM	5	F	26.2	80.5	17.2	-17.1	222.4	-49.1	209.7	-14.7	200	300	0.0007
gnm7	ChRM	6	F	15	93.3	37.8	-40.3	270.5	-61.9	225.7	-40.3	150	300	0.0004
gnm8	ChRM	3	F	37.9	62.3	321.9	3.7	145.6	-25.5	150.8	3.7	150	250	0.0002
gnm9	ChRM	7	F	26.2	80.6	48.5	-28.4	261.6	-46.3	237.4	-28.4	100	375	0.0008
gnm11	ChRM	5	F	18.4	90.1	27.1	-38.3	261.4	-68.6	210	-38.3	150	350	0.0009
gnm12	ChRM	5	A	23.4	84.2	315.2	-23.8	133	-45.4	155.1	-23.8	225	375	0.0003
gnm14	ChRM	6	F	8.4	97.8	326.4	-10	230.5	-56.9	213.5	-22.5	150	300	0.0023
gnm499	ChRM	7	A	7.5	98.3	181.8	2.1	1.4	44.1	6	14.1	0	450	0.0019
gnm18	ChRM	12	A	5.7	99	158.1	47.2	285.6	75.3	351	47.2	250	575	0.007
gnm20	ChRM	17	F	15.1	93.3	330.3	32.1	162.7	-9.2	158.2	32.1	100	575	0.0047
gnm23	ChRM	4	F	3.6	99.6	34.1	-39.9	277.2	-64.3	229	-39.9	150	300	0.0019
gnm24	ChRM	8	F	9.3	97.4	34.5	-26.9	249.3	-57.8	212.4	-26.9	100	350	0.0039
gnm27	ChRM	6	F	18.5	89.9	1.2	-8.2	184.7	-49.2	184.1	-8.2	150	320	0.003
gnm28	ChRM	4	F	15.3	93	45.5	-51.4	302.5	-61.3	235.4	-51.4	150	300	0.0017
gnm29	ChRM	15	A	12.7	95.2	37.1	-20.9	124.2	-42.9	172.5	-72.8	250	650	0.0031
gnm29a	ChRM	15	A	6.7	98.6	194.5	-24.1	38.3	51.2	28.6	14.6	100	550	0.0164
gnm30	ChRM	10	A	13.3	94.7	188.6	-13.8	28.9	21.8	28.5	-13.8	200	550	0.0049
gnm301	ChRM	10	A	9.1	97.5	149.5	23.5	328	47.8	341.4	23.5	275	550	0.0034
gnm33	ChRM	14	A	10	97	153.3	57.2	27	49.8	56.3	29.2	200	625	0.0059
gnm34	ChRM	11	A	5.7	99	154.6	48	279.3	72.9	356.5	48	275	570	0.0326
gnm35	ChRM	15	A	14.2	94	29.6	-4.9	234.7	-41.2	223.5	-4.9	0	550	0.007
gnm35b	ChRM	8	F	9.4	97.3	22.9	-58.5	264	-73.6	213.8	-43.7	100	350	0.0055
gnm37	ChRM	6	F	21.9	86.1	12.6	-50.3	296.4	-81.7	205.5	-50.3	150	300	0.0018
gnm37b	ChRM	9	A	10	97	345.7	18.9	28	-44	349.7	-41.7	150	525	0.0069
gnm38	ChRM	13	A	5.7	99	161.2	47.7	278.3	77.4	346.1	47.7	250	600	0.0129
gnm40	ChRM	11	A	7.8	98.2	12	-39.5	243.7	-77.9	205.9	-39.5	200	550	0.0106
m1	ChRM	9	A	5.4	99.1	233.7	6.6	339.9	36.4	15.2	46.6	0	400	0.023
gnm41a	ChRM	12	A	5.7	99	227.2	-28.7	52	-2.2	59.1	-28.7	150	475	0.0115
m2	ChRM	16	F	7.4	98.3	7.4	-20.8	241.1	-75.2	269.2	-39.1	100	600	0.0127
gnm41b	ChRM	10	F	12.8	95.1	34.9	-13	240.9	-46.3	221.8	-13	100	450	0.0119
m3.1	ChRM	8	F	16.4	92.1	1.8	-49.8	267.3	-56.2	273.2	-17.8	350	525	0.0011
m3.2	ChRM	5	A	6	98.9	173.2	-12.4	246.2	69.5	130.4	65.2	350	450	0.0029
gnm42	ChRM	14	A	6.5	98.7	15.5	-45.9	223.7	-73.1	199.4	-45.9	150	525	0.0107
m4	ChRM	5	F	14.4	93.8	128.3	-39.1	222.4	15.2	206.4	31.1	300	425	0.0023
gnm43a	ChRM	11	A	2.1	99.9	137.5	74.5	235.8	68.1	342.9	74.1	250	550	0.0317
gnm44	ChRM	16	A	2.1	99.9	83.5	-57.9	188.5	-16.9	200.2	-15.2	0	570	0.1954
m5	ChRM	6	F	4.3	99.4	342.3	-18.2	338.3	-72.5	300.5	-39.6	100	350	0.0115
m6	ChRM	7	F	26.2	80.5	223.4	15	321	47.7	19.5	64.5	375	525	0.0023
m7	ChRM	5	F	11.9	95.7	324.5	-80.6	272.3	-45.4	275	-6.8	200	375	0.0031
gnm48	ChRM	9	A	15.1	93.2	115.8	55.1	270.9	56.2	318.7	55.1	350	575	0.0032
gnm49	ChRM	4	F	7.3	98.4	67.2	5.5	257.2	-12.8	255.2	4.2	150	400	0.0033
m8	ChRM	4	F	10.6	96.6	138.2	1	245.6	42.6	196.5	64.4	350	425	0.0008
gnm50	ChRM	12	A	6.3	98.8	45.6	-43.3	281.4	-58.4	244.5	-43.3	100	450	0.0072
m10	ChRM	7	A	12.8	95.1	208.1	-5.2	299	47.1	359.8	77.9	300	475	0.0018
gnm52	ChRM	8	F	9	97.5	48.7	-33.9	260.5	-49.2	236.6	-33.9	100	375	0.0027
gnm53	ChRM	7	F	20.8	87.4	271.2	-43.2	190.9	-39.2	194.9	-16.3	150	350	0.0028
gnm54	ChRM	5	F	13.2	94.8	19.6	-13.6	215	-42.3	208.5	-13.6	150	275	0.0005
gnm541	ChRM	6	F	5.6	99.1	86.9	-79.2	349.3	-56.1	275.8	-79.2	0	400	0.0074
gnm55	ChRM	6	A	7	98.5	14.5	-33.9	220.3	-63.1	207.4	-33.9	100	425	0.0028
m11	ChRM	4	F	11.7	95.9	17.9	-32.2	233.7	-67.1	261.3	-33.5	100	250	0.0015
gnm63	ChRM	9	F	12.1	95.6	65.2	-32.4	285.3	-40	260.1	-32.4	150	425	0.0028
gnm65	ChRM	6	A	3.6	99.6	181	-5.6	5.2	36.4	4.9	-5.6	150	425	0.0025
gnm68	ChRM	10	A	10.1	96.9	2.4	-25.7	190.9	-64.7	188.3	-25.7	100	475	0.0045
gnm71	ChRM	6	A	9.9	97.1	6.9	-20.4	196.3	-60.9	189.8	-20.4	100	400	0.0033
gnm77	ChRM	7	A	5.9	98.9	359.8	-19.5	185.7	-57.5	185.7	-19.5	150	475	0.0033
gnm81	ChRM	13	A	8.5	97.8	353.8	-20.3	172.6	-61.8	178.7	-20.3	0	450	0.0041
gnm82	ChRM	18	A	12.3	95.5	4.6	-18.3	194.7	-60	190.5	-18.3	100	625	0.0031
gnm84	ChRM	6	F	6.9	98.6	13.7	-36.2	222.8	-71.5	199.6	-36.2	225	400	0.0021
gnm87	ChRM	18	F	17.9	90.6	37	-14.5	254.3	-46.9	232.9	-14.5	100	600	0.0036
gnm88	ChRM	11	F	9.3	97.4	220.8	-53.6	37.5	-15.4	54.7	-53.6	225	525	0.0024
gnm89	ChRM	16	F	15.2	93.2	14.2	-33.2	242.6	-73.8	209.1	-33.2	150	575	0.0032
gnm90	ChRM	7	A	15.8	92.6	1.4	-20.5	199.7	-69.5	197.3	-20.5	150	425	0.0038
gnm96	ChRM	15	A	3.2	99.7	22.4	-57.9	285.6	-78	204.3	-57.9	100	525	0.0241
gnm97	ChRM	12	A	4.6	99.4	32.2	-21.2	260.1	-52.8	237.1	-21.2	100	450	0.0083
gnm98	ChRM	4	A	9.6	97.2	338.4	-40.7	266.7	-64.7	224.1	-39.2	250	350	0.0038
gnm99	ChRM	15	A	8.8	97.7	356.6	-43.3	174.3	-84.7	207.4	-43.7	100	575	0.0201
gnm102	ChRM	16	A	7	98.5	21.6	-43.4	252.8	-72.3	212.5	-43.4	150	575	0.0089
gnm103	ChRM	12	A	9	97.5	34.1	-37	259.2	-60.7	227	-37	100	450	0.0092
gnm105	ChRM	15	A	8.8	97.7	16.9	-25	237.7	-60.9	221.8	-25	100	525	0.0049
gnm110	ChRM	14	A	7.2	98.4	355.7	-14.6	195.6	-55.4	198.6	-14.6	0	475	0.0053
gnm111	ChRM	4	F	14	94.2	23.7	-15.7	232	-50	218.6	-15.7	150	300	0.0007
gnm112b	ChRM	9	A	12.2	95.5	14	-19.4	228.6	-58.3	216.9	-19.4	100	425	0.0012
gnm117	ChRM	10	A	10.9	96.4	19.1	-33.8	235.8	-66.5	212	-33.8	100	475	0.0023
gnm118	ChRM	6	F	8.8	97.7	36.4	-42.3	233.2	-52.8	216.8	-19.5	150	300	0.0015
gnm119	ChRM	6	A	9.8	97.1	351.5	-11.3	194.4	-51.7	199.4	-11.3	200	450	0.0021

NEWARK		PIGNOLA-ABRIOLA																	
		OPTION 1		OPTION 2		OPTION 3		OPTION 4		OPTION 5		OPTION 6		OPTION 7		OPTION 8		OPTION 9	
Magnetostratigraphy	Duration (Myr)	Magnetostrat.	Thickness (m)	Magnetostrat.	Thickness (m)	Magnetostrat.	Thickness (m)	Magnetostrat.	Thickness (m)	Magnetostrat.	Thickness (m)	Magnetostrat.	Thickness (m)	Magnetostrat.	Thickness (m)	Magnetostrat.	Thickness (m)	Magnetostrat.	Thickness (m)
E1r																			
E2n	0.2																		
E2r	0.2																		
E3n	0.15																		
E3r	0.1																		
E4n	0.3																		
E4r	0.2																		
E5n_1n	0.3																		
E5n_1r	0.1																		
E5n_2n	0.1																		
E5r	0.3																		
E6n	0.5																		
E6r	0.2																		
E7n	2.5																		
E7r	0.3																		
E8n	0.6																		
E8r	1.7																		
E9n	0.5																		
E9r	1.1																		
E10n	0.5																		
E10r	0.4																		
E11n	0.15																	MPA-1n	1.7
E11r	2																	MPA-1r.1r	1.3
E12n	0.2															MPA-1n	1.7	MPA-1r.1n	0.4
E12r	0.8															MPA-1r.1r	1.3	MPA-1r.2r	1.8
E13n.1n	0.6													MPA-1n	1.7	MPA-1r.1n	0.4	MPA-2n.1n	1.4
E13n.1r	0.05													MPA-1r.1r	1.3	MPA-1r.2r	1.8	MPA-2n.1r	0.5
E13n.2n	0.9											MPA-1n	1.7	MPA-1r.1n	0.4	MPA-2n.1n	1.4	MPA-2n.2n	3.6
E13r	0.8											MPA-1r.1r	1.3	MPA-1r.2r	1.8	MPA-2n.1r	0.5	MPA-2r.1r	2.2
E14n	1.2									MPA-1n	1.7	MPA-1r.1n	0.4	MPA-2n.1n	1.4	MPA-2n.2n	3.6	MPA-2r.1n	1.0
E14r	1.4									MPA-1r.1r	1.3	MPA-1r.2r	1.8	MPA-2n.1r	0.5	MPA-2r.1r	2.2	MPA-2r.2r	1.1
E15n	0.9							MPA-1n	1.7	MPA-1r.1n	0.4	MPA-2n.1n	1.4	MPA-2n.2n	3.6	MPA-2r.1n	1.0	MPA-3n.1n	1.6
E15r.1r	0.2							MPA-1r.1r	1.3	MPA-1r.2r	1.8	MPA-2n.1r	0.5	MPA-2r.1r	2.2	MPA-2r.2r	1.1	MPA-3n.1r	0.3
E15r.1n	0.1					MPA-1n	1.7	MPA-1r.1n	0.4	MPA-2n.1n	1.4	MPA-2n.2n	3.6	MPA-2r.1n	1.0	MPA-3n.1n	1.6	MPA-3n.2n	3.2
E15r.2r	0.35					MPA-1r.1r	1.3	MPA-1r.2r	1.8	MPA-2n.1r	0.5	MPA-2r.1r	2.2	MPA-2r.2r	1.1	MPA-3n.1r	0.3	MPA-3n.2r	0.1
E16n	1.7			MPA-1n	1.7	MPA-1r.1n	0.4	MPA-2n.1n	1.4	MPA-2n.2n	3.6	MPA-2r.1n	1.0	MPA-3n.1n	1.6	MPA-3n.2n	3.2	MPA-3n.3n	2.0
E16r	0.3			MPA-1r.1r	1.3	MPA-1r.2r	1.8	MPA-2n.1r	0.5	MPA-2r.1r	2.2	MPA-2r.2r	1.1	MPA-3n.1r	0.3	MPA-3n.2r	0.1	MPA-3r	6.0
E17n	0.4	MPA-1n	1.7	MPA-1r.1n	0.4	MPA-2n.1n	1.4	MPA-2n.2n	3.6	MPA-2r.1n	1.0	MPA-3n.1n	1.6	MPA-3n.2n	3.2	MPA-3n.3n	2.0	MPA-4n	2.9
E17r	1.3	MPA-1r.1r	1.3	MPA-1r.2r	1.8	MPA-2n.1r	0.5	MPA-2r.1r	2.2	MPA-2r.2r	1.1	MPA-3n.1r	0.3	MPA-3n.2r	0.1	MPA-3r	6.0	MPA-4r	3.9
E18n	0.6	MPA-1r.1n	0.4	MPA-2n.1n	1.4	MPA-2n.2n	3.6	MPA-2r.1n	1.0	MPA-3n.1n	1.6	MPA-3n.2n	3.2	MPA-3n.3n	2.0	MPA-4n	2.9	MPA-5n.1n	1.5
E18r	0.35	MPA-1r.2r	1.8	MPA-2n.1r	0.5	MPA-2r.1r	2.2	MPA-2r.2r	1.1	MPA-3n.1r	0.3	MPA-3n.2r	0.1	MPA-3r	6.0	MPA-4r	3.9	MPA-5n.1r	0.8
E19n	0.15	MPA-2n.1n	1.4	MPA-2n.2n	3.6	MPA-2r.1n	1.0	MPA-3n.1n	1.6	MPA-3n.2n	3.2	MPA-3n.3n	2.0	MPA-4n	2.9	MPA-5n.1n	1.5	MPA-5n.2n	0.5
E19r	0.5	MPA-2n.1r	0.5	MPA-2r.1r	2.2	MPA-2r.2r	1.1	MPA-3n.1r	0.3	MPA-3n.2r	0.1	MPA-3r	6.0	MPA-4r	3.9	MPA-5n.1r	0.8	MPA-5r	15.7
E20n	0.2	MPA-2n.2n	3.6	MPA-2r.1n	1.0	MPA-3n.1n	1.6	MPA-3n.2n	3.2	MPA-3n.3n	2.0	MPA-4n	2.9	MPA-5n.1n	1.5	MPA-5n.2n	0.5		
E20r.1r	0.2	MPA-2r.1r	2.2	MPA-2r.2r	1.1	MPA-3n.1r	0.3	MPA-3n.2r	0.1	MPA-3r	6.0	MPA-4r	3.9	MPA-5n.1r	0.8	MPA-5r	15.7		
E20r.1n	0.05	MPA-2r.1n	1.0	MPA-3n.1n	1.6	MPA-3n.2n	3.2	MPA-3n.3n	2.0	MPA-4n	2.9	MPA-5n.1n	1.5	MPA-5n.2n	0.5				
E20r.2r	1.3	MPA-2r.2r	1.1	MPA-3n.1r	0.3	MPA-3n.2r	0.1	MPA-3r	6.0	MPA-4r	3.9	MPA-5n.1r	0.8	MPA-5r	15.7				
E21n	0.5	MPA-3n.1n	1.6	MPA-3n.2n	3.2	MPA-3n.3n	2.0	MPA-4n	2.9	MPA-5n.1n	1.5	MPA-5n.2n	0.5						
E21r.1r	0.2	MPA-3n.1r	0.3	MPA-3n.2r	0.1	MPA-3r	6.0	MPA-4r	3.9	MPA-5n.1r	0.8	MPA-5r	15.7						
E21r.1n	0.05	MPA-3n.2n	3.2	MPA-3n.3n	2.0	MPA-4n	2.9	MPA-5n.1n	1.5	MPA-5n.2n	0.5								
E21r.2r	0.1	MPA-3n.2r	0.1	MPA-3r	6.0	MPA-4r	3.9	MPA-5n.1r	0.8	MPA-5r	15.7								
E21r.2n	0.05	MPA-3n.3n	2.0	MPA-4n	2.9	MPA-5n.1n	1.5	MPA-5n.2n	0.5										
E21r.3r	0.35	MPA-3r	6.0	MPA-4r	3.9	MPA-5n.1r	0.8	MPA-5r	15.7										
E22n.1n	0.4	MPA-4n	2.9	MPA-5n.1n	1.5	MPA-5n.2n	0.5												
E22n.1r	0.05	MPA-4r	3.9	MPA-5n.1r	0.8	MPA-5r	15.7												
E22n.2n	0.3	MPA-5n.1n	1.5	MPA-5n.2n	0.5														
E22r	0.3	MPA-5n.1r	0.8	MPA-5r	15.7														
E23n	0.9	MPA-5n.2n	0.5																
E23r	0.1	MPA-5r	15.7																

NEWARK		PIGNOLA-ABRIOLA																	
		OPTION 10		OPTION 11		OPTION 12		OPTION 13		OPTION 14		OPTION 15		OPTION 16		OPTION 17		OPTION 18		OPTION 19	
Magnetostratigraphy	Duration (Myr)	Magnetostrat.	Thickness (m)	Magnetostrat.	Thickness (m)	Magnetostrat.	Thickness (m)	Magnetostrat.	Thickness (m)	Magnetostrat.	Thickness (m)	Magnetostrat.	Thickness (m)	Magnetostrat.	Thickness (m)	Magnetostrat.	Thickness (m)	Magnetostrat.	Thickness (m)	Magnetostrat.	Thickness (m)
E1r																					
E2n	0.2																			MPA-1n	1.7
E2r	0.2																			MPA-1r.1r	1.3
E3n	0.15																	MPA-1n	1.7	MPA-1r.1n	0.4
E3r	0.1																	MPA-1r.1r	1.3	MPA-1r.2r	1.8
E4n	0.3															MPA-1n	1.7	MPA-1r.1n	0.4	MPA-2n.1n	1.4
E4r	0.2															MPA-1r.1r	1.3	MPA-1r.2r	1.8	MPA-2n.1r	0.5
E5n_1n	0.3													MPA-1n	1.7	MPA-1r.1n	0.4	MPA-2n.1n	1.4	MPA-2n.2n	3.6
E5n_1r	0.1													MPA-1r.1r	1.3	MPA-1r.2r	1.8	MPA-2n.1r	0.5	MPA-2r.1r	2.2
E5n_2n	0.1											MPA-1n	1.7	MPA-1r.1n	0.4	MPA-2n.1n	1.4	MPA-2n.2n	3.6	MPA-2r.1n	1.0
E5r	0.3											MPA-1r.1r	1.3	MPA-1r.2r	1.8	MPA-2n.1r	0.5	MPA-2r.1r	2.2	MPA-2r.2r	1.1
E6n	0.5									MPA-1n	1.7	MPA-1r.1n	0.4	MPA-2n.1n	1.4	MPA-2n.2n	3.6	MPA-2r.1n	1.0	MPA-3n.1n	1.6
E6r	0.2									MPA-1r.1r	1.3	MPA-1r.2r	1.8	MPA-2n.1r	0.5	MPA-2r.1r	2.2	MPA-2r.2r	1.1	MPA-3n.1r	0.3
E7n	2.5							MPA-1n	1.7	MPA-1r.1n	0.4	MPA-2n.1n	1.4	MPA-2n.2n	3.6	MPA-2r.1n	1.0	MPA-3n.1n	1.6	MPA-3n.2n	3.2
E7r	0.3							MPA-1r.1r	1.3	MPA-1r.2r	1.8	MPA-2n.1r	0.5	MPA-2r.1r	2.2	MPA-2r.2r	1.1	MPA-3n.1r	0.3	MPA-3n.2r	0.1
E8n	0.6					MPA-1n	1.685	MPA-1r.1n	0.4	MPA-2n.1n	1.4	MPA-2n.2n	3.6	MPA-2r.1n	1.0	MPA-3n.1n	1.6	MPA-3n.2n	3.2	MPA-3n.3n	2.0
E8r	1.7					MPA-1r.1r	1.3	MPA-1r.2r	1.8	MPA-2n.1r	0.5	MPA-2r.1r	2.2	MPA-2r.2r	1.1	MPA-3n.1r	0.3	MPA-3n.2r	0.1	MPA-3r	6.0
E9n	0.5			MPA-1n	1.7	MPA-1r.1n	0.4	MPA-1r.1n	0.4	MPA-2n.1n	1.4	MPA-2n.2n	3.6	MPA-2r.1n	1.0	MPA-3n.1n	1.6	MPA-3n.2n	3.2	MPA-3n.3n	2.0
E9r	1.1			MPA-1r.1r	1.3	MPA-1r.2r	1.8	MPA-2n.1r	0.5	MPA-2r.1r	2.2	MPA-2r.2r	1.1	MPA-3n.1r	0.3	MPA-3n.2r	0.1	MPA-3r	6.0	MPA-4r	3.9
E10n	0.5	MPA-1n	1.7	MPA-1r.1n	0.4	MPA-2n.1n	1.4	MPA-2n.2n	3.6	MPA-2r.1n	1.0	MPA-3n.1n	1.6	MPA-3n.2n	3.2	MPA-3n.3n	2.0	MPA-4n	2.9	MPA-5n.1n	1.5
E10r	0.4	MPA-1r.1r	1.3	MPA-1r.2r	1.8	MPA-2n.1r	0.5	MPA-2r.1r	2.2	MPA-2r.2r	1.1	MPA-3n.1r	0.3	MPA-3n.2r	0.1	MPA-3r	6.0	MPA-4r	3.9	MPA-5n.1r	0.8
E11n	0.15	MPA-1r.1n	0.4	MPA-2n.1n	1.4	MPA-2n.2n	3.6	MPA-2r.1n	1.0	MPA-3n.1n	1.6	MPA-3n.2n	3.2	MPA-3n.3n	2.0	MPA-4n	2.9	MPA-5n.1n	1.5	MPA-5n.2n	0.5
E11r	2	MPA-1r.2r	1.8	MPA-2n.1r	0.5	MPA-2r.1r	2.2	MPA-2r.2r	1.1	MPA-3n.1r	0.3	MPA-3n.2r	0.1	MPA-3r	6.0	MPA-4r	3.9	MPA-5n.1r	0.8	MPA-5r	15.7
E12n	0.2	MPA-2n.1n	1.4	MPA-2n.2n	3.6	MPA-2r.1n	1.0	MPA-3n.1n	1.6	MPA-3n.2n	3.2	MPA-3n.3n	2.0	MPA-4n	2.9	MPA-5n.1n	1.5	MPA-5n.2n	0.5		
E12r	0.8	MPA-2n.1r	0.5	MPA-2r.1r	2.2	MPA-2r.2r	1.1	MPA-3n.1r	0.3	MPA-3n.2r	0.1	MPA-3r	6.0	MPA-4r	3.9	MPA-5n.1r	0.8	MPA-5r	15.7		
E13n.1n	0.6	MPA-2n.2n	3.6	MPA-2r.1n	1.0	MPA-3n.1n	1.6	MPA-3n.2n	3.2	MPA-3n.3n	2.0	MPA-4n	2.9	MPA-5n.1n	1.5	MPA-5n.2n	0.5				
E13n.1r	0.05	MPA-2r.1r	2.2	MPA-2r.2r	1.1	MPA-3n.1r	0.3	MPA-3n.2r	0.1	MPA-3r	6.0	MPA-4r	3.9	MPA-5n.1r	0.8	MPA-5r	15.7				
E13n.2n	0.9	MPA-2r.1n	1.0	MPA-3n.1n	1.6	MPA-3n.2n	3.2	MPA-3n.3n	2.0	MPA-4n	2.9	MPA-5n.1n	1.5	MPA-5n.2n	0.5						
E13r	0.8	MPA-2r.2r	1.1	MPA-3n.1r	0.3	MPA-3n.2r	0.1	MPA-3r	6.0	MPA-4r	3.9	MPA-5n.1r	0.8	MPA-5r	15.7						
E14n	1.2	MPA-3n.1n	1.6	MPA-3n.2n	3.2	MPA-3n.3n	2.0	MPA-4n	2.9	MPA-5n.1n	1.5	MPA-5n.2n	0.5								
E14r	1.4	MPA-3n.1r	0.3	MPA-3n.2r	0.1	MPA-3r	6.0	MPA-4r	3.9	MPA-5n.1r	0.8	MPA-5r	15.7								
E15n	0.9	MPA-3n.2n	3.2	MPA-3n.3n	2.0	MPA-4n	2.9	MPA-5n.1n	1.5	MPA-5n.2n	0.5										
E15r.1r	0.2	MPA-3n.2r	0.1	MPA-3r	6.0	MPA-4r	3.9	MPA-5n.1r	0.8	MPA-5r	15.7										
E15r.1n	0.1	MPA-3n.3n	2.0	MPA-4n	2.9	MPA-5n.1n	1.5	MPA-5n.2n	0.5												
E15r.2r	0.35	MPA-3r	6.0	MPA-4r	3.9	MPA-5n.1r	0.8	MPA-5r	15.7												
E16n	1.7	MPA-4n	2.9	MPA-5n.1n	1.5	MPA-5n.2n	0.5														
E16r	0.3	MPA-4r	3.9	MPA-5n.1r	0.8	MPA-5r	15.7														
E17n	0.4	MPA-5n.1n	1.5	MPA-5n.2n	0.5																
E17r	1.3	MPA-5n.1r	0.8	MPA-5r	15.7																
E18n	0.6	MPA-5n.2n	0.5																		
E18r	0.35	MPA-5r	15.7																		
E19n	0.15																				
E19r	0.5																				
E20n	0.2																				
E20r.1r	0.2																				
E20r.1n	0.05																				
E20r.2r	1.3																				
E21n	0.5																				
E21r.1r	0.2																				
E21r.1n	0.05																				
E21r.2r	0.1																				
E21r.2n	0.05																				
E21r.3r	0.35																				
E22n.1n	0.4																				
E22n.1r	0.05																				
E22n.2n	0.3																				
E22r	0.3																				
E23n	0.9																				
E23r	0.1																				

T-VALUE

Options	R-coefficient	t-value
1	-0.26452	-1.2266629
2	-0.13267	-0.5986098
3	-0.35331	-1.6889788
4	0.10037	0.45114649
5	-0.1404	-0.6341694
6	-0.32075	-1.5144555
7	0.21048	0.96286512
8	0.0005312	0.0023756
9	0.037256	0.16672965
10	-0.16305	-0.7390722
11	0.070283	0.31509433
12	-0.088208	-0.3960218
13	-0.078859	-0.3537699
14	-0.41761	-2.0554199
15	0.071673	0.32135787
16	0.25173	1.16322968
17	-0.22994	-1.0566357
18	0.022324	0.09986085
19	0.64481	3.77275435

Confidence	min t-value
90%	1.325
95%	1.725

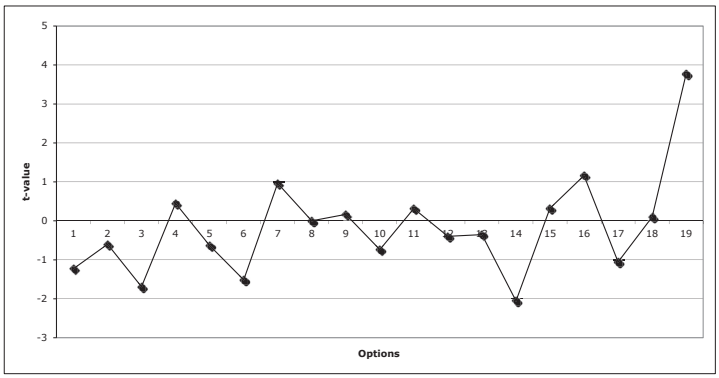

NEWARK		PIGNOLA-ABRIOLA OPTION 7.2	
Magnetostratigraphy	Duration (Myr)	Magnetostratigraphy	Thickness (m)
E13n.2n	0.9	MPA-1n	1.7
E13r	0.8	MPA-1r	3.6
E14n	1.2	MPA-2n	5.4
E14r	1.4	MPA-2r.1r	2.2
E15n	0.9	MPA-2r.1n	1.0
E15r.1r	0.2	MPA-2r.2r	1.1
E15r.1n	0.1	MPA-3n.1n	1.6
E15r.2r	0.35	MPA-3n.1r	0.3
E16n	1.7	MPA-3n.2n	3.2
E16r	0.3	MPA-3n.2r	0.1
E17n	0.4	MPA-3n.3n	2.0
E17r	1.3	MPA-3r	6.0
E18n	0.6	MPA-4n	2.9
E18r	0.35	MPA-4r	3.9
E19n	0.15	MPA-5n.1n	1.5
E19r	0.5	MPA-5n.1r	0.8
E20n	0.2	MPA-5n.2n	0.5
E20r	1.55	MPA-5r	15.7

OPTION 7.2

Options	R-coefficient	t-value
1	-0.26452	-1.2266629
2	-0.13267	-0.5986098
3	-0.35331	-1.6889788
4	0.10037	0.45114649
5	-0.1404	-0.6341694
6	-0.32075	-1.5144555
7	0.21048	0.96286512
7.2	0.87704	8.16423896
8	0.0005312	0.0023756
9	0.037256	0.16672965
10	-0.16305	-0.7390722
11	0.070283	0.31509433
12	-0.088208	-0.3960218
13	-0.078859	-0.3537699
14	-0.41761	-2.0554199
15	0.071673	0.32135787
16	0.25173	1.16322968
17	-0.22994	-1.0566357
18	0.022324	0.09986085
19	0.64481	3.77275435

Confidence	min t-value
90%	1.325
95%	1.725

T-VALUE + OPTION 7.2

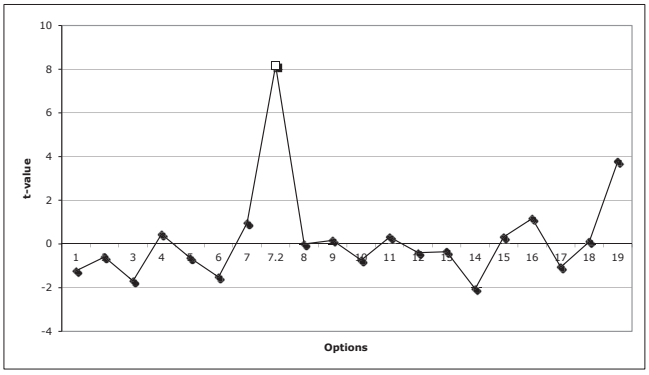

APPENDIX A.2
MOUNT MESSAPION SECTION

CHARACTERISTIC COMPONENTS OF MAGNETIZATION (ChRM)

						Core		Geographic		Tilt-Corrected				
Sample	Comp.	N	A/F	MAD	%VAR	Dec	Inc	Dec	Inc	Dec	Inc	Treatment min-max (°C)		Magnetization (10^{-2}A/m)
mes2.1	C	3	F	11.2	96.2	322.3	51.7	340.5	-8.3	326.1	-45.3	475	525	0.0004
mes4.1	C	7	F	19	89.4	292.9	74.5	358.3	14.3	356.9	-29.6	450	600	0.0023
mes6.1	C	5	A	9.8	97.1	73.6	48.4	45.9	6.9	51.7	-29	500	600	0.0011
mes8.1	C	13	A	4.4	99.4	7.5	53.7	17.6	-14	24.1	-58.3	200	575	0.0128
mes10.1	C	3	F	3.8	99.6	319.4	51.2	341.9	2.4	334.2	-36.4	475	525	0.0001
mes12.1	C	9	A	5.7	99	114.4	11.1	126.9	24.4	99.9	35.8	150	450	0.0039
mes16	C	3	A	4.5	99.4	103.1	-71	157.1	-57.3	172.3	-15.9	200	300	0.0016
mes18	C	11	A	4	99.5	111	-62.1	191.3	-24.3	191.3	20.7	250	550	0.0073
mes20.1	C	3	F	7.9	98.1	174.5	-20.8	188.8	32.9	185.3	77.9	300	375	0.0006
mes22.1	C	4	F	15.4	93	281.9	-54.7	221.3	-37.4	214.4	3	375	450	0.0007
mes24	C	4	F	22.5	85.4	353.9	46.2	16.6	16.4	17.2	-28.3	450	525	0.0005
mes26.2	C	7	A	4	99.5	128	-44.2	172.2	-25.7	173.2	17.4	250	450	0.0019
mes28.2	C	3	F	8.1	98	95.6	-72.5	172.8	-16.4	171.6	26.7	100	250	0.0005
mes30	C	3	F	22.8	85	332.5	4.3	9.8	-23.9	9.8	-69	500	550	0.0004
mes36.1	C	3	F	11	96.4	88.1	70.5	49	21.9	47.1	-14.2	300	375	0.0003
mes38.1	C	3	F	12.9	95	256.5	53.3	298.9	25.5	310.8	5.6	500	550	0.0002
mes40.1	C	13	A	7.6	98.3	44.2	-53.9	115.5	-61.5	157.1	-32.1	0	575	0.0037
mes42.1	C	9	F	8.2	98	117.5	-6.9	102.7	19.7	87.6	15.7	375	575	0.0069
mes44	C	7	F	7.6	98.3	43	-54.9	133.6	-65.3	166.7	-28.7	150	450	0.004
mes48.1	C	3	F	12.8	95.1	123.9	-9.7	197.9	-4	200.4	40.4	425	475	0.0003
mes50.1	C	3	F	13.9	94.3	130.6	15.7	108.9	42.8	71.2	34.1	100	200	0.0005
mes58.1	C	4	F	14.3	93.9	91.6	50.5	48.6	12.6	51.3	-22.7	250	375	0.0014
mes60.2	C	5	F	12.6	95.3	52.5	-25.1	38.5	-44	107.5	-69.7	200	375	0.0007
mes62.1	C	3	A	5.2	99.2	24.1	62.5	351.1	12.4	348.5	-30.1	400	450	0.0004
mes66.1	C	3	F	13	95	259	27.2	288.6	27.4	305.6	13.3	500	550	0.0004
mes70.1	C	3	F	4.6	99.4	21	32	73.1	-12.6	89.7	-27.8	475	525	0.0005
mes72.1	C	4	F	10.7	96.5	67.9	-8.6	72.7	-22.6	98	-34.8	400	475	0.0006

LEGEND	
Comp.	Type of component
N	Number of demagnetization steps used to define the magnetic component
A/F	Magnetic component anchored to origin (A) or free from origin (F)
MAD	Mean Angular Deviation of the magnetic component
%VAR	Percentage of Variance
Dec	Declination of the magnetic component
Inc	Inclination of the magnetic component

FILTERED CHARACTERISTIC COMPONENTS OF MAGNETIZATION (ChRM)

						Core		Geographic		Tilt-Corrected				
Sample	Comp.	N	A/F	MAD	%VAR	Dec	Inc	Dec	Inc	Dec	Inc	Treatment min-max (°C)		Magnetization (10^{-2}A/m)
mes16	C	3	A	4.5	99.4	103.1	-71	157.1	-57.3	172.3	-15.9	200	300	0.0016
mes38.1	C	3	F	12.9	95	256.5	53.3	298.9	25.5	310.8	5.6	500	550	0.0002
mes40.1	C	13	A	7.6	98.3	44.2	-53.9	115.5	-61.5	157.1	-32.1	0	575	0.0037
mes42.1	C	9	F	8.2	98	117.5	-6.9	102.7	19.7	87.6	15.7	375	575	0.0069
mes44	C	7	F	7.6	98.3	43	-54.9	133.6	-65.3	166.7	-28.7	150	450	0.004
mes50.1	C	3	F	13.9	94.3	130.6	15.7	108.9	42.8	71.2	34.1	100	200	0.0005
mes60.2	C	5	F	12.6	95.3	52.5	-25.1	38.5	-44	107.5	-69.7	200	375	0.0007
mes66.1	C	3	F	13	95	259	27.2	288.6	27.4	305.6	13.3	500	550	0.0004
mes72.1	C	4	F	10.7	96.5	67.9	-8.6	72.7	-22.6	98	-34.8	400	475	0.0006

APPENDIX A.3
LEG 122-SITES 759/760/761-HOLES 759B/760B/761C

LEG 122-SITE 759-HOLE B ChRM

Sample	Dec	Inc	MAD
WBB3700701	132.2	75	10.9
WBB3703601	358.7	-44.7	4.3
WBB3704601	242.3	-49.6	1.3
WBB3711801	284.3	-28.2	11.4
WBB3711901	21.7	-19.1	4.9
WBB3712001	28.8	-21	5.8
WBB3712101	348.6	-25.2	6.1
WBB3712201	310.7	-42.2	5.5
WBB3712501	110.5	-38.6	8.4
WBB3712701	359.2	-45.8	7
WBB3712801	140.4	-5.2	7.3
WBB3713101	210	-20.5	9.3
WBB3713901	23	-8.4	8.6
WBB3714001	301.3	-81.1	13.9
WBB3714101	360	55	8.1
WBB3714201	188.2	-66.7	5.3
WBB3714301	1.7	-57.2	8.1
WBB3714601	40.8	-21.2	2.9
WBB3715001	359.3	-36.2	14
WBB3716001	112	-40	17.7
WBB3716101	109.6	-63.2	8.3
WBB3716201	224.7	-54.7	4.6
WBB3716501	64.2	-54.1	4.7
WBB3717201	275	-66.4	14.7
WBB3717601	21.2	-34.2	10.7
WBB3717701	356.5	-45.4	4.9
WBB3717801	11.2	44.5	20.8
WBB3718501	99.5	-45	9.3
WBB3719401	247.3	-60.7	6.5
WBB3719701	84	-32.4	10.2
WBB3719801	282.9	-51.6	10.7
WBB3719901	0.6	-19.6	11.1
WBB3720201	182.5	-70.4	11.3
WBB3720701	326.7	-60.7	13
WBB3720801	16.7	58	9.1
WBB3715201	334.8	-40.6	5.3
WBB3715501	-64.9	27.6	10.4
WBB3715601	-179.8	55.5	11.2
WBC371580	199.3	-65.7	7.4
WBB3715901	-65.4	41.2	7.4
WBB3716901	-330.3	59.1	4.6
WBB3717001	-252	13.1	7.2
WBB3718001	257	-62.3	7.5
WBB3718201	-70.8	44.4	7.9
WBB3718301	348.1	-59.3	7.9
WBB3718601	-327	42.6	13.6
WBB3718701	-141.7	44.7	13.8
WBB3719101	-85.5	55.6	1.3
WBB3719201	-339.2	38.8	25.3
WBB3719301	-280.7	22.9	9.5
WBB3720901	-43.5	50.9	10.7
WBB3721001	-357.5	17	3.9
WBB3721201	32.6	38.1	7.9
WBB3721301	103.2	46.5	11.5
WBB3721401	39.8	0	7.6
WBB3721501	-148.5	48.5	12.4
WBB3721701	137.6	26.4	2.2
WBB3721801	103.1	-47.5	10.1
WBB3722101	40.9	-7.3	19.6
WBB3722301	36.1	-68.8	2.2
WBB3722401	46.6	-34.9	8.5
WBB3722501	343.1	51.3	5.8
WBB3722901	84.7	-34.2	2.1
WBB3723001	31.9	-28.4	17.8
WBB3723101	213.6	-49.1	10.7
WBB3723401	326.7	-50.1	16.4
WBB3723501	42.7	-47.8	4.6
WBB3723601	225.3	-16.6	9.1
WBB3724001	241	-31.9	7.7
WBB3724101	337.8	-34.8	7.8
WBB3724201	333.7	-42.9	10.8

LEG 122-SITE 760-HOLE B ChRM

Sample	Dec	Inc	MAD
WBC3724701	356.4	15.1	18
WBC372480	230.9	24.6	6.5
WBC372530	68.8	-31.9	11.2
WBC372560	299.6	17.8	6.4
WBC372580	219.9	23	11.1
WBC372620	10.1	-19.6	22.5
WBC372650	311.2	48.8	17
WBC372690	27.2	-23.4	15.5
WBC372700	79.7	9.8	2
WBC372710	255.9	9.3	18.4
WBC372720	180.2	7.1	9.2
WBC372740	150.8	19.6	11.8
WBC372750	173.6	39.1	6.7
WBC372970	356.1	-2.4	3.8
WBC373100	15.2	-53	12.5
WBC373120	203.6	-34.9	8.8
WBC373130	241.6	-44.9	2.1
WBC373140	153.7	-32	4.5
WBC373170	348.9	-16.9	4.7
WBC373180	60.8	-62	9.6
WBC373190	29.4	-4.7	7.2
WBC373200	328.5	-13.6	4.6
WBC373210	131	-16	5.9
WBC373260	349.1	-57.5	8.8
WBC373310	40	-35.9	8.2
WBC373370	20.8	-12.3	6.3
WBC374210	155.5	-25	11.9
WBC374230	326.9	-17.2	3.3
WBC374240	127.3	-32.1	6.9
WBC374250	93.1	-16.5	4.5
WBC374270	79.3	-27.1	6.6
WBC374280	84.2	-46.4	5.7
WBC374320	316.2	-26.3	14.3
WBC374330	81	-37.3	8.4
WBC374360	283.9	-75.1	17.4
WBC374380	51.6	33	12.4
WBC374470	55.5	-33.1	11
WBC374550	163.8	-20.5	9.6
WBC374590	135.1	46	5
WBC374600	336.1	-72.8	3.4
WBC374690	41.5	-58.8	5.9
WBC374700	27.5	-22.8	21.5
WBC374720	261.2	-32.8	12.8
WBC374730	63.3	31	11.2
WBC374750	106	-38	13.3
WBC374760	276.7	-29.4	8.4
WBC374770	71.6	-29.1	16
WBC374780	86	-11.5	10.6
WBC374140	59.1	-65.7	12.4
WBC374160	358.2	-16	22.7
WBC374170	20.6	-36.3	18.7
WBC374190	352	-41.9	8
WBC374480	14.3	-27.5	10.6
WBC374490	28.4	-57.9	6.9
WBC374820	65.4	-1.5	16.7
WBC374830	29	-13.5	6.1
WBC374850	55.1	-16.8	13
WBC374860	65	-43	9.6
WBC374880	210.2	-23.3	18
WBC374900	336	-41.8	11.5
WBC374910	329.1	-32.8	8.6
WBC374920	94.8	-60.5	17.6
WBC374930	261.6	-15.1	4.4
WBC374940	175.3	26.4	8.4
WBC375000	278.1	-59.7	8.7
WBC374990	260.8	-59.1	8.8
WBC375010	41.6	-47.7	13.7

LEG 122-SITE 761-HOLE C ChRM

Sample	Dec	Inc	MAD
WBA3669601	154.2	-82.4	11.4
WBA3669701	249.4	-23.8	36.2
WBA3669901	286	-26.6	11.8
WBA3670101	105.4	85.9	23.3
WBA3672001	111.9	-59.6	8.8
WBA3672101	225.9	-65.3	7.4
WBA3673001	310.4	-24.7	5.1
WBA3673301	81.6	-66	4.7
WBA3673401	198.8	-40.1	6.6
WBA3673501	195.5	30.1	25.8
WBA3673601	55.1	-68.2	17.7
WBA3673701	258.5	-9.4	27.6
WBA3674001	223.4	-30	13.6
WBA3674101	349.7	-53.7	7.5
WBA3674201	215.3	7.5	2.1
WBA3675601	246.7	58	4.8
WBA3675701	43.1	19.7	7.6
WBA3675801	75.4	-8.9	13.4
WBA3675901	243.2	-2.4	8.3
WBA3676001	263.3	-15.8	6.4
WBA3676101	289.8	48.3	6.1
WBA3676301	59.5	-34.8	12.4
WBA3676401	33.9	-29.5	18.1
WBA3676501	269.3	40.6	29.4
WBA3676601	232	-53.7	5
WBA3676701	260	-32	10.4
WBA3676901	54.7	-65.8	19.2
WBA3677001	220.2	-31	20.9
WBA3677101	277.5	-35.6	8.1
WBA3677301	333.6	-72.6	16.6
WBA3677401	55	-31.5	6.6
WBA3677501	38.4	-25.7	6.6
WBA3677701	110.7	79.2	4.5
WBA3683701	236.3	61.8	16.8
WBA3685801	44.4	-36.9	4
WBA3687401	205.8	-42.1	14.5
WBA3689101	46.1	-51.3	3.5
WBA3689401	54.7	-57.9	5.5
WBA3690101	79	75.1	15.9
WBA3690701	32.1	-82.7	13.8
WBA3691010	322.8	-28.6	8.4
WBA3691101	32.9	-65.8	34.5
WBA3691201	37.7	-18.1	15
WBA3693201	132.7	-67.5	12.7
WBA3693301	191.4	-38.9	12.1
WBA3693501	272.9	24.8	17.9
WBA3693801	142.5	-32.9	27.8
WBA3693901	302.3	-55.6	16.7
WBA3694401	344.5	33.9	1.7
WBA3694501	111.7	-59.8	14.4
WBA3694601	212	-69	6.2
WBA3694701	101.3	-53.5	10.4
WBA3694801	183.3	-35.5	4.9
WBA3694901	122.5	-34.8	10.8
WBA3695901	109	-40.1	13.7
WBA3699601	250.3	-67.2	12.9
WBA3699701	108.9	-32.7	5
WBA3699801	11.8	-61.6	2.7
WBA3699901	277.6	32.2	6
WBA3700001	354.3	-50.4	23.3

LEGEND	
MAD	Mean Angular Deviation of the magnetic component
Dec	Declination of the magnetic component
Inc	Inclination of the magnetic component

APPENDIX A.4
PIGNOLA-2 AND DIBONA SECTIONS

PIGNOLA-2 Characteristic components (ChRM)

ID Sample	Component	N° of points	Anchored/Free	MAD	VAR (%)	Core Dec.	Core Inc.	Geog. Dec.	Geog. Inc.	Mag. Dec.	Mag. Inc.	Min T (°C)	Max T(°C)	J comp. (10^{-2} A/m)
pgm0,30	C	13	A	5.2	99.2	319	76.5	9.4	60.6	36.8	35.2	100	575	0.0051
pgm0,53	C	9	A	7.4	98.3	190.6	63.9	358.7	70.2	40.7	45.3	200	550	0.0018
pgm0,79	C	3	A	6.5	98.7	161.9	41.6	81.9	76	72.2	42.3	300	375	0.001
pgm0,94	C	7	A	8.9	97.6	174	62.1	14.5	66.6	43.4	38.8	300	525	0.0015
pgm1,59	C	5	A	8.9	97.6	183.1	55.6	323.5	77.2	44.3	57	250	425	0.002
pgm1,69	C	6	A	10.8	96.5	47.6	-74.3	182.1	-56.9	210.4	-34.5	350	500	0.0008
pgm1,94	C	2	A	4.1	99.5	42.7	-10.8	170.4	-47.9	197.1	-32.1	475	500	0.0014
pgm3,16	C	10	A	14.6	93.6	11.8	-82.9	197.7	-57.9	219.4	-30.7	250	550	0.0009
pgm3,40	C	4	A	12.4	95.4	133.4	-70.2	203.7	-46.2	217.2	-18.6	425	525	0.0015
pgm3,85	C	5	A	4.5	99.4	255.1	41.1	13.6	39.6	27.2	15.9	250	475	0.0022
pgm4,48	C	9	A	5	99.2	54.6	-75.4	176.6	-63.9	213.8	-41.6	200	525	0.003
pgm4,76	C	2	A	8.2	97.9	3.2	-64.7	184.5	-63.2	216.5	-38.7	425	450	0.0012
pgm5,56	C	7	A	8.2	97.9	37.5	-36.4	150.2	-57.4	195.3	-47.5	350	500	0.0024
pgm5,83	C	7	A	17.7	90.8	18.4	-28.9	166.9	-72.1	219.6	-49.5	350	500	0.004
pgm6,23	C	14	A	4.9	99.3	217.4	13	355.5	53.7	24.4	34.4	100	550	0.0162
pgm6,63	C	6	A	3.3	99.7	0.7	-51.2	187.3	-68.7	222.3	-42.2	300	475	0.0028
pgm7,03	C	6	A	13.9	94.2	23.5	-63.9	131.9	-70.5	211	-59.6	200	425	0.0056
pgm7,41	C	4	A	11.8	95.8	351	-78	185.9	-55.8	211.6	-32.4	350	550	0.0019
pgm7,51	C	11	A	6.8	98.6	204.8	69.6	3	43	21.7	23	150	525	0.0188
rad8	C	8	A	18.1	90.3	225.4	42.5	323.8	51.3	3.7	45.6	400	575	0.0039
rad7	C	12	A	3.9	99.5	261.2	-4.6	279.7	5.5	287.2	32.5	250	575	0.0349
rad3	C	15	A	9	97.5	182.4	67.7	5.5	52.2	28	28.8	150	625	0.0049
rad1	C	5	A	9	97.5	236.4	74.3	346.3	42.4	9.4	28.6	350	500	0.0025
pgm13,50	C	13	A	5.9	98.9	25.5	-40.5	189.2	-60.8	216.9	-35.5	250	675	0.0392
pgm13,83	C	6	A	6.4	98.7	212.2	26.1	313.4	61.3	14.4	56.8	375	550	0.0065
pgm14,06	C	8	A	12.1	95.6	213	15.8	343.9	58.4	22.8	42.4	350	550	0.0028
pgm14,18	C	10	A	11.3	96.1	193.6	18.5	2.6	73.8	45.8	46.9	150	625	0.0061
pgm14,31	C	10	A	5.9	99	255.9	70.3	359	52.4	25.5	32.1	300	550	0.0031
pgm14,54	C	10	F	16.1	92.3	213.2	34.7	346.8	61.7	27.5	43.4	350	575	0.0028
pgm14,64	C	6	A	7.2	98.4	219	28.1	348.8	54.8	21.8	37.9	250	475	0.0045
pgm15,15	C	7	A	4.4	99.4	213.8	19.7	334.6	53.9	13.5	43.4	300	475	0.0046
pgm15,30	C	11	A	3.1	99.7	217.3	47.8	344.3	54.3	18.9	39.5	150	550	0.0232
pgm15,50	C	6	A	14.3	93.9	201.9	54.8	354.3	51.5	22	33.2	250	425	0.0019
pgm15,80	C	13	A	13.1	94.9	202.9	56	5.6	57.5	32.7	33.9	100	650	0.0038
pgm16,00	C	11	A	4.8	99.3	190.7	40.6	359.7	65.6	36.5	41.9	150	525	0.006
pgm16,20	C	7	A	18.6	89.8	193.1	42.5	2.9	58.4	32	35.5	250	575	0.0037
pgm16,27	C	5	A	5	99.2	178.7	44.3	355.4	60.7	30.3	39.7	250	425	0.0036
pgm16,61	C	7	A	15	93.3	183	43.3	344.8	62.6	27.5	44.7	150	425	0.0041
pgm16,85	C	8	A	11.7	95.9	179.4	59.8	352	52.2	21.3	34.7	300	600	0.0043
pgm17,30	C	4	A	8.7	97.7	164	42.8	13.7	59	37.9	32.7	250	450	0.0025
pgm17,44	C	5	A	8.2	98	182.5	54.2	344.8	57.8	22.5	41.6	350	450	0.0028
pgm17,58	C	5	A	10.8	96.5	165	48	19.7	66.8	45.8	38	300	475	0.0009
pgm17,86	C	7	A	13.6	94.5	192.8	67.3	8.4	52.9	31.1	29.3	100	525	0.0036
pgm18,65	C	7	A	16.9	91.6	193	55.9	7.7	62.5	37.4	37.3	250	600	0.0054
pgm18,84	C	9	A	9.5	97.3	234	42.7	343.2	44.4	9.8	32.7	300	550	0.0041
pgm19,56	C	9	A	8.6	97.8	208.6	36	323.1	65	23.2	54.1	0	525	0.0109
pgm20,05	C	4	A	14.8	93.5	40.8	-32.1	183	-56.4	210.5	-33.8	525	600	0.0022

DIBONA Characteristic component (ChRM)

ID Sample	Component	N° of points	Anchored/Free	MAD	VAR (%)	Core Dec.	Core Inc.	Geog. Dec.	Geog. Inc.	Mag. Dec.	Mag. Inc.	Min T (°C)	Max T(°C)	J comp. (10^{-2} A/m)
md9,5	C	3	A	10.2	96.9	155.6	85.1	5.2	38.5	30	39	150	250	0.0031
md14,5	C	2	A	5.9	99	167.5	56.3	12.9	66.1	65	54.3	0	100	0.0014
md15,9	C	3	F	3	99.7	234.9	-24.2	165	19.5	160.3	1.4	425	475	0.0007
md17,8	C	5	A	6.5	98.7	351.3	-55.3	151.3	-66.9	237	-70.2	300	500	0.0057
md24,3	C	3	A	3.3	99.7	106.4	67.8	5	38.2	29.7	38.9	250	425	0.0079
md25,8	C	13	A	6.4	98.8	318	-8.3	220.4	-48	242	-31.4	150	550	0.5262
md28,0	C	5	A	5.5	99.1	112.8	68.8	318.1	33.3	337.8	57	150	375	0.0115
md38,1	C	6	A	7.1	98.5	303.1	-34	197.9	-33.5	216.3	-28.9	200	400	0.0994
md39,0	C	2	F	0	0	248.5	-50.4	215.9	-13	219.9	-2.5	250	300	0.0043
md39,9	C	3	A	10.7	96.5	53	-61.1	146.1	-33.2	168	-53.7	400	450	0.0145
md42,7	C	4	F	26.6	79.9	302.3	85.9	332.8	21.8	347.8	40.8	100	250	0.0021
md48,0	C	3	F	12.6	95.2	256.8	65.3	19.4	40.2	40.2	43.4	100	200	0.0014
md51,7	C	3	F	14.3	93.9	123.6	26.3	38.9	41.3	57.5	36.9	100	200	0.0007
d2	C	3	A	9.6	97.2	240.6	50.8	0.3	32.4	16.4	42.8	150	350	0.0012
d4	C	3	A	6.5	98.7	92.9	39.2	12.1	27.8	25.6	34.3	100	200	0.0027
mtv1	C	3	A	14.6	93.7	268.4	45	312.6	28.1	325.7	46.7	150	250	0.0013
mtv2	C	3	F	17.4	91	289.4	-43.7	223.1	-30.6	231.1	-14.2	375	425	0.0011
mtv5	C	3	A	4.4	99.4	44.6	-8.5	127.3	-45.4	152.1	-64.3	200	300	0.0024
mtv6	C	6	A	4.8	99.3	169.9	53.9	12.7	65	51.9	53.4	150	375	0.0014
mtv7	C	2	A	10.5	96.7	83.2	-68.3	153.7	-25.7	167.5	-36.8	425	450	0.0014
mtv8	C	5	F	20.3	88	59.6	7.7	168.9	-29.3	184.3	-33.8	200	375	0.0004
mtv11	C	3	F	7.8	98.2	258.5	27.5	336.4	20.8	347.7	31.5	150	300	0.0016
mtv12	C	3	F	11.4	96.1	287.2	51	13.1	9.2	16.4	5.6	400	475	0.0054
mtv13	C	11	A	3	99.7	169	29.2	351.4	53.6	25.8	52.7	250	550	0.0809
mtv51	C	2	F	0	0	94.1	29.8	24.6	11	27.3	2.7	200	250	0.0046
mtv52	C	12	A	4.2	99.5	132	43.2	10.3	36.8	27.2	31.5	200	550	0.1105
mtv53	C	5	A	4.4	99.4	181.3	18	10.4	43	31.1	36.7	200	450	0.4367
mtv55	C	3	F	7.6	98.2	336	-8.6	195.2	-66.3	234.6	-53.6	150	250	0.1271
mtv64	C	3	F	6.9	98.5	306.2	26.6	214.1	-26.2	221.9	-13.1	150	250	0.001
mtv67	C	3	A	5.2	99.2	180.7	44.6	19	69.6	60.3	54.8	150	250	0.0109
mtv68	C	3	F	8.7	97.7	107.9	77.9	29.6	13.6	32.9	3.1	200	300	0.0051
mtv69	C	2	A	10.6	96.6	157.8	65	37.9	52.4	56.6	35.8	350	375	0.0002
mtv72	C	2	A	1.5	99.9	137.6	84.5	16.6	14.1	21.5	8.6	150	200	0.0004

LEGEND	
Comp.	Type of component
N	Number of demagnetization steps used to define the magnetic component
A/F	Magnetic component anchored to origin (A) or free from origin (F)
MAD	Mean Angular Deviation of the magnetic component
%VAR	Percentage of Variance
Dec	Declination of the magnetic component
Inc	Inclination of the magnetic component

STATISTIC CORRELATION OPTIONS

NEWARK		PIGNOLA 2																							
		Option 1		Option 2		Option 3		Option 4		Option 5		Option 6		Option 7		Option 8		Option 9		Option 10		Option 11		Option 12	
Magnetostratigraphy	Duration (Myr)	M zone	Thick	M zone	Thick	M zone	Thick	M zone	Thick	M zone	Thick	M zone	Thick	M zone	Thick	M zone	Thick	M zone	Thick	M zone	Thick	M zone	Thick	M zone	Thick
E1r																									
E2n	0.4	MPA1n	164																						
E2r	0.4	MPA1r	198.5																						
E3n	0.2	MPA2n	54	MPA1n	164																				
E3r	0.2	MPA2r	186.5	MPA1r	198.5																				
E4n	0.4	MPA3n	40	MPA2n	54	MPA1n	164																		
E4r	0.2	MPA3r	103	MPA2r	186.5	MPA1r	198.5																		
E5n.1n	0.3	MPA4n	321.5	MPA3n	40	MPA2n	54	MPA1n	164																
E5n.1r	0.1	MPA4r	83	MPA3r	103	MPA2r	186.5	MPA1r	198.5																
E5n.2n	0.2	MPA5n	171.5	MPA4n	321.5	MPA3n	40	MPA2n	54	MPA1n	164														
E5r	0.4	MPA5r	54	MPA4r	83	MPA3r	103	MPA2r	186.5	MPA1r	198.5														
E6n	0.7	MPA6n	604.5	MPA5n	171.5	MPA4n	321.5	MPA3n	40	MPA2n	54	MPA1n	164												
E6r	0.3			MPA5r	54	MPA4r	83	MPA3r	103	MPA2r	186.5	MPA1r	198.5												
E7n	1.3			MPA6n	604.5	MPA5n	171.5	MPA4n	321.5	MPA3n	40	MPA2n	54	MPA1n	164										
E7r	0.3					MPA5r	54	MPA4r	83	MPA3r	103	MPA2r	186.5	MPA1r	198.5										
E8n	0.6					MPA6n	604.5	MPA5n	171.5	MPA4n	321.5	MPA3n	40	MPA2n	54	MPA1n	164								
E8r	1.7							MPA5r	54	MPA4r	83	MPA3r	103	MPA2r	186.5	MPA1r	198.5								
E9n	0.5							MPA6n	604.5	MPA5n	171.5	MPA4n	321.5	MPA3n	40	MPA2n	54	MPA1n	164						
E9r	1.1									MPA5r	54	MPA4r	83	MPA3r	103	MPA2r	186.5	MPA1r	198.5						
E10n	0.5									MPA6n	604.5	MPA5n	171.5	MPA4n	321.5	MPA3n	40	MPA2n	54	MPA1n	164				
E10r	0.4											MPA5r	54	MPA4r	83	MPA3r	103	MPA2r	186.5	MPA1r	198.5				
E11n	0.15											MPA6n	604.5	MPA5n	171.5	MPA4n	321.5	MPA3n	40	MPA2n	54	MPA1n	164		
E11r	2													MPA5r	54	MPA4r	83	MPA3r	103	MPA2r	186.5	MPA1r	198.5		
E12n	0.2													MPA6n	604.5	MPA5n	171.5	MPA4n	321.5	MPA3n	40	MPA2n	54	MPA1n	164
E12r	0.8															MPA5r	54	MPA4r	83	MPA3r	103	MPA2r	186.5	MPA1r	198.5
E13n.1n	0.6															MPA6n	604.5	MPA5n	171.5	MPA4n	321.5	MPA3n	40	MPA2n	54
E13n.1r	0.05																	MPA5r	54	MPA4r	83	MPA3r	103	MPA2r	186.5
E13n.2n	0.9																	MPA6n	604.5	MPA5n	171.5	MPA4n	321.5	MPA3n	40
E13r	0.8																			MPA5r	54	MPA4r	83	MPA3r	103
E14n	1.2																			MPA6n	604.5	MPA5n	171.5	MPA4n	321.5
E14r	1.4																					MPA5r	54	MPA4r	83
E15n	0.9																					MPA6n	604.5	MPA5n	171.5
E15r.1r	0.2																							MPA5r	54
E15r.1n	0.1																							MPA6n	604.5
E15r.2r	0.35																								
E16n	1.7																								
E16r	0.3																								
E17n	0.4																								
E17r	1.3																								
E18n	0.6																								
E18r	0.35																								
E19n	0.15																								
E19r	0.5																								
E20n	0.2																								
E20r.1r	0.2																								
E20r.1n	0.05																								
E20r.2r	1.3																								
E21n	0.5																								
E21r.1r	0.2																								
E21r.1n	0.05																								
E21r.2r	0.1																								
E21r.2n	0.05																								
E21r.3r	0.35																								
E22n.1n	0.4																								
E22n.1r	0.05																								
E22n.2n	0.3																								
E22r	0.3																								
E23n	0.9																								
E23r	0.1																								

NEWARK		Option 13		Option 14		Option 15		Option 16		Option 17		Option 18		Option 19		Option 20		Option 21		Option 22		Option 23		Option 24	
Magnetostratigraphy	Duration (Myr)	M zone	Thick	M zone	Thick	M zone	Thick	M zone	Thick	M zone	Thick	M zone	Thick	M zone	Thick	M zone	Thick	M zone	Thick	M zone	Thick	M zone	Thick	M zone	Thick
E1r																									
E2n	0.4																								
E2r	0.4																								
E3n	0.2																								
E3r	0.2																								
E4n	0.4																								
E4r	0.2																								
E5n.1n	0.3																								
E5n.1r	0.1																								
E5n.2n	0.2																								
E5r	0.4																								
E6n	0.7																								
E6r	0.3																								
E7n	1.3																								
E7r	0.3																								
E8n	0.6																								
E8r	1.7																								
E9n	0.5																								
E9r	1.1																								
E10n	0.5																								
E10r	0.4																								
E11n	0.15																								
E11r	2																								
E12n	0.2																								
E12r	0.8																								
E13n.1n	0.6	MPA1n	164																						
E13n.1r	0.05	MPA1r	198.5																						
E13n.2n	0.9	MPA2n	54	MPA1n	164																				
E13r	0.8	MPA2r	186.5	MPA1r	198.5																				
E14n	1.2	MPA3n	40	MPA2n	54	MPA1n	164																		
E14r	1.4	MPA3r	103	MPA2r	186.5	MPA1r	198.5																		
E15n	0.9	MPA4n	321.5	MPA3n	40	MPA2n	54	MPA1n	164																
E15r.1r	0.2	MPA4r	83	MPA3r	103	MPA2r	186.5	MPA1r	198.5																
E15r.1n	0.1	MPA5n	171.5	MPA4n	321.5	MPA3n	40	MPA2n	54	MPA1n	164														
E15r.2r	0.35	MPA5r	54	MPA4r	83	MPA3r	103	MPA2r	186.5	MPA1r	198.5														
E16n	1.7	MPA6n	604.5	MPA5n	171.5	MPA4n	321.5	MPA3n	40	MPA2n	54	MPA1n	164												
E16r	0.3			MPA5r	54	MPA4r	83	MPA3r	103	MPA2r	186.5	MPA1r	198.5												
E17n	0.4			MPA6n	604.5	MPA5n	171.5	MPA4n	321.5	MPA3n	40	MPA2n	54	MPA1n	164										
E17r	1.3					MPA5r	54	MPA4r	83	MPA3r	103	MPA2r	186.5	MPA1r	198.5										
E18n	0.6					MPA6n	604.5	MPA5n	171.5	MPA4n	321.5	MPA3n	40	MPA2n	54	MPA1n	164								
E18r	0.35							MPA5r	54	MPA4r	83	MPA3r	103	MPA2r	186.5	MPA1r	198.5								
E19n	0.15							MPA6n	604.5	MPA5n	171.5	MPA4n	321.5	MPA3n	40	MPA2n	54	MPA1n	164						
E19r	0.5									MPA5r	54	MPA4r	83	MPA3r	103	MPA2r	186.5	MPA1r	198.5						
E20n	0.2									MPA6n	604.5	MPA5n	171.5	MPA4n	321.5	MPA3n	40	MPA2n	54	MPA1n	164				
E20r.1r	0.2											MPA5r	54	MPA4r	83	MPA3r	103	MPA2r	186.5	MPA1r	198.5				
E20r.1n	0.05											MPA6n	604.5	MPA5n	171.5	MPA4n	321.5	MPA3n	40	MPA2n	54	MPA1n	164		
E20r.2r	1.3													MPA5r	54	MPA4r	83	MPA3r	103	MPA2r	186.5	MPA1r	198.5		
E21n	0.5													MPA6n	604.5	MPA5n	171.5	MPA4n	321.5	MPA3n	40	MPA2n	54	MPA1n	164
E21r.1r	0.2															MPA5r	54	MPA4r	83	MPA3r	103	MPA2r	186.5	MPA1r	198.5
E21r.1n	0.05															MPA6n	604.5	MPA5n	171.5	MPA4n	321.5	MPA3n	40	MPA2n	54
E21r.2r	0.1																	MPA5r	54	MPA4r	83	MPA3r	103	MPA2r	186.5
E21r.2n	0.05																	MPA6n	604.5	MPA5n	171.5	MPA4n	321.5	MPA3n	40
E21r.3r	0.35																			MPA5r	54	MPA4r	83	MPA3r	103
E22n.1n	0.4																			MPA6n	604.5	MPA5n	171.5	MPA4n	321.5
E22n.1r	0.05																					MPA5r	54	MPA4r	83
E22n.2n	0.3																					MPA6n	604.5	MPA5n	171.5
E22r	0.3																							MPA5r	54
E23n	0.9																							MPA6n	604.5
E23r	0.1																								

T-VALUE

Options	R	t-value
Option 1	0.674150	2.738241
Option 2	0.713510	3.055085
Option 3	0.322390	1.021723
Option 4	0.001064	0.003192
Option 5	-0.382530	-1.242057
Option 6	-0.519850	-1.825620
Option 7	-0.358790	-1.153149
Option 8	-0.160100	-0.486576
Option 9	0.108760	0.328227
Option 10	0.421240	1.393375
Option 11	0.180860	0.551678
Option 12	-0.277120	-0.865247
Option 13	0.439070	1.466087
Option 14	-0.215130	-0.660864
Option 15	0.167620	0.510077
Option 16	-0.400550	-1.311451
Option 17	-0.354430	-1.137108
Option 18	-0.246160	-0.761925
Option 19	-0.083658	-0.251857
Option 20	-0.322480	-1.022041
Option 21	-0.107330	-0.323861
Option 22	0.067149	0.201903
Option 23	0.062290	0.187234
Option 24	0.838320	4.613095

Confidence Limit (%)	t-value
90%	1.383
95%	1.833

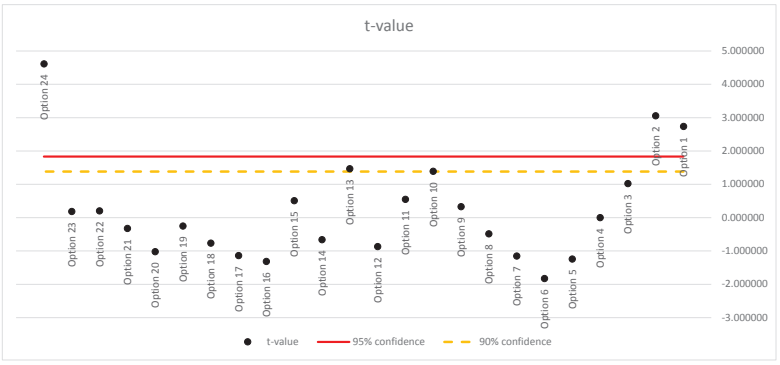

APPENDIX B

GEOMAGNETIC POLARITY TIME SCALE

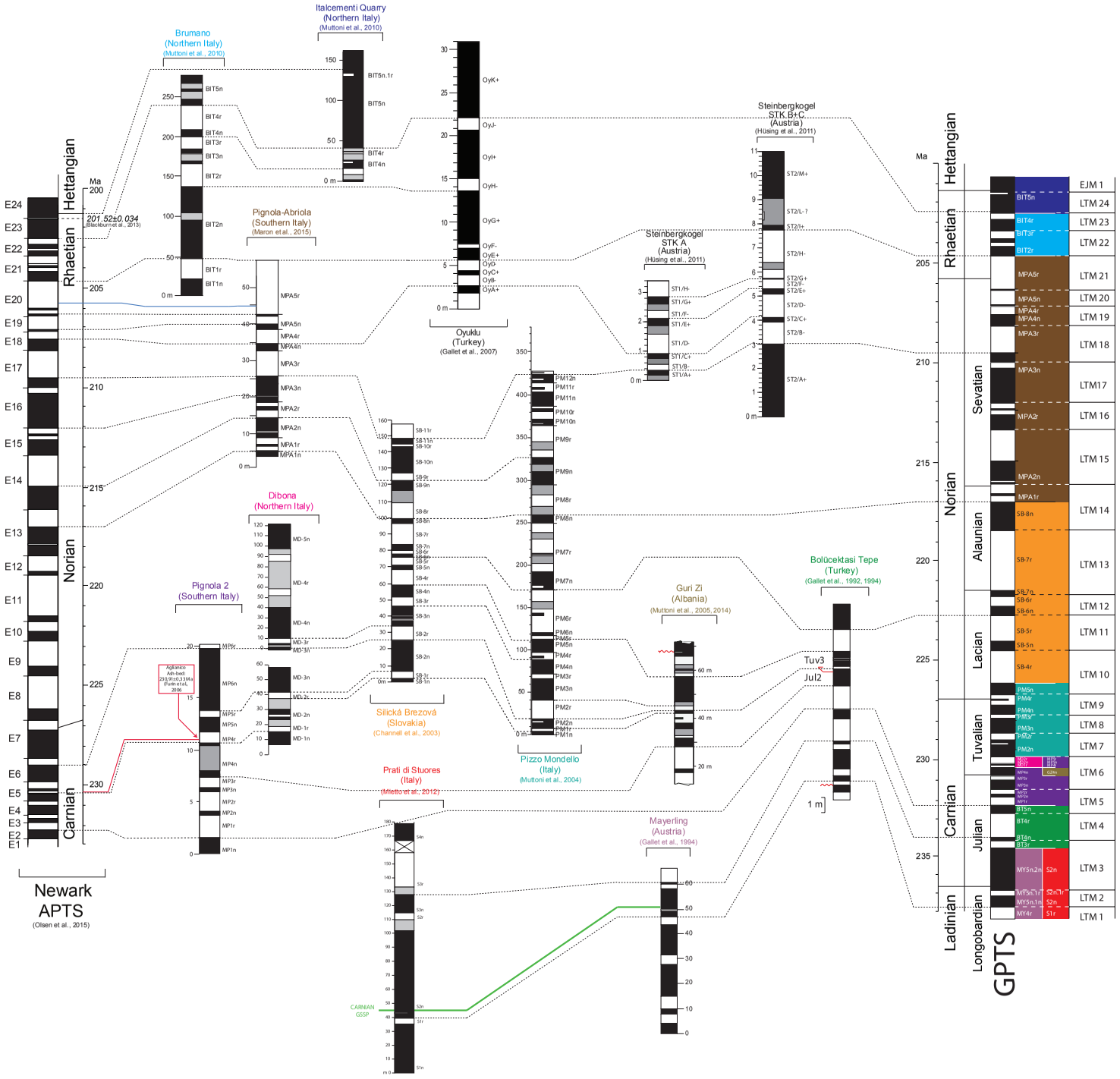

The Geomagnetic Polarity Time Scale (GPTS) here proposed (on the right) is based on the magnetostratigraphic correlations between Tethyan marine sections and the Newark APTS (Olsen and Kent, 1999; Olsen et al., 2015). The marine sections considered are Brumano/Italcementi Quarry (Muttoni et al., 2010), Pignola-Abriola (Chapter 4.1.1; Maron et al., 2015; Rigo et al., 2015), Steinbergkogel (Hüsing et al., 2011), Pizzo Mondello (Muttoni et al., 2004), Silická Brezová (Channell et al., 2003), Pignola-2 (Chapter 4.2.1), Dibona (Chapter 4.2.1), Guri Zi (Muttoni et al., 2005, 2014), Bolücektasi Tepe (Gallet et al., 1992, 1994), Prati di Stuores/Stuores Wiesen (Mietto et al., 2012), and Mayerling (Gallet et al., 1994). A composite magnetostratigraphy based on these Tethyan marine sections have been compared to the Newark APTS, following the statistical correlations between the APTS and Pizzo Mondello (Muttoni et al., 2004), Pignola-Abriola (Chapter 4.1.1; Maron et al., 2015), and Pignola-2 (Chapter 4.2.1). The correlation between the APTS and Brumano/Italcementi Quarry is based on the proposal of Muttoni et al (2004) and is confirmed by the correlation with the Pignola-Abriola section (Chapter 4.1.1; Maron et al., 2015). The Newark APTS does not reach the Ladinian/Carnian boundary, so is not possible to date directly the magnetostratigraphy of Prati di Stuores and Mayerling. In this interval, the time scale is calculated assuming a constant sedimentation rate for Prati di Stuores and Mayerling (both deposited in a basin, where the accumulation rates normally show slight fluctuations) and as a tie-point the U/Pb age of 237.773±0.052 Ma at the Ladinian/Carnian boundary (Mietto et al., 2012). The colored intervals besides the GPTS represent the contribution of the considered sections in the Late Triassic composite magnetostratigraphy (matching the colored names above each section), containing the names of the considered magnetozones.
For a detailed description of the GPTS see Chapter 5.2.

ATTACHED PUBLICATIONS

Maron, M., Rigo, M., Bertinelli, A., Katz, M.E., Godfrey, L., Zaffani, M., and Muttoni, G., 2015. Magnetostratigraphy, biostratigraphy and chemostratigraphy of the Pignola-Abriola section: New constraints for the Norian-Rhaetian boundary. *Geological Society of America Bulletin, v. 127, p. 962-974.*

Maron, M., Muttoni, G., Dekkers, M.J., Mazza, M., Roghi, G., Breda, A., Krijgsman, W., and Rigo, M., submitted. Improving the Geomagnetic Polarity Time Scale for the Late Triassic: new magneto-biostratigraphic constraints from Pignola-2 and Dibona sections, Italy. *Newsletter on Stratigraphy.*

Geological Society of America Bulletin

Magnetostratigraphy, biostratigraphy, and chemostratigraphy of the Pignola-Abriola section: New constraints for the Norian-Rhaetian boundary

Matteo Maron, Manuel Rigo, Angela Bertinelli, Miriam E. Katz, Linda Godfrey, Mariachiara Zaffani and Giovanni Muttoni

Geological Society of America Bulletin 2015;127, no. 7-8;962-974
doi: 10.1130/B31106.1

Notes

Magnetostratigraphy, biostratigraphy, and chemostratigraphy of the Pignola-Abriola section: New constraints for the Norian-Rhaetian boundary

Matteo Maron[1,†], Manuel Rigo[1], Angela Bertinelli[2], Miriam E. Katz[3], Linda Godfrey[4], Mariachiara Zaffani[1], and Giovanni Muttoni[5]

[1]*Department of Geosciences, University of Padova, via G. Gradenigo 6, 35131 Padova, Italy*
[2]*Department of Physics and Geology, University of Perugia, via G. Pascoli, 06123 Perugia, Italy*
[3]*Department of Earth and Environmental Sciences, Rensselaer Polytechnic Institute, 110 8th Street, Troy, New York 12180, USA*
[4]*Department of Earth and Planetary Sciences, Rutgers University, Piscataway, New Jersey 08854, USA*
[5]*Department of Earth Sciences, University of Milan, via L. Mangiagalli 34, 20133 Milan, Italy*

ABSTRACT

A detailed magnetostratigraphic investigation of the Pignola-Abriola section of Norian to Rhaetian age permits the identification of 22 magnetic polarity reversals grouped in 10 magnetozones. We correlate the magnetostratigraphy of the Pignola-Abriola section with the Newark astrochronological polarity time scale (APTS). In total, 19 correlation options were tested, and only one (option 7) yielded a statistically significant correlation that was consistent with the available information on the stratigraphic age of the Newark APTS. After some adjustments to minimize erratic variations in sediment accumulation rates, a final correlation (option 7.1) was used to generate an age model of sedimentation for the Pignola-Abriola section. The Pignola-Abriola section has been correlated with Rhaetian sections from the literature, notably the current global boundary stratotype section and point candidate for the base of the Rhaetian at Steinbergkogel, Austria, where the Norian-Rhaetian boundary is proposed to be placed at a stratigraphic level containing the first appearance datum (FAD) of conodont *Misikella posthernsteini*, traced on the Newark APTS to ca. 209–210 Ma. Issues regarding the taxonomy of *M. posthernsteini*, a species characterized by transitional forms with its ancestor *Misikella hernsteini*, lead us to propose the alternative option of placing the Norian-Rhaetian boundary at a prominent negative $\delta^{13}C_{org}$ spike observed in the Pignola-Abriola section at meter 44.5, 50 cm below the level containing the FAD of *M. posthernsteini* sensu stricto and close to the base of radiolarian *Proparvicingula moniliformis* zone. This level has been magnetostratigraphically correlated to Newark magnetozone E20r.2r at ca. 205.7 Ma. Assuming an age of ca. 201.3 Ma for the Triassic-Jurassic boundary, the Rhaetian Stage would have a duration of ~4.4 m.y.

INTRODUCTION

Current generations of time scales for the Triassic System (e.g., Ogg, 2012) are based on magnetostratigraphic correlations between marine sections and the continental Newark astrochronological polarity time scale (APTS). For marine sections, magnetostratigraphy is tied to stage boundaries that are defined biostratigraphically (e.g., Channell et al., 2003; Muttoni et al., 2004; Gallet et al., 2007), whereas the magnetostratigraphy of the Newark APTS (Kent et al., 1995; Kent and Olsen, 1999; Olsen and Kent, 1999; Olsen et al., 2011) is constrained by terrestrial biostratigraphy such as sporomorphs, tetrapod footprints, and conchostracans (e.g., Cornet, 1977, 1993; Olsen and Sues, 1986; Fowell et al., 1994; Lucas and Huber, 1993; Kozur and Weems, 2005, 2010; Lucas et al., 2012).

The base of the Rhaetian Stage (Norian-Rhaetian boundary), pending formal designation by the International Commission on Stratigraphy, is currently proposed at a stratigraphic level of the Steinbergkogel section (Austria) containing the first appearance datum (FAD) of the conodont *Misikella posthernsteini* (Krystyn, 2010). This level was magnetostratigraphically correlated to magnetozone E16r of the Newark APTS (Hüsing et al., 2011), in substantial agreement with previous inferences based on magnetostratigraphic correlations between the Pizzo Mondello (Italy) and Silická Brezová (Slovakia) marine sections, which are Carnian–Norian in age, and the Newark APTS (Muttoni et al., 2004; Channell et al., 2003). The base of Newark magnetozone E16r is currently dated at ca. 210.3 Ma as the result of rescaling the Newark APTS (Kent and Olsen, 1999) from the base of the Orange Mountain Basalts of the Central Atlantic magmatic province (CAMP), recently dated at ca. 201.5 Ma (Blackburn et al., 2013). This would imply a duration for the Rhaetian Stage of ~9 m.y., in broad agreement with the long-Rhaetian option of Muttoni et al. (2010; see also Muttoni et al., 2004) and in contrast to the short-Rhaetian option (~2 m.y.) of Gallet et al. (2007; see discussions in Muttoni et al., 2010; Hüsing et al., 2011). The short-Rhaetian option was recently revived by Callegaro et al. (2012), who associated negative $^{87}Sr/^{86}Sr$ and $^{187}Os/^{188}Os$ (Cohen and Coe, 2007; Kuroda et al., 2010) excursions observed starting at the base of the Rhaetian (defined by the occurrence of *M. posthernsteini*) with the emplacement of the CAMP which was considered to have started as early as ca. 202–203 Ma on the basis of $^{40}Ar/^{39}Ar$ dates (Marzoli et al., 2011; Callegaro et al., 2012), albeit recent U-Pb dates suggest rapid emplacement around ca. 201.56 Ma, coincident with the end-Triassic extinction event (Blackburn et al., 2013).

The debate over the duration of the Rhaetian (and Norian) is not yet settled, with two options proposed in the *Geological Time Scale 2012* (Ogg, 2012): The long-Tuvalian option places the Norian-Rhaetian boundary at 205.4 Ma and the Carnian-Norian boundary at 221 Ma, whereas the long-Rhaetian option has a Norian-Rhaetian boundary at 209.5 Ma and a Carnian-Norian boundary at 228.4 Ma. These alternative options arise from different approaches to time scale construction. The long-Tuvalian option is grounded in biostratigraphic correlations of terrestrial groups (conchostracans, pollens, tetrapods) between the

†E-mail: matteo.maron.1@studenti.unipd.it.

GSA Bulletin; July/August 2015; v. 127; no. 7/8; p. 962–974; doi: 10.1130/B31106.1; 7 figures; 2 tables; Data Repository item 2015069; published online 3 February 2015.

continental sequences of the Germanic Basin and the Newark Supergroup–based APTS (Lucas et al., 2012). The long-Rhaetian option is based on magnetostratigraphic correlations between marine sections bearing stage-defining fossils (conodonts, ammonoids) and the Newark APTS (Channell et al., 2003; Muttoni et al., 2004, 2010; Hüsing et al., 2011). In our opinion, the terrestrial correlation approach as the basis for the long-Tuvalian option (Lucas et al., 2012) is flawed by inherent difficulties in correlating terrestrial associations of, e.g., freshwater clam shrimps (conchostracans) to marine-based stage boundaries. The base of the Rhaetian was assigned directly in the Newark Supergroup using sporomorphs (base of the Upper Balls Bluff–Upper Passaic palynofloral zone of Cornet 1977, 1993), although the typical Rhaetian taxa of Europe and Greenland have not been found in the Newark Supergroup (Cornet, 1977). As a consequence, the Rhaetian as originally defined in the Newark Supergroup cannot be related to the Rhaetian as proposed by Krystyn (2010) and reported in the *Geological Time Scale 2012* (Ogg, 2012).

In this paper, we contribute to the definition of the Norian-Rhaetian boundary by presenting new biostratigraphic, magnetostratigraphic, and chemostratigraphic data from the Pignola-Abriola section of Italy. This section records the FAD of *M. posthernsteini*, occurring in the lower *Proparvicingula moniliformis* radiolarian zone (Giordano et al., 2010). We date these events by means of magnetostratigraphic correlation with the Newark APTS, while addressing in detail the taxonomic complexities vexing the use of the conodont *M. posthernsteini* as proxy for the Norian-Rhaetian boundary level. We also illustrate the occurrence of a prominent negative $\delta^{13}C_{org}$ excursion at meter level 44.5, ~0.5 m below the FAD of *M. posthernsteini* (within the base of the *P. moniliformis* zone), which serves as a useful geochemical proxy for the Norian-Rhaetian boundary level. The levels containing the negative $\delta^{13}C_{org}$ excursion and the FAD of *M. posthernsteini* are traced to Newark magnetozone E20r.2r at ca. 205.7 Ma, providing a younger age for the Norian-Rhaetian boundary relative to Hüsing et al. (2011), and very similar to the Norian-Rhaetian boundary in the long-Tuvalian option described in Ogg (2012).

GEOLOGICAL SETTING

The Pignola-Abriola section crops out on the western side of Mount Crocetta, along the road SP5 connecting the village of Pignola to Abriola (Potenza, southern Italy; Fig. 1, section A, coordinates: 40°33′23.50″N, 15°47′1.71″E). The road section is ~58 m thick (Fig. 2, left panel) and is complemented by an ancillary 7-m-thick

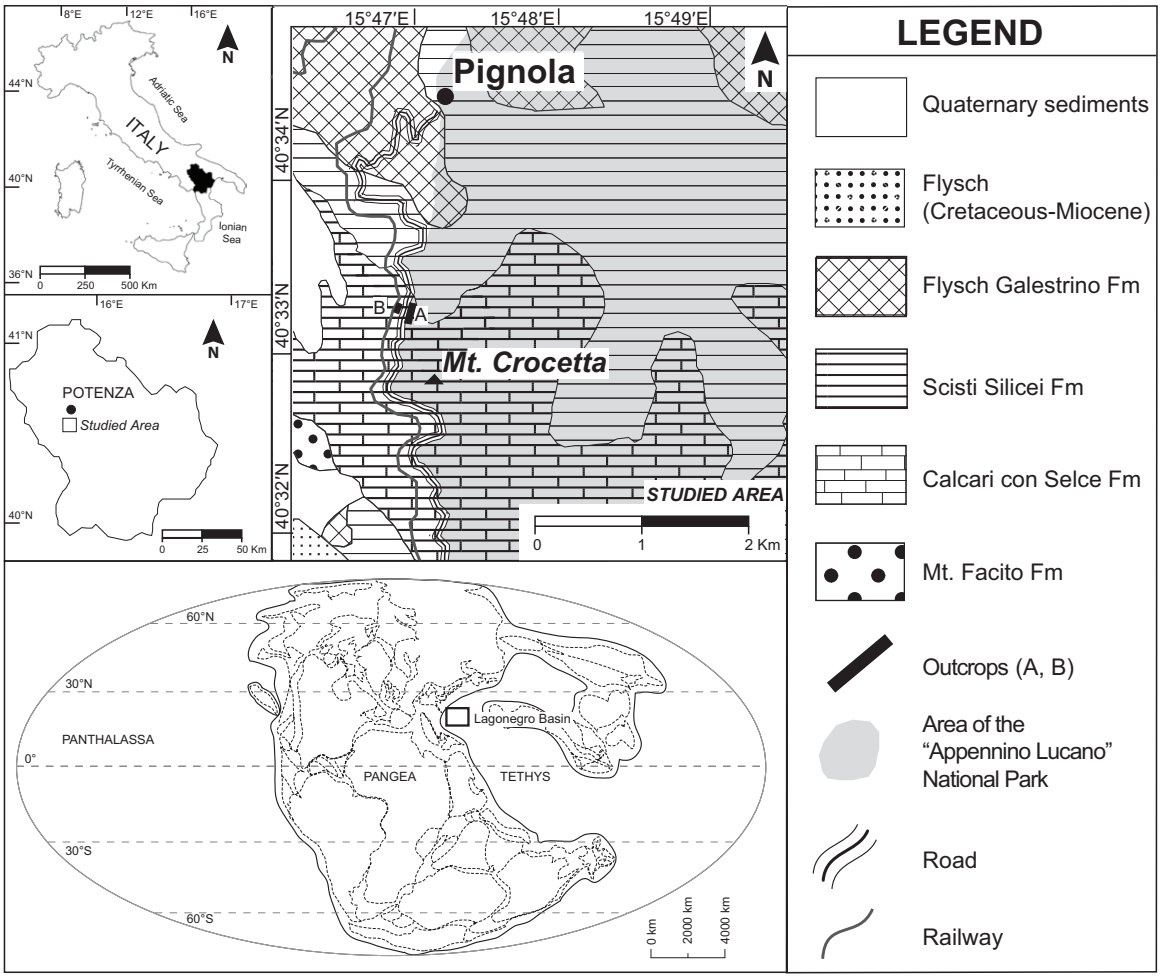

Figure 1. The Pignola-Abriola sections (A, B) are located in the southern Apennines, near Potenza (southern Italy). The main section (A) crops out on the western flank of Mount Crocetta, along the main road SP5 connecting the towns of Pignola and Abriola (40°33′23.50″N, 15°47′1.71″E), whereas the auxiliary subsection (B) crops out close to an unused railway tunnel located ~10 m below the SP5 road level (40°33′24.74″N, 15°46′59.59″E).

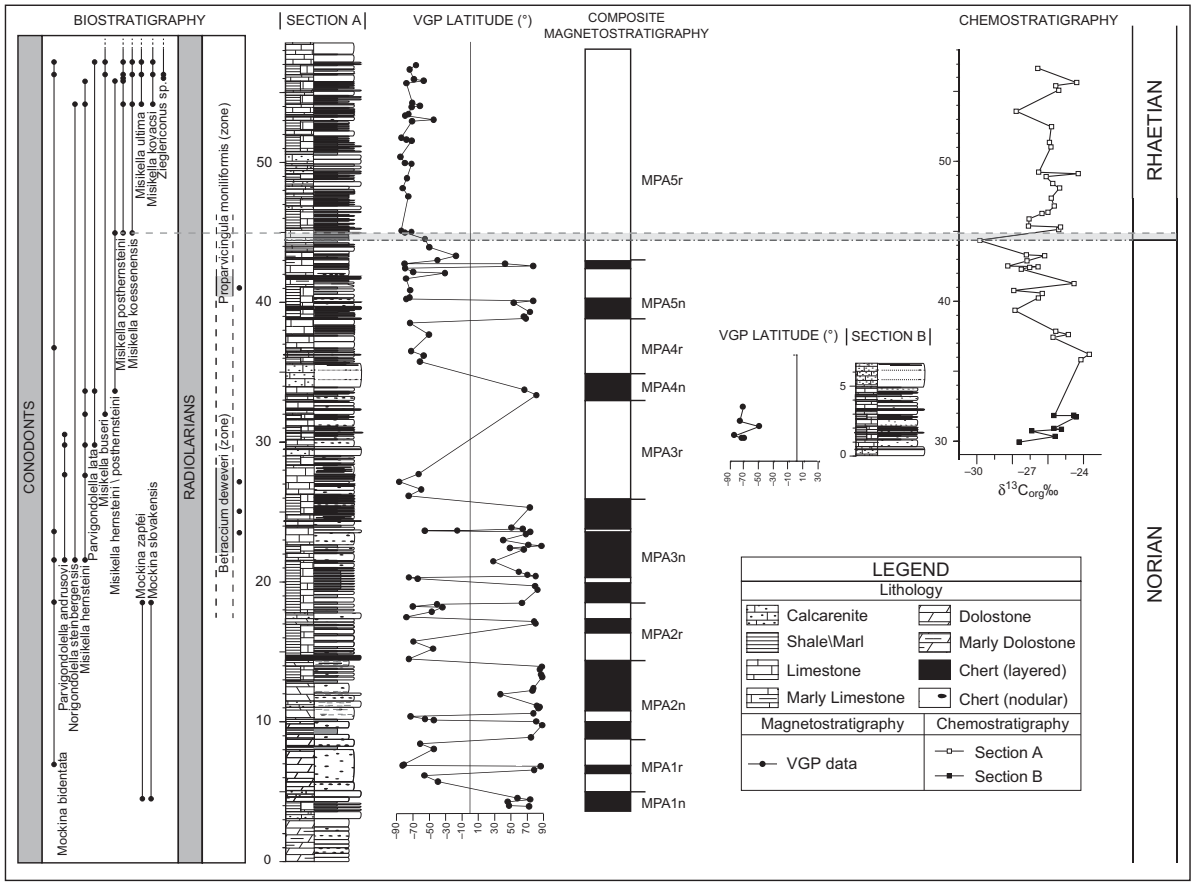

Figure 2. The Pignola-Abriola sections. From left to the right: conodont and radiolarian biostratigraphy (see Table 1 for key species), lithostratigraphy, virtual geomagnetic pole (VGP) latitudes calculated from characteristic remanent magnetization (ChRM) component directions, and derived magnetostratigraphy and chemostratigraphy ($\delta^{13}C_{org}$) of the Pignola-Abriola section. To the right is lithostratigraphy and VGP latitudes of the auxiliary subsection B. Black is normal polarity, and white is reverse polarity. The levels containing the first appearance datum (FAD) of conodont *Misikella posthernsteini* sensu stricto and the marked decrease in the $\delta^{13}C_{org}$ to ~–30‰ used to define the Norian-Rhaetian boundary are highlighted by dashed horizontal lines.

subsection (Fig. 2, right panel) outcropping close to a unused railway tunnel located ~10 m below the SP5 road level (Fig. 1, section B, coordinates: 40°33′24.74″N, 15°46′59.59″E). The stratigraphic sequence is composed of the Calcari con Selce (i.e., Cherty Limestone) Formation, which was deposited in the Lagonegro Basin, a branch of the western Tethys Ocean characterized by pelagic sedimentation since the Permian (Finetti, 1982, 2005; Catalano et al., 2001; Ciarapica and Passeri, 2002, 2005; Argnani, 2005; Rigo et al., 2012). The Calcari con Selce Formation consists of thinly bedded cherty hemipelagic to pelagic limestones (mudstones, wackestones, and rare packstones), interbedded with shales and marls, with common radiolarians, conodonts, and sporadic bivalves. The lower part of the section is dominated by cherty limestones, often dolomitized, intercalated with very thin marls or clayey levels (Fig. 2). The upper portion is instead dominated by an alternation of silicified limestones and black to brown or greenish, thinly laminated shales (Fig. 2), which are rich in organic matter, indicating deposition in dysoxic or anoxic conditions. Calcarenitic intercalations are also present through the section (Fig. 2). In particular, a 1.5-m-thick calcarenitic bank at ~35 m from the base of the measured section has been used as a lithostratigraphic marker to correlate the Pignola-Abriola road section (Fig. 2, left panel) to the railway tunnel subsection (Fig. 2, right panel).

BIOSTRATIGRAPHY

The fossil content of the Pignola-Abriola section consists mainly of conodonts and pyritized radiolarians. Here, we present an updated conodont and radiolarian biostratigraphy (Fig. 2) after recent biostratigraphic data published by Rigo et al. (2005), Bazzucchi et al. (2005), and Giordano et al. (2010).

Conodonts are well distributed along the entire section (representative specimens are listed in Table 1) and are characterized by a conodont alteration index (CAI) of 1.5 (Epstein et al., 1977; Bazzucchi et al., 2005; Rigo et al., 2005). The following main events have been recognized (Fig. 2):

(1) the first occurrence (FO) of *Mockina bidentata* at meter 7;

(2) the FO of *Misikella hernsteini* at meter 21.5, associated with the FO of *Parvigondolella andrusovi*;

(3) the FO of the *Misikella hernsteini/posthernsteini* morphocline at meter 33.5;

(4) the FO of *Misikella buseri* at meter 32;

(5) the FAD of *Misikella posthernsteini* at meter 45 in sample PIG24, in association with *Misikella koessenensis*; and

(6) the FO of *Misikella ultima* at meter 54.

The radiolarian associations are well preserved and conform to the biozonation proposed by Carter (1993):

(1) Sample PR14 at meter 25 yielded a radiolarian assemblage referable to the *Betraccium deweveri* zone (Carter, 1993) and consisting of *Betraccium deweveri* Pessagno and Blome, *Praemesotaturnalis gracilis* Kozur and Mostler, *Tetraporobrachia* sp. aff. *T. composita* Carter, *Ayrtonius elizabethae* Sugiyama, *Citriduma* sp. A sensu Carter (1993), *Globolaxtorum* sp. cf. *G. hullae* Yeh and Cheng, *Lysemela* sp. cf. *L. olbia* Sugiyama, *Livarella valida* Yoshida and *Livarella* sp. sensu Carter (1993) (Giordano et al., 2010); a similar assemblage was found also in sample PR15 at meter 23.5, and sample PR13 at meter 27. The presence of *Globolaxtorum* sp. cf. *G. hullae* Yeh and Cheng in this assemblage is atypical, because the genus *Globolaxtorum* is usually referred only to the *Proparvicingula moniliformis* and *Globolaxtorum tozeri* zones (O'Dogherty et al., 2009).

(2) Sample PA25 at meter 41 yielded a radiolarian assemblage referable to the *Proparvicingula moniliformis* zone assemblage 1 (U.A. 2–5 *in* Carter, 1993) for the presence of *Fontinella primitiva* Carter, *Praemesosaturnalis* sp. cf. *P. sandspitensis* Blome, *Globolaxtorum* sp. cf. *G. hullae* Yeh and Cheng, and *Livarella densiporata* Kozur and Mostler (Bazzucchi et al., 2005; Giordano et al., 2010).

The Norian-Rhaetian boundary is conventionally placed in stratigraphic levels where the FAD of *Misikella posthernsteini* is documented (Krystyn, 2010), which is a phylogenetic descendent of *M. hernsteini* (e.g., Mostler et al., 1978; Kozur and Mock, 1991; Giordano et al., 2010). The transition from drop-shaped to heart-shaped basal cavity along with a reduction of the number of blade denticles characterize the evolution of the *M. hernsteini*/*posthernsteini* morphocline (Giordano et al., 2010). Specimens characterized by an evident furrow on the backside of the cusp and the associated inflection of the posterior margin of the basal cavity are here considered *Misikella posthernsteini* sensu stricto, as suggested by Giordano et al. (2010). At Pignola-Abriola, the presence of the *Misikella hernsteini*/*posthernsteini* morphocline, as well as the presence of the FAD of *M. posthernsteini* sensu stricto (m 45, sample PIG24) provide a reliable (and continuous) biostratigraphic signal. Furthermore, in the Pignola-Abriola section, the conodont *Misikella posthernsteini* sensu stricto appears 4 m above the base of radiolarian *Proparvicingula moniliformis* zone assemblage 1 (Fig. 2), which is commonly adopted to define the early Rhaetian (e.g., Carter, 1993; Bertinelli et al., 2005; Giordano et al., 2010).

Table 1 (*on following page*). Scanning electron microscope (SEM) micrographs of Upper Norian and Rhaetian radiolarians and conodonts from the Calcari con Selce Formation, Pignola-Abriola section. Radiolarians: samples PR13, PR14, and PR15 are referred to the *Betraccium deweveri* zone; sample PA25 is referred to the *Proparvicingula moniliformis* zone, assemblage 1. Scale bar = 100 µm for 1–2, 7, 9, 11–14; 112.5 µm for 3–5, 8; 150 µm for 6, 10 (after Bazzucchi at al., 2005; Giordano et al., 2010, modified). 1–2—*Betraccium deweveri* Pessagno and Blome, sample PR14. 3—*Praemesotaturnalis gracilis* (Kozur and Mostler), sample PR14. 4—*Tetraporobrachia* sp. aff. *T. composita* Carter, sample PR14. 5—*Ayrtonius elizabethae* Sugiyama, sample PR15. 6—*Citriduma* sp. A, sensu Carter (1993), sample PR13. 7—*Globolaxtorum* sp. cf. *G. hullae* (Yeh and Cheng), sample PR14. 8—*Lysemela* sp. cf. *L. olbia* Sugiyama, sample PR15. 9—*Livarella valida* Yoshida, sample PR15. 10—*Livarella* sp., sensu Carter (1993), sample PR14. 11—*Fontinella primitiva* Carter, section sample PA 25. 12—*Praemesosaturnalis* sp. cf. *P. sandspitensis* (Blome), sample PA25. 13—*Globolaxtorum hullae* (Yeh and Cheng), sample PA25. 14—*Livarella densiporata* Kozur and Mostler, sample PA25. Conodonts: Scale bar = 75 µm (after Bazzucchi at al., 2005; Giordano et al., 2010, modified): 15 (a, b, c)—*Mockina zapfei* (Kozur), sample PIG 0. 16 (a, b, c)—*Mockina slovakensis* (Kozur), sample PIG 0. 17 (a, b, c)—*Misikella hernsteini* (Mostler), sample PIG 16. 18 (a, b)—*Misikella posthernsteini* Kozur and Mock, sample PIG 24. 19 (a, b)—*Misikella kovacsi* Orchard, sample PIG 40. 20 (a, b, c)—*Misikella ultima* Kozur and Mock, sample PIG 40.

GEOCHEMISTRY

In total, 41 samples, mostly black to brown shales, from the upper portion of the Pignola-Abriola section (from meter 30 to the top of the section) were analyzed for $\delta^{13}C_{org}$ (worksheet 1 in GSA Data Repository[1]). The rock samples were pulverized and acid-washed with 10% HCl in a 70 °C water bath for 3 h, and the process was repeated at least three times to thoroughly remove pyrite and carbonates. The samples were subsequently neutralized with high-purity water, dried at 30 °C overnight, and then wrapped in tin capsules and analyzed for their isotopic composition. The analyses were carried out using a GVI Isoprime continuous flow–isotope ratio mass spectrometer (CF-IRMS) at Rutgers University, adding multiple blank capsules and isotope standards for each batch of isotopic analyses (NBS 22 = –30.03‰; Coplen et al., 2006) plus a matrix matched in-house standard. Standard deviations for $\delta^{13}C_{org}$ standards during the period of analysis were better than $\sigma = 0.2‰$.

The $\delta^{13}C_{org}$ values of the Pignola-Abriola section are between –29.95‰ and –23.70‰ (Fig. 2). After a moderate increase in $\delta^{13}C_{org}$ (from ~–27.5‰ to –24‰ from meter 30 to 36), a large decrease to ~–30‰ was recorded for meter 36 to meter 44.5, immediately followed by a rapid return to higher values (~–25‰, ~20 cm above). A subsequent decrease of ~2‰ is recorded at meter 53.5 (close to the level containing the FO of *Misikella ultima*; Fig. 2). Notably, the low $\delta^{13}C_{org}$ of ~–30‰ at meter 44.5 is just below the level containing the FAD of *Misikella posthernsteini* sensu stricto, and within the base of the *Proparvicingula moniliformis* zone (Fig. 2).

[1]GSA Data Repository item 2015069, $\delta^{13}C_{org}$ data, paleomagnetic data, Newark and Pignola-Abriola correlation statistics, and isothermal remanent magnetization statistics, is available at http://www.geosociety.org/pubs/ft2015.htm or by request to editing@geosociety.org.

PALEOMAGNETISM

In total, 220 oriented core samples were collected from the Pignola-Abriola section and analyzed at the Alpine Laboratory of Paleomagnetism (Peveragno, Italy). Rock magnetic properties were studied on a representative set of samples by means of thermal decay of a three-component isothermal remanent magnetization (IRM) imparted at fields of 2.5 T, 0.4 T, and 0.12 T (Lowrie, 1990) and IRM acquisition curves.

The lower part of the section (samples P1.34, P3.10, P3.43; Fig. 3A) is characterized by a high-coercivity mineral with maximum unblocking temperatures (T_B) of 650–675 °C, attributed to hematite, coexisting with a lower-coercivity mineral with T_B of 525–575 °C, interpreted as magnetite; an inflection at ~350 °C in the 0.4 T curve observed in sample P1.34 suggests the presence of iron sulfides. Samples from the upper part of the section (GNM497 at 33 m; GNM48 at 43.5 m; GNM119 at 57 m) appear dominated by the high-coercivity hematite phase (Fig. 3A). IRM curves of these samples show no tendency to saturate even at applied fields of 2.5 T (Fig. 3B). The cumulative log-Gaussian (CLG) analysis (Kruiver et al., 2001) reveals the presence in these samples of two magnetic phases with contrasting coercivities: a high-coercivity phase with coercivity of remanence ($B_{1/2}$) = 1.6–2 T, which accounts

TABLE 1. RADIOLARIANS AND CONODONTS FROM THE PIGNOLA-ABRIOLA SECTION

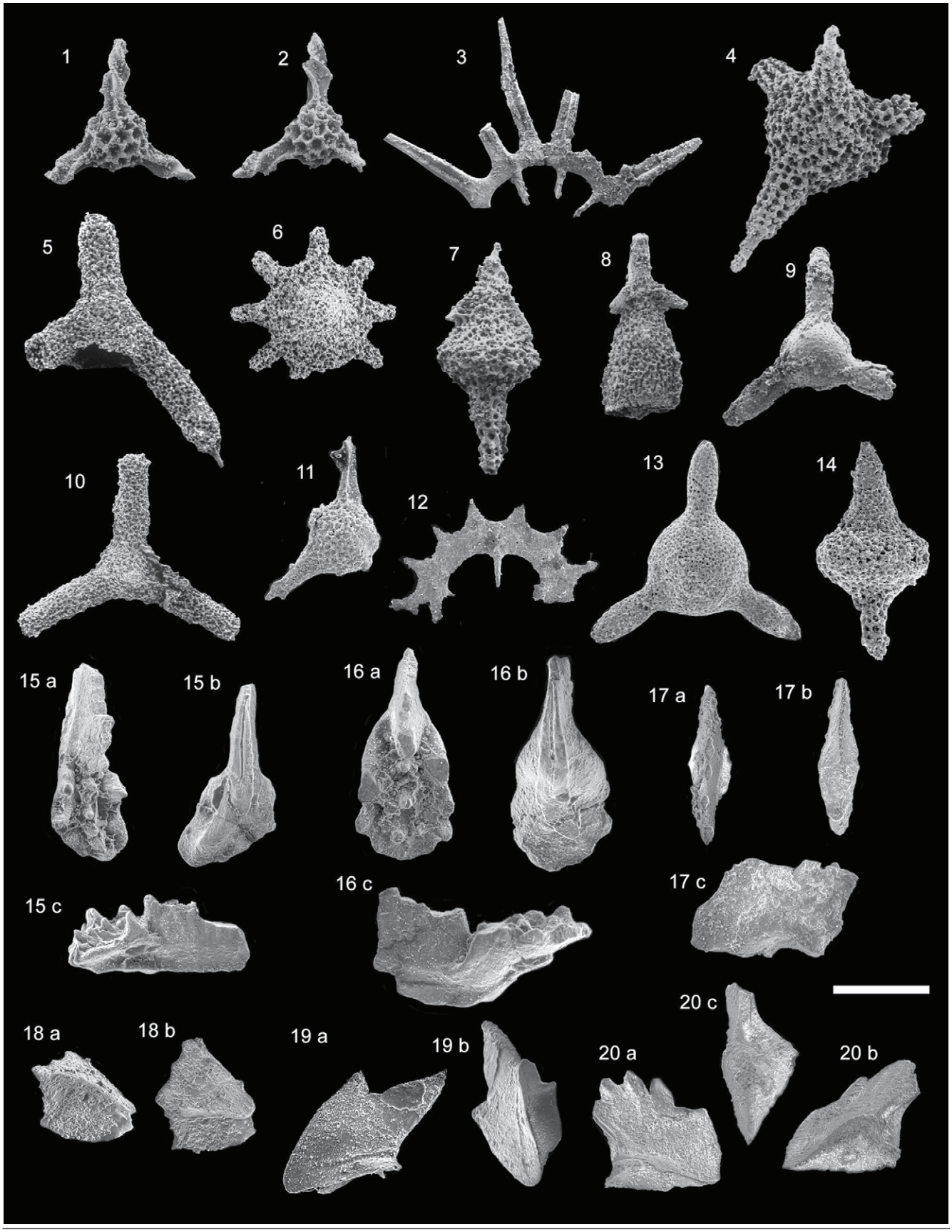

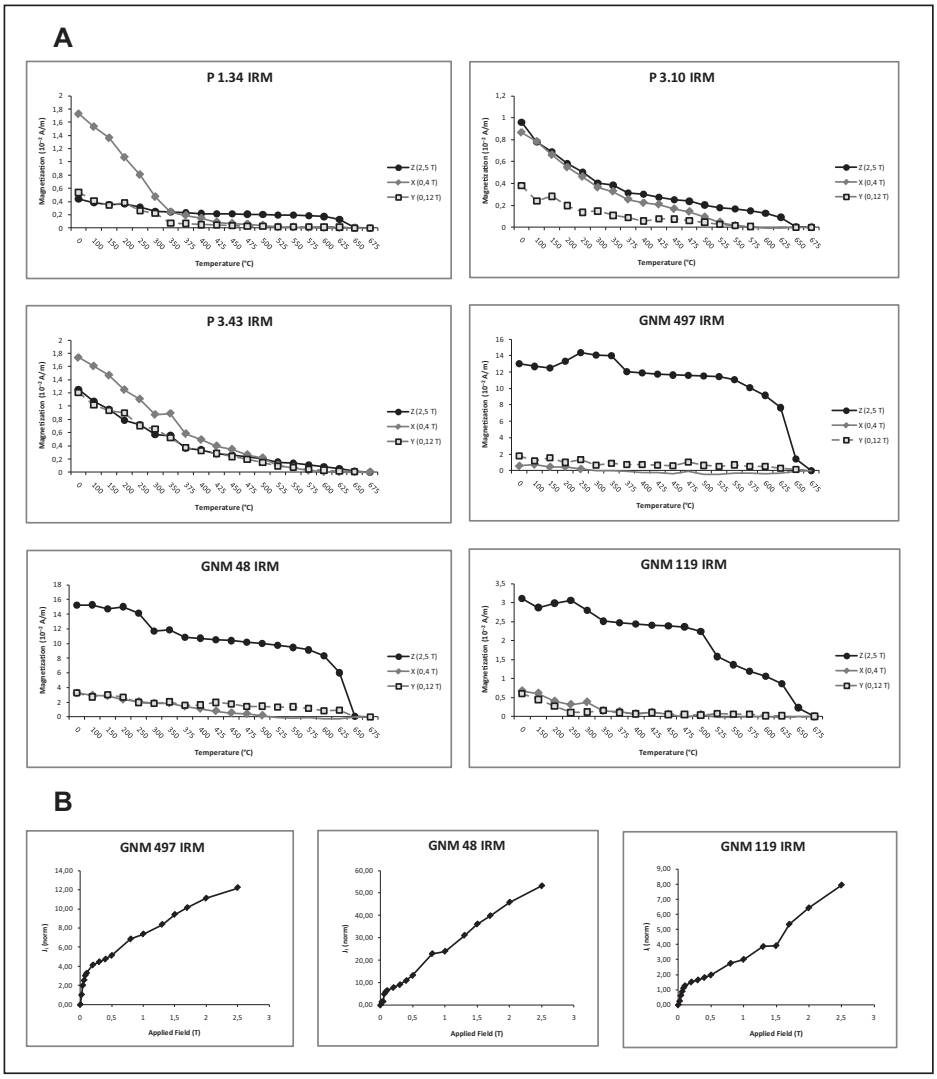

Figure 3. Thermal demagnetization of a three-component isothermal remanent magnetization (IRM) (A) and IRM acquisition curves (B) for representative samples from Pignola-Abriola showing the presence of a variable mixture of hematite and magnetite. See text for discussion.

for ~60%–85% of the IRM, and a subordinate low-coercivity phase with $B_{1/2}$ = 0.1 T, which accounts for the reminder of the IRM (Fig. 1; GSA Data Repository [see footnote 1]). The presence of higher amounts of (detrital) hematite in the upper part of the section may correlate with the increase in terrigenous input (shales and marls) observed in the upper part of the section (Fig. 2).

The natural remanent magnetization (NRM) of samples, measured on a 2G Enterprises DC-SQUID cryogenic magnetometer, is on average 0.08 mA/m. All samples were thermally demagnetized in steps of 50 °C or 25 °C up to a maximum of 675 °C, and the component structure of the NRM was plotted on vector end-point demagnetization diagrams (Fig. 4; Zijderveld, 1967). After removal of spurious magnetizations between room temperature and ~100–300 °C, a characteristic remanent magnetization (ChRM) was isolated up to 450–550 °C (maximum of 625 °C) in ~55% of the samples (N = 121; worksheet 3, GSA Data Repository [see footnote 1]) and found to be broadly oriented either N and down or S and up in tilt-corrected coordinates (Fig. 5). These ChRM component directions are distributed in tilt-corrected coordinates around an overall mean of Dec = 15.9°E, Inc = 32.5° (k = 8.4, α_{95} = 4.7°, N = 121; Table 2). No fold test could be performed because of the homoclinal bedding tilt of the section, whereas the reversal test (McFadden and McElhinny, 1990) was positive (for detailed statistics, see worksheet 3, GSA Data Repository [see footnote 1]). Based on these results and the consistent magnetostratigraphic correlations with sections from the literature, as discussed later herein, we regard the ChRM component as primary in origin. We checked the ChRM component directions for sedimentary inclination shallowing due to sedimentary and/or compaction processes. The elongation/inclination (E/I) statistical method of Tauxe and Kent (2004) was applied to the ChRM directions, obtaining a flattening factor of f = 0.6 and a corrected mean inclination of 47.7° (min = 39.0°, max = 53.7°), corresponding to a paleolatitude for Pignola-Abriola of ~28.8°N (Table 2). A paleomagnetic pole was calculated for Pignola-Abriola using the tilt-corrected mean ChRM direction corrected for inclination shallowing (lat. = 72.5°N, long. = 143.0°E; Table 2) and compared to the 201 Ma Adria-Africa paleopole of Muttoni et al. (2013) located at lat. = 69.3°N, long. = 243.8°E. The Pignola-Abriola paleopole is displaced by ~32.8° clockwise relative to the reference Adria-Africa paleopole, probably as a result of vertical-axis tectonic rotation of the sampling area during Apennine tectonics.

A virtual geomagnetic pole (VGP) was calculated for each ChRM component direction in tilt-corrected coordinates. The latitude of the sample VGP relative to the north pole of the paleomagnetic axis was used for interpreting the magnetic polarity stratigraphy, where VGP latitudes approaching +90° or –90° are attributed to normal or reverse polarity, respectively. An overall sequence of five polarity magnetozones, labeled from magnetozone MPA1 to MPA5, was established starting at the base of the section (Fig. 2). Each magnetozone was subdivided into a lower, predominantly normal and an upper, predominantly reverse portion, in which submagnetozones can be embedded. No obvious relation was observed between magnetic polarity stratigraphy and the magnetic mineralogy of the samples. The FAD of *Misikella posthernsteini* sensu stricto falls within magnetozone MPA5r at ~45 m, while the new proposed Norian-Rhaetian boundary coincident with the $\delta^{13}C_{org}$ negative spike occurs inside the same magnetozone at ~44.5 m (Fig. 2).

DISCUSSION

Correlations with Tethyan Sections from the Literature

The magnetostratigraphy of the Pignola-Abriola section is comparable with that of the Steinbergkogel section (Hüsing et al., 2011), which at present is the only global boundary stratotype section and point (GSSP) candidate

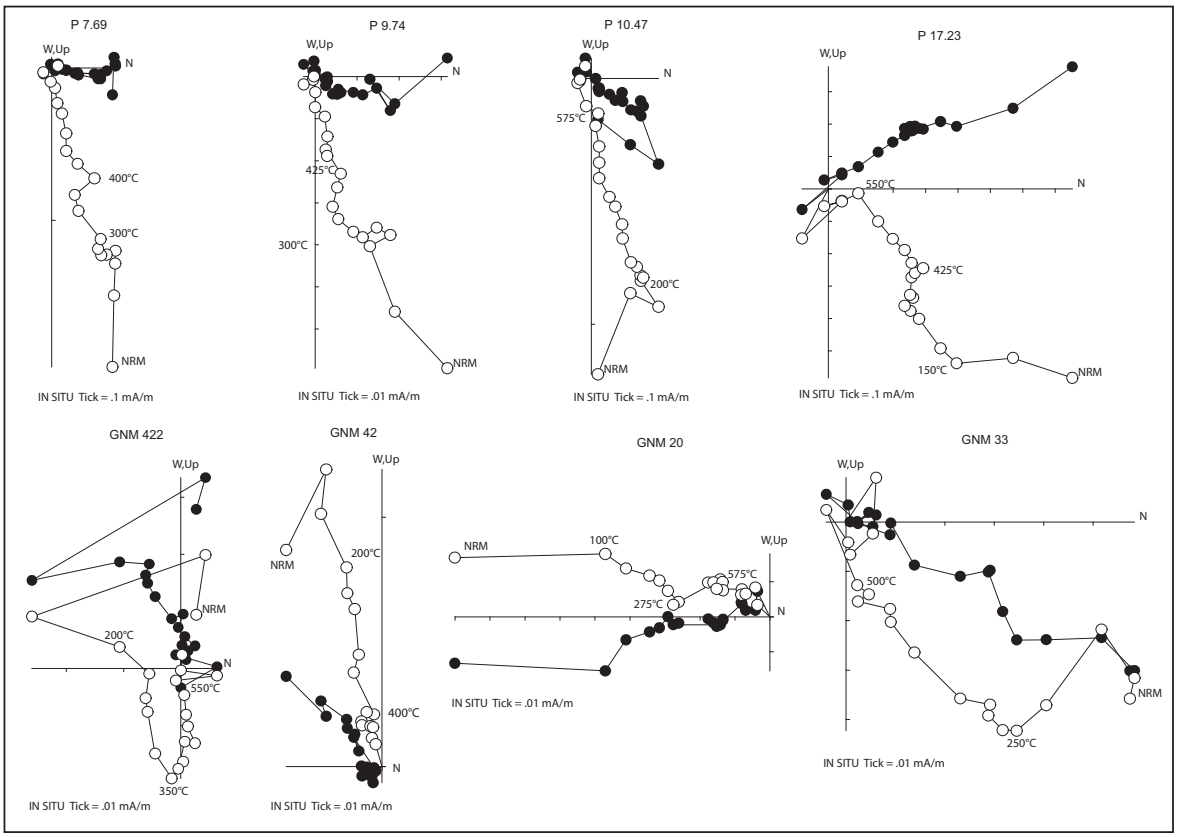

Figure 4. Vector end-point demagnetization diagrams for representative samples from Pignola-Abriola. Closed circles are projections onto the horizontal plane, and open circles are projections onto the vertical plane for in situ (geographic) coordinates. Temperatures are expressed in °C. NRM—natural remanent magnetization.

for the base of the Rhaetian Stage (Krystyn et al., 2007a, 2007b), assuming that the occurrence of conodont *Misikella posthernsteini* at Steinbergkogel (plate 1 in Krystyn et al., 2007a) is equivalent to the FO of *Misikella hernsteini/posthernsteini* transitional forms at Pignola-Abriola (sensu Giordano et al., 2010). Hence, the main reversal portion of the Steinbergkogel magnetostratigraphy from magnetozone ST1/B– to magnetozone ST1/H– at Steinbergkogel STKA section (equivalent to ST2/B– to ST2/H– at Steinbergkogel STKB+C section), has been correlated to magnetozones MPA3r to MPA5r of the Pignola-Abriola section (Fig. 6). Also, part of the magnetostratigraphy of the Oyuklu section (Gallet et al., 2007), from magnetozone OyB– to OyD–, is comparable with MPA4r to MPA5r of the Pignola-Abriola section, and with ST/D– to ST/H– of the Steinbergkogel section (Fig. 6). Furthermore, the lower portion of the Pignola-Abriola section is magnetostratigraphically correlated with the upper part of the Pizzo Mondello section (Muttoni et al., 2004). Using the updated biostratigraphic calibration of the Pizzo Mondello magnetostratigraphy (Mazza et al., 2012),

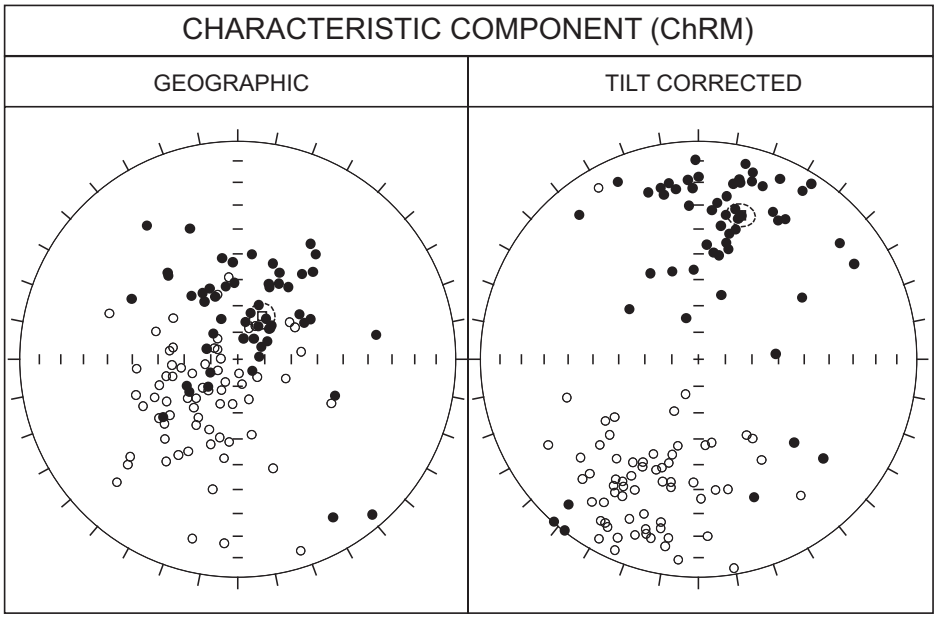

Figure 5. Equal-area projections for characteristic remanent magnetization (ChRM) component directions isolated at Pignola-Abriola for in situ (geographic) and tilt-corrected coordinates (see Table 2 for Fisher statistics parameters). For the ChRM component directions, see also worksheet 3, GSA Data Repository (see text footnote 1).

TABLE 2. PALEOMAGNETIC DIRECTIONS AND POLE FROM THE PIGNOLA-ABRIOLA SECTION

Mean directions from the Pignola-Abriola section

In situ						Tilt-corrected							
Comp.	N	k	α_{95}	Dec.	Inc.	k	α_{95}	Dec.	Inc.	Inc. corr.	Inc. corr. Max.	Inc. corr. Min.	*f*
ChRM	121	8.2	4.8°	30°E	71.5°	8.4	4.7°	15.9°E	32.5°	47.7°	53.7°	39.0°	0.6

Paleomagnetic pole, paleolatitude, and rotation from tilt-corrected filtered 'Ch' directions, corrected for inclination flattening:

Lat. (°N)	Long. (°E)	A_{95}	Paleolatitude (°N)	Paleolatitude (°N) Max.	Paleolatitude (°N) Min.	Rotation
72.5	143.0	4.0°	28.8	34.2	22.0	32.8°CW

Note: Comp.—paleomagnetic component; *N*—number of samples; *k*, α_{95}—standard Fisher precision parameters; Dec.—mean declination; Inc.—mean inclination; Inc. corr.—mean inclination corrected for inclination flattening; *f*—flattening factor; Lat.—Latitude; Long.—Longitude; A_{95}—95% circular confidence about the pole; Rotation—tectonic rotation of the site (relative to the 201 Ma Adria-Africa reference paleopole of Muttoni et al., 2013), where CW—clockwise.

magnetozones MPA1n to MPA3n at Pignola-Abriola have been correlated to magnetozones PM-8n to PM-12n at Pizzo Mondello (Fig. 6). Moreover, data from Pignola-Abriola have been compared with the magnetobiostratigraphy of the Brumano and Italcementi Quarry sections (Lombardian Basin, southern Alps, Italy), which encompasses a portion of the Rhaetian (with specimens attributed to *Misikella*) up to the Triassic-Jurassic boundary as defined by pollens (Muttoni et al., 2010, 2014). Awaiting for a formal redefinition of the *Misikella* specimens in the Brumano section following the new definition of *Misikella posthernsteini* sensu stricto adopted in this study (after Giordano et al., 2010), we stress that all *Misikella* specimens at Brumano occur below the recovered magnetostratigraphy (Muttoni et al., 2010, 2014), and thus the sequence of Brumano-Italcementi Quarry magnetozones from BIT1n to BIT5n is regarded as largely younger than the Pignola-Abriola magnetostratigraphy (Fig. 6).

Correlation with the Newark APTS

The correlation between the Pignola-Abriola section and the Newark APTS was performed using the statistical approach proposed in Muttoni et al. (2004). Assuming that thickness is a linear proxy of time, the duration of Newark magnetozones was compared with the thickness of Pignola-Abriola magnetozones (Fig. 7). The Pignola-Abriola polarity reversal sequence in linear depth coordinates was placed alongside the top of the Newark APTS (at magnetozone E23r) in linear age coordinates. A linear correlation coefficient (*R*) relating the thickness of each of the $N = 22$ complete Pignola-Abriola magnetozones to the duration of the correlative Newark magnetozones was calculated, from which a *t* value was derived, where $t = R^*\mathrm{sqrt}([N - 2]/[1 - R^2])$, *R* is the linear correlation coefficient, and *N* is the number of matching magnetozones in the moving window, i.e., 22. The Pignola-Abriola sequence was then slid by two polarity zones along the Newark APTS (in order to maintain internal polarity consistency in correlation), *R* and *t* were recalculated, and the exercise was repeated until all 19 possibilities were explored (Fig. 7; statistical procedure with correlation options and analysis of *t*-values is reported in worksheet 2 of GSA Data Repository [see footnote 1]).

For $N = 22$ (the number of matching reversals in moving window), each correlation has 20 degrees of freedom. A Student *t*-test shows that only correlation coefficients with a *t* value larger than 1.725 are significant at the 95% level. According to the Student *t*-test, only correlation option 19 is reliable at more than 95% confidence level (Fig. 7), though it can be excluded on stratigraphic grounds. Precisely, option 19 places the Norian-Rhaetian boundary of the Pignola-Abriola section in the Carnian-Norian portion of the Newark sequence, as deduced from correlations of the Pizzo Mondello and Silická Brezová sections to the Newark APTS (Muttoni et al., 2004; Channell et al., 2003). For this reason, we decided to contemplate correlation options characterized by lower values of *t* (around 1). As a consequence, options 16 and 7 were considered as acceptable (Fig. 7). Option 16 is affected by the same problem as option 19 insofar as it places the Norian-Rhaetian boundary within the Norian Stage as implied by the Pizzo Mondello and Silická Brezová to Newark correlations discussed earlier. In addition, option 16 also implies sudden (and unexplained) variations in sediment accumulation rates of the Pignola-Abriola section.

Correlation option 7 results are more coherent with the available magneto-biostratigraphic correlations of Tethyan sections to the Newark APTS and will be investigated in detail. Option 7 links Pignola-Abriola magnetozone MPA1n with Newark E13n.1n at the base, and magnetozone MPA11r with E20r at the top (Fig. 7). However, this correlation implies sudden variations in sediment accumulation rates in the middle of the Pignola-Abriola section. Moreover, the lower part of Pignola-Abriola is considered Sevatian (late Norian) in age, but according to correlation 7, it should correspond to Newark

Figure 6 (*on following page*). The Norian-Rhaetian magnetostratigraphy, biostratigraphy, and chemostratigraphy of the Pignola-Abriola section correlated to data from marine sections from the literature, such as Steinbergkogel (Hüsing et al., 2011), which is the current global stratotype section and point (GSSP) candidate for the Rhaetian Stage (Krystyn et al., 2007a, 2007b), Oyuklu (Gallet et al., 2007), Brumano-Italcementi Quarry (Muttoni et al., 2010, 2014), and Pizzo Mondello (Muttoni et al., 2004). In this work, specimens originally attributed to *Misikella posthernsteini* at Steinbergkogel (Krystyn et al., 2007a, 2007b) are here considered *M. posthernsteini* sensu lato (s.l.) and attributed to the *M. hernsteini/posthernsteini* "transitional forms" (sensu Giordano et al., 2010). Key biostratigraphic events at Pizzo Mondello are after Mazza et al. (2012). The Pignola-Abriola section is correlated to the Newark astrochronological polarity time scale (APTS; left column) using preferred correlation option 7.1. The lower-right panel shows the derived age model of sedimentation for Pignola-Abriola with an increase in sedimentation rate in the upper part of the section where the terrigenous input is higher. The Norian-Rhaetian boundary, placed at a level coincident with a rapid decrease in $\delta^{13}C_{org}$ to ~–30‰, which virtually coincides with the level containing the first appearance datum (FAD) of conodont *Misikella posthernsteini* sensu stricto within the *Proparvicingula moniliformis* radiolarian zone, is traced within Newark magnetozone E20r at 205.7 Ma.

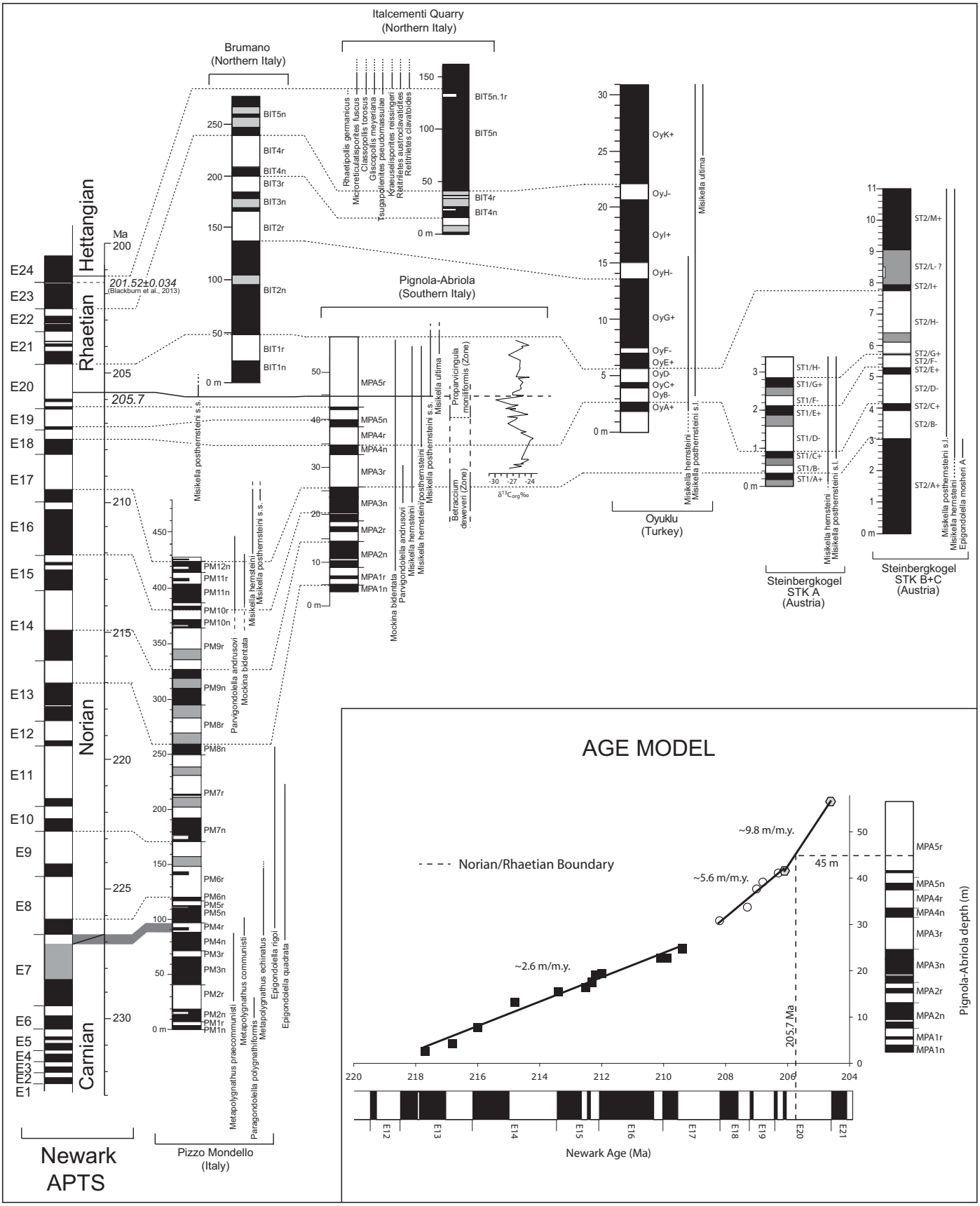
Italcementi Quarry
(Northern Italy)
Brumano
(Northern Italy)
Pignola-Abriola
(Southern Italy)
Oyuklu
(Turkey)
Steinbergkogel
STK A
(Austria)
Steinbergkogel
STK B+C
(Austria)
Newark
APTS
Pizzo Mondello
(Italy)
Hettangian
Rhaetian
Norian
Carnian
Ma
201.52±0.034
(Blackburn et al., 2013)
205.7
Misikella posthernsteini s.s.
Misikella hernsteini
Misikella posthernsteini s.s.
Misikella ultima
Proparvicingula moniliformis (Zone)
Betraccium deweveri (Zone)
Mockina bidentata
Parvigondolella andrusovi
Misikella hernsteini
Misikella posthernsteini
Misikella ultima
Misikella hernsteini
Misikella posthernsteini s.l.
Misikella posthernsteini s.l.
Epigondolella mosheri A
Metapolygnathus praecommunisti
Metapolygnathus communisti
Paragondolella polygnathiformis
Metapolygnathus echinatus
Epigondolella rigoi
Epigondolella quadrata
δ13Corg‰
AGE MODEL
Norian/Rhaetian Boundary
~9.8 m/m.y.
~5.6 m/m.y.
~2.6 m/m.y.
45 m
205.7 Ma
Pignola-Abriola depth (m)
Newark Age (Ma)

Figure 6.

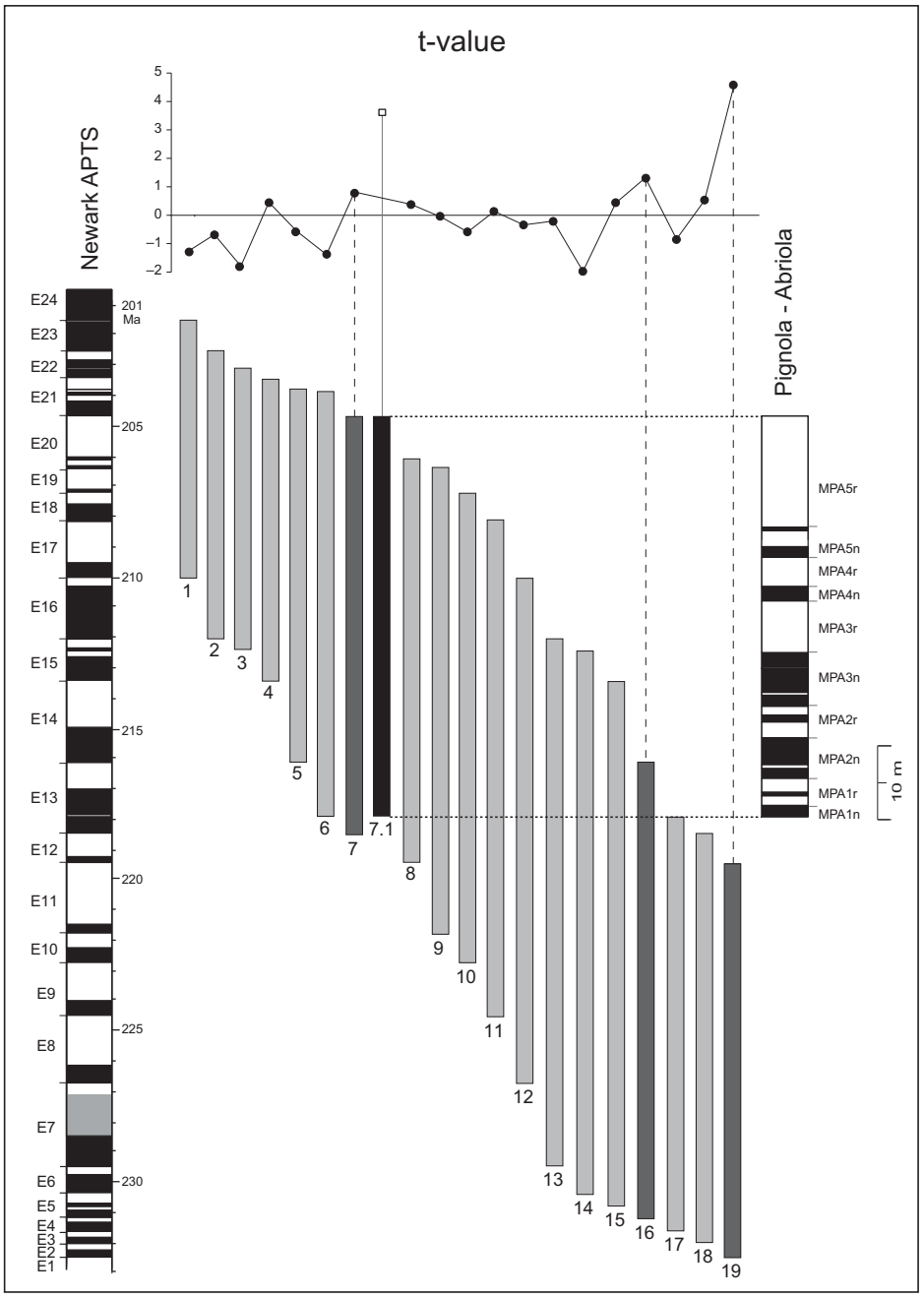

Figure 7. Pignola-Abriola geomagnetic reversal sequence in linear depth coordinates was slid aside the Newark astrochronological polarity time scale (APTS) in linear age coordinates maintaining the internal polarity coherency, and a *t* value was calculated for each of the 19 possible correlation options. Positive (negative) *t*-values refer to positive (negative) slopes of the linear function relating Pignola-Abriola magnetozone thickness to Newark magnetozone duration. Statistically significant options 16 and 19 were rejected for incoherence with the available stratigraphic data, whereas a modified version of correlation option 7, termed option 7.1, is considered the best solution that is in agreement with (or does not violate) the available stratigraphic data. See text for discussion.

magnetozones considered close to the Carnian-Norian boundary (Fig. 7; see also Muttoni et al., 2004).

In conclusion, no statistical correlation matches perfectly, and some "adjustments" are necessary. An alternative version of statistical correlation option 7, termed option 7.1 (black bar in Fig. 7), solves the problems outlined for option 7, increases statistical significance, and is coherent with the Pizzo Mondello and Pignola-Abriola magneto-biostratigraphies and correlations to the Newark APTS. Preferred option 7.1 is similar to statistical option 7 in range (MPA1n corresponding to E13n.1n, and MPA11r corresponding to E20r.2r) but differs from statistical option 7 in linking MPA1n with E13n.2n, MPA1r (0.1r, 0.1n, 0.2r) with E13r, MPA2n (0.1n, 0.1r, 0.2n) with E14n, and MPA11r with E20r, whereas magnetozones from MPA2r to MPA11n have been correlated with Newark magnetozones from E14r to E20n. Preferred correlation option 7.1 implies a correlation of the Steinbergkogel section to the Newark APTS from magnetozone E17n to E21n (Fig. 6) that is substantially equivalent to the correlation originally proposed by Hüsing et al. (2011). The correlation of the largely younger Brumano-Italcementi Quarry sections to the Newark APTS is the same of Muttoni et al. (2010, 2014), pending a formal redefinition of the *Misikella* specimens at Brumano (see also earlier discussion).

Using preferred correlation option 7.1, an age model for the Pignola-Abriola section can be derived. The age model shows a change in sedimentation rate from the lower to the upper part of the section (Fig. 6). From the base to meter 24.5, the mean sedimentation rate is of ~2.6 m/m.y., while from meter 24.5 to 40, the mean sedimentation rate increases to ~5.6 m/m.y. From meter 40 to the section top, the sedimentation rate increases further to ~9.8 m/m.y. This is coherent with the lithostratigraphy of the section, suggesting a general increase of terrigenous input in the upper part of the section. According to the proposed age model, the Norian-Rhaetian boundary defined by the level containing the FAD of *M. posthernsteini* sensu stricto at meter 45 should correspond to an estimated age of ca. 205.7 Ma (Fig. 6), which is substantially equivalent to the age of the prominent negative $\delta^{13}C_{org}$ excursion to ~–30‰ observed at meter 44.5 (Fig. 6).

GSSP Proposal for the Base of the Rhaetian Stage

Based on our magneto-bio-chemostratigraphic study of the Pignola-Abriola section, coupled with the recognition of the taxonomic complexities concerning conodont *Misikella posthernsteini*, the current candidate species for

the definition of the base of the Rhaetian Stage, we suggest an alternative option for the definition of the Norian-Rhaetian boundary. We favor placing the boundary at the prominent negative $\delta^{13}C_{org}$ spike observed in the Pignola-Abriola section at meter 44.5 (immediately below the level containing the FAD of *M. posthernsteini* sensu stricto and within the base of the radiolarian *Proparvicingula moniliformis* zone). A similar $\delta^{13}C_{org}$ perturbation around the Norian-Rhaetian boundary was documented in Canada by Ward et al. (2001, 2004) and Whiteside and Ward (2011), coinciding with the disappearance of large *Monotis* (Ward et al., 2004), a typical proxy for the Norian-Rhaetian boundary (McRoberts et al., 2008). The stratigraphic level in the Pignola-Abriola section containing the ~–30‰ spike has been magnetostratigraphically correlated to Newark magnetozone E20r.2r at ca. 205.7 Ma. This age was obtained from the Newark astrochronology, calibrated with the new numerical age of 201.5 Ma from the base of the Orange Mountain Basalts in the Newark Supergroup (Blackburn et al., 2013). Assuming an age of ca. 201.3 Ma for the Triassic-Jurassic boundary (Guex et al., 2012), which is broadly consistent with previous estimates (Schoene et al., 2010), and a proposed age of ca. 205.7 Ma for the Norian-Rhaetian boundary, the Rhaetian Stage would have a duration of ~4.4 m.y. (Fig. 6). Using a Carnian-Norian boundary at ca. 227 Ma (Muttoni et al., 2004), the Norian would be the longest stage of the Phanerozoic with a duration of ~21.3 m.y. (but see Lucas et al., 2012). Using an approximated Ladinian-Carnian age of 238 Ma, derived from an uppermost Ladinian radiometric age of 237.77 ± 0.14 Ma (Mietto et al., 2012), the Carnian would have lasted almost 10 m.y. According to these figures, the Late Triassic may have lasted ~36 m.y.

Comparison with Previous Time Scales

We compared our solution with alternative proposals from the literature. Krystyn et al. (2002) used Carnian-Norian data from several Tethyan sections (Kavaalani, Kavur Tepe, Pizzo Mondello lower part, Bolücektasi Tepe, and Scheiblkogel; see references in Krystyn et al., 2002) to construct a Tethyan composite magneto-biostratigraphic sequence that was correlated to Newark magnetozones E3–E22 and used it to infer a duration of the Rhaetian of only ~2 m.y. Later, Gallet et al. (2007) correlated data from Oyuklu, Pizzo Mondello (upper part), and the Tethyan composite sequence of Gallet et al. (2003) to the Newark APTS, suggesting that part of the Rhaetian is missing in the Newark sequence, and supporting the ~2 m.y. duration of the Rhaetian as proposed by Krystyn et al. (2002). Muttoni et al. (2010) illustrated that middle Norian (Alaunian) magnetozones in the composite magneto-biostratigraphic sequence of Krystyn et al. (2002) may encompass Newark magnetozones ~E13–E15 rather than ~E13–E17, so that the overlying Sevatian magnetozones may correlate to Newark levels at and immediately above E15 rather than at and above E17 as proposed by Krystyn et al. (2002), thus supporting the existence of a longer (>2 m.y.) Rhaetian.

Coming to more recent times, the long-Tuvalian option of the *Geological Time Scale 2012* (Ogg, 2012), which is essentially based on data from Lucas et al. (2012), is characterized by a Carnian-Norian boundary placed at 221 Ma, a Norian-Rhaetian boundary at 205.4 Ma, and a large hiatus in the Newark Supergroup based on inferences from conchostracan biostratigraphy (Lucas et al., 2012, and references therein). According to this option, the preserved portion of the Rhaetian in the Newark Supergroup should have a duration of only ~0.2 m.y. (Lucas et al., 2012). A duration of ~8 m.y. for the Rhaetian, as proposed using marine-Newark magnetostratigraphic correlations by several authors (Channell et al., 2003; Muttoni et al., 2004, 2010; Hüsing et al., 2011), was rejected by Lucas et al. (2012) based on the inference that inserting 7.8 m.y. of missing Rhaetian in the claimed Rhaetian gap of the Newark Supergroup (7.8 m.y. = 8 m.y. of total duration of Rhaetian – 0.2 m.y. of preserved Rhaetian in the Newark) would produce an age for the base of the Newark Supergroup of 240.5 Ma; as Lucas et al. (2012) considered the base of the Newark Supergroup to coincide with the base of the Carnian (based on continental [palynomorphs, conchostracans, tetrapods] biostratigraphy), an age of 240.5 Ma is regarded as inappropriate because it would place the base of the Newark Supergroup close to the age of the Anisian-Ladinian boundary (Mundil et al., 2010). Therefore, a duration of ~8 m.y. for the Rhaetian is considered unacceptable according to Lucas et al. (2012), who instead adopted a duration of ~4 m.y. from Ogg (2004). Under the assumption of a 4 m.y. duration for the Rhaetian and only 0.2 m.y. of Rhaetian time preserved in the Newark Supergroup, Lucas et al. (2012) (and Ogg [2012] in his long-Tuvalian option) estimated an age of 221.5 Ma for the Carnian-Norian boundary, based on continental biostratigraphy, by counting ~405 k.y. McLaughlin cycles of Newark astrochronology.

In our opinion, the Rhaetian gap of Lucas et al. (2012) at the basis of the long-Tuvalian option (Ogg, 2012) is flawed by lack of convincing correlations between terrestrial groups and marine-based stage boundaries. For example, conchostracans from the Weser Formation of the Germanic Basin are assigned an early Tuvalian age (late Carnian) because the Weser Formation is considered correlative with the Dolomie de Beaumont of France, which contains marine bivalves considered to be of such age (Lucas et al., 2012). As a further example, the conchostracan fauna from the Coburg Sandstein of the Germanic Basin is considered late Carnian, seemingly because it lies immediately below the beginning of a sporomorph association considered to be late Tuvalian. In general, we find difficult to decipher in Lucas et al. (2012) where and in which stratigraphic context a given continental association was found in direct association with stage-defining marine fossils.

The long-Rhaetian option of the *Geological Time Scale 2012* (Ogg, 2012) is essentially based on magnetostratigraphic correlations between marine sections bearing stage-defining fossils and the Newark APTS assumed to be continuous in the Rhaetian (Channell et al., 2003; Muttoni et al., 2004, 2010; Hüsing et al., 2011), and it shows a Carnian-Norian boundary at ca. 228.4 Ma and a Norian-Rhaetian boundary at ca. 209.5 Ma. Our new time scale for the Late Triassic could be considered an "update" of the long-Rhaetian option of (Ogg, 2012), with a Norian-Rhaetian boundary at 205.7 Ma based on data from this study and a Carnian-Norian boundary at ca. 227 Ma based on correlation of the Pizzo Mondello section with the Newark APTS (both numerical estimates obtained by rescaling the Newark APTS using an age of ca. 201.5 Ma for the base of the Orange Mountain Basalts in the Newark Supergroup; Blackburn et al., 2013). Moreover, our age of 205.7 Ma for the Norian-Rhaetian boundary is coherent with recent U/Pb ages of Wotzlaw et al. (2014) that constrain the Rhaetian base between 205.70 ± 0.15 Ma and 205.3 ± 0.14 Ma.

CONCLUSIONS

Paleomagnetic data obtained from the Pignola-Abriola section provided a sequence of 22 polarity reversals grouped in 10 magnetozones. The correlation between the Pignola-Abriola section and additional Norian and Rhaetian Tethyan marine sections from the literature (Steinbergkogel, Oyuklu, Brumano, Italcementi Quarry, and Pizzo Mondello) reveals significant internal consistency.

To provide numerical age constraints on the Pignola-Abriola section, we applied a statistical correlation to the Newark APTS, which is assumed to be continuous in its younger part (contra Lucas et al., 2012). Three out of a total of 19 explored correlation options produced statistically reliable results, and after a thorough analysis, one option (7.1) is considered as the

most reliable. According to this option, the Pignola-Abriola section correlates to Newark magnetozones E13n to E20r. We place the Norian-Rhaetian boundary at Pignola-Abriola at a level coincident with a rapid decrease in $\delta^{13}C_{org}$ to ~–30‰, which virtually coincides with the level containing the FAD of conodont *Misikella posthernsteini* sensu stricto within the *Proparvicingula moniliformis* radiolarian zone. This level is traced within Newark magnetozone E20r at 205.7 Ma.

Assuming an age of ca. 201.3 Ma for the Triassic-Jurassic boundary (Schoene et al., 2010; Guex et al., 2012), our study shows that the Rhaetian is ~4.4 m.y. long. Assuming a Carnian-Norian boundary age of ca. 227 Ma (Muttoni et al., 2004, 2014, and references therein), our study shows that the Norian is ~21.3 m.y. long.

ACKNOWLEDGMENTS

This manuscript benefited from comments by reviewers Conall Mac Niocaill and Paul E. Olsen. Special thanks go to G. Gattolin and J. Dal Corso for helping in the field. Field and laboratory activities were funded by grants 60A05-2288/09, CPDA090175/09, and PRIN 2008BEF5Z7_005 to M. Rigo, PRIN 20107ESMX9_002 to N. Preto, and PRIN 2008BEF5Z7_004 to A. Bertinelli. Acknowledgment is made to the donors of the American Chemical Society Petroleum Research Fund for partial support of this research (grant 49637-DN18 to M. Katz). Stable isotope analyses were funded through National Science Foundation grant EAR-0844252 to L. Godfrey, D. Rosa, P. Mancusi, and L. Pietrafesa (Municipality of Pignola), I. Petrone (mayor of the town of Pignola), the Corpo Forestale dello Stato (Stazione di Pignola), and D. Totaro (president of the Appennino Lucano National Park) are thanked for assistance.

REFERENCES CITED

Argnani, A., 2005, Possible record of a Triassic ocean in the southern Apennines: Bollettino della Società Geologica Italiana, v. 124, p. 109–121.

Bazzucchi, P., Bertinelli, A., Ciarapica, G., Marcucci, M., Passeri, L., Rigo, M., and Roghi, G., 2005, The Late Triassic-Jurassic stratigraphic succession of Pignola (Lagonegro-Molise Basin, southern Apennines), Italy: Bollettino Società Geologica Italiana, v. 124, p. 143–153.

Bertinelli, A., Ciarapica, G., De Zanche, V., Marcucci, M., Passeri, L., Rigo, M., and Roghi, G., 2005, Stratigraphic evolution of the Triassic-Jurassic Sasso di Castalda succession (Lagonegro basin, southern Apennines, Italy): Bollettino Società Geologica Italiana, v. 124, p. 161–175.

Blackburn, T.J., Olsen, P.E., Bowring, S.A., McLean, N.M., Kent, D.V., Puffer, J., McHone, G., Rasbury, E.T., and Et-Touhami, M., 2013, Zircon U-Pb geochronology links the end-Triassic extinction with the Central Atlantic magmatic province: Science, v. 340, p. 941–945, doi:10.1126/science.1234204.

Callegaro, S., Rigo, M., Chiaradia, M., and Marzoli, A., 2012, Latest Triassic marine Sr isotopic variations, possible causes and implications: Terra Nova, v. 24, p. 130–135, doi:10.1111/j.1365-3121.2011.01046.x.

Carter, E.S., 1993, Biochronology and Paleontology of Uppermost Triassic (Rhaetian) Radiolarians, Queen Charlotte Islands, British Columbia, Canada: Mémoires de Géologie, Lausanne, v. 11, 176 p.

Catalano, R., Doglioni, C., and Merlini, S., 2001, On the Mesozoic Ionian Basin: Geophysical Journal International, v. 144, p. 49–64, doi:10.1046/j.0956-540X.2000.01287.x.

Channell, J.E.T., Kozur, H.W., Sievers, T., Mock, R., Aubrecht, R., and Sykora, M., 2003, Carnian-Norian biomagnetostratigraphy at Silická Brezová (Slovakia): Correlation to other Tethyan sections and to Newark Basin: Palaeogeography, Palaeoclimatology, Palaeoecology, v. 191, p. 65–109, doi:10.1016/S0031-0182(02)006545.

Ciarapica, G., and Passeri, L., 2002, The palaeogeographic duplicity of the Apennines: Bollettino della Società Geologica Italiana, v. 121, no. 1, p. 67–75.

Ciarapica, G., and Passeri, L., 2005, Ionian Tethydes in the southern Apennines, *in* Finetti, I.R., ed., Crop Project: Deep Seismic Exploration of the Central Mediterranean and Italy: Amsterdam, Elsevier, p. 209–224.

Cohen, A.S., and Coe, A.L., 2007, The impact of the Central Atlantic magmatic province on climate and on the Sr- and Os-isotope evolution of seawater: Palaeogeography, Palaeoclimatology, Palaeoecology, v. 244, p. 374–390, doi:10.1016/j.palaeo.2006.06.036.

Coplen, T.B., Brand, W.A., Gehre, M., Gröning, M., Meijer, H.A.J., Toman, B., and Verkouteren, R.M., 2006, New guidelines for $\delta^{13}C$ measures: Analytical Chemistry, v. 78, p. 2439–2441, doi:10.1021/ac052027c.

Cornet, B., 1977, The Palynostratigraphy and Age of the Newark Supergroup [Ph.D. thesis]: University Park, Pennsylvania, The Pennsylvania State University, 527 p.

Cornet, B., 1993, Applications and limitations of palynology in age, climatic, and paleoenvironmental analyses of Triassic sequences in North America, *in* Lucas, S.G., and Morales, M., eds., The Non-Marine Triassic: New Mexico Museum of Natural History and Science Bulletin 3, p. 67–81.

Epstein, A.G., Epstein, J.B., and Harris, L.D., 1977, Conodont Color Alteration: An Index to Organic Metamorphism: US Geological Survey Professional Paper 995, p. 1–27.

Finetti, I.R., 1982, Structure, stratigraphy and evolution of central Mediterranean: Bollettino di Geofisica Teorica e Applicata, v. 24, p. 247–315.

Finetti, I.R., 2005, CROP Project, Deep Seismic Exploration of the Central Mediterranean and Italy: Amsterdam, Elsevier, Volume 1, 794 p.

Fowell, S.J., Cornet, B., and Olsen, P.E., 1994, Geologically rapid Late Triassic extinctions: Palynological evidence from the Newark Supergroup, *in* Klein, G.O., ed., Pangea: Paleoclimate, Tectonics, and Sedimentation during Accretion, Zenith, and Breakup of a Supercontinent: Geological Society of America Special Paper 288, p. 197–206, doi:10.1130/SPE288-p197.

Gallet, Y., Krystyn, L., Besse, J., and Marcoux, J., 2003, Improving the Upper Triassic numerical timescale from cross-correlation between Tethyan marine sections and the continental Newark Basin sequence: Earth and Planetary Science Letters, v. 212, p. 255–261, doi:10.1016/S0012-821X(03)00290-5.

Gallet, Y., Krystyn, L., Marcoux, J., and Besse, J., 2007, New constraints on the end-Triassic (Upper Norian-Rhaetian) magnetostratigraphy: Earth and Planetary Science Letters, v. 255, p. 458–470, doi:10.1016/j.epsl.2007.01.004.

Giordano, N., Rigo, M., Ciarapica, G., and Bertinelli, A., 2010, New biostratigraphical constraints for the Norian/Rhaetian boundary: Data from Lagonegro Basin, southern Apennines, Italy: Lethaia, v. 43, p. 573–586, doi:10.1111/j.1502-3931.2010.00219.x.

Guex, J., Schoene, B., Bartolini, A., Spangenberg, J., Schaltegger, U., O'Dogherty, L., Taylor, D., Bucher, H., and Atudorei, V., 2012, Geochronological constraints on post-extinction recovery of the ammonoids and carbon cycle perturbation during the Early Jurassic: Palaeogeography, Palaeoclimatology, Palaeoecology, v. 346–347, p. 1–11, doi:10.1016/j.palaeo.2012.04.030.

Hüsing, S.K., Deenen, M.H.L., Koopmans, J.G., and Krijgsman, W., 2011, Magnetostratigraphic dating of the proposed Rhaetian GSSP at Steinbergkogel (Upper Triassic, Austria): Implications for the Late Triassic time scale: Earth and Planetary Science Letters, v. 302, p. 203–216, doi:10.1016/j.epsl.2010.12.012.

Kent, D.V., and Olsen, P.E., 1999, Search for the Triassic/Jurassic long normal and the J1 cusp: Eos, Transactions, American Geophysical Union, supplement, v. 80, no. 46, p. F306.

Kent, D.V., Olsen, P.E., and Witte, W.K., 1995, Late Triassic–Early Jurassic geomagnetic polarity and paleolatitudes from drill cores in the Newark rift basin (eastern North America): Journal of Geophysical Research, v. 100, p. 14,965–14,998, doi:10.1029/95JB01054.

Kozur, H., and Mock, R., 1991, New middle Carnian and Rhaetian conodonts from Hungary and the Alps. Stratigraphic importance and tectonic implications for the Buda Mountains and adjacent areas: Jahrbuch der Geologischen Bundesanstalt, v. 134, p. 271–297.

Kozur, H., and Weems, R., 2005, Conchostracan evidence for a late Rhaetian to early Hettangian age for the CAMP volcanic event in the Newark Supergroup, and a Sevatian (late Norian) age for the immediately underlying beds: Hallesches Jahrbuch Geowissenschaft, ser. B, v. 27, p. 21–51.

Kozur, H., and Weems, R., 2010, The biostratigraphic importance of conchostracans in the continental Triassic of the Northern Hemisphere, *in* Lucas, S.P., ed., The Triassic Timescale: Geological Society of London Special Publication 334, p. 315–417, doi:10.1144/SP334.13.

Kruiver, P.P., Dekkers, M.J., and Heslop, D., 2001, Quantification of magnetic coercivity components by the analysis of acquisition curves of isothermal remanent magnetization: Earth and Planetary Science Letters, v. 189, p. 269–276, doi:10.1016/S0012-821X(01)00367-3.

Krystyn, L., 2010, Decision report of the defining event for the base of the Rhaetian Stage: Albertiana, v. 38, p. 11–12.

Krystyn, L., Gallet, Y., Besse, J., and Marcoux, J., 2002, Integrated Upper Carnian to Lower Norian biochronology and implications for the Upper Triassic magnetic polarity time scale: Earth and Planetary Science Letters, v. 203, p. 343–351, doi:10.1016/S0012-821X(02)00858-0.

Krystyn, L., Bouquerel, H., Kuerschner, W., Richoz, S., and Gallet, Y., 2007a, Proposal for a candidate GSSP for the base of the Rhaetian Stage, *in* Lucas, S.G., and Spielman, J.A., eds., The Global Triassic: New Mexico Museum of Natural History and Science Bulletin 41, p. 189–199.

Krystyn, L., Richoz, S., Gallet, Y., Bouquerel, H., Kürschner, W.M., and Spötl, C., 2007b, Updated bio- and magnetostratigraphy from Steinbergkogel (Austria), candidate GSSP for the base of the Rhaetian Stage: Albertiana, v. 36, p. 164–173.

Kuroda, J., Hori, R.S., Suzuki, K., Grocke, D.R., and Ohkouchi, N., 2010, Marine osmium isotope record across the Triassic-Jurassic boundary from a Pacific pelagic site: Geology, v. 38, p. 1095–1098, doi:10.1130/G31223.1.

Lowrie, W., 1990, Identification of ferromagnetic minerals in a rock by coercivity and unblocking temperature properties: Geophysical Research Letters, v. 17, p. 159–162, doi:10.1029/GL017i002p00159.

Lucas, S.G., and Huber, P., 1993, Revised internal correlation of the Newark Supergroup Triassic, eastern United States and Canada, *in* Lucas, S.G., and Morales, M., eds., The Non-Marine Triassic: New Mexico Museum of Natural History and Science Bulletin 3, p. 311–319.

Lucas, S.G., Tanner, L.H., Kozur, H.W., Weems, R.E., and Heckert, A.B., 2012, The Late Triassic timescale: Age and correlation of the Carnian-Norian boundary: Earth-Science Reviews, v. 114, p. 1–18, doi:10.1016/j.earscirev.2012.04.002.

Marzoli, A., Jourdan, F., Puffer, J.H., Cuppone, T., Tanner, L.H., Weems, R.E., Bertrand, H., Cirilli, S., Bellieni, G., and De Min, A., 2011, Timing and duration of the Central Atlantic magmatic province in the Newark and Culpeper Basin, eastern U.S.: Lithos, v. 122, p. 175–188, doi:10.1016/j.lithos.2010.12.013.

Mazza, M., Rigo, M., and Gullo, M., 2012, Taxonomy and biostratigraphic record of the Upper Triassic conodonts of the Pizzo Mondello section (western Sicily, Italy), GSSP candidate for the base of the Norian: Rivista Italiana di Paleontologia e Stratigrafia, v. 118, no. 1, p. 85–130.

McFadden, P.L., and McElhinny, M.W., 1990, Classification of the reversal test in palaeomagnetism: Geophysical Journal International, v. 103, p. 725–729, doi:10.1111/j.1365-246X.1990.tb05683.x.

McRoberts, C.A., Krystyn, L., and Shea, A., 2008, Rhaetian (Late Triassic) *Monotis* (Bivalvia:Pectinoida) from the eastern Northern Calcareous Alps (Austria) and the end-Norian crisis in pelagic faunas: Palaeontology, v. 51, no. 3, p. 721–735, doi:10.1111/j.1475-4983.2008.00776.x.

Mietto, P., Manfrin, S., Preto, N., Rigo, M., Roghi, G., Furin, S., Gianolla, P., Posenato, R., Muttoni, G., Nicora, A., Buratti, N., Cirilli, S., Spötl, C., Ramezani, J., and Bowring, S.A., 2012, The global boundary stratotype section and point (GSSP) of the Carnian Stage (Late Triassic) at Prati di Stuores/Stuores Wiesen section (southern Alps, NE Italy): Episodes, v. 35, no. 3, p. 414–430.

Mostler, H., Scheuring, B., and Urlihs, M., 1978, Zur Mega-Mikrofauna und Mikroflora der Kössener Schichten (alpine Obertrias) vom Weissloferbach in Tirol unter besonderer Berücksichtigung der in der suessi- und marshi-Zone auftretenden Conodonten: Schriftenreihe der Erdwissenschaftlichen Kommissionen, v. 4, p. 141–174.

Mundil, R., Pálfy, J., Renne, P.R., and Brack, P., 2010, The Triassic time scale: New constraints and a review of geochronological data, *in* Lucas, S.G., ed., The Triassic Timescale: Geological Society of London Special Publication 334, p. 41–60.

Muttoni, G., Kent, D.V., Olsen, P.E., DiStefano, P., Lowrie, W., Bernasconi, S.M., and Hernandez, F.M., 2004, Tethyan magnetostratigraphy from Pizzo Mondello (Sicily) and correlation to the Late Triassic Newark astrochronological polarity time scale: Geological Society of America Bulletin, v. 116, p. 1043–1058, doi:10.1130/B25326.1.

Muttoni, G., Kent, D.V., Jadoul, F., Olsen, P.E., Rigo, M., Galli, M.T., and Nicora, A., 2010, Rhaetian magnetobiostratigraphy from the southern Alps (Italy): Constraints on Triassic chronology: Palaeogeography, Palaeoclimatology, Palaeoecology, v. 285, p. 1–16, doi:10.1016/j.palaeo.2009.10.014.

Muttoni, G., Dallanave, E., and Channell, J.E.T., 2013, The drift history of Adria and Africa from 280 Ma to present, Jurassic true polar wander, and zonal climate control on Tethyan sedimentary facies: Palaeogeography, Palaeoclimatology, Palaeoecology, v. 386, p. 415–435, doi:10.1016/j.palaeo.2013.06.011.

Muttoni, G., Mazza, M., Mosher, D., Katz, M.E., Kent, D.V., and Balini, M., 2014, A Middle-Late Triassic (Ladinian-Rhaetian) carbon and oxygen isotope record from the Tethyan Ocean: Palaeogeography, Palaeoclimatology, Palaeoecology, v. 399, p. 246–259, doi:10.1016/j.palaeo.2014.01.018.

O'Dogherty, L., Carter, E.S., Dumitrica, P., Goričcan, Š., and De Wever, P., 2009, An illustrated and revised catalogue of Mesozoic radiolarian genera—Objectives, concepts and guide for users: Geodiversitas, v. 31, no. 2, p. 191–212, doi:10.5252/g2009n2a2.

Ogg, J.G., 2004, The Triassic Period, *in* Gradstein, F.G., Ogg, J.G., and Smith, A.G., eds., A Geologic Time Scale 2004: Cambridge, UK, Cambridge University Press, p. 271–306.

Ogg, J.G., 2012, Triassic, *in* Gradstein, F.M., Ogg, J.G., Schmitz, M., and Ogg, G., eds., The Geological Time Scale 2012: Amsterdam, Elsevier, Volume 2, p. 681–730.

Olsen, P.E., and Kent, D.V., 1999, Long-period Milankovitch cycles from the Late Triassic and Early Jurassic of eastern North America and their implications for the calibration of the early Mesozoic time scale and the long-term behaviour of the planets: Philosophical Transactions of the Royal Society, ser. A, v. 357, p. 1761–1786, doi:10.1098/rsta.1999.0400.

Olsen, P.E., and Sues, H.D., 1986, Correlation of the continental Late Triassic and Early Jurassic sediments, and patterns of the Triassic-Jurassic tetrapod transition, *in* Padian, K., ed., The Beginning of the Age of Dinosaurs, Faunal Change Across the Triassic-Jurassic Boundary: Cambridge, UK, Cambridge University Press, p. 321–351.

Olsen, P.E., Kent, D.V., and Whiteside, J.H., 2011, Implications of the Newark Supergroup–based astrochronology and geomagnetic polarity time scale (Newark-APTS) for the tempo and mode of the early diversification of the Dinosauria: Earth and Environmental Science Transactions of the Royal Society of Edinburgh, v. 101, p. 201–229, doi:10.1017/S1755691011020032.

Rigo, M., De Zanche, V., Mietto, P., Preto, N., and Roghi, G., 2005, Biostratigraphy of the Calcari con Selce formation: Bollettino della Società Geologica Italiana, v. 124, p. 293–300.

Rigo, M., Preto, N., Franceschi, M., and Guaiumi, C., 2012, Stratigraphy of the Carnian-Norian Calcari con Selce Formation in the Lagonegro Basin, southern Apennines: Rivista Italiana di Paleontologia e Stratigrafia, v. 118, p. 143–154.

Schoene, B., Guex, J., Bartolini, A., Schaltegger, U., and Blackburn, T.J., 2010, A correlation between the Triassic-Jurassic boundary mass extinction and flood basalt eruption at the 100-ka level using ID-TIMS U/Pb zircon geochronology: Geology, v. 38, p. 387–390, doi:10.1130/G30683.1.

Tauxe, L., and Kent, D.V., 2004, A simplified statistical model for the geomagnetic field and the detection of shallow bias in paleomagnetic inclinations: Was the ancient magnetic field dipolar?, *in* Channel, J.E.T., ed., Timescales of the Paleomagnetic field: American Geophysical Union Geophysical Monograph 145, p. 101–115.

Ward, P.D., Haggart, J.W., Carter, E.S., Wilbur, D., Tippert, H.W., and Evans, T., 2001, Sudden productivity collapse associated with the Triassic-Jurassic boundary mass extinction: Science, v. 292, p. 1148–1151, doi:10.1126/science.1058574.

Ward, P.D., Garrison, G.H., Haggart, J.W., Kring, D.A., and Beattie, M.J., 2004, Isotopic evidence bearing on Late Triassic extinction events, Queen Charlotte Islands, British Columbia, and implications for the duration and cause of the Triassic/Jurassic mass extinction: Earth and Planetary Science Letters, v. 224, p. 589–600, doi:10.1016/j.epsl.2004.04.034.

Whiteside, J., and Ward, P.D., 2011, Ammonoid diversity and disparity track episodes of chaotic carbon cycling during the early Mesozoic: Geology, v. 39, p. 99–102, doi:10.1130/G31401.1.

Wotzlaw, J.F., Guex, J., Bartolini, A., Gallet, Y., Krystyn, L., McRoberts, C.A., Taylor, D., Schoene, B., and Schaltegger, U., 2014, Towards accurate numerical calibration of the Late Triassic: High-precision U-Pb geochronology constraints on the duration of the Rhaetian: Geology, doi:10.1130/G35612.1, (in press).

Zijderveld, J.D.A., 1967, A.C. demagnetization of rocks: Analysis of results, *in* Collinson, D.W., Creer, K.M., and Runcorn, S.K., eds., Methods in Paleomagnetism: Amsterdam, Elsevier, p. 254–286.

Science Editor: A. Hope Jahren
Associate Editor: Massimo Mattei

Manuscript Received 3 April 2014
Revised Manuscript Received 20 November 2014
Manuscript Accepted 31 December 2014

Printed in the USA

IMPROVING THE GEOMAGNETIC POLARITY TIME SCALE FOR THE LATE TRIASSIC: NEW MAGNETO-BIOSTRATIGRAPHIC CONSTRAINTS FROM PIGNOLA-2 AND DIBONA MARINE SECTIONS, ITALY

Matteo Maron[a], Giovanni Muttoni[b], Mark J. Dekkers[c], Michele Mazza[b], Guido Roghi[d], Anna Breda[a], Wout Krijgsman[c] and Manuel Rigo[a,d]

[a]Department of Geosciences, University of Padova, via G. Gradenigo 6, 35131 Padova, Italy. E-mail: matteo.maron.1@studenti.unipd.it, anna.breda@unipd.it; manuel.rigo@unipd.it

[b]Department of Earth Sciences, University of Milano, via L. Mangiagalli 34, 20133 Milano, Italy. E-mail: giovanni.muttoni1@unimi.it, michele.mazza@unimi.it

[c]Paleomagnetic Laboratory "Fort Hoofddijk", Department of Earth Sciences, Utrecht University, Budapestlaan 17, 3584 CD Utrecht, The Netherlands. E-mail: M.J.Dekkers@uu.nl, W.Krijgsman@uu.nl

[d]Institute of Geosciences and Earth Resources - CNR, Via G. Gradenigo 6, 35131 Padova, Italy. E-mail: guido.roghi@igg.cnr.it, manuel.rigo@unipd.it

Corresponding Author: Matteo Maron – address: via G. Gradenigo 6, 35131 Padova, Italy – phone: +39 328 7589539 – e-mail: matteo.maron.1@studenti.unipd.it

Keywords: Late Triassic, Carnian, Magnetostratigraphy, Geochronology

Abstract

To contribute to the calibration of the Late Triassic time scale, two sections in Italy were investigated for magnetostratigraphy: the Pignola-2 (Southern Apennines) and the Dibona sections (Dolomites). These sections reveal a sequence of biostratigraphically (conodonts and palynomorphs) calibrated magnetic polarity reversals encompassing the Julian/Tuvalian boundary (Carnian). A total of 63 samples have been collected from the Pignola-2 section that helped defining 12 magnetozones. From the Dibona section, 81 samples have been collected, revealing 9 magnetozones. These data are furthermore constrained by a published radiometric U/Pb age of 230.91±0.33 Ma from the Aglianico ash-bed in the Pignola-2 section. Correlations of the Pignola-2 and the Dibona stratigraphic successions with other Carnian sections from the literature were used to further define the magnetostratigraphy around the Julian/Tuvalian boundary in the Tethys realm. A statistical correlation between the Pignola-2 and the Newark Astrochronological Polarity Time Scale (APTS) provides new constraints on the chronology of the Carnian, also suggesting a duration for the Carnian Pluvial Event (CPE) of ~1 Myr, between ~229.7 and 230.7 Ma.

1. Introduction

Substantial progress has been made in the recent years on the chronology of the Late Triassic, particularly on the duration of the Carnian, Norian and Rhaetian stages, by means of magnetostratigraphic correlations of marine fossil-bearing Tethyan sections and the Newark Astrochronological Polarity Time Scale (APTS) (e.g. Kent and Olsen 1999, Olsen et al. 2015). A first step forward came from the correlation between the Pizzo Mondello section (Southern Italy) and the Newark APTS, which helped assigning a numerical age of ~227 Ma to the level hosting the Carnian/Norian boundary based on conodonts (first appearance datum of *Carnepigondolella gulloae*; Mazza et al., 2012a) close to a positive $\delta^{13}C$ excursion of ~1‰ (Muttoni et al. 2004, Mazza et al. 2010). Recently, a similar

50 correlation exercise applied to the Pignola-Abriola section of Southern Italy assigned an
51 age of 205.7 Ma to the level containing the Norian/Rhaetian boundary based on conodonts
52 (first appearance of *Misikella posthernsteini*), which was found to fall close to a negative
53 $\delta^{13}C_{org}$ spike of ~-30 ‰ (Maron et al. 2015, Rigo et al. 2015). This latter numerical age
54 estimate for the N/R boundary, derived from correlation with the Newark APTS, is
55 compatible with radiometric (U/Pb) age estimates of 205.3±0.14 Ma, 205.4±0.09 Ma, and
56 205.7±0.15 Ma obtained from a level in the Levanto section of Peru close to the N/R
57 boundary approximated by the last occurrence of the bivalve *Monotis subcircularis*
58 (Wotzlaw et al. 2014).
59 In this paper, we focus on the Carnian interval by providing new magnetostratigraphic and
60 biostratigraphic data from the Pignola-2 section of the Southern Apennines and the Dibona
61 section of the Dolomites (both in Italy), which have been correlated to the Newark APTS
62 in order to provide an independent control on the astrochronological ages of the older
63 (Carnian) part of the Newark APTS (Kent and Olsen 1999, Olsen and Kent 1999).
64 Furthermore, we provide a numerical age estimation of a major event occurring in the
65 Carnian, known as the Carnian Pluvial Event (CPE; Simms and Ruffell 1989). The CPE is
66 represented by a widespread deposition of siliciclastic materials recognized in most of the
67 Carnian sections around the world (e.g., Ruffell et al. 2015). The CPE is attributed to a
68 climatic shift to more humid conditions (Simms and Ruffell 1989), triggered by the
69 emplacement of the Large Igneous Province (LIP) of Wrangellia in North America (e.g.,
70 Furin et al. 2006, Rigo et al. 2007, Preto et al. 2010, Dal Corso et al. 2012, Xu et al. 2014)
71 and consequent emission of greenhouse gasses in the atmosphere. The CPE is well
72 expressed by the most siliciclastic intervals in both the Pignola-2 and Dibona sections.
73
74 **2. Geological Setting**

75

76 2.1 Pignola-2

77 The Pignola-2 section (Lat: 40°32'51.44"N, Long: 15°47'17.43"E) crops out in the
78 Southern Apennines, south of the town of Potenza, along the road connecting the two
79 Pignola and Abriola villages (Fig. 1). The section is comprised of a 40 m-thick succession
80 of cherty limestones pertaining to the Calcari con Selce Formation Fm. (Scandone 1967,
81 Miconnet 1983, Amodeo 1999, Rigo et al. 2012), encompassing the Julian/Tuvalian
82 substage boundary (Carnian; Rigo et al. 2007, 2012). The section includes a ~5 m-thick
83 (from meter 8 to 13) green shale and radiolaritic interval (the "green clay-radiolaritic
84 horizon" of Rigo et al. 2007), representing the first documentation of the CPE in Tethyan
85 basinal successions (Rigo et al. 2007, 2012a). In the upper part of the "green clay-
86 radiolaritic horizon" (hereafter "green horizon"), a tuff level, named "Aglianico ash-bed"
87 (meter 12) provided a U/Pb radiometric age of 230.91±0.33 Ma (Furin et al. 2006) (Fig. 2).
88 The "green horizon" has been interpreted as resulting from a transient rise of pCO_2 levels
89 that triggered the shoaling of the calcite compensation depth (CCD). This inferred CCD
90 shoaling is possibly coupled with increased detrital and nutrient input in the basin as a
91 consequence of the CPE, a warm and humid period that fostered silicate weathering and
92 runoff on land (Rigo et al. 2007, 2012b, Rigo and Joachimski 2010, Trotter et al. 2015). A
93 distinct rise of pCO_2 in the coupled ocean-atmosphere system may have been provided by
94 the emplacement of the Wrangellia LIP (e.g., Furin et al. 2006, Rigo et al. 2007, Preto et
95 al. 2010, Dal Corso et al. 2012, Xu et al. 2014), radiometrically dated with Ar/Ar between
96 ~233 and ~222 Ma, with the most likely age comprised between ~230 and ~225 Ma
97 (Greene et al. 2010). The oldest radiometric ($^{207}Pb/^{206}Pb$) age available for Wrangellia
98 comes from gabbros in Yukon, associated to the Wrangellian effusions and dated at 232.2

99 ±1 Ma (Mortensen and Hulbert 1992; see also Greene et al. 2010). This age interval
100 includes the age of the CPE at Pignola-2 from the "Aglianico ash-bed" (Furin et al. 2006).
101
102 2.2 Dibona
103 The Dibona section (Lat: 46°32'2.50"N, Long: 12°04'21.68"E) is a ~370 m thick shallow-
104 water sedimentary succession located in the Dolomites (Southern Alps), on the southern
105 side of the Tofana di Rozes Mountain, near the Dibona Hut (Fig. 1). The section is
106 characterized by mixed carbonate-siliciclastic deposits of shallow-marine
107 (Heiligkreuz/Santa Croce Formation) to marginal-marine (Travenanzes Formation)
108 environments (e.g. Breda et al. 2009). The ~160 m Heiligkreuz Fm. (De Zanche et al. 1993,
109 Preto and Hinnov 2003, Neri et al. 2007, Gattolin et al. 2013, 2015) is subdivided into three
110 members, which from the base to the top are subsequently the Borca Mb., ~100 m-thick,
111 consisting of limestones and arenites passing to dolostones; the Dibona Sandstones Mb.,
112 ~60 m-thick, consisting of arenites, conglomerates, pelites and limestones; the Lagazuoi
113 Mb., ~30 m-thick, consisting mainly of strongly dolomitized oolitic limestones (Fig. 3).
114 The shales and arenites of the Borca and Dibona Sandstones Mbs record the CPE in a
115 coastal environment (Breda et al. 2009, Preto et al. 2010). A major negative $\delta^{13}C$ spike
116 linked to the eruption of Wrangellia flood basalts has been observed at the base of the
117 Heiligkreuz Fm., close to Dibona section, confirming the connection of the clastic input to
118 the CPE climatic event (Dal Corso et al. 2012). Above the Lagazuoi Mb., the ~180 m
119 Travenanzes Fm. (De Zanche et al. 1993, Neri et al. 2007, Breda and Preto 2011) starts
120 with ~25 m of dark clays and aphanitic dolostones passing upwards to multicolored clays
121 with carbonatic and evaporitic intercalations deposited in sabkha-like environments. The
122 top of the Travenanzes Fm. is dominated by dolomitic peritidal cycles of carbonate tidal-

123 flat and shallow lagoon environments, with thin dark clay intercalations. It represents the
124 transition to the overlying Dolomia Principale carbonate platform (Breda and Preto 2011).
125
126 **3. Biostratigraphy**
127 The Pignola-2 section has a detailed conodont and palynomorph biostratigraphy (Rigo et
128 al. 2007, 2012). According to the conodont biostratigraphy, the Julian/Tuvalian
129 (middle/late Carnian) boundary is placed at the base of the "green horizon". In fact, below
130 the "green horizon" a typical Julian conodont association composed of *Paragondolella*
131 *praelindae*, *P. polygnathiformis*, and *Gladigondolella* spp is present. Above the "green
132 horizon", the section bears Tuvalian conodont species, i.e. *Carnepigondolella nodosa*, *C.*
133 *carpathica*, *Paragondolella noah*, *P. oertlii*, and *Metapolygnathus praecommunisti* (Fig.
134 2) (Rigo et al. 2012). Specifically, the Julian/Tuvalian boundary is placed at the level with
135 the last occurrence (LO) of the *Gladigondolella* genus (Rigo et al. 2007). Palynomorphs
136 from Pignola-2 have been grouped in two main assemblages (Rigo et al. 2007): Assemblage
137 A is typical of the Julian/Tuvalian interval, while Assemblage B covers a narrower range
138 in the upper Tuvalian (see Rigo et al. 2007 for additional details) (Fig. 2).
139 The Dibona section has a detailed pollen and spore biostratigraphy (Roghi 2004, Roghi et
140 al. 2010). The typical uppermost Julian-lower Tuvalian association with *Patinasporites*
141 *densus*, *Aulisporites astigmosus* and *Duplicisporites continuus* (Borca Mb, Dibona
142 Sandstone Mb) and *Equisetosporites chinleanus* (Dibona Sandstones Mb) is found in the
143 Heilgkreuz Fm. It is followed by a Tuvalian association of *Granuloperculatipollis rudis*
144 and *Riccisporites cf. R. tuberculatus,* found at the base of the overlying Travenanzes Fm
145 (Fig. 3). The former association, belonging to the *Granuloperculatipollis rudis* Assemblage
146 of Roghi et al. (2006, 2010), is similar to Assemblage B found in the Pignola-2 section.
147 Moreover, additional sections coeval to the Dibona section reveal pollens and spores

148 comparable with the biostratigraphic record of Pignola-2, e.g. the Cave del Predil section
149 in the Southern Alps of Friuli (Roghi 2004), and the Lunz (Köppen 1997) and Rubland
150 (Kraus 1969) sections in the Northern Calcareous Alps of Austria. Six samples for
151 conodont analysis have been collected from the Dibona section immediately below the base
152 of the Lagazuoi Mb, in the last 10 meters of the Dibona Sandstones Mb. The conodont
153 association consists of *Paragondolella polygnathiformis*, *Paragondolella noah*,
154 transitional forms from *P. noah* to *Metapolygnathus praecommunisti*, and early
155 representatives of *M. praecommunisti* (Fig. 3, Pl. 1) attributed to the early Tuvalian age
156 (Mazza et al. 2010, Mazza et al. 2011). Furthermore, the ammonoid *Shastites* cf. *pilari* has
157 been found below the Lagazuoi Mb, in the nodular limestone corresponding to the upper
158 portion of the Dibona Sandstone Mb of the Heiligkreuz Fm. (Gianolla et al. 1998, De
159 Zanche et al. 2000, Gattolin et al. 2015).
160
161 **4. Paleomagnetism**
162 4.1 Sampling and laboratory methods
163 A total of 63 oriented paleomagnetic core samples (~10cc) have been collected from the
164 Pignola-2 section, 55 from limestones beds and 8 from the radiolaritic intervals within the
165 "green horizon", with a stratigraphic interval of approximately 0.5 m (Fig. 2). The clayey
166 intervals of the "green horizon" have not been sampled because they are both too thin and
167 chipped. From the Dibona section a total of 45 cores have been collected from the upper
168 Borca Mb. to the base of the Lagazuoi Mb. (Heiligkreuz Fm.), and 36 samples from the
169 Travenanzes Fm. To isolate the ChRM, all samples have been thermally demagnetized
170 (with an ASC TD48 furnace, residual field < 10 nT) and measured with a 2G Enterprises
171 DC-SQUID magnetometer (magnetic moment noise level $<10^{-12}$ Am^2) at the Alpine
172 Laboratory of Paleomagnetism – ALP (Peveragno, Italy). Samples have been demagnetized

by steps of 50°C from 100°C to 350°C, then 25°C until 675°C. Single sample directions of the magnetization vectors have been plotted on an end-point vector graph (Zijderveld 1967) for each step of demagnetization (Fig. 4). Samples showing magnetization components made of less than three end-points in sequence (representing three subsequent temperature steps) have been rejected.

The low-field magnetic susceptibility (κ) was measured with a AGICO Kappabridge KLY-3 instrument (sensitivity: 2×10^{-8} SI; at the ALP, Peveragno) for all samples. Further, to support the paleomagnetic interpretation, thermomagnetic runs were performed on a modified horizontal translation Curie balance (paleomagnetic laboratory 'Fort Hoofddijk', Utrecht University, The Netherlands; noise level $5x10^{-9}$ Am^2, typical signals at least an order of magnitude higher; Mullender et al. 1993) for a subset of the samples. About 70-80 mg of powdered sample was measured in several cycles to increasingly higher temperature up to 670°C; the field was cycled between 100 and 300 mT, heating and cooling rates were 10°C/minute. Measurements were performed in air. Three samples from the Pignola-2 section were investigated and 6 from the Dibona section (3 from the Heiligkreuz Fm. and 3 from the Travenanzes Fm.).

Samples PGM0.30, RAD4 and PGM14.64 from the Pignola-2 section and samples MDS12.4, MDS29.1 and MDS52.3 from the Dibona section have been analyzed using the Curie balance.

4.2 Magnetic properties

The limestones of the Pignola-2 section reveal a very low κ, usually smaller than 5×10^{-6} SI (Fig. 2). In the "green horizon" the initial magnetic susceptibility is considerably higher (from ~70×10^{-6} to ~110×10^{-6} SI) than in the rest of the sampled interval, due to an increase of the terrigenous fraction (Fig. 3). Interestingly, magnetic susceptibility is high (from

198 25×10^{-6} to 55×10^{-6} SI) also in the carbonatic strata delimiting the "green horizon" (~1 or 2
199 meters above and below), indicating a significant siliciclastic component we associate to
200 the CPE.
201 The Curie balance results are shown in Fig. 5 and the stratigraphic position of the sample
202 is in Fig. 3. The limestones of the Pignola-2 section (PGM0.30 and 14.64; Fig. 5A, 5C) are
203 very weak, only slightly above instrumental noise level. Nonetheless there seems to be a
204 marginally convex magnetization vs. temperature behavior between ~100-200 and ~450-
205 500°C, that is reversible on intermittent cooling. The final cooling segment from 600°C
206 back to room temperature, however, does not reveal that behavior. It is difficult to interpret
207 this behavior that may be associated with titanomagnetite (sensu lato) with a varying Ti-
208 content. However, a minute amount of magnetic sulfides cannot be excluded with certainty.
209 The "green horizon" sample RAD4 (Fig. 5B) is much stronger (but still weak, it remains a
210 sediment) and shows a Curie point (determined by the two-tangent method, Grommé et al.
211 1969) of ~350°C that is reversible on cooling after the final heating temperature of 600°C.
212 The Dibona Sandstones Mb samples (MDS12.4, Fig. 5D; MDS29.1, Fig. 5E; MDS52.3,
213 Fig. 5F; stratigraphic position in Fig. 3) from the Dibona section all show a variable portion
214 of non-magnetic pyrite (FeS_2) that is oxidized during the thermomagnetic analysis, first to
215 magnetite and finally to hematite, explaining the occasionally huge increase in
216 magnetization between 400 and 600°C. There are no indications for magnetic sulfides
217 below 400°C since the analysis shows reversible heating and cooling segments in that
218 temperature range and no Curie temperature of ~320°C. Plausibly traces of magnetite
219 represent the original magnetic mineralogy but it is impossible to discriminate between left
220 overs of neo-formed magnetite (most of it oxidizes further to hematite) and original
221 magnetite. The three samples from the Travenanzes Fm (MTV9, Fig. 5G; MTV52, Fig.
222 5H; MTV67, Fig. 5I; stratigraphic position in Fig. 3) are all very weak demonstrating

223 paramagnetic behavior only. During the heating above 600°C a minute amount of magnetic
224 minerals (presumably fine-grained magnetite) is formed because the final cooling curves
225 lie slightly above the corresponding heating curves.
226
227 4.3 Magnetostratigraphy
228
229 4.3.1 Pignola-2
230 The mean intensity of the starting NRM is ~0.02 mA/m in the pelagic carbonates, ~0.06
231 mA/m in the radiolarites of the "green horizon", and ~0.2 mA/m in the carbonatic levels
232 just above the "green horizon". Vector end-point demagnetization diagrams (Fig. 4A;
233 Zijderveld 1967) reveal the presence of spurious (viscous) magnetic components from
234 room temperature to 250-300°C; at higher temperatures the characteristic component
235 remanent magnetization (ChRM) direction is isolated (Fig. 4A). The demagnetization
236 trajectory trends toward the origin up to a maximum temperature of 675°C. This behavior
237 is observed in 47 samples. Equal area stereographic projections reveal that the ChRM is
238 bipolar being oriented north-and-down or south-and-up in *in situ* coordinates, and
239 northwest-and-down or southeast-and-up after correction for bedding tilt (Fig. 6). The
240 mean direction in tilt-corrected coordinates, calculated with standard Fisher statistics, is of
241 Dec: 28.4°E; Inc: 39.6° (k=23.9; α_{95}=4.3°; N = 47; Table 2). No fold test could be
242 performed because the bedding attitude trough the section is essentially the same. The
243 reversals test (McFadden and McElhinny 1990) is positive, suggesting that the ChRM is
244 the original magnetization acquired during or shortly after deposition. The mean directions
245 in *in situ* coordinates (Dec: 353.5°E; Inc: 59.7°; k: 24.1; α_{95}: 4.3°) are similar to the
246 inclination of the geomagnetic axial dipole (GAD Inc: ~59.8°), so we cannot exclude some
247 contamination of the ChRM by VRM for normal polarity components. The latitudes of the

Virtual Geomagnetic Poles, derived from the ChRM directions, provided a sequence of 12 magnetic polarity reversals defining 12 magnetozones labeled from MP1n to MP6r (Fig. 2). The shales of the "green horizon" were not sampled for magnetostratigraphy (see above).

4.3.2 Dibona

The mean intensity of the samples from the Heiligkreuz Fm. is ~0.04 mA/m and in the Travenanzes Fm. is ~0.05 mA/m. The vector end-point diagrams (Fig. 4B; Zijderveld 1967) reveal the ChRM between 200°C and 550°C in 25 of 45 samples of the Heiligkreuz Fm. (named MDS), and between 150°C and 400°C in 18 of 36 samples from the Travenanzes Fm (named MTV). The diagrams shows both north-down and south-up directions, sometimes scattered (Fig. 4B) (typical MAD: ~11). The equal-area stereographic projection reveal fairly scattered directions (Fig. 6), failing the reversals test (McFadden and McElhinny 1990). As for the Pignola-2 section, also here fold test cannot be performed due to homoclinality of the succession. The sequence of VGPs of the Dibona section shows nine magnetozones labeled MD, where MD1r, 2r and 4r are rather uncertain (grey intervals, Fig. 3), due to the poor preservation of NRM in these intervals (only three robust paleomagnetic directions).

5. Discussion

5.1 Correlations between Tethyan sections

The Pignola-2 section is correlated with other coeval Tethyan sections from the literature containing conodonts to obtain a complete magneto-biostratigraphic record for the Carnian

273 Stage (Fig. 7). The upper part of the Pignola-2 magnetostratigraphy (magnetozones MP2n
274 to MP3r) is considered correlative to the basal portion of the Silická Brezová section (up
275 to SB2r) (Channel et al. 2003) and the Pizzo Mondello section (up to PM2r) (Muttoni et al.
276 2004), whereas the entire Pignola-2 section is comparable with the Guri Zi section in
277 Albania (up to GZ5r) (Muttoni et al. 2005, 2014) (Fig. 7). The conodont biostratigraphy of
278 Silická Brezová has been updated in this study by reclassifying the taxa illustrated in Figs.
279 A1-A3 in Channell et al. (2003), using the new taxonomic criteria illustrated in Mazza et
280 al. (2010, 2011, 2012a,b) (Fig. 7).
281 The magnetostratigraphy of the Dibona section straddling the Dibona Sandstones Mb. of
282 the Heiligkreuz Fm. should be partially coeval with the magnetostratigraphy across the
283 "green horizon" in the Pignola-2 section, as suggested by the first occurrence of conodont
284 *Metapolygnathus praecommunisti* (Figs. 3, 7). Consequently, magnetozones MD1n-1r-2n-
285 2r-3n at Dibona have been correlated to Pignola-2 magnetozones MP4n-4r-5n-5r-6n,
286 respectively. Based on the first occurrence of *M. praecommunisti*, magnetozone MD3n is
287 considered coeval to magnetozone SB2n at Silická Brezová and PM2n at Pizzo Mondello
288 (Fig. 7).
289 The correlation between Pignola-2 and Dibona sections implies that the onset of the CPE
290 at Dibona should fall in the lower part of the Heiligkreuz Fm. (basal Borca Mb, as suggested
291 by Dal Corso et al., 2012) and its acme is reasonably represented by the terrigenous-rich
292 levels of the Dibona Sandstone Mb (Fig. 3). The absence of strong biostratigraphic
293 constraints does not allow a solid magnetostratigraphic correlation between the upper
294 Dibona section and other Tethyan sections.
295
296 5.2 Correlation with the Newark APTS

297 The Pignola-2 magnetostratigraphy has been compared with the Newark APTS (Kent and
298 Olsen 1999; see also Olsen et al. 2015) and then been exploited also in Olsen et al. (2015)
299 using the statistical approach described in Muttoni et al. (2004) and Maron et al. (2015).
300 The radiometric age of 230.91±0.33 Ma from the Aglianico ash-bed (Furin et al. 2006),
301 comprised within the Pignola-2 magnetozone MP4r, has been taken into account for the
302 correlation. The Dibona section was not considered for statistical correlation with the
303 Newark APTS because of the unreliability of its magnetostratigraphy, due the variable
304 sedimentation rate typical of shallow-water environments.
305 We compared the thickness of the Pignola-2 magnetozones with the duration of the
306 magnetozones in the Newark APTS, testing the magnetostratigraphy of Pignola-2 along the
307 APTS and obtaining 24 possible correlation options (Fig. 8). The interval of unknown
308 polarity within the Pignola-2 "green horizon" is tentatively interpreted as dominated by
309 normal polarity.
310 Each correlation is analyzed using linear regression, obtaining 24 t-test values; the higher
311 the t-value, the more reliable the correlation. Only options 1, 2 and 24 pass the 95%
312 confidence level threshold (Fig. 8). Option 24 is not considered because it is inconsistent
313 with the U/Pb radiometric age of 230.91±0.33 Ma from the "green horizon" (Furin et al.
314 2006). Option 1 and 2 are consistent with this age. The main features of Option 1 and 2 are
315 as follows:
316
317 Option 1:
318 – High t-value (~2.7).
319 – The radiometric age of Pignola-2 fits more closely (0.6 M.y. older) with the age
320 provided by the Newark APTS for the equivalent stratigraphic level (Fig. 9).

- Fits with the correlation of Pizzo Mondello and the APTS. Specifically, magnetozones MP4r and MP5n of Pignola-2 are correlated respectively to E5r and E6n in Newark, as well as to the PM1r and PM2n in Pizzo Mondello. PMr1 and PM2n were correlated to the same Newark magnetozones by Muttoni et al. (2004) (Fig. 7).

Option 2:

- High t-value (~3.1)
- The correlation with the Newark APTS leads to a 0.9 M.y. discrepancy between the radiometric age of Pignola-2 and the age of the APTS (Fig. 9).
- This option does not fit with the previous correlation between Pizzo Mondello and the Newark APTS (Muttoni et al. 2004).

Option 1 implies only a minor discrepancy between the Pignola-2 U/Pb age and the Newark astrochronology, considering that in the lower Stockton Fm astrochronology is extrapolated from the upper Stockton and Lockatong Fms, where the 404 kyr McLaughlin cycles are better expressed (Kent and Olsen 1999, Olsen and Kent 1999). Moreover, Option 1 is coherent with previous correlations from the literature (Pizzo Mondello; Muttoni et al. 2004) and is preferred over Option 2.

We derived an age model from Option 1 that reveals a complex pattern of sedimentation rate along the Pignola-2 section (Fig. 10). In the cherty limestones, the sedimentation rate is mostly constant, except for a decrease just below and above the “green horizon”. In the “green horizon” the sedimentation rate increases, probably due to an enhanced runoff of siliciclastic sediments from the continent caused by increased rainfall and weathering, in consequence of the intensification of the humid conditions at the CPE.

346 The age model derived from Option 1 (Fig. 10) suggests an age of ~230.7 Ma for the
347 Julian/Tuvalian boundary, approximated in Pignola-2 by the LO of conodont
348 *Gladigondolella* spp.. Assuming a Carnian/Norian boundary at ~227 Ma (Muttoni et al.
349 2004) and a Ladinian/Carnian boundary at ~237 Ma (Mietto et al, 2012), the Julian should
350 be ~6.3 My-long and the Tuvalian ~3.7 My-long. Assuming the magnetic susceptibility
351 anomaly in Pignola-2 (covering the "green horizon" and the closest limestone beds) as
352 expression of the CPE, its duration was about 1 My.
353
354 **6. Conclusions**
355 The paleomagnetic analyses of the Carnian sections of Pignola-2 (Southern Apennines,
356 Italy) and Dibona (Dolomites, Italy) provided respectively a sequence of 12 and 8
357 magnetozones.
358 The correlation with other Tethyan sections of the same time interval (Pizzo Mondello,
359 Silická Brezová, Guri Zi) reveals a virtually continuous magnetostratigraphic record for the
360 Carnian, constrained by a radiometric age of 230.91±0.33 Ma.
361 Using a statistical approach, we performed a correlation between the Pignola-2 section and
362 the Newark APTS that led to three statistically relevant options. Only two of them (Options
363 1 and 2) appear to be broadly consistent with both the radiometric age of the Pignola-2 ash-
364 layer and their correlative ages in the Newark APTS. Although Option 2 was statistically
365 slightly more robust, Option 1 is provisionally preferred as it shows the highest matching
366 between radiometric and astrochonologic age estimates of the Pignola-2 ash-layer and does
367 not violate the correlation between the Newark APTS and the Pizzo Mondello section as
368 proposed by Muttoni et al (2004) using the same statistical method adopted in this study.
369 Ages of the main events of the Pignola-2 and Dibona sections were calculated using a
370 model derived from Option 1. The level containing the Julian/Tuvalian boundary defined

by conodonts is now calibrated at ~230.7 Ma, and the levels attributed to the Carnian Pluvial Event should have deposited between ~229.7 and 230.7 Ma.

7. Acknowledgments

Nereo Preto, Leonardo Solazzi and Jacopo Dal Corso are acknowledged for their help during the fieldwork at the Dibona section. The "Fort Hoofddijk" crew is thanked for the help during the analysis and for the hospitality. Field and laboratory activities were funded by grants ex-60% (60A05-7013/15) to M. Rigo, ex-60% (60A05-0287/142) to A. Breda.

8. References

Amodeo, F., 1999. Il Triassico terminale-Giurassico del Bacino Lagonegrese. Studi stratigrafici sugli Scisti Silicei della Basilicata (Italia meridionale). Mémoire de Géologie, Lausanne, 33, 121 p.

Breda, A., Preto, N., Roghi, G., Furin, S., Meneguolo, R., Ragazzi, E., Fedele, P., Gianolla, P., 2009. The Carnian Pluvial Event in the Tofane Area (Cortina d'Ampezzo, Dolomites, Italy). Geo.Alp 6, 80-115

Breda, A., Preto, N., 2011. Anatomy of an Upper Triassic continental to marginal-marine system: the mixed siliciclastic-carbonate Travenanzes Formation (Dolomites, Northern Italy). Sedimentology 58, 1613-1647.

Blackburn, T.J., Olsen, P.E., Bowring, S.A., McLean, N.M., Kent, D.V., Puffer, J., McHone, G., Rasbury, E.T., Et-Touhami, M., 2013. Zircon U-Pb geochronology links the end-Triassic extinction with the Central Atlantic magmatic province. Science 340, 941–945.

Channell, J.E.T., Kozur, H.W., Sievers, T., Mock, R., Aubrecht, R., Sykora, M., 2003. Carnian-Norian biomagnetostratigraphy at Silická Brezová (Slovakia): correlation

to other Tethyan sections and to Newark Basin. Palaeogeography, Palaeoclimatology, Palaeoecology 191, 65-109.

Dal Corso, J., Mietto, P., Newton, R.J., Pancost, R.D., Preto, N., Roghi, G., Wignall, P.B., 2012. Discovery of a major negative $\delta^{13}C$ spike in the Carnian (Late Triassic) linked to the eruption of Wrangellia flood basalts. Geology 40, 79-82.

De Zanche, V., Gianolla, P., Mietto, P., Siorpaes, C. Vail, P.R., 1993. Triassic sequence stratigraphy in the Dolomites (Italy). Memorie di Scienze Geologiche 45, 1–27.

De Zanche, V., Gianolla, P., Roghi, G., 2000. Carnian stratigraphy in the Raibl/Cave del Predil area (Julian Alps, Italy). Eclogae Geologicae Helvetiae 93, 331-347.

Furin, S., Preto, N., Rigo, M., Roghi, G., Gianolla, P., Crowley, J.L., Bowring, S.A., 2006. High-precision U-Pb zircon age from the Triassic of Italy: Implications for the Triassic time scale and the Carnian origin of calcareous nannoplankton and dinosaurs. Geology 34, 1009-1012.

Gattolin, G., Breda, A., Preto. N., 2013. Demise of Late Triassic carbonate platforms triggered the onset of a tide-dominated depositional system in the Dolomites, Northern Italy. Sedimentary Geology 297, 38-49.

Gattolin, G., Preto, N., Breda, A., Franceschi, M., Isotton, M., Gianolla, P., 2015. Sequence Stratigraphy after the demise of a high-relief carbonate platform (Carnian of the Dolomites): sea-level and climate disentangled. Palaeogeography, Palaeoclimatology, Palaeoecology 423, 1-17.

Gianolla, P., Ragazzi, E., Roghi, G., 1998. Upper Triassic amber from the Dolomites (Northern Italy). A paleoclimatic indicator?. Rivista Italiana di Paleontologia e Stratigrafia 104, 381-390.

419 Greene, A.R., Scoates, J.S., Weis, D., Katvala, E.C., Israel, S., Nixon, G.T., 2010. The
420 architecture of oceanic plateaus revealed by the volcanic stratigraphy of the accreted
421 Wrangellia oceanic plateau. Geosphere 6, 47-73.
422 Grommé, C.S., Wright, T.L., Peck, D.L., 1969. Magnetic Properties and Oxidation of Iron-
423 Titanium Oxide Minerals in Alae and Makaopuhi Lava Lakes, Hawaii. Journal of
424 Geophysical Research 74, 5277-5293.
425 Kent, D.V., Olsen, P.E., 1999. Astronomically tuned geomagnetic polarity time scale for
426 the Late Triassic. Journal of Geophysical Research 104, 12831–12841.
427 Köppen, A., 1997. Faziesentwicklung in der frühen Obertrias Mitteleuropas – ein
428 sequenzstratigraphischer Vergleich. Gaea Heidelbergensis 2, 1-233.
429 Kraus, O., 1969. Die Raibler Schichten des Drauzunges (Südliche Kalk-alpen).
430 Lithofazielle, sedimentpetrographische un paläogeographische Untersuchungen.
431 Jahrbuch der Geologischen Bundesanstalt 112, 81-152.
432 Maron, M., Rigo, M., Bertinelli, A., Katz, M.E., Godfrey, L., Zaffani, M., Muttoni, G.,
433 2015. Magnetostratigraphy, biostratigraphy and chemostratigraphy of the Pignola-
434 Abriola section: New constraints for the Norian-Rhaetian boundary. Geological
435 Society of America Bulletin 127, 962-974.
436 Mazza, M., Furin, S., Spötl, C., Rigo, M., 2010. Generic turnovers of Carnian/Norian
437 conodonts: Climatic controls or competition?. Palaeogeography,
438 Palaeoclimatology, Palaeoecology 290, 120- 137.
439 Mazza, M., Rigo, M., Nicora, A., 2011. A new *Metapolygnathus* platform conodont species
440 and its implications for Upper Carnian global correlations. Acta Palaeontologica
441 Polonica 56, 121-131.

442 Mazza, M., Rigo, M., Gullo, M., 2012a. Taxonomy and biostratigraphic record of the Upper
443 Triassic of the Pizzo Mondello section (Western Sicily, Italy), GSSP candidate for
444 the base of the Norian. Rivista Italiana di Paleontologia e Stratigrafia 118, 85-130.
445 Mazza, M., Cau, A., Rigo, M., 2012b. Application of numerical cladistic analyses to the
446 Carnian–Norian conodonts: a new approach for phylogenetic interpretations.
447 Journal of Systematic Palaeontology 10, 401-422.
448 McFadden, P.L., McElhinny, M.W., 1990. Classification of the reversal test in
449 palaeomagnetism. Geophysical Journal International 103, 725–729.
450 Mietto, P., Manfrin, S., Preto, N., Rigo, M., Roghi, G., Furin, S., Gianolla, P., Posenato,
451 R., Muttoni, G., Nicora, A., Buratti, N., Cirilli, S., Spötl, C., Ramezani, J., Bowring,
452 S.A., 2012. The Global Boundary Stratotype Section and Point (GSSP) of the
453 Carnian Stage (Late Triassic) at Prati di Stuores/Stuores Wiesen Section (Southern
454 Alps, NE Italy). Episodes – Newsmagazine of the International Union of Geological
455 Sciences 35, 414-430.
456 Miconnet, P., 1983. La région de Lagonegro (Italie méridionale): évolution géologique
457 d'un bassin dans son cadre alpin. PhD Thesis, Université des Sciences et
458 Techniques de Lille, Lille, France, 185 p.
459 Mortensen, J.K., Hulbert, L.J., 1992. A U-Pb zircon age for a Maple Creek gabbro sill,
460 Tatamagouche Creek area, southwestern Yukon Territory, in Radiogenic age and
461 isotopic studies: Report 5. Geological Survey of Canada Paper 91, 175–179.
462 Mullender, T.A.T., van Velzen, A.J., Dekkers, M.J., 1993. Continuous drift correction and
463 separate identification of ferromagnetic and paramagnetic contributions in
464 thermomagnetic runs. Geophysical Journal International 114, 663-672.
465 Muttoni, G., Kent, D.V., Olsen, P.E., Di Stefano, P., Lowrie, W., Bernasconi, S.M.,
466 Hernández, F.M., 2004. Tethyan magnetostratigraphy from Pizzo Mondello (Sicily)

467 and correlation to the Late Triassic Newark astrochronological polarity time scale.
468 Geological Society of America Bulletin 116, 1043-1058.
469 Muttoni. G., Meço, S., Gaetani, M., 2005. Magnetostratigraphy and biostratigraphy of the
470 Late Triassic Guri Zi section, Albania: constraint on the age of the Carnian-Norian
471 boundary. Rivista Italiana di Paleontologia e Stratigrafia 111, 233-245.
472 Muttoni, G., Mazza, M., Mosher, D., Katz, M.E., Kent, D.V., Balini, M., 2014. A Middle-
473 Late Triassic (Ladinian-Rhaetian) carbon and oxygen isotope record from the
474 Tethyan Ocean. Palaeogeography, Palaeoclimatology, Palaeoecology 399, 246-
475 259.
476 Neri, C., Gianolla, P., Furlanis, S., Caputo, R., Bosellini, A., 2007. Note illustrative della
477 Carta Geologica d'Italia alla scala 1:50000, foglio 029 Cortina d'Ampezzo. APAT,
478 Rome, Italy, 200 p.
479 Olsen, P.E., Kent, D.V., 1999. Long-period Milankovitch cycles from the Late Triassic and
480 Early Jurassic of eastern North America and their implications for the calibration of
481 the Early Mesozoic time-scale and the long-term behaviour of the planets. Royal
482 Society of London Philosophical Transactions 357, 1761–1786.
483 Olsen, P.E., Reid, J.C., Taylor, K.B., Whiteside, J.H., Kent, D.V., 2015. Revised
484 stratigraphy of Late Triassic age strata of the Dan River Basin (Virginia and North
485 Carolina, USA) based on drill core and outcrop data. Southeastern Geology 51, 1-
486 31.
487 Preto, N., Hinnov, L.A., 2003. Unraveling the origin of carbonate platform cyclothems in
488 the Upper Triassic Durrenstein Formation (Dolomites, Italy). Journal of
489 Sedimentary Research 73, 774-789.
490 Preto, N., Kustatscher, E., Wignall, P.B., 2010. Triassic climates – State of the art and
491 perspectives. Paleaeogeography, Palaeoclimatology, Palaeoecology 290, 1-10.

492 Rigo, M., Preto, N., Roghi, G., Tateo, F., Mietto, P., 2007. A rise in the Carbonate
493 Compensation Depth of western Tethys in the Carnian (Late Triassic): deep-water
494 evidence for the Carnian pluvial event. Paleaeogeography, Palaeoclimatology,
495 Palaeoecology 246, 188-205.
496 Rigo, M., Joachimski, M.M., 2010. Palaeoecology of Late Triassic conodonts: constraints
497 from oxygen isotopes in biogenic apatite. Acta Palaeontologica Polonica 55, 471-
498 478.
499 Rigo, M., Preto, N., Franceschi, M., Guaiumi, C., 2012a. Stratigraphy of the Carnian-
500 Norian Calcari con Selce Formation in the Lagonegro Basin, Southern Apennines.
501 Rivista Italiana di Paleontologia e Stratigrafia 118, 143-154.
502 Rigo M, Trotter, J.A., Preto, N., Williams, I.S., 2012. Oxygen isotopic evidence for Late
503 Triassic monsoonal upwelling in the northwestern Tethys. Geology 40, 515-518.
504 Rigo M., Bertinelli, A., Concheri G., Gattolin, G., Godfrey, L., Katz, M.E., Maron, M.,
505 Mietto, P., Muttoni, G., Sprovieri, M., Stellin, F., Zaffani, M., 2015. The Pignola-
506 Abriola section (southern Apennines, Italy): a new GSSP candidate for the base of
507 the Rhaetian Stage. Lethaia, doi: 10.1111/let.12145 .
508 Roghi, G., 2004. Palynological investigations in the Carnian of the Cave del Predil area
509 (Julian Alps, NE Italy). Review of Palaeobotany and Palynology 132, 1-35.
510 Roghi, G., Gianolla, P., Minarelli, L., Pilati, C., Preto, N., 2010. Palynological correlation
511 of Carnian humid pulses throughout western Tethys. Paleaeogeography,
512 Palaeoclimatology, Palaeoecology 290, 89-106.
513 Ruffell, A., Simms, M.J., Wignall, P.B., 2015. The Carnian Humid Episode of the Late
514 Triassic: a review. Geological Magazine, doi: 10.1017/S0016756815000424 .
515 Scandone, P., 1967. Studi di geologia lucana: la serie calcareo-silico-marnosa. Bollettino
516 della Società dei Naturalisti in Napoli 76, 1-175.

517 Simms, M.J., Ruffell, A.H., 1989. Synchroneity of climatic change and extinction in the
518 Late Triassic. Geology 17, 265-268.
519 Trotter, J.A., Williams, I.S., Nicora, A., Mazza, M., Rigo, M., 2015. Long-term cycles of
520 Triassic climate change: a new $\delta^{18}O$ record from conodont apatite. Earth and
521 Planetary Science Letters 415, 165-174.
522 Xu, G., Hannah, J.L., Stein, H.J., Mørk, A., Vigran, J.O., Blingen, B., Schutt, D.L.,
523 Lundschien, B.A., 2014. Cause of Upper Triassic climate crisis revealed by Re-Os
524 geochemistry of Boreal black shales. Paleaeogeography, Palaeoclimatology,
525 Palaeoecology 395, 222-232.
526 Zijderveld, J.D.A., 1967. A.C. demagnetization of rocks: analysis of results. In: Collinson,
527 D.W., Creer, K.M., Runcorn, S.K. (Eds.), Methods in Paleomagnetism. Elsevier,
528 Amsterdam, p. 254–286.
529

530 **9. Figure captions, Table captions**

531

532 Figure 1: The Pignola-2 section (coord.: Lat: 40°32'51.44"N, Long: 15°47'17.43"E) is
533 located in the Southern Apennines, near Potenza (Southern Italy). The outcrop is
534 along the main road connecting Pignola to Abriola, on the southern side of the Mt
535 Crocetta. The Dibona section (coord.: Lat: 46°32'2.50"N, Long: 12°04'21.68"E) is
536 located in the Dolomites, near Cortina d'Ampezzo (Belluno, Northern Italy). The
537 outcrop is on the southern side of the Tofane di Rozes. Pignola-2 and Dibona
538 sections were located in central Tethys during the Late Triassic.
539 Figure 2: The Pignola-2 section. From left to right: lithostratigraphy, conodonts and
540 palynomorphs biostratigraphy, Virtual Geomagnetic Pole (VGP) latitudes (from
541 ChRM directions), magnetostratigraphy and magnetic susceptibility. In the

magnetostratigraphy, black is normal polarity and white is reversed polarity. A total of 6 magnetozones have been identified, with a 5 meters interval of unknown polarity (grey shading) corresponding to the shales of the green clay-radiolaritic horizon (that could not be sampled). The U/Pb radiometric age of 230.91±0.33 Ma (Furin et al. 2006) comes from an ash-bed inside the green clay-radiolaritic horizon. Anomaly in the magnetic susceptibility around the "green horizon" represents the Carnian Pluvial Event in basinal environment (light-grey shaded interval).

Figure 3: The Dibona section. From left to right: lithostratigraphy of the investigated portion, palynomorph and conodont biostratigraphy, magnetostratigraphy, Virtual Geomagnetic Pole (VGP) latitudes (from ChRM directions), magnetic susceptibility and lithostratigraphy of the whole Dibona section. In the magnetostratigraphy, black is normal polarity and white is reversed polarity. In the lower panel is the Dibona Sandstone Mb (Heiligkreuz Fm) site and in the upper panel is the Travenanzes Fm site. A total of 8 magnetozones have been identified, 5 from the Dibona Sandstones and 3 from the Travenanzes Fm. The large portion of unknown polarity (grey shading) in the Travenanzes portion is due to sparse seemingly robust paleomagnetic data (only three menaingful VGP points). Extension of the Carnian Pluvial Event is illustrated with the grey shaded area in the whole Dibona section lithostratigtaphy (on the right).

Figure 4: Vector end-point demagnetization diagrams (Zijderveld 1967) of the Pignola-2 section (panel A) and the Dibona section (panel B). Open circles are projections onto the vertical plane, and closed circle are projections onto the horizontal plane for in situ (geographic) coordinates.

Figure 5: Thermomagnetic curves determined with a Curie balance of samples PGM (Pignola-2, Calcari con Selce Fm; panels A, C), RAD (Pignola-2, Green clay-

567 radiolaritic horizon; panel B), MDS (Dibona, Heiligkreuz Fm; panels D, E, F), and
568 MTV (Dibona, Travenanzes Fm; panels G, H, I). The PGM samples of Pignola-2
569 reveal a mixture of different minerals, including magnetite, in the cherty limestones,
570 whereas in the green horizon (RAD sample) there is an increase in more Ti-rich
571 magnetite. Samples MDS from the Heiligkreuz Fm in the Dibona section show a
572 magnetization increase above 400-450°C, coherent with the reaction of pyrite to
573 magnetite.

574 Figure 6: Equal area projections for ChRM (characteristic remanent magnetization) of the
575 Pignola-2 (upper panel) and Dibona (lower panel).

576 Figure 7: Correlations between Tethyan sections of Late Triassic and their calibration with
577 the Newark Astrochronological Polarity Time Scale (APTS). The Norian to
578 Rhaetian calibration and correlations are after Maron et al. (2015). All correlations
579 between Tethyan sections are based on integrated conodont bio-
580 magnetostratigraphy. Biostratigraphy of Silická Brezová has been updated after
581 Mazza et al. (2010, 2011, 2012a,b). Pignola-2 provides a chronological tie point
582 with the Newark APTS (U/Pb age of 230.91±0.33 Ma; Furin et al., 2006) and part
583 of the Dibona magnetostratigraphy (MD1n) covers the missing interval in Pignola-
584 2. Correlation between Pignola-2 and the Newark APTS based on the statistical
585 method of Muttoni et al. (2004) and Maron et al. (2015).

586 Figure 8: Sequence of 24 correlation options between the Pignola-2 section and the Newark
587 APTS. Dark grey bars indicate the correlations that are reliable at the 90%, black
588 bars are the correlations reliable at the 95%. Only three options are reliable at 95%:
589 Options 1, 2 and 24. Option 24 was rejected because being inconsistent with the age
590 of Pignola-2, while Options 1 and 2 both covers an interval consistent with the
591 radiometric age of 230.91 Ma. In particular, preferred Option 1 is perfectly coherent

592 with the time constraint in Pignola-2 and with the previous correlation between
593 Pizzo Mondello section and the Newark APTS (Muttoni et al. 2004), performed
594 using the same statistical method.
595 Figure 9: Comparison between Option 1 and Option 2. Both Options 1 and 2 show a
596 discrepancy between the radiometric age of 230.91 (Furin et al. 2006) and the
597 corresponding level in the Newark APTS. In Option 1 is the age discrepancy (0.6
598 M.y.) is smaller than in Option 2 (0.9 M.y.). A possible cause of this age discrepancy
599 is the absence of astronomic cycles recorded below E8n, and the age is presumed
600 assuming sedimentation rates similar to the upper Lockatong Formation (Olsen and
601 Kent 1999).
602 Figure 10: Age model based on Option 1. The inclination of the trend lines of the plot
603 reflects the sedimentation rates, which decrease just after and before the "green
604 clay-radiolaritic horizon". The model provides an age of ~230.7 Ma for the
605 Julian/Tuvalian boundary and a duration of ~1 M.y. for the Carnian Pluvial Event.
606 Plate 1: Conodonts from samples DIN2 and DIN6. The fauna illustrated in the plate
607 includes *Paragondolella polygnathiformis*, *Paragondolella noah*, transitional
608 forms from *P. noah* to *Metapolygnathus praecommunisti* and *M. praecommunisti*.
609 The specimens of *M. praecommunisti* are basal, showing the accessorial node
610 behind the cusp, the posterior prolongation of the keel and a quite centrally located
611 pit, but no nodes on the anterior platform margins. The occurrence of basal
612 representatives of this species in sample DIN6, together with advanced *P. noah*,
613 suggests a lower Tuvalian age (Mazza et al. 2011; Mazza et al. 2012a). 1:
614 *Paragondolella polygnathiformis* (Budurov and Stefanov 1965) (DIN2); 1c: the
615 blade of the specimen got broken; 2: *Paragondolella noah* (Hayashi 1968)
616 transitional to *Metapolygnathus praecommunisti* Mazza, Rigo and Nicora 2011

(DIN6); 3: *Metapolygnathus* cf. *praecommunisti* (DIN6) Figs b-c: the blade termination got broken; 4: *Metapolygnathus* cf. *praecommunisti* (DIN6); 5-7: *Metapolygnathus praecommunisti* (DIN6). a: view from above; b: lateral view; c: view from below. All the conodonts are at the same scale.

Table 1: Mean directions from Pignola-2 and Dibona.

FIGURE 1

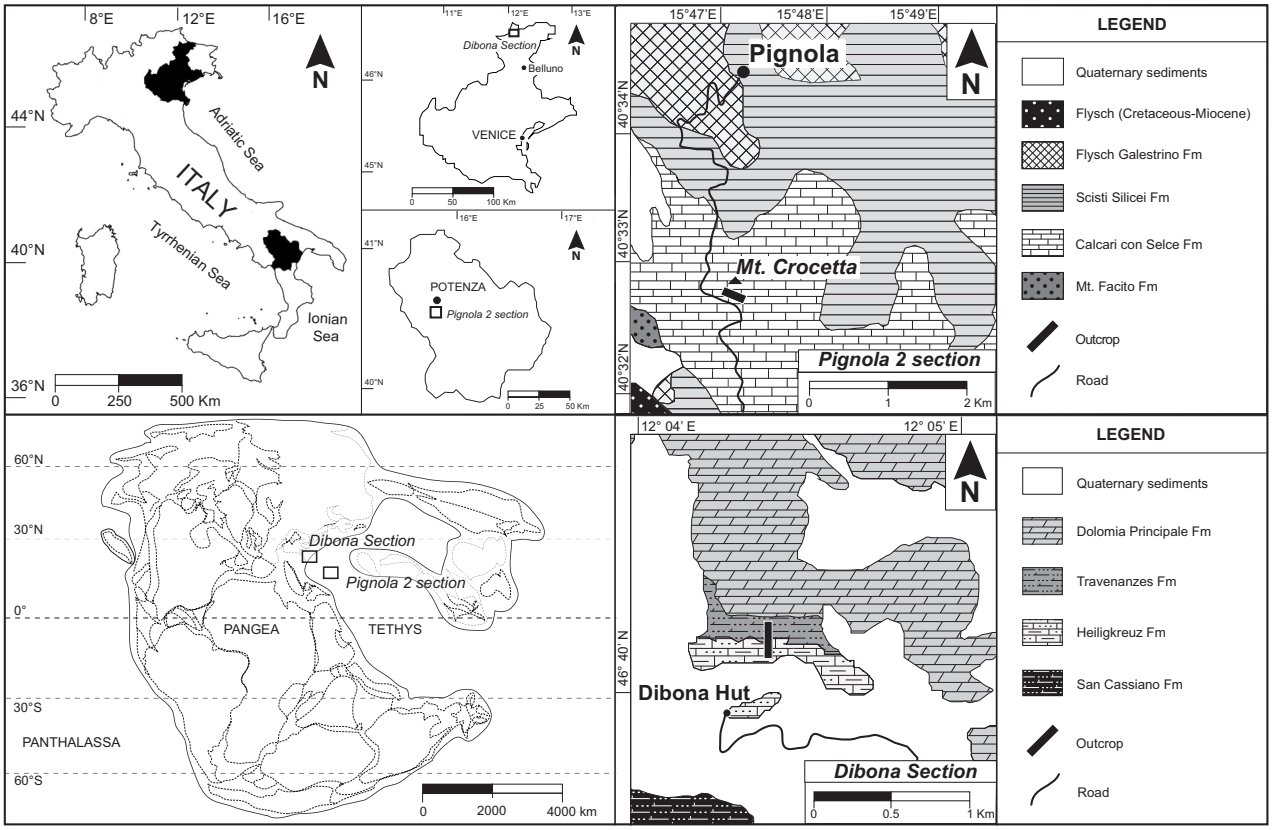

FIGURE 2

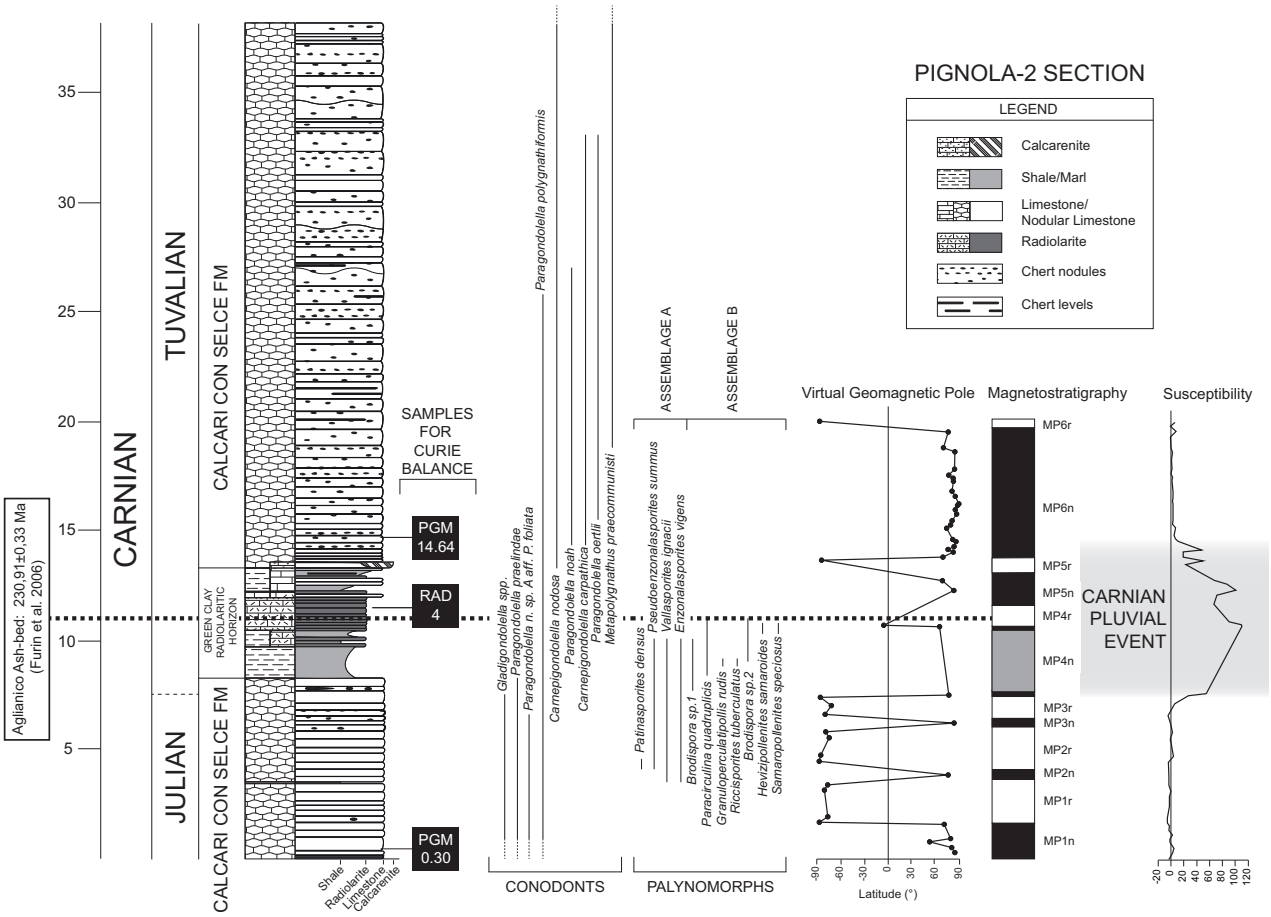

FIGURE 3

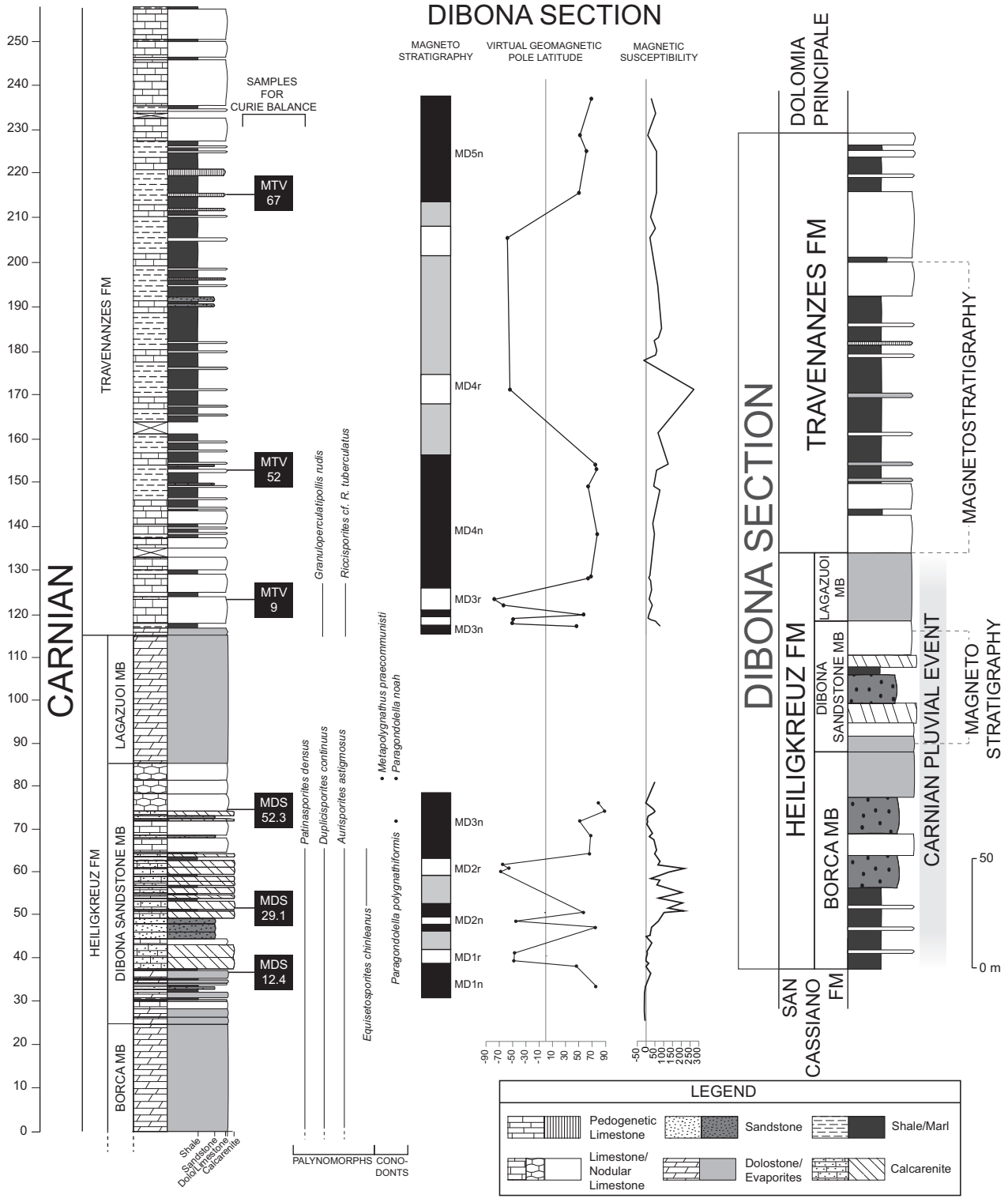
DIBONA SECTION
CARNIAN
TRAVENANZES FM
HEILIGKREUZ FM
LAGAZUOI MB
DIBONA SANDSTONE MB
BORCA MB
SAMPLES FOR CURIE BALANCE
MTV 67
MTV 52
MTV 9
MDS 52.3
MDS 29.1
MDS 12.4
Granuloperculatipollis rudis
Ricciisporites cf. R. tuberculatus
Patinasporites densus
Duplicisporites continuus
Aurisporites astigmosus
Equisetosporites chinleanus
• Metapolygnathus praecommunisti
• Paragondolella noah
Paragondolella polygnathiformis •
Shale
Sandstone
Dolostone
Limestone
Calcarenite
PALYNOMORPHS
CONO-DONTS
MAGNETO STRATIGRAPHY
VIRTUAL GEOMAGNETIC POLE LATITUDE
MAGNETIC SUSCEPTIBILITY
MD5n
MD4r
MD4n
MD3r
MD3n
MD3n
MD2r
MD2n
MD1r
MD1n
-90 -70 -50 -30 -10 10 30 50 70 90
-50 0 50 100 150 200 250 300
DOLOMIA PRINCIPALE
DIBONA SECTION
TRAVENANZES FM
HEILIGKREUZ FM
LAGAZUOI MB
DIBONA SANDSTONE MB
BORCA MB
SAN CASSIANO FM
MAGNETOSTRATIGRAPHY
CARNIAN PLUVIAL EVENT
MAGNETO STRATIGRAPHY
50
0 m
LEGEND
Pedogenetic Limestone
Sandstone
Shale/Marl
Limestone/ Nodular Limestone
Dolostone/ Evaporites
Calcarenite

FIGURE 4

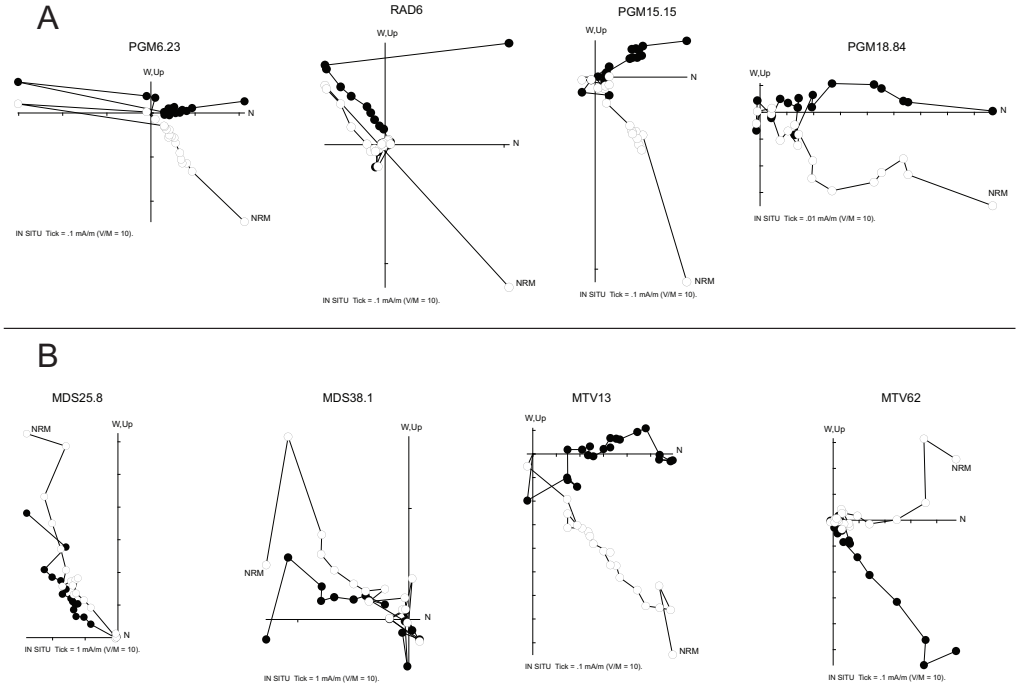

FIGURE 5

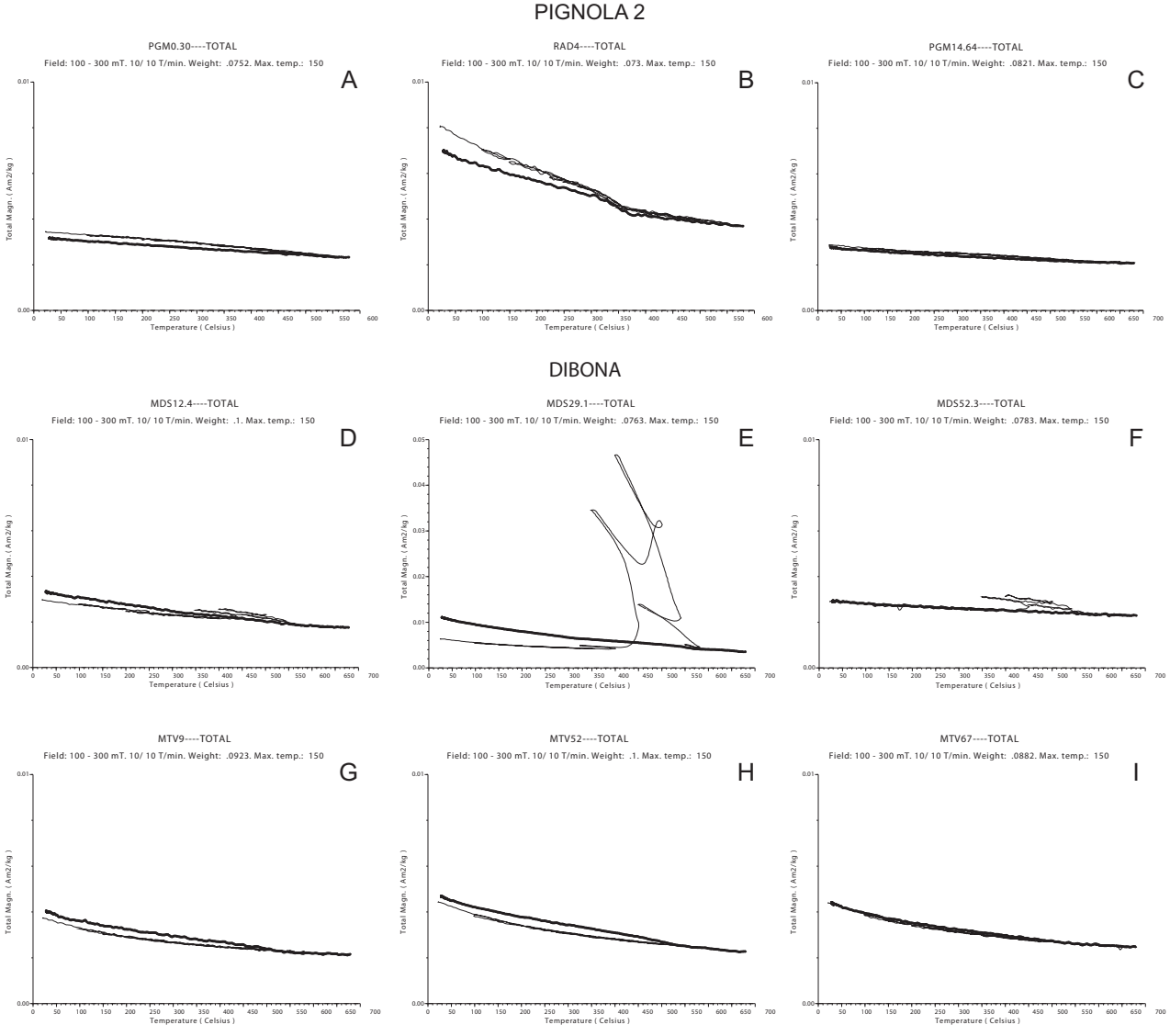

FIGURE 6

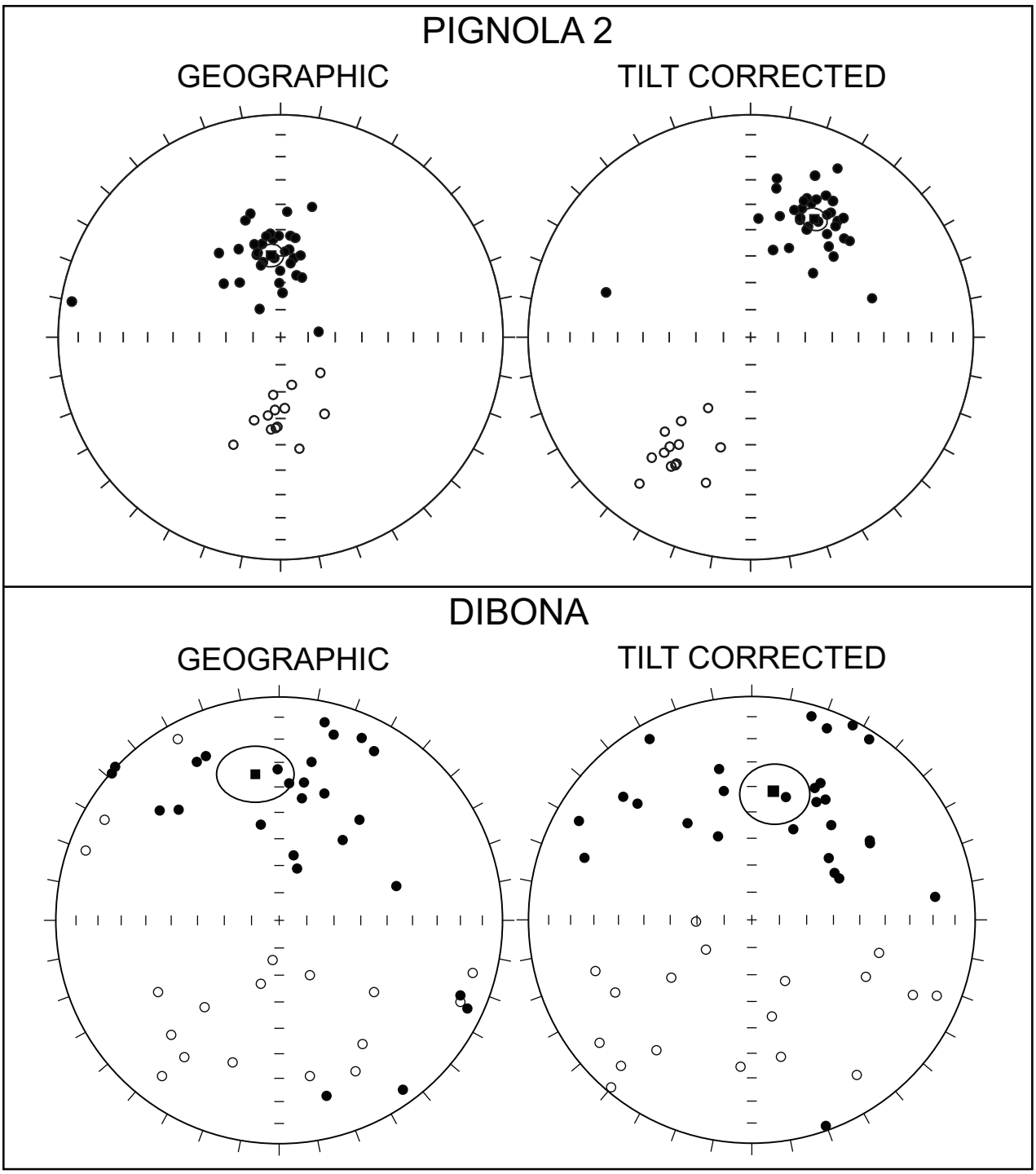
PIGNOLA 2
GEOGRAPHIC
TILT CORRECTED
DIBONA
GEOGRAPHIC
TILT CORRECTED

FIGURE 7

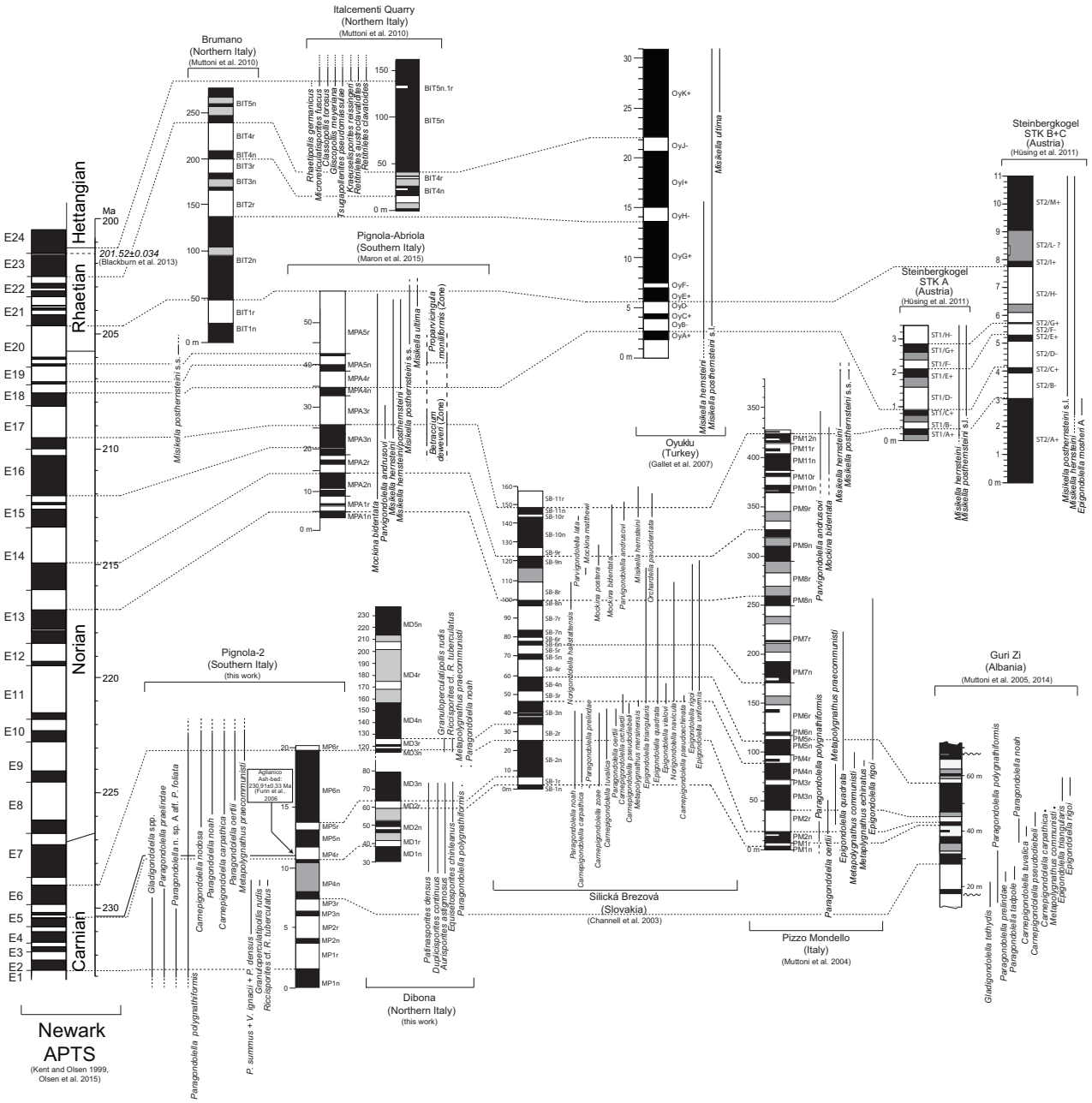
Newark APTS
(Kent and Olsen 1999, Olsen et al. 2015)
Hettangian
Rhaetian
Norian
Carnian
Ma
201.52±0.034
(Blackburn et al. 2013)
Brumano
(Northern Italy)
(Muttoni et al. 2010)
Italcementi Quarry
(Northern Italy)
(Muttoni et al. 2010)
Pignola-Abriola
(Southern Italy)
(Maron et al. 2015)
Oyuklu
(Turkey)
(Gallet et al. 2007)
Steinbergkogel
STK B+C
(Austria)
(Hüsing et al. 2011)
Steinbergkogel
STK A
(Austria)
(Hüsing et al. 2011)
Pignola-2
(Southern Italy)
(this work)
Silická Brezová
(Slovakia)
(Channell et al. 2003)
Guri Zi
(Albania)
(Muttoni et al. 2005, 2014)
Pizzo Mondello
(Italy)
(Muttoni et al. 2004)
Dibona
(Northern Italy)
(this work)
Agliancio
Ash-bed:
230.91±0.33 Ma
(Furin et al., 2006)

FIGURE 8

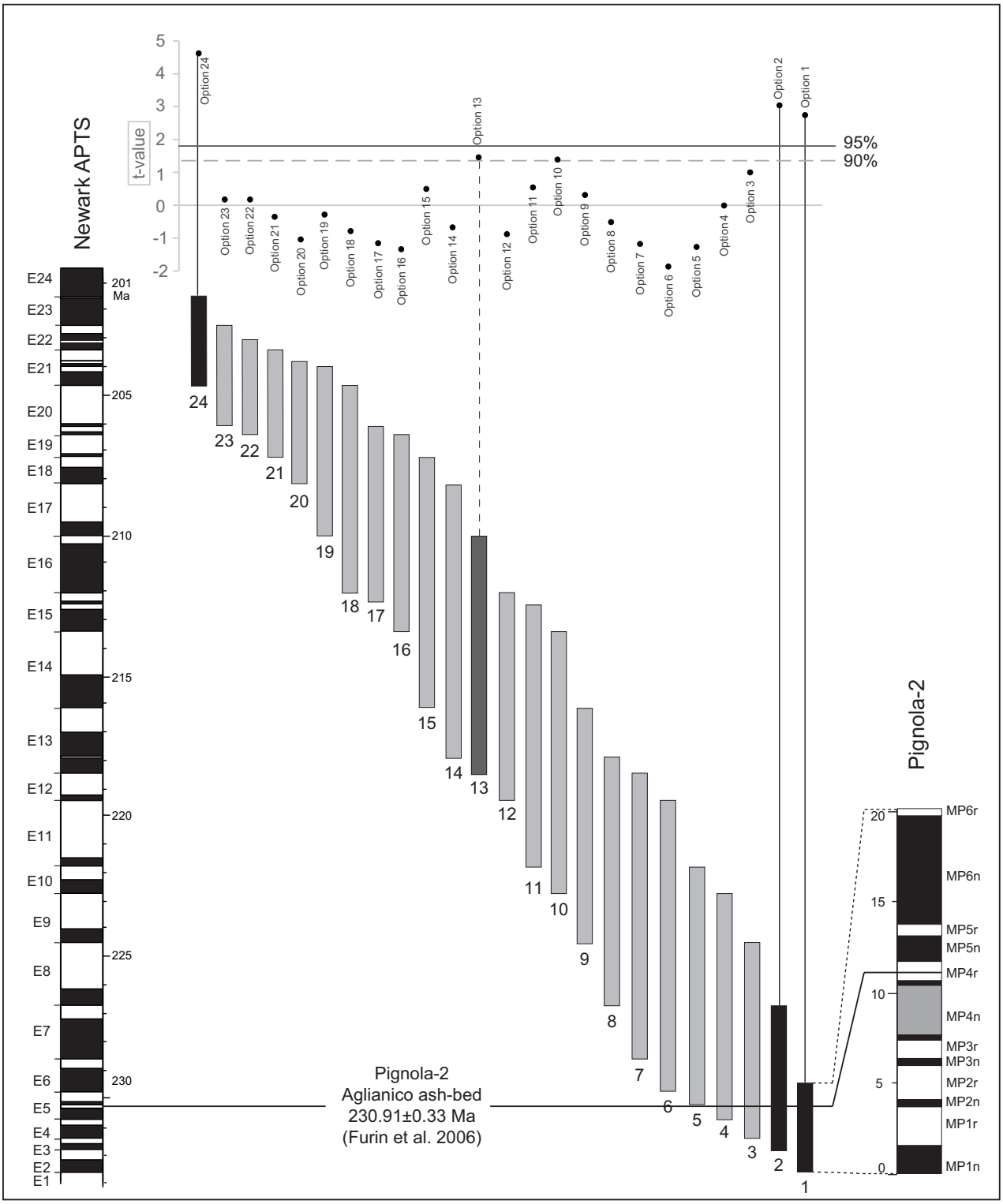
Newark APTS
t-value
5
4
3
2
1
0
-1
-2
95%
90%
Option 24
Option 23
Option 22
Option 21
Option 20
Option 19
Option 18
Option 17
Option 16
Option 15
Option 14
Option 13
Option 12
Option 11
Option 10
Option 9
Option 8
Option 7
Option 6
Option 5
Option 4
Option 3
Option 2
Option 1
E24
E23
E22
E21
E20
E19
E18
E17
E16
E15
E14
E13
E12
E11
E10
E9
E8
E7
E6
E5
E4
E3
E2
E1
201 Ma
205
210
215
220
225
230
24
23
22
21
20
19
18
17
16
15
14
13
12
11
10
9
8
7
6
5
4
3
2
1
Pignola-2
Aglianico ash-bed
230.91±0.33 Ma
(Furin et al. 2006)
Pignola-2
20
15
10
5
0
MP6r
MP6n
MP5r
MP5n
MP4r
MP4n
MP3r
MP3n
MP2r
MP2n
MP1r
MP1n

FIGURE 9

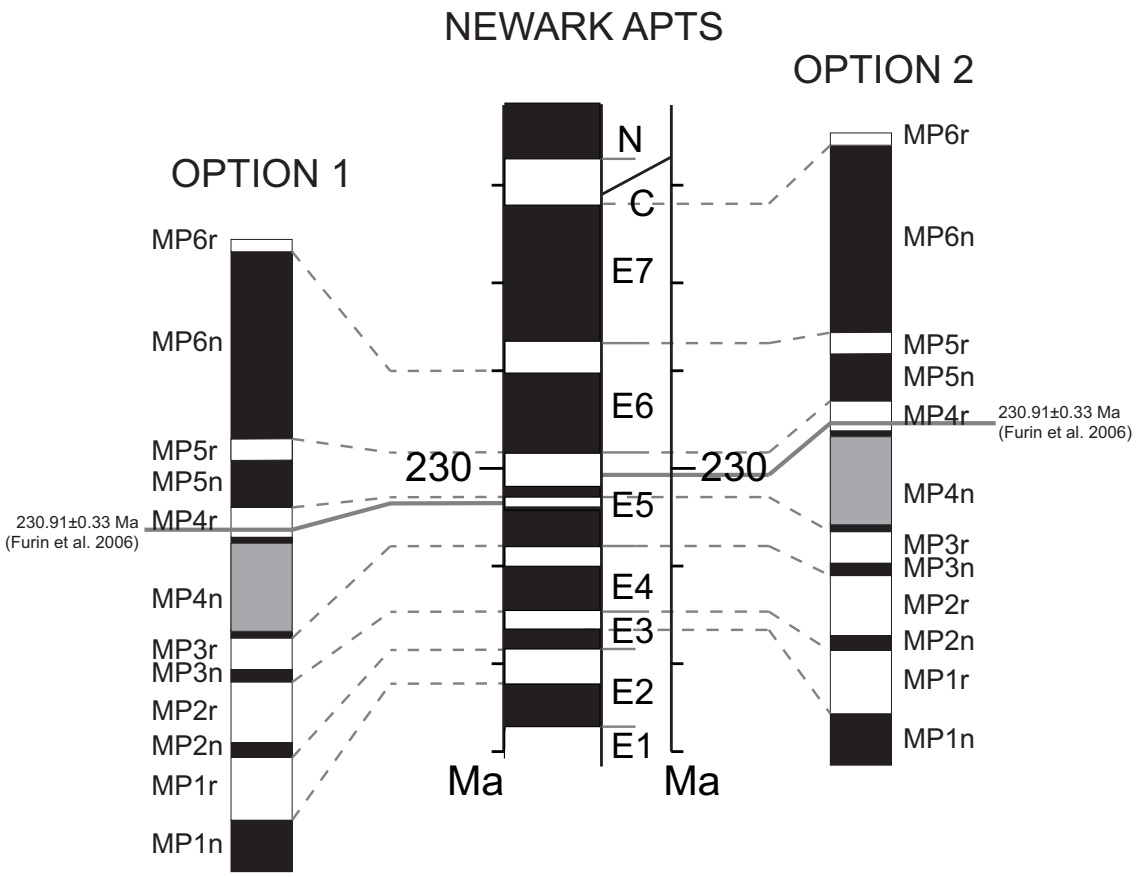

FIGURE 10

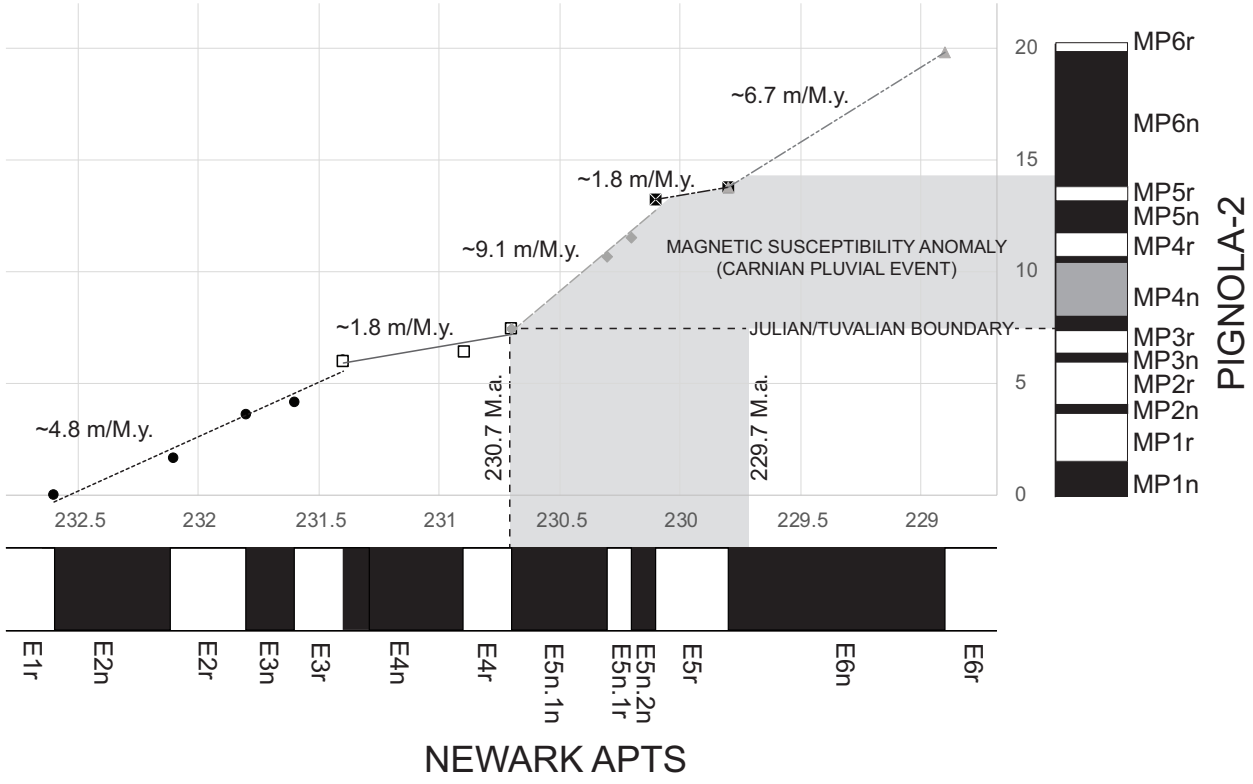

PLATE 1

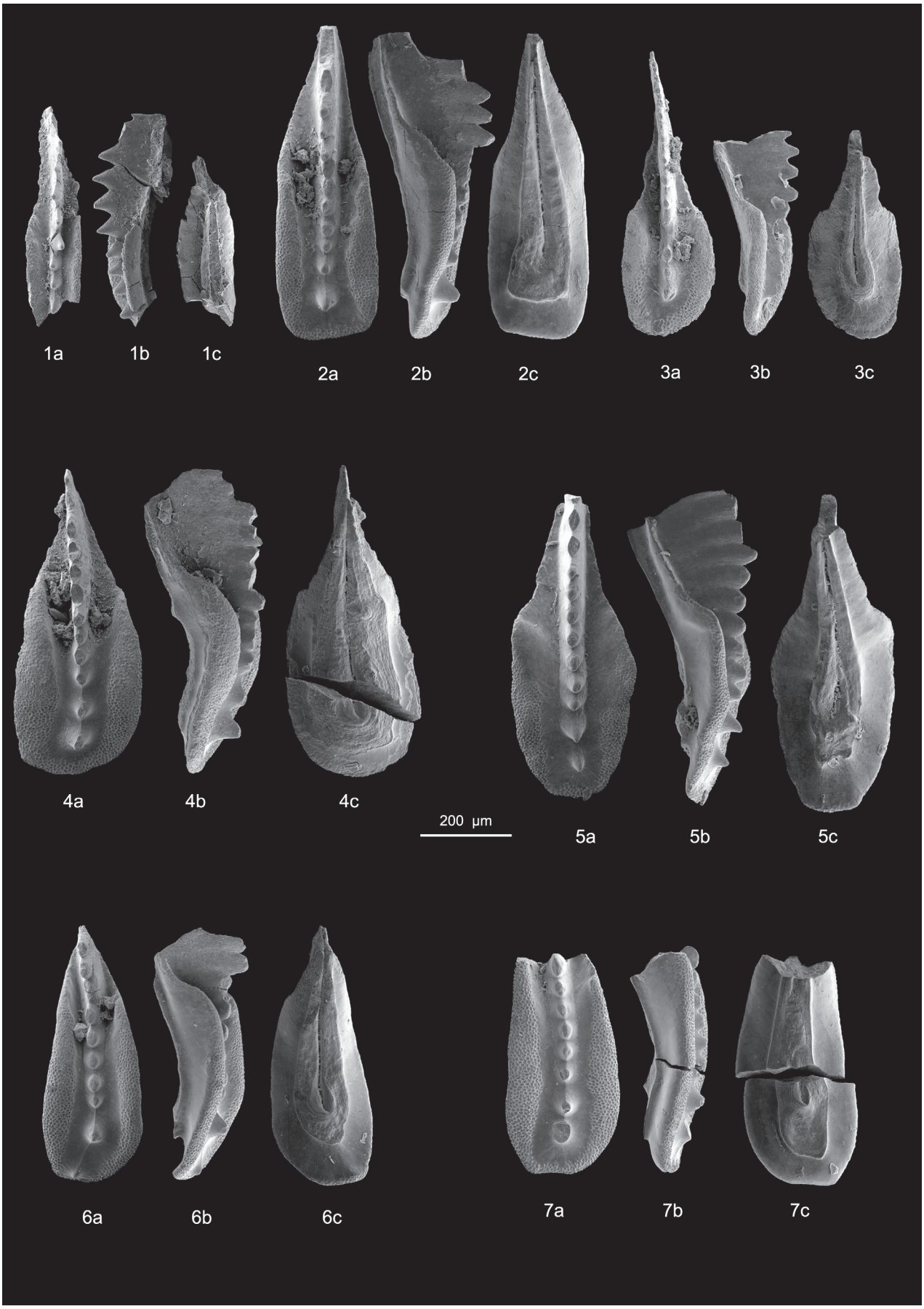

TABLE 1. PALEOMAGNETIC DIRECTIONS FROM PIGNOLA-2 AND DIBONA SECTIONS

			IN SITU				TILT-CORRECTED			
Site	Comp.	N	k	α_{95}	Dec.	Inc.	k	α_{95}	Dec.	Inc.
Pignola-2	ChRM	47	24.1	4.3°	353.5°E	59.7°	23.9	4.3°	28.4°E	39.6°
Dibona	ChRM	46	4.2	11.8°	350.5°E	33.9°	4.2	11.8°	10.2°E	41.4°

LEGEND

Comp.: paleomagnetic component N: number of samples k, α_{95}: Fisher statistics parameters Dec.: mean declination Inc.: mean inclination